A Search for a Heavy Majorana Neutrino at ATLAS Using 4.7 fb^{-1} of pp Collisions at $\sqrt{s} = 7$ TeV

A thesis submitted to the University of Manchester for the degree of Doctor of Philosophy in the Faculty of Engineering and Physical Sciences

2012

John Almond

Particle Physics Group
School of Physics and Astronomy

Contents

Total word count: 35288

Abstract

The discovery of neutrino oscillations provides evidence that the Standard Model neutrinos have mass. Many models generate the mass for the light neutrinos by postulating the existence of heavy neutrinos. This thesis presents the search for a heavy Majorana neutrino decaying into a W boson and a muon that was performed using the ATLAS detector at the LHC. The search is performed using final states with two same-sign muons, two or more high momentum jets and low missing transverse energy. The events are required to pass the ATLAS muon trigger and the improvements made in the muon trigger algorithms are also presented. The data used in this thesis were collected using pp collisions at $\sqrt{s} = 7$ TeV in 2011 and correspond to an integrated luminosity of 4.7 fb^{-1}. In the search no excess of events above the background prediction is observed and 95% confidence level upper limits are set on the cross section times branching ratio for the production of heavy Majorana neutrinos. Limits are set for heavy Majorana neutrinos with masses ranging from 100 to 300 GeV, in which the observed limits range between 28 to 3.4 fb. These are most stringent direct limits to date for heavy neutrino masses larger than 100 GeV.

Declaration

No portion of the work referred to in the thesis has been submitted in support of an application for another degree or qualification of this or any other university or other institute of learning.

Copyright

[1]See http://www.campus.manchester.ac.uk/medialibrary/policies/intellectual-property.pdf
[2]See http://www.manchester.ac.uk/library/aboutus/regulation

Acknowledgements

First of all I would like to thank my two supervisors, Professor Un-Ki Yang and Dr Mark Owen, for guiding me through the past four years, with much help and encouragement. Special thanks must be given to Mark, who has been there each step of the way and without whom this thesis would not have been possible. I would also like to give many thanks to all the friends I have made during this time, both at Manchester or at CERN, in particular Gareth and Vikash who have been with me for the full four years.

Without the work of Apostolos Pilaftsis I would not have had a model to search for, so I thank him also. I must also thank Bhupal Dev for taking the time to explain much of the theoretical side to me. My family have also helped me through this PhD. I would like to thank my Mother, Father as well as Ian and Corinne for their loving support.

Chapter 1

Introduction

This thesis presents a search for a heavy Majorana neutrino with mass at the electroweak scale, using final states with two same-sign muons and jets. The search uses data corresponding to an integrated luminosity of 4.7 fb^{-1} from pp collisions at $\sqrt{s} = 7$ TeV. This data was collected by the ATLAS detector of the Large Hadron Collider (LHC) at CERN during the 2011 operations. In addition the work on optimising the performance of the higher level ATLAS muon trigger is presented.

The aim of particle physics is to understand the fundamental building blocks of the universe. The most successful theory at present is the Standard Model (SM) which describes the fundamental particles of matter and the forces that act upon them. Predictions made by the SM have been extensively tested and are found to be in good agreement with experimental results, including the discovery of the $W^{\pm}$ and Z bosons in 1983 at the Super Proton Synchrotron collider at CERN.

One of the questions that was unanswered until recently was how the particles obtain their mass. The gauge symmetries in the SM describe the interaction of the fundamental particles but, require particles to be massless. In 1964 the theorist Peter Higgs [1] explained how mass can be given to particles in the SM through spontaneous symmetry breaking of the gauge symmetries. This theory, known as the Higgs Mechanism, predicts the existence of a new particle, called the Higgs particle. A new particle with the characteristics of the SM Higgs was discovered at the Large Hadron Collider in 2012 [2, 3]. Neutrinos in the SM are massless. However the recent discovery [4] of neutrino oscillations established that at least two of the observed neutrinos have non-zero mass. This discovery requires new physics beyond the SM and one common extension of the SM involves adding right-handed neutrinos such that the light neutrinos obtain a Majorana mass through the see-saw mechanism [5, 6, 7].

The simplest extension of the SM to include Majorana neutrinos is to add at least two right-handed singlet neutrinos. This generates massive neutrinos, N, which are produced without any additional new interactions. As a consequence the heavy neutrinos can be

produced and decay through mixing with the leptons of the SM. Unlike in the case of the traditional see-saw mechanism, which requires the mass of the heavy neutrinos, m_N, to be several orders of magnitude heavier than the electroweak scale, the heavy neutrino masses can be generated by inter generational mixing, allowing m_N to be at the electroweak scale [8].

The discovery of heavy neutrinos would have a huge impact on many fields, including particle physics, cosmology and nuclear physics, and may help to understand the symmetries of physics at beyond the SM. It will provide a direct observation of the lepton number violation and open a door to probe CP violation in the neutrino sector at the LHC.

The main body of this thesis describes the search for such a heavy neutrino at the LHC. The thesis is structured as follows: The theory and the motivation behind the search for a Majorana neutrino are discussed in chapter 2. This includes the calculation of the leading order cross section for the model of interest and also reviews the previous searches. In chapter 3 the LHC accelerator chain is discussed and a detailed description of the ATLAS detector is given. The muon triggers used in this analysis and the improvements made on these triggers by the author are presented in chapter 4. The Monte Carlo samples for signal and background processes are described in section 5, with the reconstruction of the physics objects introduced in chapter 6.

Chapter 7 describes the data sample used in the search, as well as the event selection criteria. Also discussed is the optimisation of the signal region. Various correction applied to the physics objects are discussed in chapter 8. A description of the background estimation is given in chapter 9. These background estimations are validated using the data in chapter 10, which also contains a discussion of the systematic uncertainties. The comparison of the data with the expected backgrounds in the signal region, and the results of the search are presented in chapter 11. The thesis finishes with the conclusions in chapter 12.

Chapter 2

Theoretical Background

This chapter describes the motivation behind the search presented in this thesis. Section 2.1 is an overview of the Standard Model, describing the particles that makes up the known universe and the forces that act upon them. A more extensive description of the Standard Model can be found in [9]. The generation of mass in the Standard Model is discussed in section 2.2. Section 2.3 discusses neutrino physics, and explains how neutrino oscillations imply non-zero neutrino masses and requires a new theory beyond the Standard Model to explain these experimental results. It also proposes new models that may introduce mass to the Standard Model neutrinos. Section 2.4 discusses previous searches for these models, outlining the current limits and introduces the possible search modes at the LHC. The cross section for the simplest extension to the Standard Model is calculated in section 2.5, where the expected sensitivity is discussed.

2.1 The Standard Model

During the past few decades a set of theories have been introduced, that describe the interactions of all the known elementary particles, through the strong, weak and electromagnetic forces. Collectively these theories make up the Standard Model of elementary particle physics.

In the view of the Standard Model all matter consists of two classes of elementary particles: bosons and fermions. There are 12 fermions, all with spin 1/2, including six quarks (the up, down, strange, charm, bottom and top), and three leptons (the electron, muon and tau), with each lepton having an associated neutrino. Furthermore each of these particles, which we can describe mathematically as a fermion field, Ψ, has an associated anti-particle, $\bar{\Psi}$.

The fermions are grouped into three generations, each with two leptons and two quarks. These are listed in Table 2.1. Within each generation the particles are classified by their electrical charge and the generations are ordered in mass. The leptons and quarks are assigned distinct quantum numbers. The leptons are assigned a lepton number (L) equal to 1 while

Generation	I	II	III	Electrical Charge
Leptons	$\begin{pmatrix} \nu_e \\ e^- \end{pmatrix}$	$\begin{pmatrix} \nu_\mu \\ \mu^- \end{pmatrix}$	$\begin{pmatrix} \nu_\tau \\ \tau^- \end{pmatrix}$	0 -1
Quarks	$\begin{pmatrix} u \\ d \end{pmatrix}$	$\begin{pmatrix} c \\ s \end{pmatrix}$	$\begin{pmatrix} t \\ b \end{pmatrix}$	$2/3$ $-1/3$

Table 2.1: The fundamental fermions in the Standard Model, grouped into generations.

anti-leptons are assigned a lepton number of -1. The quarks and anti-quarks are assigned a baryon number (B) of $\pm 1/3$ respectively. The Standard Model upholds the conservation of these quantum numbers. For any interaction that occurs the sum of L and B of the incoming particles has to be equal to the sum of the outgoing particles. However cosmology expects there to be baryon number violating processes, to explain the asymmetry in the baryons and anti-baryons in the universe. This would allow the decay of the proton, which has not yet been observed experimentally. Although lepton flavour violation is known to exist (i.e., in neutrino oscillations, where an electron neutrino from the sun may oscillate into a muon or tau neutrino as it propagates through space), charged lepton violation has not yet been observed (i.e., the sum of all leptons minus the sum of all anti-leptons is conserved in all interactions). Some Grand Unified Theories (GUT) allow for the violation of both these quantum numbers simultaneously, but postulate that the sum of baryon and lepton number is a conserved quantity.

A multiplicative quantum number that is not conserved in all interactions is charge parity. This quantum number describes the behaviour of a particle under the symmetry operation of charge conjugation. The charge conjugation operator C changes the sign of all quantic charges i.e., electrical charge, baryon number, lepton number, isospin, flavour charges, but leaves spatial properties such as momentum and spin unchanged.

A fundamental property of the Standard Model is gauge invariance of the theory under local transformations. The Standard Model is constructed by building an interaction Lagrangian that satisfies gauge invariance. As a result of the gauge invariance under the $\mathrm{SU}(3)_C \times \mathrm{SU}(2)_L \times \mathrm{U}(1)_Y$ gauge transformations, five gauge bosons for strong, electromagnetic and weak interactions are predicted, as presented in Table 2.2. The interaction of matter is understood as the exchange of these gauge bosons, which include the photon, known to mediate the electromagnetic force, the gluon that mediates the strong force and the $W^\pm$ and Z vector bosons that mediate the weak force. The gravitational force is not included in the model, and a Grand Unified Theory to include the gravitational force is still the aim of many theorists.

In the case of the weak and the strong forces the non-abelian nature of the theory has the consequence that they can have self interactions. Evidence of all four gauge bosons have been seen experimentally, with the photon and gluon known to be massless and the W and Z

Interaction	Mediator(s)	Range [m]	Relative Strength
strong	gluon	10^{-15}	1
electromagnetic	photon (γ)	∞	1/137
weak	Z, $W^{\pm}$	10^{-17}	10^{-5}
gravity	graviton	∞	10^{-39}

Table 2.2: Fundamental forces of the Standard Model. The relative strengths taken from [9].

boson masses measured as 91.187 ± 0.0021 GeV [10] and 80.375 ± 0.023 GeV [11] respectively. The electromagnetic and weak forces were unified into the Glashow-Weinberg-Salam theory of electroweak (EW) interactions and the strong force is described by the theory of Quantum Chromo Dynamics (QCD).

2.1.1 Quantum Chromo Dynamics

The theory of QCD describes the strong interactions between the quarks and gluons under the $\mathrm{SU(3)}_C$ gauge group. A field that is invariant under $\mathrm{SU(N)}_C$ transformation has N degrees of freedom. The field transformation under this group is

$$\Psi \rightarrow \Psi' = e^{-i\omega^a T^a}\Psi \tag{2.1}$$

where T^a are the $N^2 - 1$ generators of the gauge group. The generators do not commute i.e., $[T^a, T^b] = if^{abc}T^c$, where f_{abc} are the structure constants of the group. This results in 8 generators (gluons) with three degrees of freedom for the $\mathrm{SU(3)}_C$ transforms, that can occur self interactions. The degrees of freedom are referred as colour (blue, green and red), which is why the gauge group adopts the index C. The Lagrangian that describes the massless fermions, Ψ, is given by

$$\mathcal{L}_{Dirac} = \bar{\Psi}(i\gamma^\mu \partial_\mu)\Psi \tag{2.2}$$

where γ^μ are the Dirac matrices (with γ^0 being a unit matrix and $\gamma^{1,2,3}$ representing the Pauli matrices $\sigma_{1,2,3}$) and ∂_μ are the spatial and time partial derivatives. This Lagrangian is not invariant under the transform shown in equation 2.1. To restore the symmetry the partial derivative, ∂_μ, is replace by a covariant derivative, D_μ, which is a 3×3 matrix in this representation, and is given by

$$\mathbf{D}_\mu = \partial_\mu \mathbf{I} + ig_s T^a G^a_\mu \tag{2.3}$$

where $\mathbf{I}$ is the unit matrix. This suggests that the spinor quark field Ψ interacts with the eight gluon fields, G^a_μ, with a coupling strength g_s. We must consider terms involving G^a_μ that can be added to the theory. In order to keep the Lagrangian invariant the only term

that can be added is the kinematic term,

$$-\frac{1}{4}G^a_{\mu\nu}G^{a\mu\nu} \tag{2.4}$$

where the gluon strength tensor, $G^a_{\mu\nu}$, is given by

$$G^a_{\mu\nu} = \partial_\mu G^a_\nu - \partial_\nu G^a_\mu - g_s f^{abc} G^b_\mu G^c_\nu. \tag{2.5}$$

These terms in the Lagrangian provide gluon self interactions.

This Lagrangian is used to calculate the cross section for quark gluon interactions. The leading order cross section for interactions involving gluons and quarks is related to the coupling g_s. In reality the leading order term is not sufficient, and higher order terms are required for a precise calculation. The coupling term g_s depends on the scale at which we measure (probe) at. The convention to define the strong coupling is to use α_s, where $\alpha_s = g_s^2/4\pi$. In the leading order, the dependence of α_s on the probing energy scale Q is given by

$$\alpha_S(Q^2) = \frac{12\pi}{(33 - 2n_f)\log(Q^2/\Lambda^2)} \tag{2.6}$$

where n_f is the number of available quark flavours with mass below Q^2. As Q^2 becomes large (when quarks are close together), the strength of the coupling becomes weak and quarks and gluons behave as free particles, known as asymptotic freedom. Thus it is possible to compute these interactions in terms of α_s (perturbation theory). However as $Q^2 \to \Lambda$ the coupling becomes infinite, meaning that perturbation theory is not applicable. The scale Λ is the hadron scale where α_S is so strong that coloured objects are bound into colourless states, which is known as quark confinement. The hadron scale is a free parameter of the theory and is measured experimentally to be $\Lambda = 217 \pm 25$ MeV, for $n_f = 5$ [12].

2.1.2 Electro-Weak Theory

In 1967 Glashow, Salam and Weinberg unified the theories of quantum electro dynamics with the theory of the weak interactions. The underlying symmetry of this theory is based on the $\mathrm{SU}(2)_L \times \mathrm{U}(1)_Y$ gauge group. Considering $\mathrm{U}(1)_Y$ transforms, where Y is the hypercharge of the field, it is noted that $\mathcal{L}_{Dirac}$ is not invariant under the local phase transform

$$\Psi \to e^{i\omega(x)Y}\Psi \tag{2.7}$$

in which the addition term

$$\Delta\mathcal{L} = Y\bar{\Psi}\gamma_\mu[\partial_\mu\omega(x)]\Psi \tag{2.8}$$

is added to the $\mathcal{L}_{Dirac}$. Similarly to the procedure used to restore the symmetry in QCD the partial derivative, ∂_μ, is replaced with the covariant derivative, D_μ,

$$\partial_\mu \rightarrow D_\mu + ig'YB_\mu \tag{2.9}$$

with the requirement that this new vector field, B_μ, transforms as

$$B_\mu \rightarrow B_\mu + \frac{1}{g'}\partial_\mu\omega(x) \tag{2.10}$$

under the local transform. As a result a new field B_μ is introduced to the theory, and a new interaction term is added to the Lagrangian

$$\mathcal{L}_{int} = -g'Y\gamma^\mu\bar{\Psi}B_\mu\Psi. \tag{2.11}$$

This implies the fermion fields interact with the field B_μ with a coupling strength g'. The Lagrangian to describe leptons under this theory can be expressed in terms of the Dirac spinors Ψ_ℓ and Ψ_ν as

$$\mathcal{L} = i(\bar{\Psi}_\ell\gamma^\mu\partial_\mu\Psi_\ell) + i(\bar{\Psi}_\nu\gamma^\mu\partial_\mu\Psi_\nu). \tag{2.12}$$

The Standard Model is a chiral theory, where particles can either have left- or right-handed chirality. This handedness associates the spin of the particle to its direction of motion. As a result the lepton spinor, and similarly for the quark spinors, can be separated into left-handed and right-handed terms such as

$$\Psi_\ell = \Psi_{\ell L} + \Psi_{\ell R}. \tag{2.13}$$

The left- or right-handed state can be obtained using the projection operator

$$P_{R,L} = \frac{1}{2}(1 \pm \gamma^5), \tag{2.14}$$

such that $P_L\Psi = \Psi_L$ and $P_R\Psi = \Psi_R$. The left-handed fermions transform under SU(2) as doublets, with the left-handed lepton doublet, L_ℓ having the form

$$L_\ell = \begin{pmatrix} \Psi_{\nu_\ell,L} \\ \Psi_{\ell,L} \end{pmatrix}. \tag{2.15}$$

However right-handed neutrinos do not exist in the Standard Model, meaning that right-handed leptons transform as singlets under SU(2). This is known from observations of parity violating processes in weak interactions. The Lagrangian can therefore be expressed in terms

of left- and right-handed doublets and left-handed singlets

$$\mathcal{L}_{Dirac,\ell} = i\left(\bar{\Psi}_{\nu L}\bar{\Psi}_{\ell L}\right)\gamma^{\mu}\partial_{\mu}\begin{pmatrix}\Psi_{\nu L}\\ \Psi_{\ell L}\end{pmatrix} + i(\bar{\Psi}_{\nu R}\gamma^{\mu}\partial_{\mu}\Psi_{\nu R}) \tag{2.16}$$

For the first term to be invariant under an SU(2) transform a covariant derivative D_{μ} is introduced that replaces the partial derivative given by

$$\partial_{\mu} \rightarrow \partial_{\mu} + ig\frac{1}{2}W_{\mu}^{k}\sigma_{k} \tag{2.17}$$

where $\sigma_{k=1,2,3}$ are the Pauli matrices and are the generators of the SU(2) group, and $W_{\mu}^{k=1,2,3}$ are three new gauge fields. Expanding the Pauli matrices and substituting in $W^{\pm} = \frac{1}{\sqrt{2}}(W^{1} \mp iW^{2})$, the weak Lagrangian can be written as

$$\begin{aligned}\mathcal{L}_{Dirac,\ell} &= -\frac{g}{2}(W_{\mu}^{3}(\bar{\Psi}_{\nu L}\gamma^{\mu}\Psi_{\nu L} - \bar{\Psi}_{\ell L}\gamma^{\mu}\Psi_{\ell L}) \\ &= -\frac{g}{\sqrt{2}}W_{\mu}^{+}(\bar{\Psi}_{\nu L}\gamma^{\mu}\Psi_{\ell L}) - \frac{g}{\sqrt{2}}W_{\mu}^{-}(\bar{\Psi}_{\ell L}\gamma^{\mu}\Psi_{\nu L})\end{aligned} \tag{2.18}$$

The $W^{\pm}$ are identified as the physical $W^{\pm}$ bosons we observe in nature. The Z boson and photon can be introduced by including the Lagrangian from equation 2.11. The choice then is that

$$\begin{pmatrix}A_{\mu}\\ Z_{\mu}\end{pmatrix} = \begin{pmatrix}\cos\theta_{W} & \sin\theta_{W}\\ -\sin\theta_{W} & \cos\theta_{W}\end{pmatrix}\begin{pmatrix}B_{\mu}\\ W_{\mu}^{3}\end{pmatrix} \tag{2.19}$$

where A_{μ} is the photon field and θ_{W} is the weak mixing angle relating the electromagnetic and weak coupling strengths.

2.2 Masses in the Standard Model

The massive spin half fermions are described by the Dirac equation,

$$(i\gamma_{\mu}\partial^{\mu} - m)\,\Psi = 0 \tag{2.20}$$

where m is the fermion mass. As explained, this fermion field can be written in terms of left- and right-handed components with $\Psi = (\Psi_{\mathrm{L}}, \Psi_{\mathrm{R}})$. Then, the Dirac equation can be written in terms of left- and right-handed fields as:

$$\begin{pmatrix}-m & i\left(\frac{\partial}{\partial t} + \sigma\cdot\bigtriangledown\right)\\ i\left(\frac{\partial}{\partial t} - \sigma\cdot\bigtriangledown\right) & -m\end{pmatrix}\begin{pmatrix}\Psi_{\mathrm{L}}\\ \Psi_{\mathrm{R}}\end{pmatrix} = \begin{pmatrix}0\\ 0\end{pmatrix} \tag{2.21}$$

where δ_0 is the time derivative. This leads to coupled equations where Ψ_L and Ψ_R are mixed by a mass term. This form is not gauge invariant as there are terms that mix left- and right-handed states. Thus the Standard Model requires all fermions to be massless. But this is not what we observe in nature, for example the muon mass is known to very high precision of $105.6583715 \pm 0.0000035$ MeV [10], using natural units, with $\hbar = c = 1$.

In addition the theory predicts the gauge bosons to be massless, the mass terms for bosons, $mV^\dagger V$, where V denotes the boson gauge field, is not gauge invariant.

Spontaneous Symmetry Breaking In Electro-Weak Sector

In the Standard Model, masses of both the fermions and the bosons can be introduced by including the Higgs Mechanism [1], which gives mass to the particles via spontaneous symmetry breaking of the electroweak gauge symmetries. This is achieved by adding a complex scalar field, Φ, that transforms as a doublet in SU(2) and has Y=1/2. The scalar field Φ is described by the Lagrangian

$$\mathcal{L}_{scalar} = (\partial_\mu \Phi)^* (\partial^\mu \Phi) - V(\Psi) \tag{2.22}$$

with the potential V chosen as

$$V = \mu^2 (\Phi^* \Phi) + \lambda (\Phi^* \Phi)^2 \tag{2.23}$$

where $\mu^2 < 0$ and $\lambda > 0$. The potential has a minimum when $\Phi_1^2 + \Phi_2^2 + \Phi_3^2 + \Phi_4^2 = -\frac{\mu^2}{\lambda} = v^2$. There are infinite choices that satisfy this condition, i.e., there are an infinite number of ground states for this potential. As a result the ground state is no longer invariant under the $\mathrm{SU}(2)_L$ transform. Using the fact we know the photon is massless, Φ is taken to be

$$\phi = \frac{1}{\sqrt{2}} \begin{pmatrix} 0 \\ v + H \end{pmatrix} \tag{2.24}$$

where H is the Higgs field, that has a vacuum energy of v. Inserting this doublet into the Lagrangian of the electroweak theory, a set of interaction terms between the Higgs and the gauge bosons appear as well as the mass terms

$$\frac{g^2 v^2}{4} W^{+,\mu} W^-_\mu + \frac{g^2 v^2}{8} \left(W^3_\mu - \frac{g'}{g} B_\mu \right)^2 . \tag{2.25}$$

This predicts a W boson mass of $\frac{gv}{2}$ and a Z boson with mass $\frac{gv}{2} \cos\theta_W$, using equation 2.19.

With $v = 246$ GeV, $\sin^2\theta_W = 0.2315$, $e = \sqrt{4\pi\alpha_{EM}}$, with $\alpha_{EM} \approx 1/128$ the predicted masses of the W and Z bosons are $M_W^\pm \approx 80$ GeV/c^2 and $M_Z^\pm \approx 91$ GeV/c^2. This agrees

very well with experimental measurement [10].

The masses of the fermions in the Standard Model are generated by Yukawa couplings with the Higgs field. The Yukawa terms for the leptons include

$$\begin{aligned}\mathcal{L}_{\text{Yuk}} &= -Y_c(\bar{L}_{\ell\text{L}}\Phi\Psi_{\ell R}) + \text{h.c} \\ &= -\frac{Y_c v}{\sqrt{2}}\bar{\Psi}_\ell\Psi_\ell - \frac{Y_c}{\sqrt{2}}\bar{\Psi}_\ell H\Psi_\ell\end{aligned} \tag{2.26}$$

where Y_c is the Yukawa coupling. The first term gives rise to the lepton masses, and the second term is an interaction term between the leptons and the Higgs field. It is not possible to add a mass term in this way for neutrinos as there are no right-handed neutrinos in the Standard Model. There must therefore be some new physics.

For the quarks the picture is different as the mass eigenstates are not the same as the weak eigenstates that couple to the W or Z bosons. The mixing between the mass eigenstates q and flavour eigenstates q' can be described by the Cabibbo-Kobayashi-Maskawa (CKM) matrix [13, 14]. The matrix is given as

$$\begin{bmatrix} d' \\ s' \\ b' \end{bmatrix} = \begin{bmatrix} V_{ud} & V_{us} & V_{ub} \\ V_{cd} & V_{cs} & V_{cb} \\ V_{td} & V_{ts} & V_{tb} \end{bmatrix} \begin{bmatrix} d \\ s \\ b \end{bmatrix} \tag{2.27}$$

The terms relate to the coupling between any two quarks.

In addition to providing mass to the particles in the Standard Model, this Higgs Mechanism predicts a spin-0 Higgs boson. A new particle with the characteristics of the Standard Model Higgs boson, was discovered by the ATLAS and CMS experiments during 2012 and found to have mass of about 125 GeV [2, 3], suggesting that the Higgs mechanism is behind the mass generation of the Standard Model particles. It is important to note again that since the Standard Model does not have right-handed neutrinos, the neutrinos do not get a Yukawa coupling term. As a result the neutrinos do not acquire mass through spontaneous symmetry breaking and this suggests a new physics mechanism.

2.3 Neutrinos

Neutrinos are electrically neutral spin-1/2 particles, first postulated by Pauli in 1930. Due to their weak interaction with matter they were first detected by Reines, Cowen, Harrison, Kruse and McGuire in 1956 [15]. Their experiment, for which Cowan and Reines won the Nobel Prize in 1995, used a nuclear reactor to produce a large flux of neutrinos, which were detected by placing a scintillator material in a large tank of water. The scintillator material would give off light in response to gamma rays which are produced by the interaction of a neutrino with protons in the tank of water. There are now known to be three active light neutrinos [16]. Since neutrinos have no electrical charge they are a candidate for being Majorana in nature, where a Majorana particles is its own anti-particle. See Table 2.4 for comparisons of Majorana and Dirac particles.

The sun produces a large number of ν_e through nuclear fusion. This is described by the Solar Model. In 1964 an experiment performed in the Homestake mine, by Raymond Davis [17], gave birth to the 'The Solar Neutrino Problem', by observing a deficit in neutrinos (electron neutrinos) from the sun. Pontecorvo and Gribov in 1969 [18] theorised the idea of neutrino oscillations, a quantum mechanical process where the neutrino can change flavour.

The first direct evidence of neutrino oscillations came in 1998 when the Super-Kamiokande experiment [4] observed a deficit of muon neutrinos from the atmosphere and showed first signs of ν_μ disappearance. This was later supported by the Kamland reactor experiment that confirmed the disappearance of $\bar{\nu}_e$. The SNO experiment was the first experiment to be sensitive to both electron and muon neutrino flavours, and concluded that the total number of neutrinos observed agreed with the solar model prediction.

2.3.1 Neutrino Oscillations and their Implications

Neutrino oscillations imply that a neutrino produced in a well defined flavour eigenstate, after propagating large enough distances, can be detected in a different flavour eigenstate. This means that neutrinos have mass, and that the neutrino flavour eigenstates are different from the mass eigenstates. For simplicity we consider just two generations of neutrinos, for which we label the two mass states ν_1 and ν_2 respectively. The two flavour states, (ν_e, ν_μ), are given by

$$\begin{pmatrix} \nu_e \\ \nu_\mu \end{pmatrix} = V \begin{pmatrix} \nu_1 \\ \nu_2 \end{pmatrix} = \begin{pmatrix} \cos\theta_{12} & \sin\theta_{12} \\ -\sin\theta_{12} & \cos\theta_{12} \end{pmatrix} \begin{pmatrix} \nu_1 \\ \nu_2 \end{pmatrix} \tag{2.28}$$

If we consider the time dependent Schrodinger equation,

$$H.\Psi = i\frac{d\Psi}{dt} \tag{2.29}$$

with H being the diagonal Hamiltonian $\begin{pmatrix} E_1 & 0 \\ 0 & E_2 \end{pmatrix}$, the evolution of the mass states in a vacuum are then given by:

$$\nu_1(t) = e^{-iE_1 t}\nu_1(0) \tag{2.30}$$

$$\nu_2(t) = e^{-iE_2 t}\nu_2(0). \tag{2.31}$$

If we then rotate this basis by the rotational matrix V in equation 2.28, we form a new representation, where the new flavour basis, ν_e and ν_μ, are a superposition of the original basis, ν_1 and ν_2. In this new basis the Schrodinger equation still holds with $\Psi \to \tilde{\Psi}$ and $H \to \tilde{H} = VHV^{-1}$, where the new Hamiltonian that is no longer diagonal, and is given by

$$\tilde{H} = \begin{pmatrix} \frac{1}{2}(E_1+E_2) + \frac{1}{2}(E_1-E_2)\cos 2\theta_{12} & \frac{1}{2}(E_2-E_1)\sin 2\theta_{12} \\ \frac{1}{2}(E_2-E_1)\sin 2\theta_{12} & \frac{1}{2}(E_1+E_2) - \frac{1}{2}(E_1-E_2)\cos 2\theta_{12} \end{pmatrix}. \tag{2.32}$$

We are now able to write the evolution of the flavour states with time as

$$\begin{pmatrix} \nu_e(t) \\ \nu_\mu(t) \end{pmatrix} = \begin{pmatrix} e^{-iE_1 t}\cos\theta_{12} & e^{-iE_2 t}\sin\theta_{12} \\ -e^{-iE_1 t}\sin\theta_{12} & e^{-iE_2 t}\cos\theta_{12} \end{pmatrix} \begin{pmatrix} \nu_1 \\ \nu_2 \end{pmatrix}. \tag{2.33}$$

The probability that a particle with initial flavour state α is in a state β at some time t is given by the amplitude squared of the initial and final states,

$$P_{\alpha\beta} = |<\beta|\alpha(t)>|^2 \tag{2.34}$$

$$= \sin^2(2\theta_{12})\sin^2\frac{(E_2-E_1)}{2}t \tag{2.35}$$

$$= \sin^2(2\theta_{12})\sin^2\frac{(m_2^2-m_1^2)}{4E}t \qquad = \sin^2(2\theta_{12})\sin^2\left(\frac{\Delta m_{12}^2}{4E}t\right) \tag{2.36}$$

where θ_{12} and Δm_{12} are the mixing angle and mass differences between the two mass states.

If we now reconsider oscillation in three neutrino generations. The eigenstates ν_α ($\alpha = e, \mu, \tau$) can be related to the mass eigenstates, ν_i, by $\nu_\alpha = \sum_i U_{\alpha i}\nu_i$. The matrix U is unitary and can be written as VK, where V is parametrised as

$$V = \begin{bmatrix} c_{12}c_{13} & s_{12}c_{13} & s_{13}e^{-i\delta} \\ -s_{12}c_{23} - c_{12}s_{23}s_{13}e^{-i\delta} & c_{12}c_{23} - s_{12}s_{23}s_{13}e^{-i\delta} & s_{23}c_{13} \\ s_{12}c_{23} - c_{12}s_{23}s_{13}e^{-i\delta} & -c_{12}c_{23} - s_{12}s_{23}s_{13}e^{-i\delta} & c_{23}c_{13} \end{bmatrix} \tag{2.37}$$

while K = $\mathrm{diag}(1, e^{i\phi_1}, e^{i(\phi_2+\delta)})$. This is known as the Pontecorvo-Maki-Nakagawa-Sakata (PMNS) neutrino mixing matrix [19, 20]. The c_{ij} and s_{ij} refer to the sine and cosine of the mixing angles while Δm_{ij} are the mass differences of the flavour states. The phase angles ϕ_1 and ϕ_2 are only meaningful if the neutrinos are Majorana and the phase factor δ relates to

Oscillation parameter	best fit $\pm 1\sigma$	2σ	3σ
Δm^2_{21} [10^{-5} eV^2]	$7.59^{+0.20}_{-0.18}$	7.24-7.99	7.09-8.19
Δm^2_{31} [10^{-3} eV^2]	2.45 ± 0.09	2.28-2.64	2.18-2.73
	-($2.34^{+0.10}_{-0.09}$)	-(2.17-2.54)	-(2.08-2.64)
$\sin^2\theta_{12}$	$0.312^{+0.017}_{-0.015}$	0.28-0.35	0.27-0.36
$\sin^2\theta_{23}$	0.51 ± 0.06	0.41-0.61	0.39-0.64
	0.51 ± 0.06	0.41-0.61	
$\sin^2\theta_{13}$	$0.010^{+0.009}_{-0.006}$	≤ 0.027	≤ 0.039
	$0.013^{+0.009}_{-0.007}$	≤ 0.031	≤ 0.039

Table 2.3: Summary of current measurements on neutrino oscillation parameters [22]. For Δm^2_{31}, $\sin^2\theta_{23}$ and $\sin^2\theta_{13}$, the upper (lower) row correspond to normal (inverted) neutrino mass hierarchy.

the level of Charge-Parity (CP) violation in the neutrino sector. Neutrino experiments have now measured the value of all the mass differences and mixing angles which are summarised in Table 2.3. However the δ, $\phi_{1,2}$ and the sign of Δm^2_{23} are still all unknown. The atmospheric mass splitting and angles are measured at the Super-Kamiokande experiment along with the K2K and MINOS long baseline accelerator experiments, which observed disappearance of ν_μ and $\bar{\nu}_\mu$. A number of experiments have seen a deficit in the solar neutrino flux, and have contributed to the measurement on θ_{12} from $\nu_e \to \nu_e$, along with the KamLand experiment. The last mixing angle to be measured was θ_{13}, and was measured by a number of experiments including Daya Bay and the RENO experiment in 2012 [21]. A recent update on the global neutrino data analysis was performed, see Ref. [22]. The results are presented in Table 2.3. The discovery of neutrino oscillations along with the oscillation parameters shown in Table 2.3 indicate that at least 2 out of the 3 Standard Model neutrinos do indeed have mass. While the observation of neutrino oscillations shows neutrinos have mass, the results are only sensitive to the difference between the square of the masses, and the absolute mass scale is still unknown.

The most stringent upper limits on the sum of light neutrino masses come from cosmology, such as studies of the cosmic microwave background and Lyman-alpha forest, which constrain the summed masses of the three light neutrinos to be less than 0.3 eV [16]. The are also strong limits on the mass of the neutrinos from experiments. The electron neutrino mass has an upper limit of 2.2 eV from the Mainz experiment [23], which uses the beta decay spectrum of Tritium. A future tritium beta decay experiment, KATRIN [24], is believed to be capable of having sub-eV sensitivity.

The remaining questions still unanswered on the theory of neutrino physics include:

- What is the absolute mass scale of the neutrinos and why are the observed neutrino masses so small?
- What is the mass hierarchy of the neutrinos?

Dirac	Majorana
$\nu \neq \bar{\nu}$	Its own anti-particle $\nu = \bar{\nu}$
4 states ν_R,ν_L, $\bar{\nu_R}$, $\bar{\nu_L}$ Two sterile neutrinos	2 states ν_L, $\bar{\nu_R}$
mass term $-\mathcal{L} = m_D(\bar{\psi_L}\psi_R + \bar{\psi_R}\psi_L)$	mass term $-\mathcal{L} = \frac{1}{2}m_L(\bar{\psi_L}\psi_R^C + \bar{\psi_R^C}\psi_L) + (\bar{\psi_L^C}\psi_R + \bar{\psi_R}\psi_L^C)$

Table 2.4: Table listing the different characteristics between Dirac particles and Majorana particles.

- What is the size of the CP violation in the neutrino sector?
- Are neutrinos Dirac or Majorana?

The answers to these questions will contribute in the understanding the physics at high energies of the early universe, and can help us to decipher the physics beyond the Standard Model.

2.3.2 How to Generate Neutrino Masses

We know that in the SM, the left-handed neutrinos are massless mainly due to the absence of a right-handed counterpart, which removes the possibility of gaining a Dirac mass term. In addition the conservation of a global $B-L$ symmetry removes the possibility of Majorana mass terms. As a consequence, in order to generate non-zero neutrino masses, one must extend the SM neutrino sector by either adding at least one right-handed neutrino or by introducing some $(B-L)$-breaking fields or even both [25].

If we simply add the right-handed neutrinos, while preserving $(B-L)$, then we would require the new Yukawa coupling (Y_ν), which involves the interaction of the right-handed neutrino (N) and the left-handed neutrino (ν_L) given by $Y_\nu \bar{L} H N$, to be many orders of magnitude smaller than the Yukawa couplings for the other SM fermions, i.e., we would require $Y_\nu \lesssim 10^{-12}$ in order to give sub-eV left-handed neutrino masses. In the absence of a natural understanding of such smallness of Y_ν, a more elegant way to explain the smallness of the mass of ν_L is by breaking the $(B-L)$.

The simplest way to parametrize the $B-L$ symmetry breaking in SM extensions is by adding a Weinberg's dimension-5 [26] operator

$$\mathcal{L}_{eff} = \lambda_{ij}\frac{L_i L_j H H}{M}(i,j = e,\mu,\tau) \tag{2.38}$$

which could be added to the SM lagrangian, where M is the scale of some new physics. After EWSB, due to the Higgs' vev v, this new operator leads to a non-zero neutrino mass term

with the form $m_\nu = \lambda v^2/M$. For light neutrino masses at the sub-eV scale this leads to $M/\lambda \geq 10^{14}$ GeV, and for very small Yukawa coupling the new physics scale M can be in the TeV range, which is accessible at the LHC. The tree-level realisation of equation 2.38 is the well known seesaw mechanism.

Seesaw Type-I Mechanism

The simplest seesaw is the type-I seesaw [27, 28, 29], in which the heavy particles are right-handed neutrino singlets (N), which couple to the left-handed doublets through Dirac Yukawa terms,

$$\mathcal{L}_Y = (Y_\nu \bar{L} H N + h.c) + N M_N N, \tag{2.39}$$

where M_N is the Majorana mass of the right-handed neutrino N. The neutrino mass matrix that is formed after EWSB has the form,

$$\mathcal{M}_\nu = \begin{bmatrix} 0 & M_D \\ M_D^T & M_N \end{bmatrix}, \tag{2.40}$$

where $M_D = vY_\nu$. The mass eigenvalues for the light neutrinos are then given by

$$m_\nu = -v^2 Y_\nu M_N^{-1} Y_\nu^T. \tag{2.41}$$

From equation 2.41 we see that if M_N is at the TeV scale, then the size of the Dirac Yukawa term must satisfy $Y_\nu \lesssim 10^{-6}$, unless there is some form of cancellations due to underlying symmetries [30]. These cancellations may result in light neutrinos with small or even zero mass. In the case where the tree level mass is zero, it is possible that the mass of the light neutrino be introduced radiatively through loop level processes [8]. Since the heavy right-handed neutrino is a SM singlet it can be produced at colliders only via light and heavy neutrino mixing after virtual bosons are produced in parton collisions and decay leptonically ($l(\bar{\nu}) + \nu$). The interaction Lagrangian for the new heavy neutrino and the SM bosons are

$$\begin{aligned}
\mathcal{L}_W &= -\frac{g}{\sqrt{2}} \left(\bar{\ell} \gamma^\mu V_{\ell N} P_L N \, W_\mu + \bar{N} \gamma^\mu V_{\ell N}^* P_L \ell \, W_\mu^\dagger \right), \\
\mathcal{L}_Z &= -\frac{g}{2c_W} \left(\bar{\nu}_\ell \gamma^\mu V_{\ell N} P_L N + \bar{N} \gamma^\mu V_{\ell N}^* P_L \nu_\ell \right) Z_\mu, \\
\mathcal{L}_H &= -\frac{g \, m_N}{2 M_W} \left(\bar{\nu}_\ell \, V_{\ell N} P_R N + \bar{N} \, V_{\ell N}^* P_L \nu_\ell \right) H,
\end{aligned} \tag{2.42}$$

where the mixing elements $V_{\ell N}$ determine the coupling between the heavy neutrinos and SM leptons and $P_{L(R)}$ are the left(right)-handed projection operators. This thesis concentrates on searches for heavy neutrinos in the seesaw type-I model. The LHC sensitivity to this model has been discussed extensively in the literature [8, 31, 32, 33, 34, 35], with an estimated

sensitivity of $10 < m_{\mathrm{N}} < 400$ GeV with 30 fb^{-1} of 14 TeV data.

Seesaw Type-II Mechanism

An alternative way of writing the operator in equation 2.38 is $(L^T\vec{\tau}L).(H^T\vec{\tau}H)/M$, where τ^i are the Pauli matrices. This operator can be implemented by adding an $\mathrm{SU(2)_L}$ scalar triplet $\vec{\Delta} \equiv (\Delta^{++}, \Delta^{+}, \Delta^{0})$ which couples to the SM leptons through Majorana coupling terms. This model is known as a type-II seesaw [36, 29, 37, 38, 39]. Since Δ are SM non-singlets they can couple to the SM bosons, and be produced at the LHC if their mass is at the TeV scale [40, 41].

Seesaw Mechanism Type-III

Again another way of writing the operator shown in equation 2.38 is $(L^T\vec{\tau}H)^2/M$. This can be implemented by adding an $\mathrm{SU(2)_L}$ fermionic triplet ($\vec{\Sigma}$) which couples to leptons though Dirac Yukawa terms in a similar way to the type-I seesaw. This model is known as a type-III seesaw [42]. The difference between type-I and type-III is that in this case the triplet fermions couple directly to the SM W [43].

Inverse Seesaw Mechanism

A completely different seesaw mechanism is the inverse seesaw [44, 45, 46]. In this case one does not add one set of SM singlet fermions but instead adds two sets: N (Dirac) and S (Majorana).

A summary of these different mechanisms can be found in Ref. [47]. In the seesaw mechanism the Majorana mass terms are regarded as a by product of a more fundamental model. Some of these include models with exotic Higgs, R-Parity violating interactions in Supersymmetry (SUSY) and Left-Right symmetric gauge theories.

2.3.3 Left-Right Symmetric Model

The Left-Right Symmetric Model [48, 49, 50] (LRSM) is a GUT-inspired extension of the SM to a gauge symmetry of higher order represented by $\mathrm{SU(3)}_C \times \mathrm{SU(2)_L} \times \mathrm{SU(2)_R} \times \mathrm{U(1)_{B-L}}$, in which left- and right chiral fields are treated equally. This theory provides a natural explanation for the seesaw scale in terms of the $\mathrm{SU(2)_R} \times \mathrm{U(1)_{B-L}}$ breaking scale.

One of the consequences of this model is that it requires the presence of a new heavy W_R gauge boson. This can lead to an enhanced production cross section for the heavy neutrinos in the seesaw type-I model, as exploited by the current LHC searches in this channel [51, 52].

2.4 Searches for Heavy Neutrinos

This section outlines the previous searches for heavy Majorana neutrinos, and the limits on the coupling between this neutrino and the Standard Model leptons.

2.4.1 Review of Previous Searches

In non-collider experiments, a number of searches have been performed looking for sterile neutrinos in the mass range 100 eV - 100 GeV, with no evidence of sterile neutrinos to date [53, 54, 55]. The mixing parameter can be tested in searches for kinks in the energy spectrum of leptons from decays of pions and kaons. Such searches provide useful probes for investigating the coupling between heavy neutrinos with both electrons and muons. A heavy neutrino produced from a light meson decay would produce a monochromatic line at

$$E_\ell = \frac{m_M^2 + m_\ell^2 - m_N^2}{2m_M} \tag{2.43}$$

where E_ℓ and m_ℓ are the lepton energy and mass respectively, m_M is the mass of the meson and m_N is the mass of the heavy neutrino [56]. This is helped by the fact that the helicity suppression of the leptonic decays of the pion and kaon are weakened at large neutrino masses. Another possibility is to search for the decay of heavy neutrinos into visible particles, as performed by the LEP experiment, where the decay of Z bosons into heavy neutrinos was investigated. This provides the limits on the coupling over a large mass range. However if a decay mode to non-visible particles is dominant, these limits would be weakened. A detailed discussion on the current limits can be found in Ref. [31].

In 2011 the ATLAS and CMS experiments at the LHC set limits on the production of heavy Majorana neutrinos [57, 52] in the context of the Left-Right Symmetric Model.

Mixing with ν_e

Figure 2.1 reports the most stringent limits on this coupling $|V_{eN}|$, from equation 2.42, for neutrino masses below 100 GeV from limits on π [58] and K [59] peak searches and from L3 [60] and DELPHI [61] experiments at LEP, looking for heavy neutrinos in Z decays. The area within the contour lines are excluded by the searches at 90% Confidence Level (C.L.). The limits from DELPHI and L3 are at 95% C.L.. The stringent limits set by neutrinoless double beta decay are also shown.

Mixing with ν_μ

The limits on the coupling $|V_{\mu N}|$ come from searches for peaks in muon decays of light mesons [62] which have sensitivity up to the scale of 100 MeV and decays of N in muon

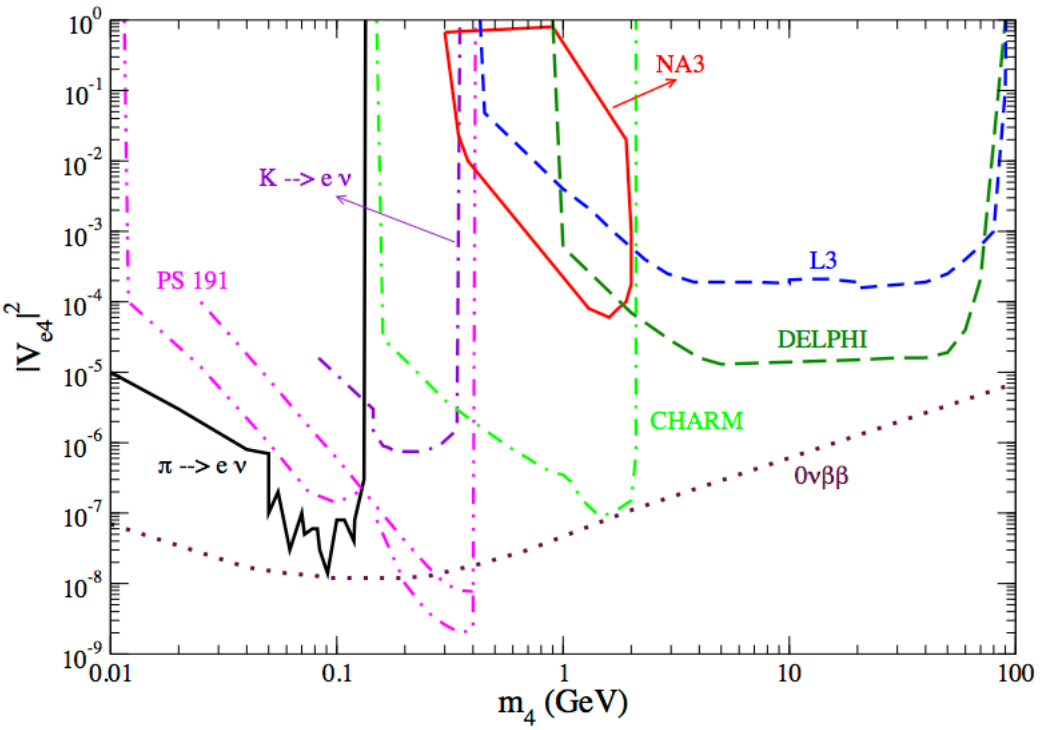

Figure 2.1: Bounds on $|V_{eN}|^2$ vs heavy neutrino mass in the range 10 MeV to 100 GeV [31].

neutrino beams from the CHARM experiment and the L3 experiments which are sensitive to neutrino masses between 0.3 and 100 GeV. Figure 2.2 reports the most stringent limits on this coupling term for masses below 100 GeV.

Mixing with ν_τ

The only limits on the coupling of heavy neutrinos with τ leptons come from searches for heavy neutrino decays. These are presented in Figure 2.3, where the results from CHARM [63] and NOMAD [64] assumed production of the heavy neutrino via D meson and τ decays. The DELPHI experiment looks for heavy neutrinos in Z decays.

Electroweak Precision Tests

There are a number of precision measurements made in the Standard Model that are used to constrain the coupling $|V_{\ell N}|$. Additional heavy neutral fermions affect decay processes below their mass due to their mixing with Standard Model neutrinos [65]. This allows for stringent bounds to be set on the couplings using electroweak data. The effective μ-decay constant G_μ, measured in muon decays, is modified with respect to the Standard Model value. The

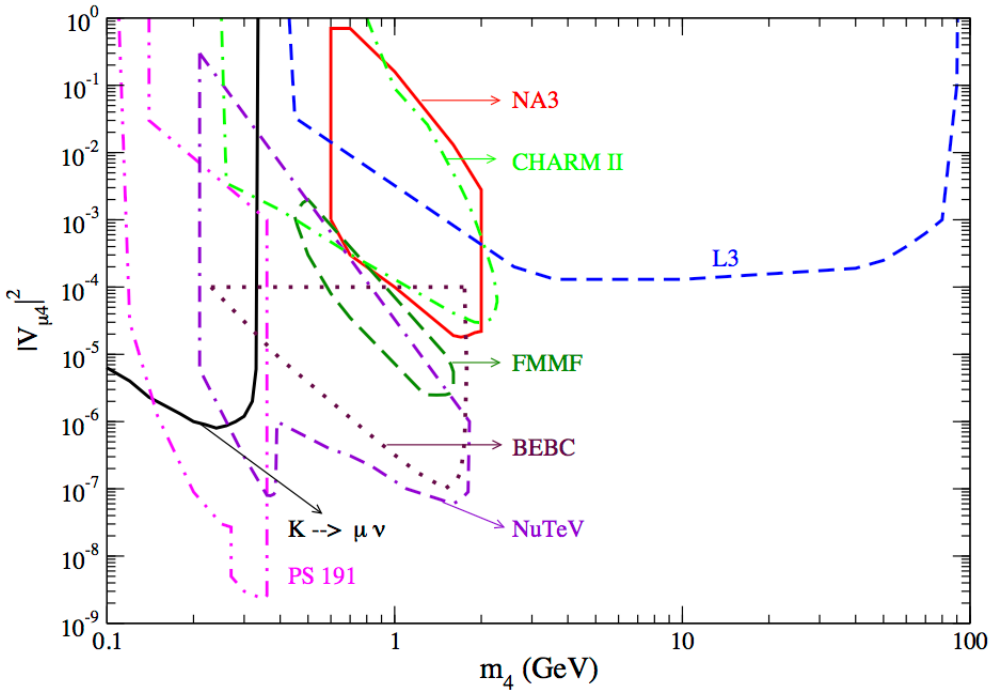

Figure 2.2: Limits on $|V_{\mu N}|^2$ versus heavy neutrino mass in the mass range 100 MeV to 100 GeV [31].

decay rates of the pion into electrons and muons can be used to constrain the ratio

$$\frac{1-|\mathrm{V}_{eN}|^2}{1-|\mathrm{V}_{\mu N}|^2} \tag{2.44}$$

for the case that the mass of the neutrino is larger than the pion mass [65, 66]. Using the unitarity constraint of the CKM matrix [10] we have

$$\sum_{i=1,2,3} |V_{ui}^{CKM}|^2 = \frac{1}{1-|V_{\mu N}|^2} = 0.9992 \pm 0.0011, \tag{2.45}$$

providing strong bounds on the coupling $|\mathrm{V}_{\mu N}|$.

Overall Limits on the Coupling Terms $|\mathrm{V}_{\ell N}|$

A combined analyses of the results mentioned above have set bounds on the coupling parameters at 90 % C.L. [66, 67], constraining the quantities

$$\Omega_{\ell\ell'} \equiv \delta_{\ell\ell'} - \sum_{i=1}^{3} V_{\ell\nu_i} V_{\ell'\nu_i}^* = \sum_{j=1}^{n} V_{\ell N_j} V_{\ell' N_j}^* \tag{2.46}$$

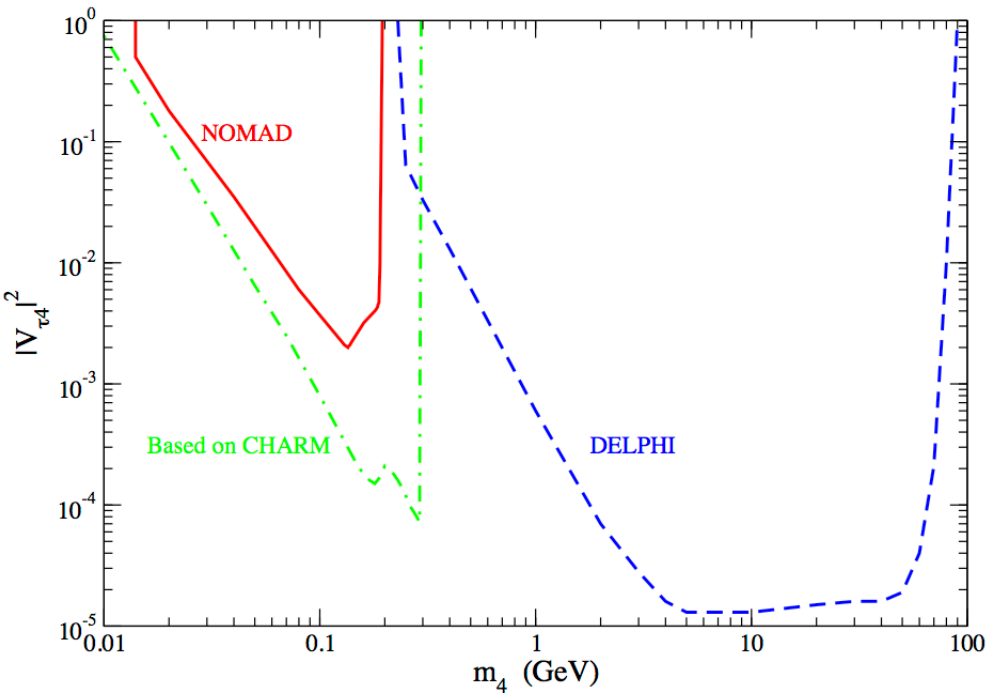

Figure 2.3: Bounds on $|V_{\tau N}|^2$ versus heavy neutrino masses from searches of decays of heavy neutrinos, given by (CHARM) and in (NOMAD) at 90% C.L., and in (DELPHI) at 95% C.L.. [31]

to be

$$\Omega_{ee} \leq 3.0 \times 10^{-3}\,, \quad \Omega_{\mu\mu} \leq 3.2 \times 10^{-3}\,, \quad \Omega_{\tau\tau} \leq 6.2 \times 10^{-3}. \tag{2.47}$$

A stringent bound on the coupling of the heavy neutrinos to the electron comes from the limits on neutrinoless double beta decay [68], as depicted in Figure 2.4, which constrains

$$\left| \sum_{i=1}^{n} \frac{V_{eN_i}^2}{m_{N_i}} \right| < 5 \times 10^{-8} \ \ \text{GeV}^{-1}. \tag{2.48}$$

For a neutrino mass of $m_{\rm N} = 300$ GeV, this corresponds to a limit on $|V_{eN}^2| < 1.5 \times 10^{-5}$, which is more than one order of magnitude stronger than the limits for the muon coupling shown in equation 2.47.[1] The flavour violating final states such as $e^{\pm}\mu^{\pm}$ are further disfavoured by constraints on flavour changing neutral-current processes. In the limit $m_{N_j}^2 \gg M_W^2 \gg |V_{\ell N_j}|^2 m_{N_j}^2$, these constraints imply [69]

$$|\Omega_{e\mu}| \leq 0.0001\,, \quad |\Omega_{e\tau}| \leq 0.01\,, \quad |\Omega_{\mu\tau}| \leq 0.01\,, \tag{2.49}$$

[1]Note, it is possible to avoid the neutrinoless double beta decay limits by arranging for cancellations in the term $\sum_{i=1}^{n} \frac{V_{eN_i}^2}{m_{N_i}}$. However, this is highly model dependent and so we do not consider this situation in this thesis.

that the final state of a same-sign electron and muon pair is disfavoured. Due to the tight limits on the coupling on the electron and the constraints of flavour mixing final states, only the muon channel is considered in this analysis, i.e., $V_{eN} = V_{\tau N} = 0$.

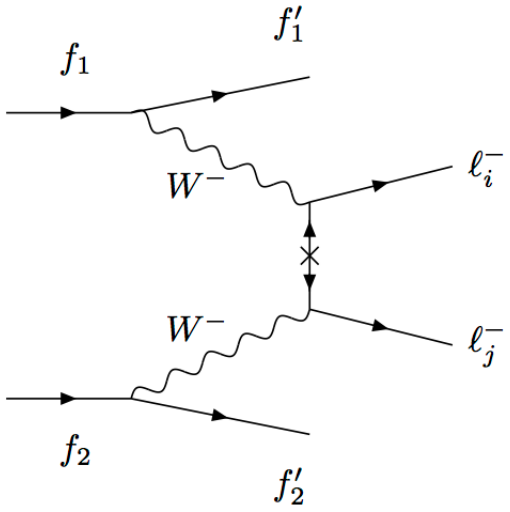

Figure 2.4: Diagram for a possible $\Delta L = 2$ process via Majorana neutrino exchange between two leptons.

2.4.2 Novel Searches for Heavy Neutrinos at the LHC

Prior to the start of the LHC, no direct limits had been set on the coupling between a heavy neutrino and leptons above m_{N}=100 GeV. If a heavy neutrino existed in nature with mass just above 100 GeV it would be possible for this to be discovered at the LHC. The heavy neutrino can decay in one of the three channels $N \to Z\nu$, $N \to H\nu$ or $N \to W\ell$. The branching ratios for these decays are presented in Figure 2.6(a) as a function of neutrino mass [31]. The dominant decay for heavy neutrinos with mass less than 1 TeV is $N \to W_L$. The heavy neutrino decay length is shown in Figure 2.6(b) as a function of neutrino mass [31]. A heavy neutrino with mass of 100 GeV decays within 10^{-12} m. The production of a heavy neutrino from Standard Model $W^{\pm}$ allows for search modes of neutrino decays with lepton number violating processes ($\Delta L = 2$). The decay of these heavy neutrinos to $W^{\pm}\ell^{\mp}$ is studied in this thesis. This is a signature which has few backgrounds at hadron colliders. The Feynman diagram for this process is shown in Figure 2.5. From the indirect limits on the couplings we consider only the case where the neutrino mass is greater than the mass of the W boson. The fully hadronic decay of the $W^{\mp}$ is considered as this allows for a very clean and rare signature of two high momentum same-sign leptons and two high momentum hadronic jets with no missing energy from neutrinos leaving the detector volume. The process produces same-sign lepton pairs in 50% of the time as a result of the Majorana nature of the heavy

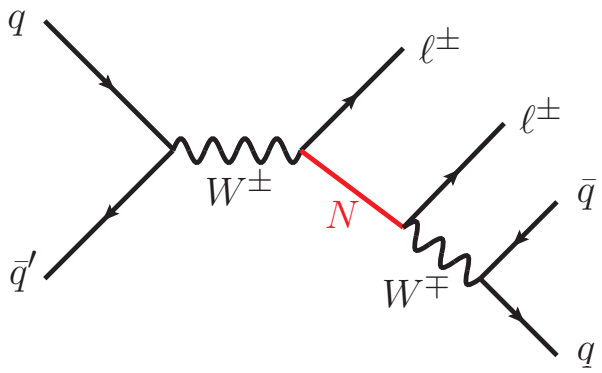

Figure 2.5: Feynman diagram for the production of a heavy Majorana neutrino via an off-shell Standard Model W boson decaying to two same-signed leptons.

neutrino. A search for the resonance heavy neutrino production in the channel

$$\begin{aligned} q\bar{q} \to W^{\pm} \to \ell^{\pm} N_{\ell}, \\ \ell^{\pm} N_{\ell} \to \ell^{\pm}\ell^{\pm} W \to \ell^{\pm}\ell^{\pm} jj, \\ \ell = \mu \end{aligned} \tag{2.50}$$

is performed.

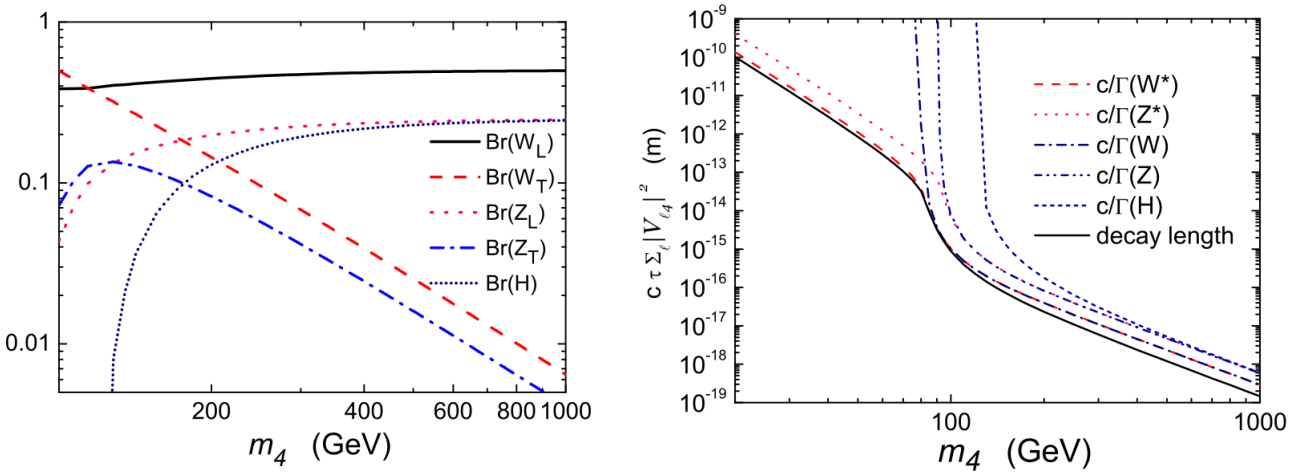

(a) (b)

Figure 2.6: (a) Branching ratio of heavy neutrino decays to longitudinal and transverse gauge bosons and (b) decay length as a function of heavy Majorana neutrino mass, for real and virtual gauge bosons, assuming a Higgs mass of 125 GeV.

As a note the search mode at the LHC for a heavy neutrino produced in the LRSM is similar to that for the heavy neutrinos via an off-shell W in the Standard Model. But the difference is the presence of the right-handed W_R resonance production as shown in Figure 2.7. With the assumption that the heavy Majorana neutrino has mass below that of W_R, this

W_R-boson can decay into a lepton and a heavy Majorana neutrino. The decay of a heavy Majorana produces a second lepton while one or two jets are the result of the off-shell W_R decay:

$$\begin{aligned} q\bar{q} &\to W_R \to \ell N_\ell, \\ N_\ell &\to \ell W_R^* \to \ell jj, \\ \ell &= (e, \mu, \tau). \end{aligned} \tag{2.51}$$

The author contributed to this analysis, but results shown in this thesis will only be for the search in the minimal extension to the Standard Model.

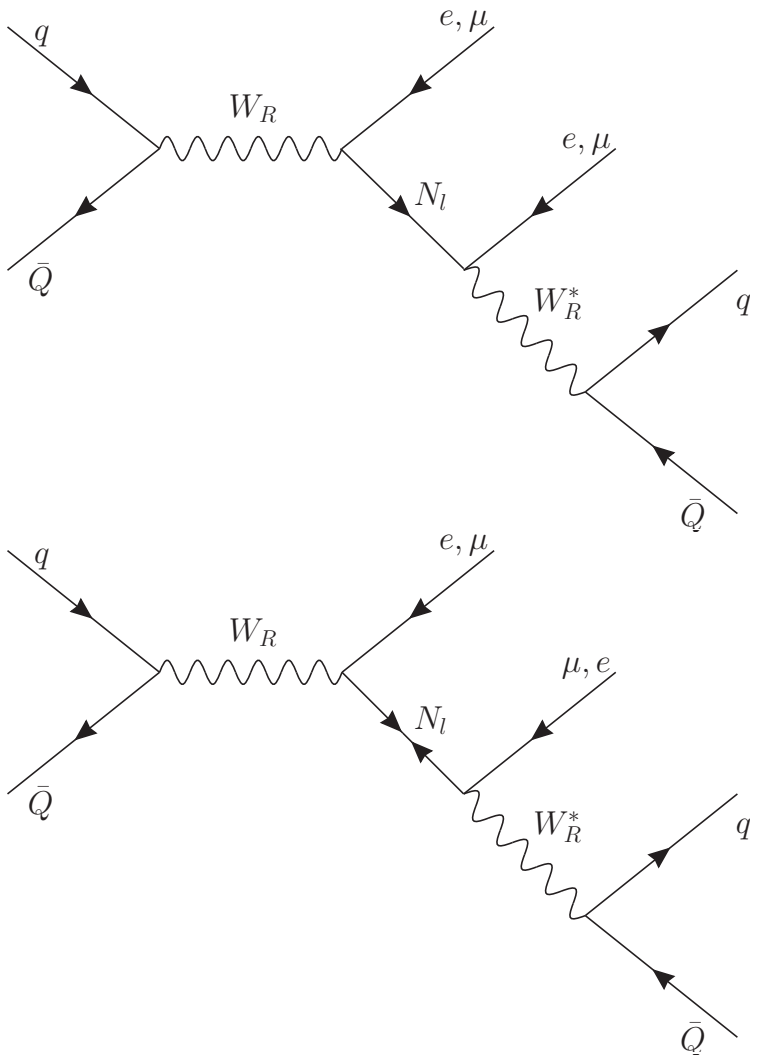

Figure 2.7: Feynman diagram for the production of a heavy Majorana neutrino via W_R decay in the case of no mixing of heavy Majorana neutrino (top) and in the assumption of non-zero heavy Majorana neutrino mixing between the first and the second generations (bottom).

2.5 Heavy Majorana Neutrino Production at the LHC

A good knowledge of the production cross section for the production of a heavy neutrino via an off-shell W boson is important to understand the sensitivity of this search, and is discussed in this section.

2.5.1 Physics of Proton-Proton Collisions

At proton-proton colliders the probability of producing a final state is calculated based on the interactions predicted by the Standard Model. A cross section can be defined for a specific process and deviations of the theory can be tested, looking for signs of new physics. The differential cross section for a $2 \to N$ process can be written as

$$d\sigma = \frac{1}{2\sqrt{\hat{s}}} \sum |\mathcal{M}|^2 d\Phi_N \tag{2.52}$$

where $\mathcal{M}$ is the invariant amplitude, $\sqrt{\hat{s}}$ is the centre of mass energy of the colliding particles and $d\Phi_N$ is the Lorentz invariant phase space term and represents the full set of allowed kinematics of the final state. The initial state consists of two colliding partons (either quark or gluons), as illustrated in Figure 2.8. This collision is referred to as the hard scatter. Factorisation theorem implies that the cross section for the hard scatter, (short distant component), can be calculated using perturbation theory, while the long distance component are dealt with by a set of universal parton distribution functions (PDFs). In perturbation theory the cross section of a process is expressed in terms of a power expansion of the coupling α_s, given by

$$\sigma = \sigma_0 + \alpha_s \times \sigma_1 + \alpha^2{}_s \times \sigma_2 ... \tag{2.53}$$

If this coupling is small then the power series converges quickly and the first term of the series (leading order term) is a good approximation. This breaks down when the coupling is large, as the series becomes infinite. The cross section is determined in this region by convoluting the matrix element calculation with a PDF of choice. The factorised cross section is given by

$$d\sigma_{p_A, p_B, Q^2} = \sum_{a,b} \int_0^1 dx_a f_a^A(x_a, \mu_F^2) \int_0^1 dx_b f_b^B(x_b, \mu_F^2) d\hat{\sigma}_{ab \to cd} \tag{2.54}$$

where $f_i^p(x_a, \mu_F^2)$ are the PDFs, which give the probability of an incoming parton i from the incoming proton p, to have the fraction x_a of the proton's momentum.

The PDFs depend on the factorisation scale, μ_F. Interactions above μ_F are associated with the hard scatter, while below this they are absorbed by the PDF. The PDFs cannot be calculated and they are measured from the inelastic lepton-nucleon, hadron collision scatter-

ing data, such as that taken at HERA [70, 71].

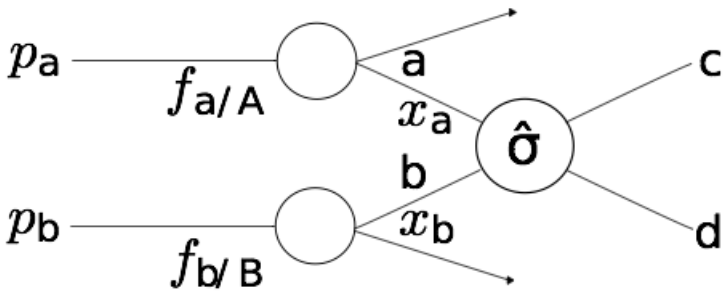

Figure 2.8: Illustration of a hard process in a pp collision. Figure from [72].

2.5.2 Calculation of Heavy Neutrino Cross Sections

The cross section for the production of heavy neutrinos at a centre of mass energy, $\sqrt{s}$, of 7 TeV is calculated and can be written as

$$\sigma(\sqrt{s}) = 2 \int \mathrm{d}x_a \int \mathrm{d}x_b [f_{\bar{u}}^p(x_a, \mu^2) f_d^p(x_b, \mu^2) + f_{\bar{c}}^p(x_a, \mu^2) f_s^p(x_b, \mu^2)] \sigma(\hat{s}) \tag{2.55}$$

where $\hat{s}$ is $x_a x_b \sqrt{s}$ and $\sigma(\hat{s})$ is given by

$$\hat{\sigma}(\hat{s}) = \frac{\alpha_W^2 \pi}{72 \hat{s}^2 (\hat{s} - M_W^2)^2} |V_{\ell N}|^2 (\hat{s} - m_N^2)^2 (2\hat{s} + m_N^2) \tag{2.56}$$

as presented in [8]. f_q^p are the PDFs of quark q, x_a and x_b are the fractions of momentum carried by the two partons which produce the W boson. The range of x_a, x_b due to the kinematics are

$$\frac{m_N^2}{s_{tot}} \leq x_a \leq 1, \frac{m_N^2}{x s_{tot}} \leq x_b \leq 1. \tag{2.57}$$

The factor of two in the production cross section comes from the fact that each parton has the possibility of coming from one of two protons. The only free parameters in the cross section are $V_{\ell N}$ and m_N.

This cross section was previously calculated in [8], for the process ($qq \to W^- \to N\ell^-$), for centre of mass energies of 16 TeV and 40 TeV, using EHLQ set2 parton distribution functions [73].

The EHLQ PDF sets were extracted in 1984, before the HERA experiment began operation. HERA investigated to high precision the distribution of low momentum fraction x for the quark and gluon PDFs. The comparison of the PDFs as a function of x for both the EHLQ and CTEQ5L PDF sets can be seen in Figure 2.9. The CTEQ5L PDF [74] is a

new generation leading order PDF, and show a higher number of partons at low x compared to EHLQ, suggesting the cross section in [8] was underestimated. The cross section was recalculated using the CTEQ5L PDFs at 7 TeV for use in the search in this thesis.

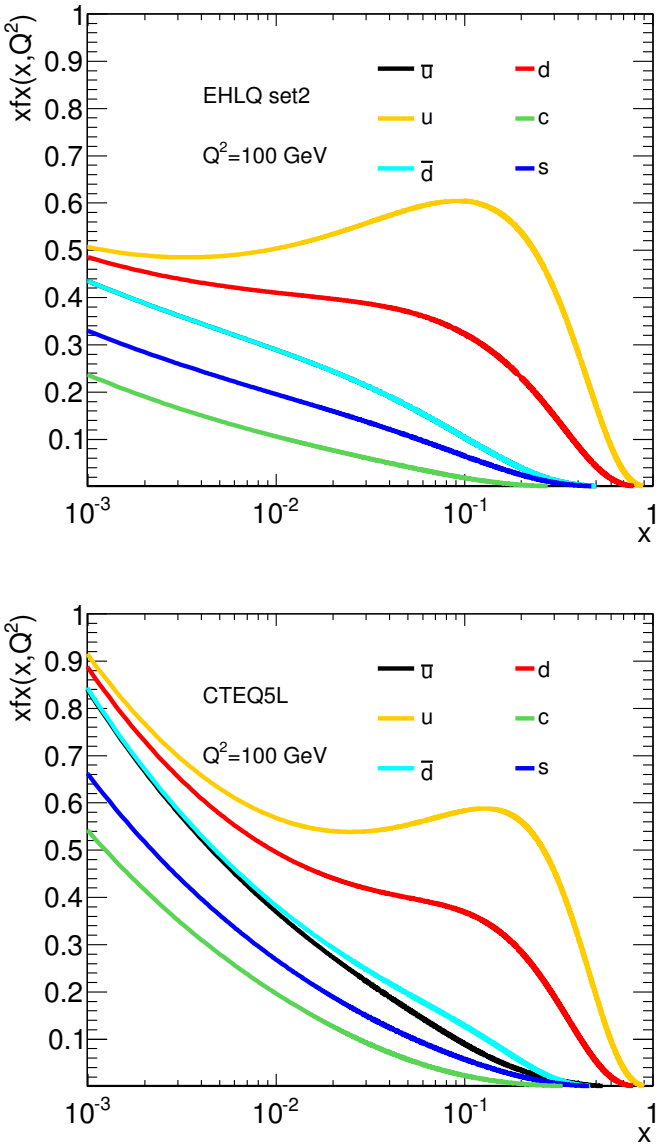

Figure 2.9: Parton distribution functions for EHLQ set 2 (top) and CTEQ5L (bottom) at Q^2=100 GeV^2.

2.5.3 Monte Carlo Integration

One approach to calculating cross sections is using the method of Monte Carlo integration. This technique is based on randomly sampling a distribution. Considering a two dimensional function, $f(x, y)$, the integral of this function, I, can be estimated using

$$I = \int_{x_1}^{x_2} \int_{y_1}^{y_2} f(x, y)\, dx\, dy \approx \frac{1}{N} \sum_{i=1}^{N} f(x_i) \prod_{j=1}^{N} (x_2^j - x_1^j). \tag{2.58}$$

where N is the number of sampling points used, picking values of x and y over the range $\{x_1, x_2\}$ and $\{y_1, y_2\}$ respectively. The function is averaged over the specified area with the integral becoming exact when $N \to \infty$. The uncertainty on this integral [75], σ_I, is given by

$$\sigma_I^2 = \prod_{x,y} \frac{(x_2^j - x_1^j)^2}{N} \left[\frac{1}{N} \sum_{i=1}^{N} f(x_i)^2 - \left(\frac{1}{N} \sum_{i=1}^{N} f(x_1) \right)^2 \right] \tag{2.59}$$

where the term in the square bracket is the variance of $f(x, y)$. It can be seen that σ_I decreases when the average spread from the mean is reduced, or by increasing the number of sampling points. To decrease the variance and the uncertainty we can introduce a weighting function, with a similar shape to the integrand. Two new integration variables, a and b are introduced such that

$$w(x) = \frac{da}{dx} \tag{2.60}$$

$$w(y) = \frac{db}{dy} \tag{2.61}$$

where $w(x)$ and $w(y)$ are the new weighting functions. By multiplying and dividing the integrand in equation 2.59 by the two weight functions, which is the same as multiplying by unity, the same integral is obtained, but with a change in variables

$$\mathrm{I} = \int_{a_1}^{a_2} \int_{b_1}^{b_2} \frac{f(x, y)}{w(x, y)} da\, db = \frac{1}{N} \sum_{i=1}^{N} \frac{f(x_i, y_i)}{w(x_i, y_i)} \prod_{j=1}^{N} (x_2^j - x_1^j). \tag{2.62}$$

The sampling points are chosen between $\{a_1, a_2\}$ and $\{b_1, b_2\}$ respectively. The idea of this is that if one now picks randomly in terms of a and b, they will be picking values of x and y which are closer to the mean, reducing the uncertainty on the integral. It can be seen from equation 2.56 that the cross section for the heavy neutrino production varies as the inverse of s, this relates as the cross section being inversely proportional to both x and y. For this

Weight Function	Cross section[pb]
1	6.10 ± 0.45
$1/xy$	6.35 ± 0.03

Table 2.5: Cross section for heavy neutrino production with $m_{\mathrm{N}} = 100$ GeV and centre of mass energy 10 TeV, sampling 100,000 points and using different weighting functions.

reason a suitable choice of weight function is

$$w(x) \times w(y) = \frac{1}{xy}. \tag{2.63}$$

The effect of this weight function on the error is shown in Table 2.5. Although the two calculations for the cross section both agree, the error is reduced by over 90% when the weighting function is introduced, for a fixed number of Monte Carlo points.

2.5.4 Signal Cross Section

The cross section for the $q\bar{q} \to W^- \to N\mu^-$ production is shown in Figure 2.10 using the CTEQ5L PDFs. The cross section for $\sqrt{s} = 40$ TeV is also shown for a direct comparison to the cross sections shown in [8]. The newly calculated cross section has increased with respect to [8], this is explained by the shapes of the two different PDFs used in the calculation. The signal cross section is then taken as the sum of both charged W^- and W^+, which can be seen separately for $\sqrt{s} = 7$ TeV in Figure 2.11. Since the LHC is a pp collider the W^+ is the dominant production mode, due to the valence quarks of the proton. The branching ratio for the decay of the heavy neutrino needs to be included, given in Figure 2.6(a). Due to the same-sign requirements of the two muons the cross section is reduced by half. The final decay of the W into $q\bar{q}$ has a BR($W \to q\bar{q}$) = 0.676, as shown in Table 2.6. The final signal region with all branching ratios included is presented in Figure 2.12 and Table 2.7 for $\sqrt{s} = 7$ TeV and 8 TeV.

W Decay Mode	Branching Ratio
hadronic	0.676
$\mu\nu_\mu$	0.106
$e\nu_e$	0.108
$\tau\nu_\tau$	0.103

Table 2.6: Branching ratios for the decay of the W boson [10].

The cross section has since been calculated in [76], agreeing with the values presented in Table 2.7.

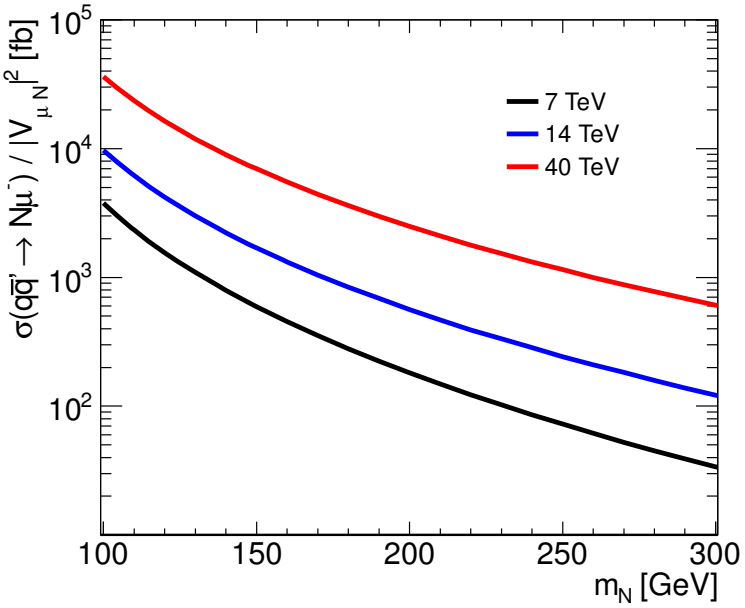

Figure 2.10: Cross section for the heavy neutrino production in the scenario that the neutrino only couples to the muon, for $\sqrt{s} = 7$, 10 and 40 TeV, using the CTEQ5L PDF.

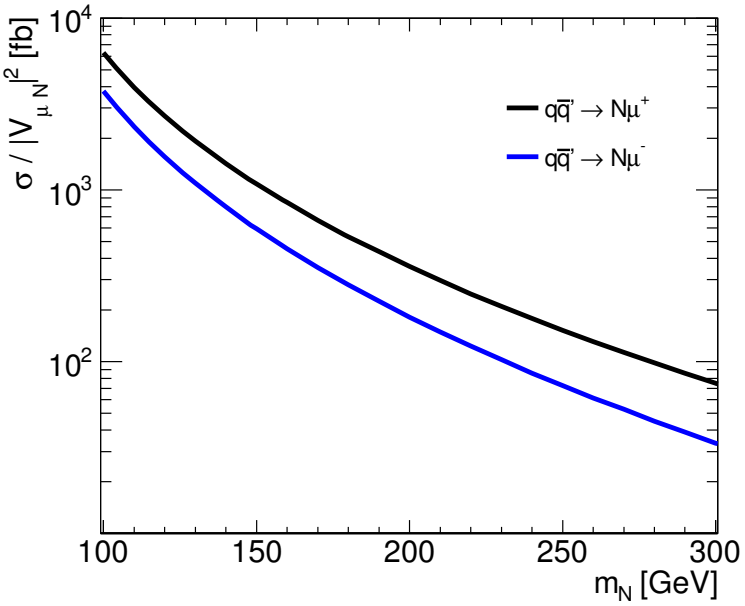

Figure 2.11: Cross section divided by coupling squared for the processes $q\bar{q}' \to N\mu^+$ and $q\bar{q}' \to N\mu^-$, at $\sqrt{s} = 7$ TeV.

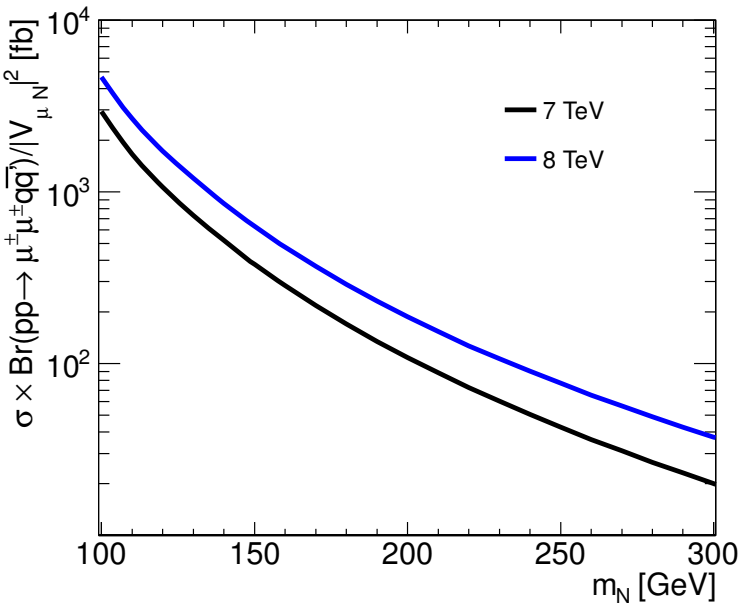

Figure 2.12: Cross section divided by coupling squared for the production of heavy neutrinos decaying to two same-sign muons, and two jets, at $\sqrt{s} = 7$ TeV and 8 TeV.

m_{N} [GeV]	σ [fb]	
	7 TeV	8 TeV
100	2939	4669
120	1062	2671
140	519	1731
160	283	1199
180	171	289
200	108	188
240	51	90
280	27	49
300	20	37

Table 2.7: List of LO cross sections divided by $|V_{N\mu}|^2$, at centre of mass energies $\sqrt{s} = 7$ TeV and $\sqrt{s} = 8$ TeV using CTEQ5L PDF, as a function of neutrino mass.

Chapter 3

The ATLAS Experiment

The motivation behind particle physics is to probe and understand the fundamental interactions of matter, for which high energies are required. Particle accelerators are used to obtain these high energies by accelerating collimated beams of particles in electromagnetic fields. These particles are collided, releasing the energy, allowing one to probe interactions at high energy.

The most advanced particle collider to date is the Large Hadron Collider (LHC), located at CERN, Geneva. At the LHC, proton *bunches*, with a centre of mass energy of 8 TeV are collided, every 50 ns at four separate interaction points, where various experiments and detector technologies are located. At one of these interaction points the ATLAS (**A** **T**oroidal **L**HC **A**pparatu**S**) detector is installed, which is found at Interaction Point 1, on the Swiss-French border. The analysis in this thesis was performed using data with $\sqrt{s} = 7$ TeV taken from the ATLAS detector during the 2011 running.

This chapter describes the operation of the LHC in section 3.1 and outlines the ATLAS detector in Section 3.2, with a brief description of the detector subsystems in Sections 3.3 and 3.4. Due to its relevance in the search a more detailed description of the ATLAS Muon Spectrometer is given in Sections 3.5. The data acquisition system is discussed in Section 3.6 and the trigger system is described in Section 3.7.

3.1 CERN and the Large Hadron Collider

The LHC is located at CERN, the European Organisation for Nuclear Research. It is an international particle physics laboratory with 20 member states. Figure 3.1 shows a schematic of the LHC and the prior accelerator chain and includes also the four interaction points.

Accelerator	Energy	Speed (%c)
Linac2	50 MeV	31.4
PSB	1.4 GeV	91.6
PS	25 GeV	99.93
SPS	450 GeV	99.9998
LHC	3.5 TeV	99.99999996

Table 3.1: The final proton energy and speed at each stage of the accelerator chain of the LHC.

3.1.1 The Accelerator Chain

The beam energy of the LHC is limited by the bending power of the magnet system. This limits the minimum and maximum energy of the protons and as such several stages and injection energies are required to minimise the operational range of the magnets. At the beginning of the injector chain, the protons are delivered using a duoplasmatron source [77] and are then injected into the PS Booster (PSB) at an energy of 50 MeV. This is after being accelerated in Linac2. The protons are accelerated in the PSB to 1.4 GeV before being fed into the Proton Synchrotron (PS) where they are accelerated to an energy of 25 GeV. Protons are then accelerated further to 450 GeV inside the Super Proton Synchrotron (SPS) before they are finally transferred to the twin rings of the LHC, both in a clockwise and anti-clockwise direction. Here the protons circulate in separate vacuum tubes, located in the beam pipe. The beams of protons are kept in their orbit using a series of dipole magnets that are placed around the LHC ring. The LHC then completes the acceleration chain by increasing the energy of the protons per cycle until the protons reach the desired collision energy. The proton bunches are finally collided at the four interaction points with the use of quadrupole magnets.

The proton beams in the LHC are accelerated with a radio frequency of 40 MHz, resulting in synchrotron oscillations which bunch the protons together to form distinct bunch groups. The LHC is designed to hold a maximum of 2808 bunches in one rotation.

The LHC is a proton-proton collider, with a circumference of approximately 27 km. It is designed to operate at centre of mass energies up to 14 TeV, running with an instantaneous luminosity, $\mathcal{L}_{\text{inst}}$, of order $10^{34}\text{cm}^{-2}\text{s}^{-1}$, resulting from on average 22 simultaneous proton-proton interactions. The instantaneous luminosity is defined as:

$$\mathcal{L}_{\text{inst}} = \frac{\mu n_{\text{b}} f_{\text{r}}}{\sigma_{\text{inel}}} \tag{3.1}$$

where μ is the average number of inelastic interactions per bunch crossing, n_{b} is the number of colliding bunch pairs, f_{r} is the machine revolution frequency, and σ_{inel} is the pp inelastic cross section. During the 2011 running the LHC was not yet performing at full capacity and

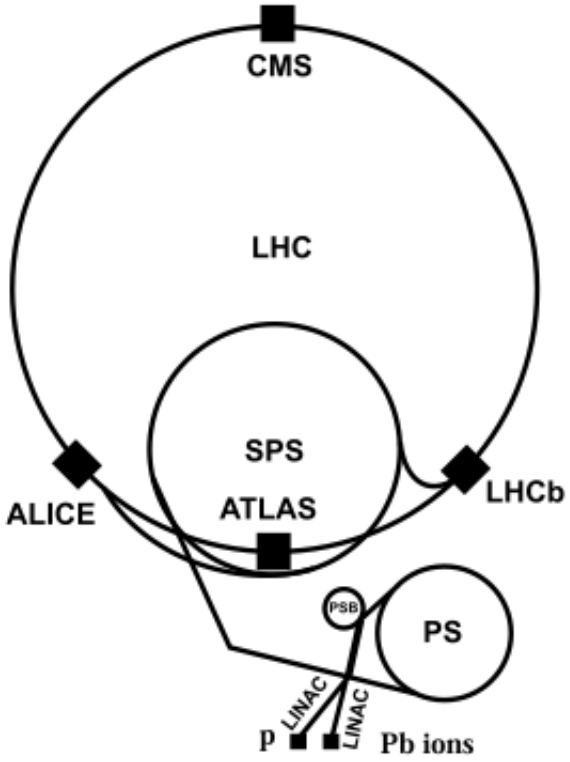

Figure 3.1: Schematic diagram of the LHC and the full proton accelerator chain.

the machine was colliding protons at a centre of mass energy of 7 TeV with an instantaneous luminosity of just under $4 \times 10^{33}\text{cm}^{-2}\text{s}^{-1}$. The comparison of the 2011 running parameters compared to the design values are given in Table 3.2.

3.1.2 Running Conditions for the LHC

The ATLAS detector has recorded proton-proton collisions since 2009. The running conditions in this time have changed dramatically, noticeably the instantaneous luminosity delivered by the LHC, which is shown in Figure 3.2. The rise in the luminosity is driven by physics needs, since for any given process the number of events per unit time is equal to the product

Parameter	Value (2011 Value)
Circumference (m)	26659
Beam energy (TeV)	7(3.5)
Injection energy (TeV)	0.45(0.45)
Luminosity ($\text{cm}^{-2}\text{s}^{-1}$)	$10^{34}(10^{33})$
Bunch spacing (ns)	25(50)
Protons per bunch	10^{11}(10^{11})
Bunches per beam	2808 (1404)

Table 3.2: The nominal design parameters of the LHC.

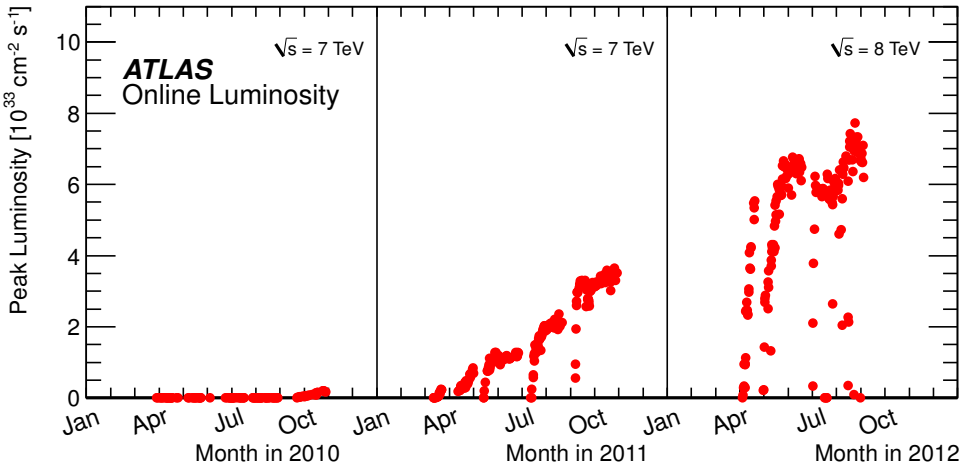

Figure 3.2: The peak instantaneous luminosity delivered by ATLAS per day during *pp* collisions of 2010, 2011 and 2012 as measured by the ATLAS luminosity detectors.

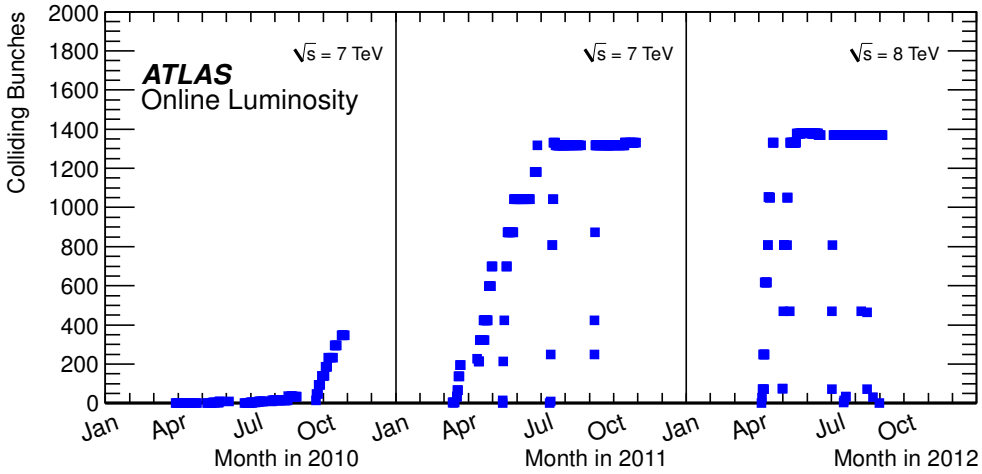

Figure 3.3: The number of colliding bunches in ATLAS versus time during the *pp* runs in 2010-2012.

of the luminosity and cross section. Many physics analyses (in particular searches beyond the SM) at the LHC look for processes with small cross sections, and therefore in order to maximise the statistics it is important to maintain large luminosities. The high luminosities achieved at the LHC are important to new physics searches.

With reference to equation 3.1, higher luminosity can be achieved in three ways. These include further squeezing of the colliding *bunches* (decreasing the transverse width of the proton beam), increasing the number of protons per bunch or by increasing the number of circulating bunches. The number of bunches per cycle of the LHC as a function of time is shown in Figure 3.3. The higher luminosity however results in an increased level of *pile-up*, which referrers to additional interactions other than the hard scatter. An increase in the number of protons per bunch or the decrease of the transverse width of the proton beam

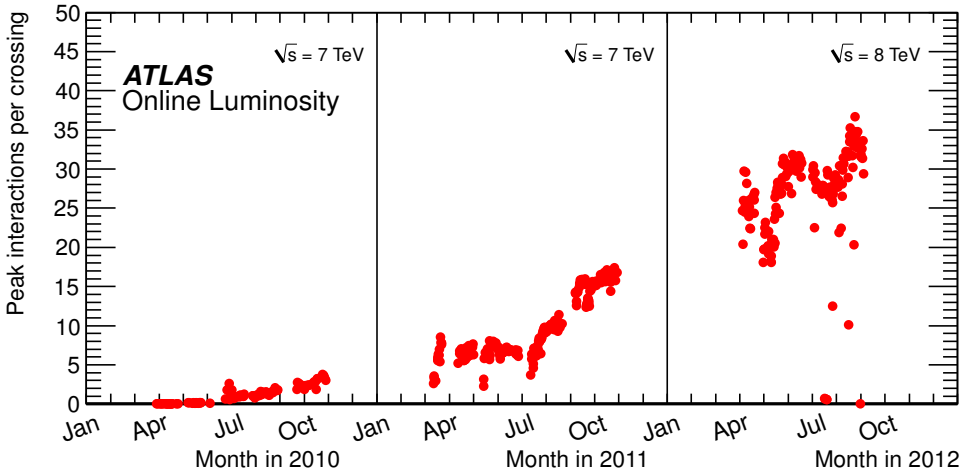

Figure 3.4: The maximum mean number of interactions per bunch crossing versus day during *pp* collisions of 2010, 2011 and 2012 as measured by the ATLAS luminosity detectors.

result in extra proton-proton interactions from the same bunch crossing, this is referred to as *in-time pile-up*. An increase in the number of bunches result in the increased number of interactions from nearby bunches, which can occupy the detector volume in the same event window, this is referred to as *out-of-time pile-up*. The number of interactions per bunch crossing as a function of time is shown in Figure 3.4.

3.2 Overview of the ATLAS Detector Systems

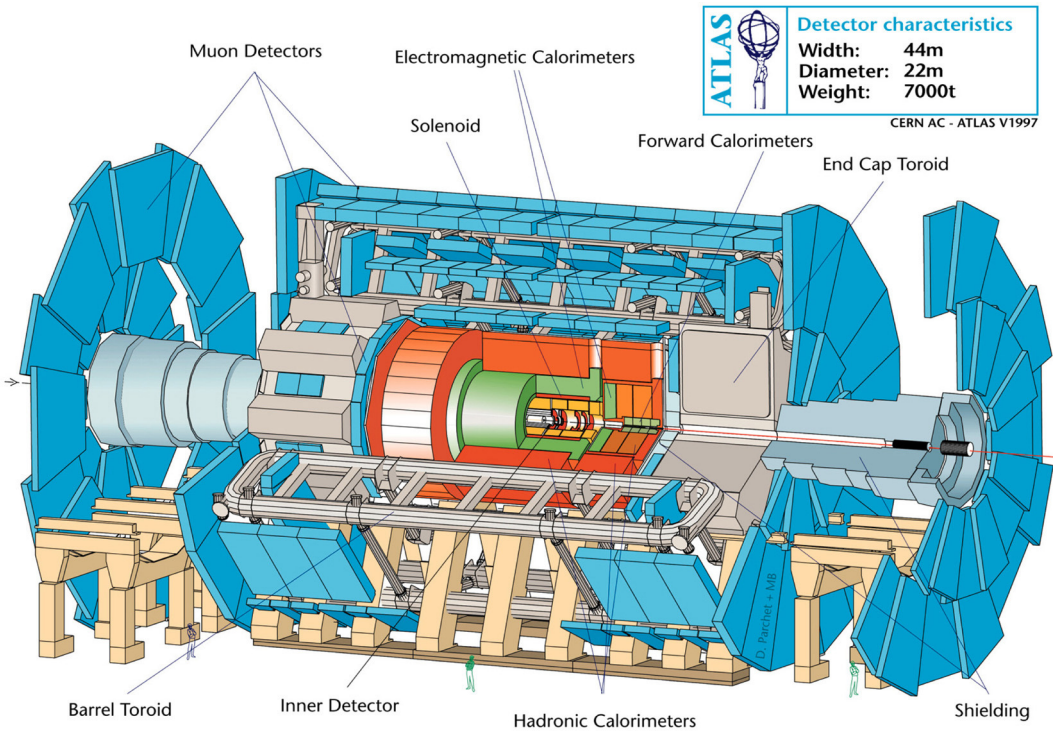

Figure 3.5: Side on view of the ATLAS detector [78].

The ATLAS detector [78] is located at point 1 of the LHC ring and is one of two general-purpose detectors of the LHC, along with the CMS detector. ATLAS is a multi purpose detector and must be able to deal with high interaction rates delivered by the LHC, covering a large spread in particle energies, enormous track multiplicities while maintaining a high measurement resolution. The search for the Higgs boson has been one of the driving forces in the design of the detector and the performance of the various sub-systems, which impose the following requirements on the design:

- Large acceptance in pseudo-rapidity (η) along with almost full coverage in azimuthal angle (ϕ) to ensure few high momentum particle are undetected.
- Muon reconstruction and identification over a large range of muon momentum. With the capability of accurate measurements of muon momentum and charge at the highest design luminosities.
- Very good electromagnetic calorimetry for electron and photon identification in addition to a hadron calorimeter with full detector coverage for accurate measurements related to jets and missing transverse energy, $E_{\mathrm{T}}^{\mathrm{miss}}$.

- Highly efficient tracking of charged particles for high-p_{T} lepton momentum measurements, electron identification at high luminosity and full event reconstruction capability at low luminosities.

- Highly efficient triggering system for particles with high transverse momentum, with a sufficient background rejection to reduce the trigger rates to a level that can be recorded to disk.

In order to achieve these goals, the ATLAS detector consists of three main sub-systems, as shown in Figure 3.5. From the interaction point outwards, a high precision inner detector tracker is deployed inside a solenoid magnetic field designed to track charged particles. Around the inner detector are two calorimeters, designed to measure the energy of the particles and jets passing through the detector. Finally the muon detector is built around the outside of the calorimeters, with the purpose of making high precision muon momentum measurements.

The ATLAS Co-ordinate System

The ATLAS detector and co-ordinate system can be seen in Figure 3.6. Here the beam direction defines the z-axis, and the x-y plane is the plane transverse to the beam. The interaction point is defined as the coordinate (0,0,0) with the positive x direction being defined as pointing towards the centre of the LHC ring from the interaction point and the positive y-axis as pointing upwards. A particle trajectory is defined in terms of the ϕ and η, where ϕ is the azimuthal angle and η is the pseudo-rapidity. The azimuthal angle ϕ is measured around the beam axis, and is defined such that $\phi = 0$ points along the x-axis and $\phi = \pi/2$ points along the y-axis. The pseudo-rapidity η is defined as $\eta = -\ln\tan(\theta/2)$, where the polar angle θ is the angle from the beam axis, such that $\eta = 0$ lies in the x-y plain and $|\eta| = \infty$ points along the z-axis. The detector is split into three distinct regions, referred to as the barrel, end-cap and forward region. The barrel is defined as the region with $|\eta| < 1.05$, the end-cap as $1.05 < |\eta| < 2.5$, while the forward region is defined as $|\eta| > 2.5$.

3.3 Inner Tracking Detectors

The Inner Detector [78] (ID) is situated closest to the interaction point and has to cope with an enormous event rate. At design luminosity the number of charged tracks in the tracker is of order 10^3 per collision. The ID is designed to track charged particles and measuring their momenta, charge and impact parameters with high precision with respect to the interaction point. Thus, the ID employs two separate silicon precision tracker technologies which are used in conjunction with straw tube radiation trackers. Figure 3.7 shows the Inner Detector

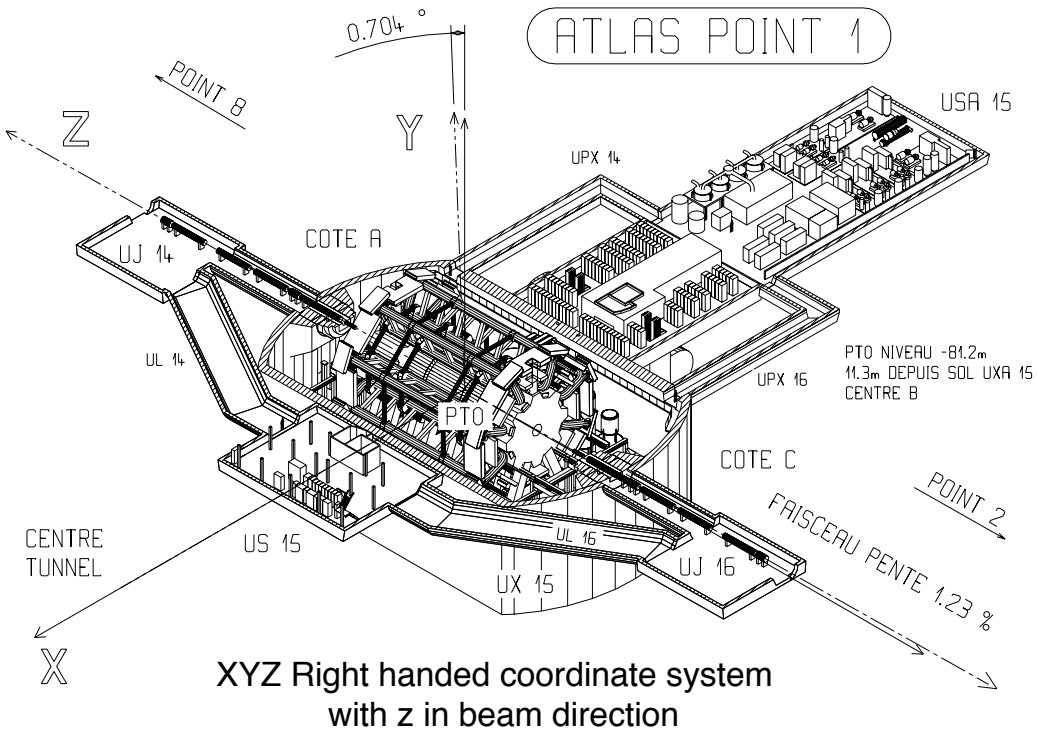

Figure 3.6: Global ATLAS coordinate system [78]; here the z-axis follows the beam line.

tracker, indicating the three separate technologies, which are described below. Each of the three sub-detectors are split into three components, one in the barrel region and one in each of the end-caps. The inner tracking detector system covers a total region of $|\eta| < 2.5$.

Closest to the beam axis are the high granularity semiconducting silicon Pixel detectors which provide an accurate 3-dimensional measurement used for vertex finding and pattern recognition. Around the Pixel detector is the silicon micro strip detectors (SCT, Semi Conductor Tracker). Finally a Transition Radiation Tracker (TRT) surrounds the SCT and is used to identify electrons from charged hadrons.

The Pixel and SCT detectors are comprised of silicon. A charged particle passing through these detectors creates electron-hole pairs, which drift to a readout electrode due to a voltage bias across the silicon. The charge is recorded and compared to a predefined threshold to determine the presence of a silicon hit.

The barrel Pixel tracker provides three space points with high efficiency for $|\eta| < 2.5$. There are three cylindrical layers in the barrel, at radius 50.5 mm, 88.5 mm and 122.5 mm, providing coverage of $|\eta| < 1.7$ and full coverage in azimuth, and eight disks in the end-caps, four on each side. The inner barrel layer is referred to as the B-layer and is important for accurate vertex positioning. The Pixel detector is composed of Pixel modules, which have an $R\phi$-z size of 50 μm $\times$400 μm^2, with a spatial resolution of approximately 12 μm in the

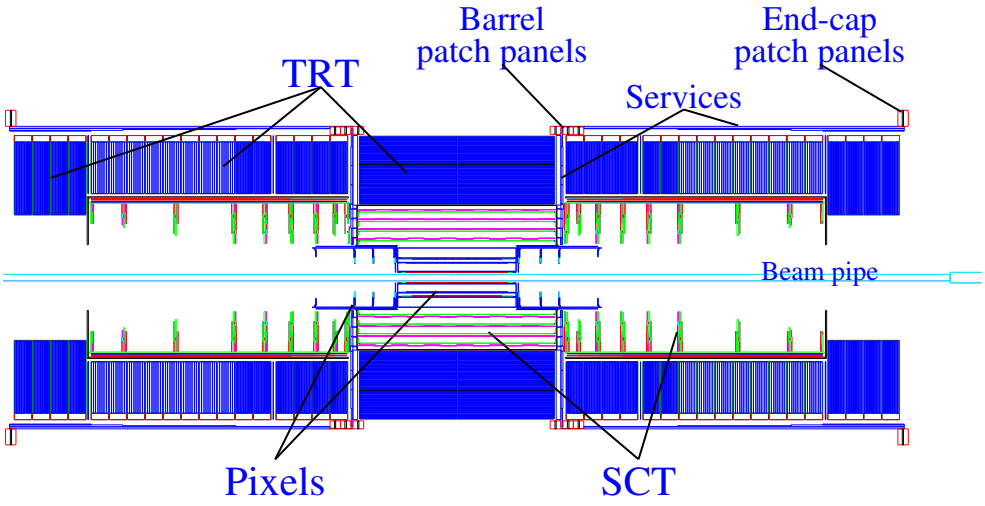

Figure 3.7: Cut-away view of the ATLAS Inner Detector. The three sub-systems, Pixel, SCT and TRT are indicated.

$R\phi$ coordinate and 100 μm in the z coordinate. The Pixel end-caps both consist of three disks covering a range $1.7 < |\eta| < 2.5$. The silicon strip detector is built of four concentric layers of SCT modules in the barrel region. The strips are arranged axially along the beam line with a strip pitch of 80 μm and each module provides a 1-dimensional measurement. Two modules are combined almost back-to-back at an angle of 40 mrad, making a second coordinate measurement possible. The spatial resolutions are 23 μm and 700 μm respectively. The SCT end-caps contain 9 concentric disks, on both side, constructed of Pixel modules mounted on concentric circles.

The TRT uses a detector straw technology. Each straw is 4 mm in diameter and filled with a mixture of Xe, CO_2 and O_2 gases, which are ionised by charge particles passing through the TRT straws. The ionised electrons drift to a tungsten wire located at the centre of each tube. The distance of the track to the wire is measured with an accuracy of 130 μm. The TRT covers the region $|\eta| < 2.0$ and has over 350,000 straws positioned along the z-axis in the barrel and radially in the end-caps.

The ID is embedded in a 2 T solenoidal magnetic field, which bends the track's trajectory, which is vital in measuring the tracks momentum and charge. For tracks with large momentum that have less curvature, the resolution of the inner detector tracking becomes important. The combination of the precision silicon detectors and the large number of space points in the TRT gives a robust pattern recognition and high precision measurement in azimuth, pseudo-rapidity, transverse impact parameter, d_0 and longitudinal impact parameter,

z_0. The resolution of the track parameters associated with muons [78, 79] are:

$$\begin{aligned}
\sigma\left(\frac{1}{p_{\mathrm{T}}}\right) &= 0.36 + \frac{13}{p_{\mathrm{T}}\sqrt{\sin\theta}}(\ \mathrm{TeV}^{-1}) \\
\sigma(\phi) &= 0.075 + \frac{1.8}{p_{\mathrm{T}}\sqrt{\sin\theta}}(\mathrm{mrad}) \\
\sigma(\cot\theta) &= \left(0.7 + \frac{2.0}{p_{\mathrm{T}}\sqrt{\sin^3\theta}}\right) \times 10^{-3} \\
\sigma(d_0) &= 11 + \frac{73}{p_{\mathrm{T}}\sqrt{\sin\theta}}(\mu\mathrm{m}) \\
\sigma(z_0) &= 87 + \frac{115}{p_{\mathrm{T}}\sqrt{\sin^3\theta}}(\mu\mathrm{m}).
\end{aligned} \tag{3.2}$$

3.4 Calorimeter System

The ATLAS calorimeter system is shown in Figure 3.8. This has the job of measuring the energy and position of particles and plays an important role in measuring the missing transverse momentum of an event by measuring the total transverse energy that particles deposit in the calorimeter system. The calorimeter system is designed to have a large absorption length (Figure 3.9) across all rapidity ranges to ensure all electromagnetic and hadronic showers are contained within the calorimeter. The calorimeter is located directly outside of the solenoid magnet of the inner detector system and consists of a four detectors. The pre-sampler covers the rapidity region of $|\eta| < 1.8$ and is used to correct for energy lost in the inner detector. This is proceeded by a finely segmented electromagnetic (EM) calorimeter, which covers a rapidity region of $|\eta| < 3.2$ and a hadronic calorimeter which covers $1.5 < |\eta| < 3.2$. The forward calorimeter covers $3.1 < |\eta| < 4.9$.

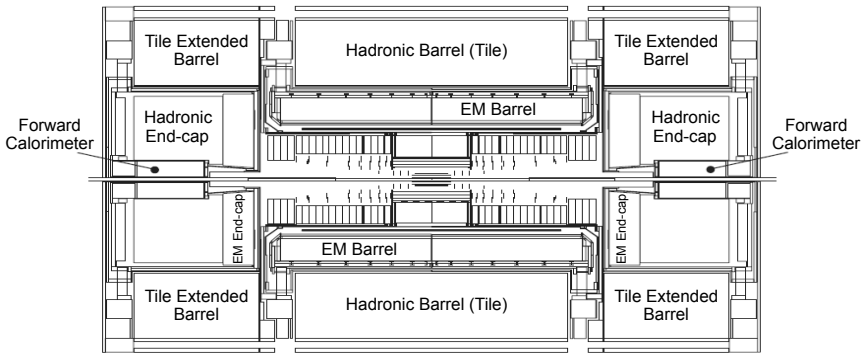

Figure 3.8: Cut-away view of the ATLAS Calorimeter system [78]. The different sub detectors are labelled.

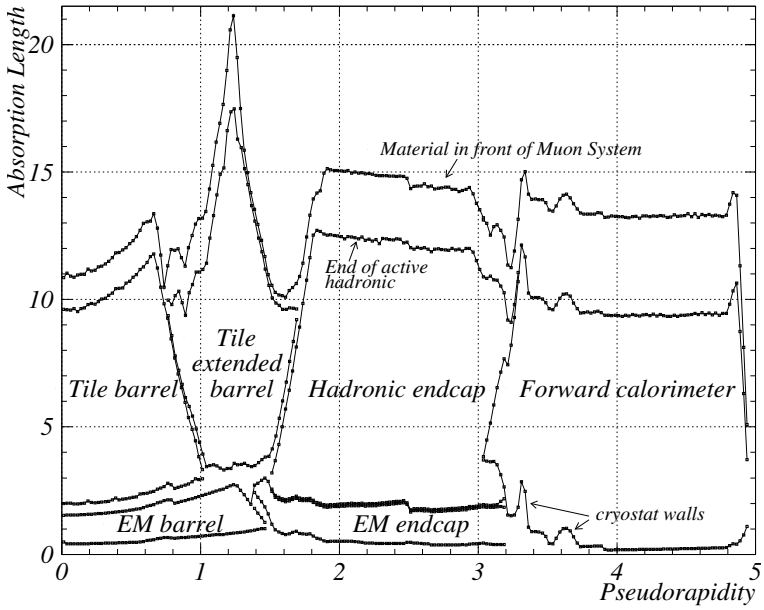

Figure 3.9: Absorption lengths of material in the ATLAS calorimetry as a function of η [78].

3.4.1 The Electromagnetic Calorimeter

The ATLAS EM calorimeter [78] is a sampling type calorimeter. It is referred to as the LAr calorimeter as it employs liquid argon (LAr) as the active material and lead for the absorbers . The LAr calorimeter is contained within a cylinder of inner radius 1.15 m and outer radius of 2.25 m from the beam line and has a total length along the beam axis of ± 6.25 m. The main purpose of the EM calorimeter is to measures the energy and position of electrons and photons. Charged particles passing through the electromagnetic calorimeter ionise the argon, where the emitted electrons drift to a copper electrode in the readout cells. The barrel calorimeter has coverage $|\eta| < 1.475$ while the end-cap calorimeter is divided into two coaxial wheels, with the outer wheel having a coverage of $1.375 < |\eta| < 2.5$ while the inner wheel has a coverage of $2.5 < |\eta| < 3.2$. There is a small *crack* region, with little coverage, which is located between $1.375 < |\eta| < 1.52$. The total thickness of the EM calorimeter is above 24 X_0 in the barrel and above 26 X_0 in the end-caps, where X_0 is the radiation length, which is the mean distance through material that a high energy electron travels before losing 1/e of its total energy.

The barrel EM calorimeter modules have an accordion like structure (Figure 3.10) which provide full ϕ symmetry, while leaving no azimuthal cracks. The LAr gap in the barrel is 2.1 mm thick, while the thickness of the lead absorber plate varies as a function of rapidity in order to optimise the energy resolution of the calorimeter. As shown in Figure 3.10, the barrel EM calorimeter is divided into three sampling layers. The first layer has a thickness of 6 X_0 over all rapidity. This layer is important for particle identification and is segmented

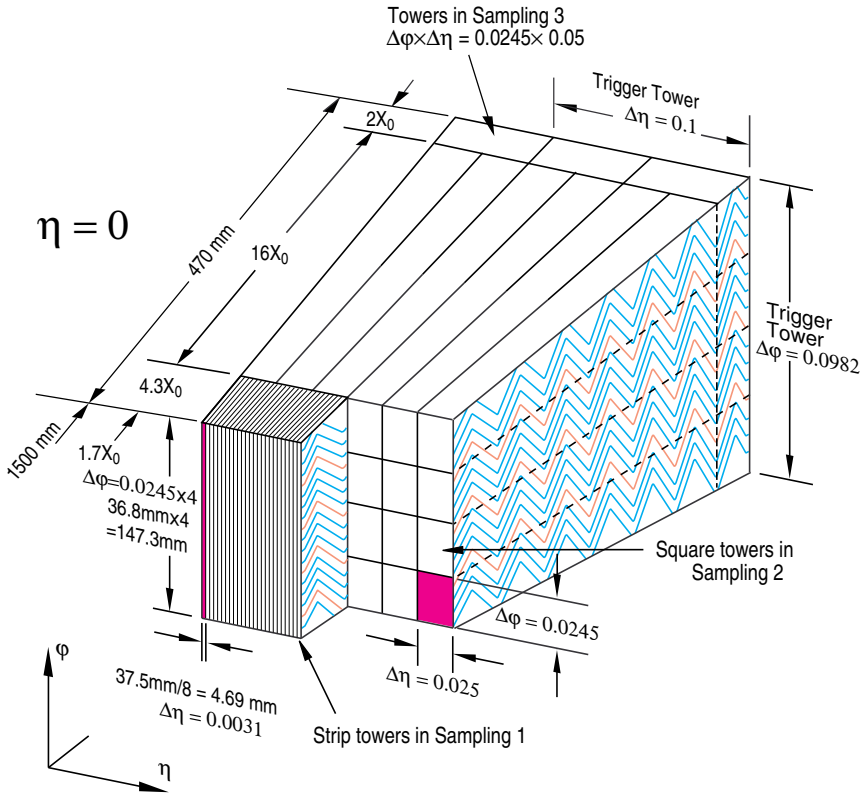

Figure 3.10: A barrel module of the ATLAS electromagnetic calorimeter showing readout granularity of the three sampling layers [78].

into strips of size $\Delta\eta \times \Delta\phi = 0.003 \times 0.1$ for precise measurements of the η position of the EM shower. The second layer is segmented into squares of size $\Delta\eta \times \Delta\phi = 0.025 \times 0.025$, covering a length of 18 X_0. The third sampling layer has much coarser granularity in η, twice that in the second layer, with a wide spread in thickness between 2 and 12 X_0. For $|\eta| > 2.5$, the calorimeter (the outer end-cap wheel) has a coarser granularity than the rest of the acceptance, but adequate for the physics needs. The EM calorimeter has an energy resolution of $\sigma_E/E = 11.5\%/\sqrt{E} \oplus 0.5\%$, where E is in units of GeV.

3.4.2 The Hadronic Calorimeter

The purpose of the ATLAS hadronic calorimeter is to measure the energy and direction of jets from hadronised quarks and gluons, and hadronically decaying particles. Hadronic showers are longer and broader than electromagnetic showers. Thus, the hadronic calorimeter has a larger coverage than the EM calorimeter, covering all of $|\eta| < 5$, including the forward calorimeter. The hadronic calorimeter employs the tile calorimeter. The tile calorimeter system has an outer radius of 4.23 m and a total length spanning ±6.10 m. It is based on a sampling technique with plastic scintillator plates tiles embedded in an iron absorber for the barrel and extended barrels, covering $0 < |\eta| < 0.8$ and $0.8 < |\eta| < 1.7$, respec-

tively. The minimum depth of this calorimeter is 10 interaction lengths [1], sufficient to reduce hadronic punch through into the muon spectrometer to a controllable rate. The 3 mm tiles are placed perpendicular to the colliding beams. Particles interact with the active medium producing scintillation light proportional to the deposited energy, which is in turn collected using wavelength-shifting fibres. Readout cells are built by grouping fibres together in projective towers in η, and the scintillation light is collected by photomultiplier tubes at each end of the tiles. The tile calorimeter consists of three layers in both barrel and extended barrel. The cell granularity varies according to pseudo-rapidity and distance from the interaction point: the granularity is $\Delta\eta \times \Delta\phi = 0.1 \times 0.1$ in the first two layers and 0.1×0.2 in the third layer. The hadronic calorimeter is determined to have an energy resolution of $\sigma_E/E = 56\%/\sqrt{E} \oplus 5.5\%$ [80], where E is in units of GeV.

[1] An interaction length is the mean free path of a high energy hadron.

3.5 Muon Spectrometer

The Muon Spectrometer [78] (MS) as seen in Figure 3.11 is the outer-most layer of the detector and has the capability of accurately measuring the muon momentum independent of the inner detector tracking system and provide an independent muon trigger. The spectrometer consists of two precision detectors and two triggering detectors, which are embedded in a toroidal magnetic field. The two precision detectors are the Monitored Drift Tubes (MDT) and the Cathode Strip Chambers (CSC) and the two triggering detectors: the Thin Gap Chambers (TGC) and the Resistive Plate Chambers (RPC). With the use of all these subdetectors the muon momentum resolution is designed to be 3% for 10-200 GeV and about 10% for 1 TeV muons.

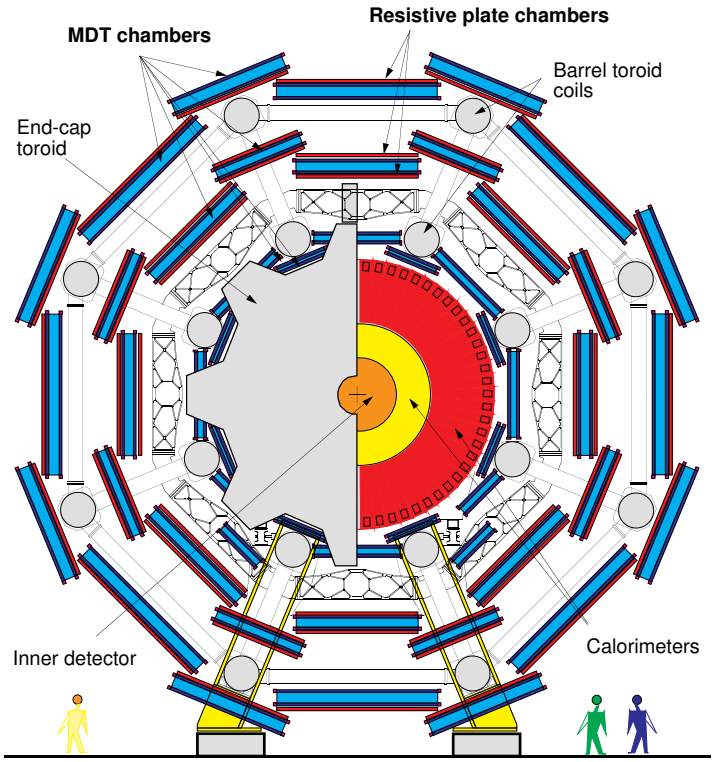

Figure 3.11: Transverse view of the muon spectrometer indicating the coverage of the four different detector technologies [78].

The MS magnetic system consists of two end-cap and one barrel superconducting air-core toroids covering the rapidity range of $0 \leq |\eta| \leq 2.7$. From the curvature of muon tracks in this field the momentum is calculated. The barrel toroid extends over a length of 25 m along the beam axis and is located between 4.7 m and 10 m from the beam line, with the two end-cap toroids inserted within the barrel toroid. Each magnet is built up of eight superconducting coils assembled radially. The structure is open in order to minimise multiple scatterings and achieve a good momentum resolution. The magnetic field provides a typical bending power

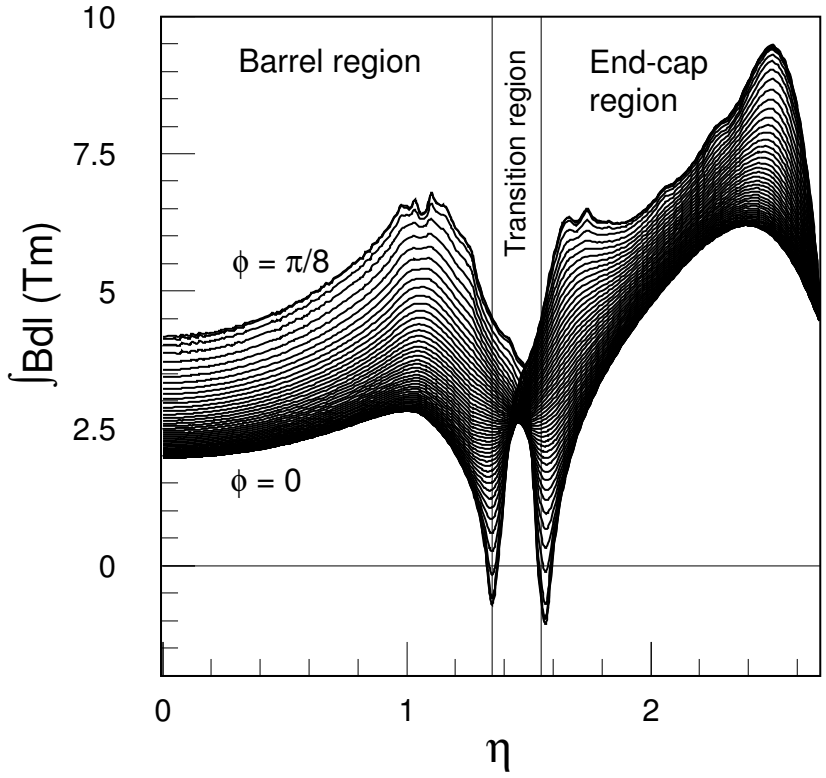

Figure 3.12: Toroidal bending power, $\int$ Bdl, of the ϕ field component as a function of the pseudo-rapidity [78].

of 3 Tm in the barrel and 6 Tm in the end-cap region. The magnetic field is not perfectly toroidal in the transition region between the barrel and end-cap, as shown in Figure 3.12, due to the finite number of coils of each magnet. As a result the muon momentum resolution is degraded in these regions. The local magnetic field throughout the MS are measured during ATLAS running by many magnetic field sensors with an accuracy of 0.3%.

Figure 3.5 shows the side on view of the MS. A muon that passes through the barrel region will cross three different stations, the *inner*, *middle* and *outer*, positioned at radii 5, 7.5 and 10 m respectively. The inner stations are situated just outside of the hadronic calorimeter and use only MDT technologies, the middle and outer layer of stations uses a combination of MDT and RPC detectors. Only the middle of the three stations is located inside the magnetic field. The design in the end-caps is different from the barrel region due to the higher background rates. The background rate is highest at large pseudo-rapidities, as a result the layer closest to the beam line is equipped with CSC instead of MDT, due to the capability of CSC to manage large rates. The second layer is equipped with MDT and TGC (which is used in the muon triggering system), which are used in the spectrometers' trigger system. The outer layer of the end-cap uses only MDT technology. The alignment of these stations was measured in cosmic data with no magnetic field. The position of the MDT stations are known to approximately 50 μm in the barrel and 100 μm in the end-cap.

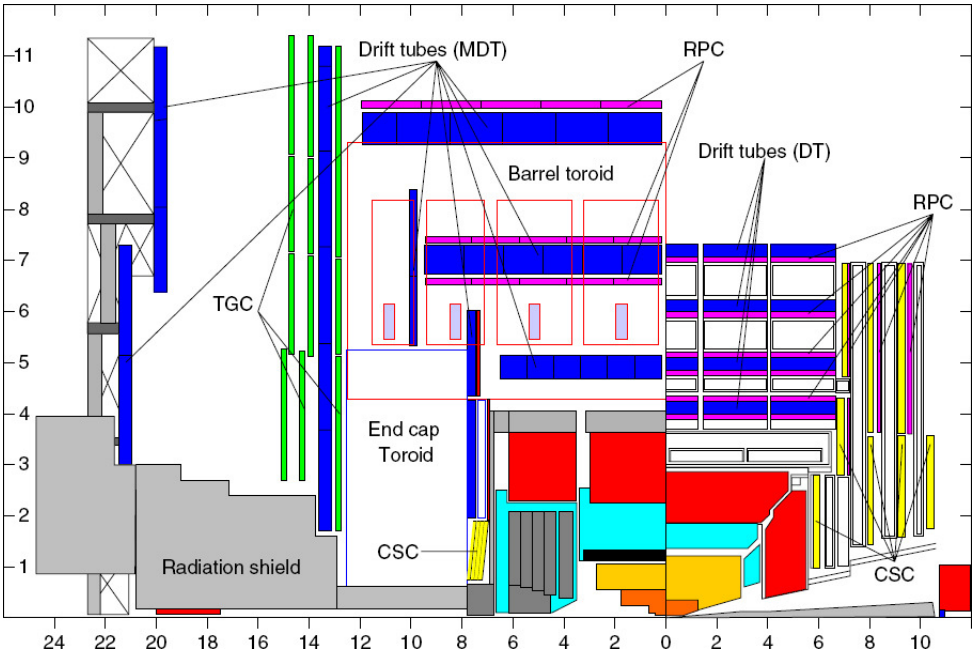

Figure 3.13: Side on view of a single quadrant of the ATLAS Muon Spectrometer [78].

The triggering system of the MS has three purposes:

- provide a muon trigger that uses well-measured muon momenta.
- provide a bunch crossing identification.
- measure the second coordinate in the precision chambers.

The inner layer of the end-cap ($2.0 < |\eta| < 2.7$) is equipped with CSCs. The CSCs are multi-wire proportional chambers with cathode strip readout and a symmetric cell in which the anode-cathode spacing is equal to the anode wire pitch. The precision coordinate is obtained by measuring the charge induced on the segmented cathode by the avalanche formed on the anode wire.

The momentum resolution of the MS is shown in Figure 3.14. The figures show the contributions from different processes that affect the resolution of the muon track momentum averaged over the region $|\eta| < 1.5$ and $|\eta| > 1.5$ separately. It can be noted that the muon resolution is between 2-4% at low momentum but rises to about 10% for TeV muons. There are three different p_{T} regions:

- At low momenta, $p_{\mathrm{T}} < 30$ GeV, the resolution in the barrel is dominated by the energy lost by the muon in the calorimeters, while for the end-cap the multiple scattering is dominant.
- For muons with $30 < p_{\mathrm{T}} < 300$ GeV the momentum resolution is limited by multiple scattering of the muon in the spectrometer.

- At high momenta, $p_{\mathrm{T}} > 300$ GeV the resolution of the MDT tubes and the alignment between the detector chambers becomes more important.

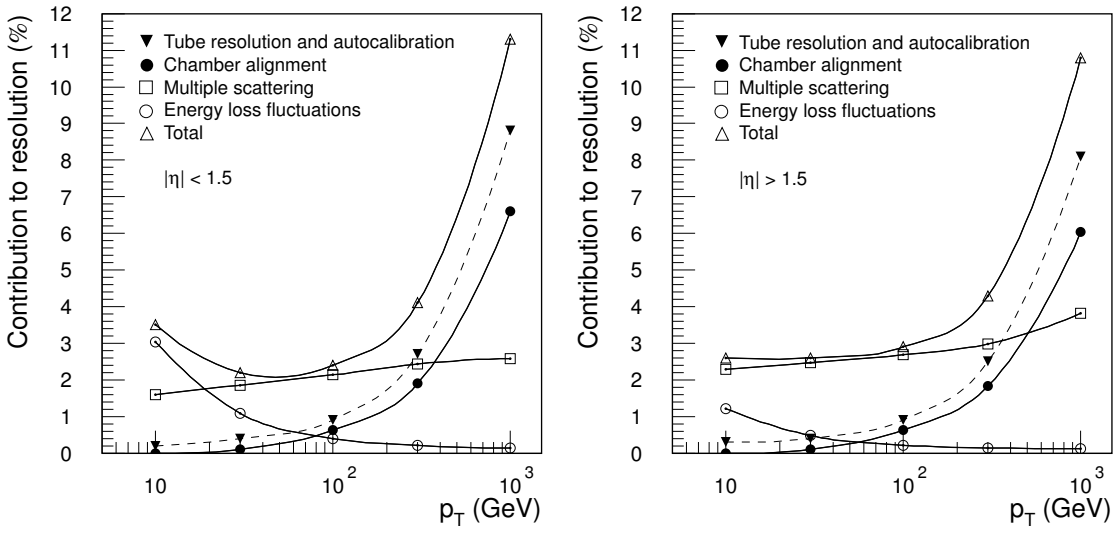

(a) (b)

Figure 3.14: Contributions to the momentum resolution [78] for muons (a) averaged over $|\eta| > 1.5$ and (b) averaged over $|\eta| < 1.5$.

MDT operations

Since the MDT operation played an important role in the work carried out on the trigger optimisation, discussed in chapter 4, details of the operation of the MDT detector are outlined.

MDT stations provide most of the precision measurements in the MS and consist of two multi-layers of aluminium tubes. There are three layers of tubes per multi-layer in the middle and outer stations, as shown in Figure 3.15 and four layers in the inner station to improve local pattern recognition, with 30 to 72 tubes per layer, depending on the position in the detector. The aluminium tubes have a radius of 15 mm with a 50 μm tungsten wire at the centre (Figure 3.16(a)). The tubes contain a $ArCO_2$ mixture with a positive high voltage of 3080 V applied to the anode wire in each tube.

A charged particle passing through the gaseous drift volume deposits energy by ionising the gas, forming free electrons. These electrons drift towards the central anode wire in the electric field, causing an avalanche of free electrons which induces a signal in the wire. The signal is propagated through the wire to a current-sensitive amplifier and discriminator which returns the time at which the signal exceeded a given threshold. This drift time t_{drift} is then converted into a distance r using their $r - t$ relation (see Figure 3.16(b)), which is determined from the data. The separation between the track and the wire per tube is known

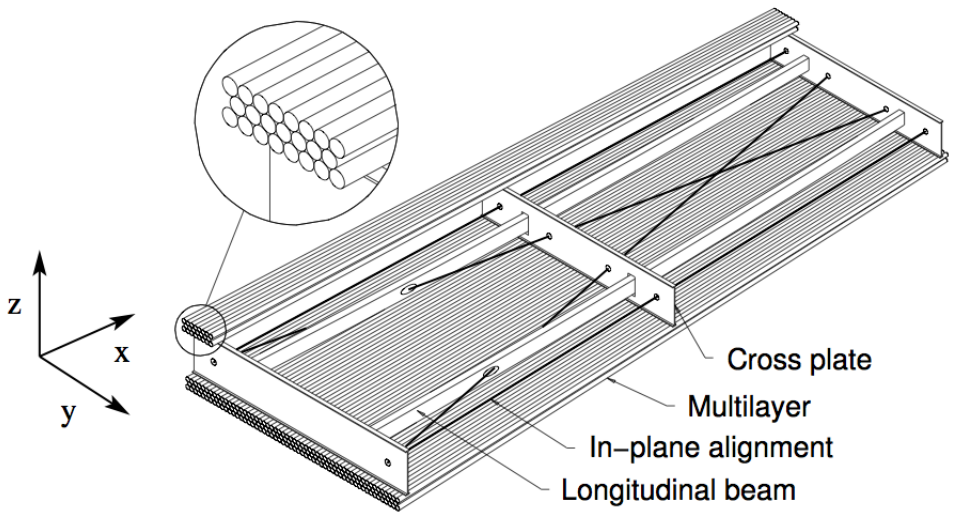

Figure 3.15: Schematic drawing of a rectangular MDT chamber [78] constructed from multilayers of three monolayers each, for installation in the barrel spectrometer. The chambers for the end-cap are of trapezoidal shape, but are of similar design otherwise.

to an accuracy of 40 μm. The position along the tube is measured by either the TGC or RPC chambers.

The MDTs (including their read-out) only measure the times of arrival of hits in the Time to Digital Converters (TDC) compared to the time of arrival of the trigger signal in the same TDC. These times need to be converted into drift distances in the corresponding MDTs. In addition to t_{drift} the total measured time includes:

- The delay due to the signal propagation in the tube, t_{prop}.
- The time of flight of the muon, t_{tof}. This is the time taken by the muon to pass from the MDT tube to the point where it passed the trigger pair of scintillators.
- Additional delays due to cables and electronics, t_0.

The values of t_{prop} and t_{tof} are measured, which leads to an arbitrary off-set for the hit time measured by the TDC. This off-set, t_0, is due to electronics and the uncertainty in cable lengths and is generally different for each tube. These off-sets could be absorbed in the $r-t$ relation, but this is not simple. A common $r-t$ relation is used, and the TDC time is shifted by t_0 for each tube. The t_0 values are determined from the lower (upper) edge of the TDC spectrum of a single tube by fitting this edge with a scaled Fermi function plus a constant background. This fit is expensive in CPU, and a preferred approach is to store the t_0 values for use in the online and offline software. This requires the timing off-sets to be calibrated and to be stable in time.

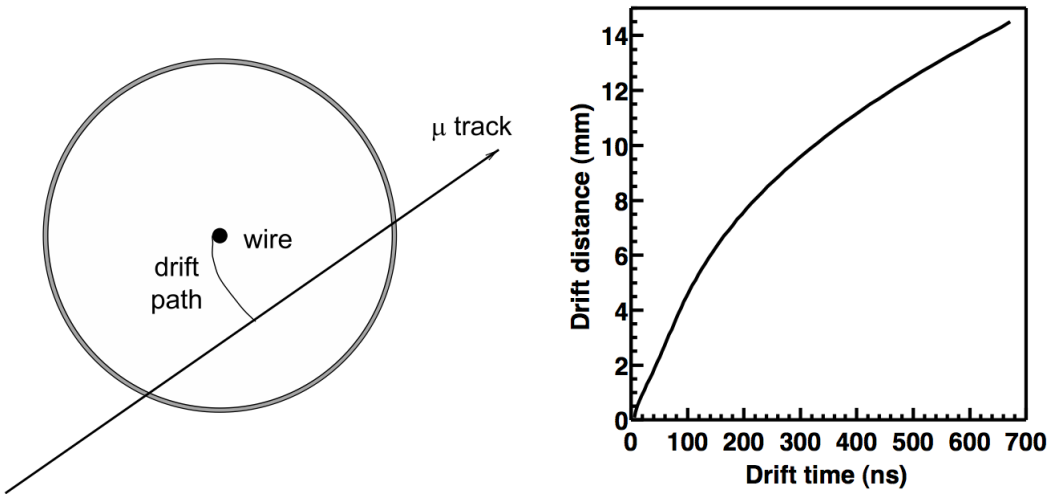

(a) (b)

Figure 3.16: (a) Drift tube operation in a magnetic field with curved drift path and (b) Relation between measured drift time and corresponding drift length in the absence of a magnetic field in MDTs.

3.6 Data Acquisition

The data used in this thesis was recorded using the ATLAS detector during the 2011 operations. The annual data taken by the ATLAS detector is divided into *collision type*, *data period*, *run number* and *luminosity block*. The 2011 running was spit into *pp* collisions, which ran from March to October, and *Heavy ion* running, which ran from November to December. During the *pp* running there were 11 distinct data periods labelled alphabetically from B-M (excluding C). Period changes occur with a major change in the operation conditions, either hardware or software based. A data period consists of numerous data runs, each assigned a specific run number, ranging from 177986-191933 for the 2011 running. A luminosity block (LB) consists of a small period of time (during the majority of 2011 running a LB lasted 120 s), with a run consisting of a collection of luminosity blocks taken over a continuous period of time. During a run the beam quality deteriorates, reducing the luminosity delivered by the LHC. A run is usually stopped when the luminosity delivered by the LHC falls below a predefined rate.

3.7 The Trigger System

The designed beam crossing frequency at the LHC is 40 MHz, with each bunch containing on average 23 proton-proton collisions. This rate largely exceeds the current capability to store these events offline. The rate that ATLAS can store data offline is determined by the capacity of the computing farm (ranging from 300 to 500 Mb/s in 2011) and the amount of information stored per event (1 MB). This limited the allowed event rate during 2011 operations between 300 and 500 Hz. With this limitation it is essential that a trigger system is used t_0 select events of interest by requiring the presence of high momentum objects (such as muons, electrons or jets). The ATLAS trigger system [78] is sub-divided into three levels as shown in Figure 3.17, comprising *Level 1* (LVL1), *Level 2* (LVL2) and the *Event Filter* (EF). Collectively the LVL2 and EF triggers are referred to as the *High Level Triggers* (HLT).

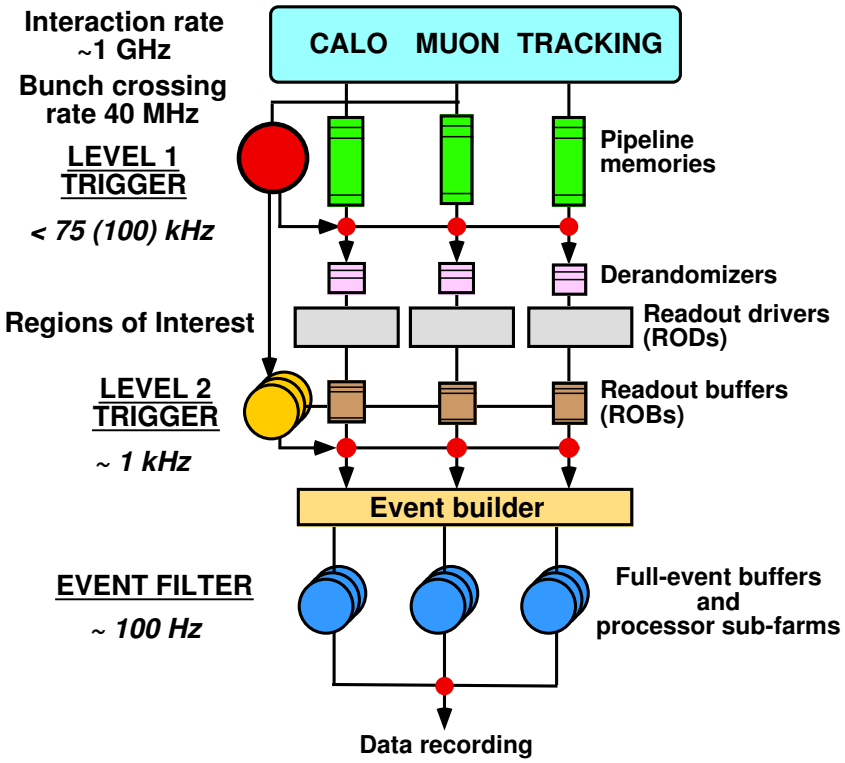

Figure 3.17: Schematic view of the ATLAS trigger system [78].

Each level refines the previous decision, lowing the event rate. The LVL1 trigger is solely hardware based and uses coarse detector information from the muon and calorimeter detectors to select *Regions of Interest* (RoIs) and use basic logic, to decide if the RoI is accepted. RoIs are selected in $\eta\phi$ space, and vary in size depending on the trigger. It is designed to reduce the 40 MHz bunch crossing rate to a rate of around 75 kHz, with a latency (decision) time of 2.5 µm (which is given in Table 3.3). An RoI that is accepted at the LVL1 stage of the trigger is passed to the LVL2 trigger to build upon the LVL1 decision. Both levels of the HLT

Level	Time
LVL1	2.5 μm
LVL2	40 ms
Event Filter	180 s

Table 3.3: Latency time of the ATLAS trigger in 2011 as a function of trigger level.

are software based, and rely on reconstruction algorithms. At the second level the trigger uses fast algorithms with the full detector information available within the RoI to reconstruct trigger objects, which is passed on to a hypothesis algorithm to accept the event based on hit and threshold criteria. This part of the trigger system has a latency time of 40 ms in order to make a decision, with the aim of realising an output event rate of 2.5 kHz. If the RoI passes the LVL2 trigger hypothesis the RoI is passed on to the EF algorithms. These algorithms have full use of the detector information and run reconstruction algorithms similar to the offline tools. With the complexity of the EF trigger it is allowed a latency time of 180 s.

Together the LVL1, LVL2 and EF triggers form a trigger chain. This chain is part of a trigger menu. The trigger menu is decided by the need of the different physics analyses and the luminosity of the LHC. Some triggers may have a rate that would saturate the bandwidth. In order to prevent this and keep the total rate within a manageable level a trigger may be pre-scaled. If a certain trigger has a pre-scale of n_p, then 1 in every n_p events that pass the trigger are accepted. All successful triggers are accepted for a trigger that has $n_p = 1$.

3.7.1 Muon Triggers

Muon triggers are used in the search for a heavy neutrino discussed in this thesis. A more detailed description of the muon triggers are discussed here. The LVL1 muon trigger (Figure 3.18) is based on the measurement of the muon trajectory through two or three different layers (stations) and it estimates the muon momentum due to the curvature of the muon in the toroidal magnetic field. The RPC1 and TGC3 stations are the pivot stations, while the rest are referred to as lever stations. There are two type of LVL1 muon trigger, low-p_{T} and high-p_{T}. The low-p_{T} triggers use predefined coincidence patterns, based on extrapolating hits in the pivot stations to the closest lever stations. The high-p_{T} triggers require coincidences in all three stations.

The LVL2 muon trigger takes RoIs from LVL1, $\Delta\eta \times \Delta\phi = 0.1 \times 0.1$, with the purpose of finding tracks in the MS. This is achieved using hits in the MDTs and information from the trigger chambers. Pattern recognition starts by defining *muon roads* based on the trigger hits of LVL1 and simple geometrical models, and then uses a contiguity algorithm within the road. The pattern recognition uses only the centre of the tubes, so no drift time information is needed. Tracks are then fitted using drift times with the tracks transverse-momentum

assigned by using a look-up table (LUT), that use a predefined relationship between the track p_{T} and the sagitta, which is the distance from the arc of a track to its base. The trigger is accepted if the RoI passes a defined hypothesis, and passed to the EF trigger.

The EF triggers makes full use of the offline algorithms. Pattern recognition is performed within a region specific to the RoI, forming local segments per station layer from reconstructing hits located in the MDT/trigger chambers. Track building algorithms are seeded by the reconstructed segments. The tracks are combined with the ID tracks for a more accurate measurement of the track momentum, with corrections applied for energy losses in the calorimeter. The trigger is then accepted if the track p_{T} is above a predefined threshold.

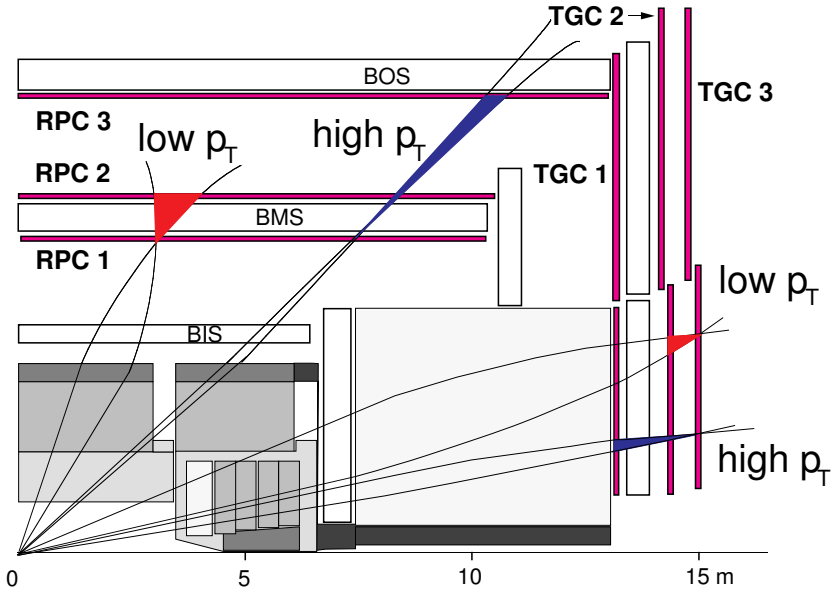

Figure 3.18: Schematic view of the ATLAS Level 1 muon trigger system [78].

3.7.2 Trigger Configuration

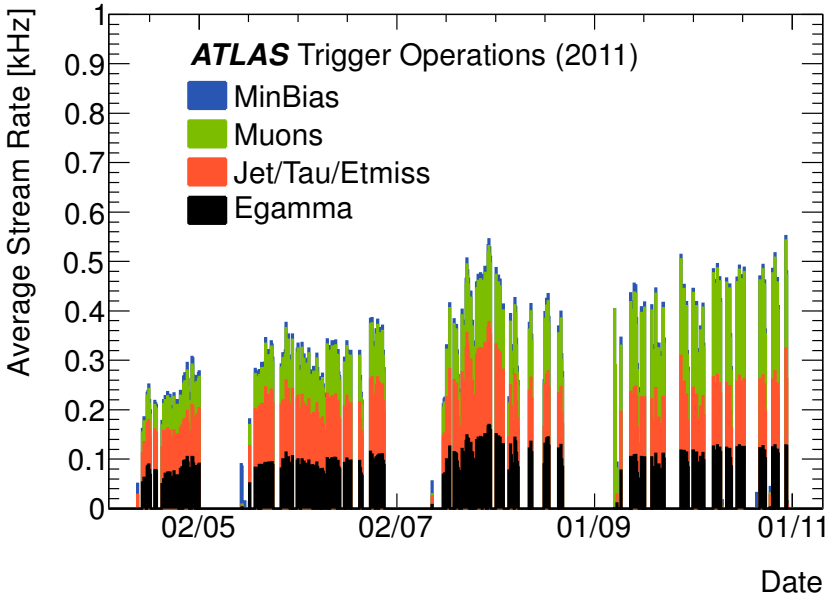

Figure 3.19: Average stream recording rates for the EF triggers in 2011. Filtered for LHC stable beams.

The Trigger Chains (the combination of LVL1, LVL2 and EF) are assigned to trigger streams, depending on the job of a trigger. The ATLAS trigger system has several different physics streams, including *muon*, *egamma*, *JetTauEtmiss* and several other streams including *MinBias*, *cosmic* streams, *calibration* streams, *express* streams and *debug* streams. A stream is essentially a group of trigger chains; all trigger chains that trigger the presence of a muon in the MS are part of the muon stream. It is possible however that a trigger chain is assigned to multiple streams, as is the case for multi-object triggers i.e., muon+jet triggers. The list of trigger chains and streams used online form the *trigger menu* which are accompanied by lists of pre-scales assigned to each chain, referred to as the pre-scale keys. The menu and pre-scale keys are predetermined, considering the physics needs and the operational conditions. Figure 3.19 shows the average online trigger rate for the different physics streams as a function of time in 2011.

The express stream is used as the primary stage of the Data Quality framework [81, 82], using a small fraction of physics stream data and fast reconstruction to quickly access the performance of the detector sub-systems. The calibration stream contains partially built events delivering the minimum amount of information needed for detector calibrations. Higher rates than the physics stream rates are achieved that way. The debug stream contains events where the trigger was unable to make a decision. This is either due to a crash in the online trigger algorithms or that the algorithms were timed out by the trigger navigation. There

are different levels of severity for events entering the debug stream. Events that timeout in the LVL2 or EF processing are sub-divided into two classifications, they enter either the *debug_EFHltTimeout* debug stream or *debug_efdProcTimeout* debug stream. These events are then reprocessed offline with less stringent processing requirements. In the case the trigger steering was able to abort the event as a result of a timeout, the event will appear in the *debug_EFHltTimeout* debug stream. However if the trigger steering was unable to abort the event then it will appear in the *debug_efdProcTimeout* debug stream. The latter case is much more severe as the computing node that is processing the event much be reset.

3.8 Luminosity Measurement

The ability to accurately determine the luminosity of data is essential to correctly determine background estimates and expected signal yield for the search presented in this thesis. The number of observed signal/background events passing our final analysis cuts is related to the process (x), with cross section (σ_{x}) by the following:

$$N^{\mathrm{x}} = \epsilon.l.p.f.\mathcal{L}.\sigma_{\mathrm{x}} \tag{3.3}$$

where N is the number of signal events, ϵ is the acceptance times efficiency and l is the live-time, p is the product of the trigger pre-scales, f is the correction factor for any losses that occur during online data collecting or offline processing and $\mathcal{L}$ is the integrated luminosity.

At present, ATLAS relies only on event-counting methods [83] for the determination of the absolute luminosity. equation 3.1 can be written as:

$$\mathcal{L}_{\mathrm{inst}} = \frac{\mu n_b f_r}{\sigma_{inel}} = \frac{\mu^{vis} n_b f_r}{\epsilon \sigma_{inel}} = \frac{\mu^{vis} n_b f_r}{\sigma_{vis}} \tag{3.4}$$

where ϵ is the efficiency for one inelastic pp collision to satisfy the event selection and μ^{vis} is the average number of visible interactions per bunch crossing. The value of μ^{vis} is determined by taking into account Poisson statistics for the probability to observe at least one event in a set of colliding bunches. To determine the value of σ_{vis} the absolute luminosity is calculated using

$$\mathcal{L}_{\mathrm{inst}} = \frac{n_{\mathrm{b}} f_{\mathrm{r}} n_1 n_2}{2\pi \Sigma_x \Sigma_y} \tag{3.5}$$

where n_1 and n_2 are the number of particles in the two colliding bunches and Σ_x and Σ_y are the widths of the horizontal and vertical beam profiles. The values of Σ_x and Σ_y are measured using dedicated *van der Meer* (vdM) scans and the observed event rate is recorded, and from which the value of $\mathcal{L}$ can be calculated using the measured visible number of interactions per bunch crossing. The luminosity is then measured during operation of the

detector approximately every second, using the extracted value of σ_{vis} and the measured value of μ^{vis}. The luminosity is then summed over all colliding bunches per luminosity block and recorded by ATLAS, as seen in Figure 3.20.

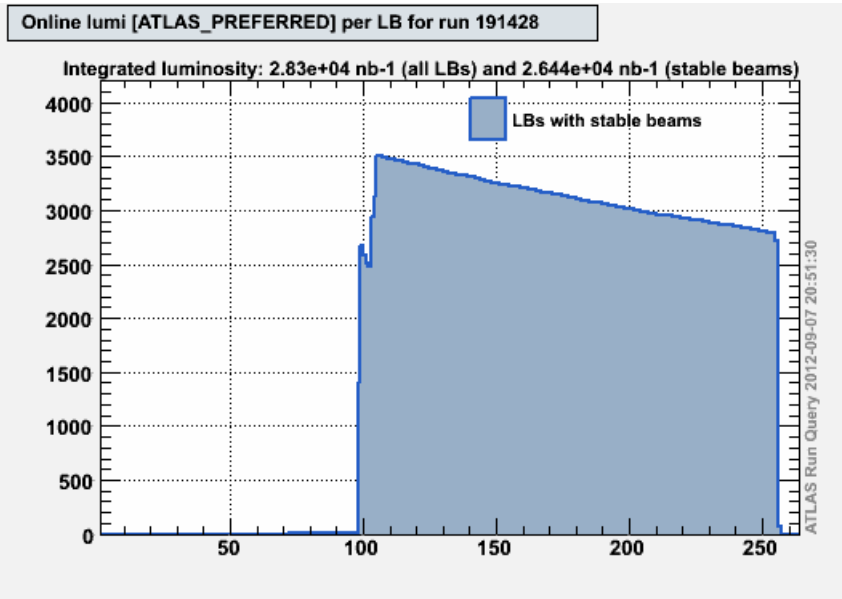

Figure 3.20: Instantaneous luminosity profile as a function of lumi-block for run 191428, Sunday October 23 2011.

Chapter 4

Optimisation of the Muon Trigger System

As discussed in section 3.7, in the case of a trigger chain exceeding the preset cutoff time allowed for a trigger hypothesis, the trigger processing is terminated by the trigger steering, and the event is passed into the debug stream. This has both a consequence on the operational side and the analysis side of the experiment. Events which cause a hard timeout or crash of the trigger require the working node to be rebooted. A large rate of timeouts would therefore result in disruptions to ATLAS operations. Even if the rate of events entering the debug stream is negligible relative to physics streams, the nature of events that enter the debug stream tend to be events with large number of hits and tracks, and are possible candidates for exotic new physics. In the case that the new physics process has a cross sections of order fb^{-1} the analysis of the debug stream is essential. Figure 4.1 shows such an event found in the debug stream in July 2010, containing high energy jets that passed the requirements for a dijet analysis.

This Chapter explains the muon trigger algorithms, and the methods used to improve the processing times [84]. The author, collaborating with offline experts, played a key role on improving the muon algorithms to optimise the timing and performance. Section 4.1 describes the muon EF algorithms, with the causes of the long time processing times discussed in section 4.2. The details on the improvements installed into the trigger algorithms are given in section 4.3.

4.1 Muon Trigger Algorithms

The group of algorithms used in the primary online EF muon trigger are known as TrigMuonEF. A schematic overview of the algorithm chain is presented in Figure 4.2. The information from the LVL2 is passed to TrigMuonEF via a Trigger Element (TE) that has

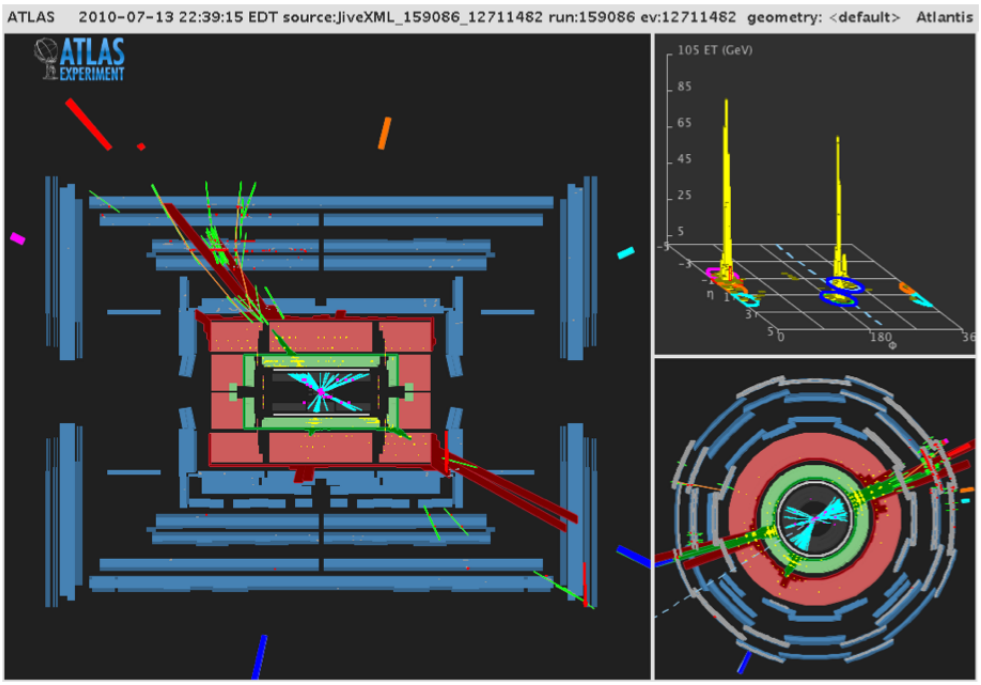

Figure 4.1: Event display from run number 159086, event number 12711482 found in the debug stream in July 13th 2010.

stored the LVL2 results. TrigMuonEF contains four separate algorithms performing different steps of the online reconstruction, including:

- Segment Finding: The segment finding algorithms look first for roads through the muon spectrometer using pattern recognition algorithms, spanning all detector stations. The roads are then investigated per station by matching MDT hits to form straight line segments.

- Track Building: The segments formed in the CSC and MDT stations are matched to form track candidates. This is seeded by segments in the outer most layer of the muon spectrometer, with segments in the middle layer fitted to the seed. This is repeated for all segments in the middle layer. If the fit is successful, the track candidate is extrapolated to the inner most layer, where another fit is performed.

- Extrapolation : The tracks are extrapolated back to the beam line, where the interaction parameters are measured at the tracks' perigee.

- Combination : The tracks are matched to tracks reconstructed in the inner detector.

The TrigMuonEF trigger uses the same tools for pattern recognition and segment finding as used by the offline reconstruction algorithms. The basis behind this decision was to guarantee high efficiency for the online muon track reconstruction with good rejection of fake

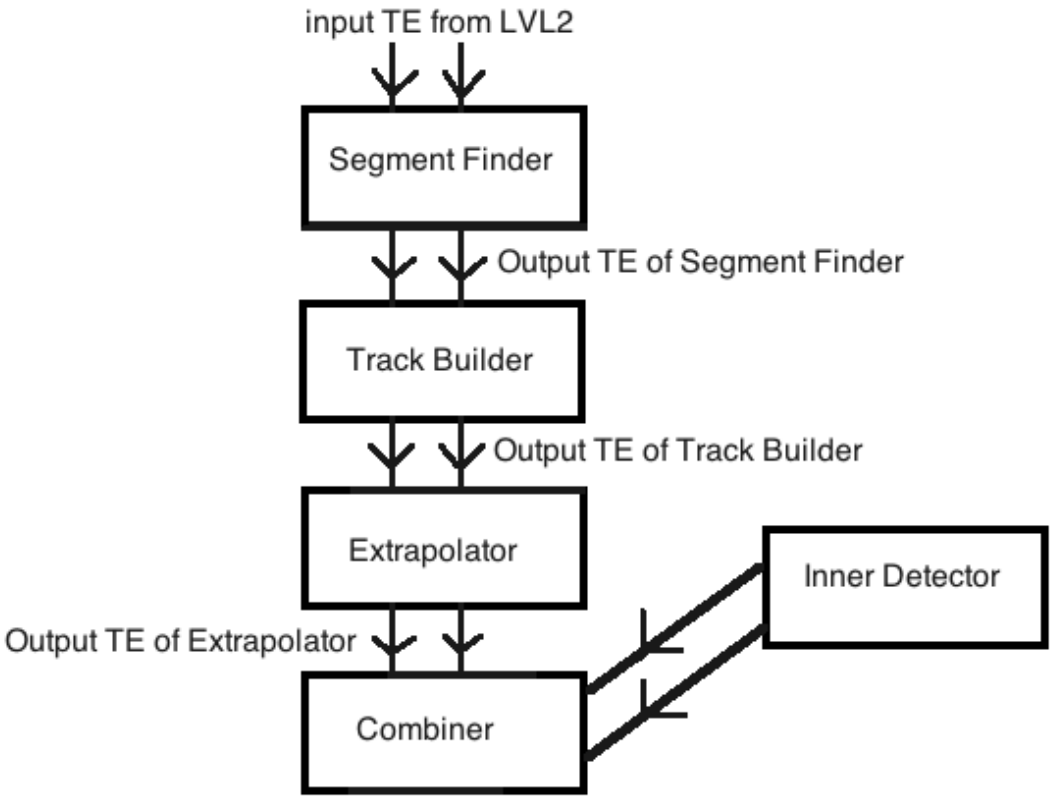

Figure 4.2: Schematic diagram of the TrigMuonEF algorithm chain. TE refers to the Trigger Element.

background sources. These tools perform complicated fits and can very time consuming. This is not an issue offline, where the cutoff time for an algorithms decision is 3600 s, while online the cutoff time is 180 s.

Monte Carlo Samples

The following samples were used in the studies to optimise the muon algorithms:

- Black-hole, SU(4) (which is a signal MC for a super symmetric extension of the SM) and QCD J6 and J8 (where J6 and J8 differ only by the momentum cuts applied to the jets in the two samples) dijet Monte Carlo samples.
- 2009 cosmic data: run number $>$ 135388.
- $t\bar{t}$ and Z Monte Carlo.
- Debug Stream (2010): runs 158116-166786.

- Muon Stream (2010): run number 167532.

The first four Monte Carlo samples in the list tend to have busy event topologies and were known to have large offline processing times in TrigMuonEF. The $t\bar{t}$ sample was used as a standard benchmark sample. The last two samples were data runs taken in 2010 operations.

The processing time per event for two of the busy simulation samples, running with the trigger setup used in 2009 operations, are shown in Figure 4.3. These processing times are acquired by running the trigger in a special configuration where the muon event filter algorithms are disabled. The normal configuration is shown in Figure 4.4, which shows numerous events that exceed the 180 s cutoff time, with one event in the J8 sample exceeding 4×10^4 s. The lack of events exceeding 180 s in Figure 4.3 indicates that TrigMuonEF is the cause of the timeouts. A break down further of the TrigMuonEF algorithms shows that the busy events that timeout spend most of their processing time either in the segment finder algorithms or the track building algorithms.

Analysis of the debug stream for the 2010 dataset was performed. The results show that the majority of events in the debug stream were from timeouts in the EF algorithms. This is seen in Figure 4.5(a). This is a breakdown of events in the debug stream for September 2010. Most entries are related to processing timeouts, while the bin labelled other streams containing events where the trigger processing crashed. A further breakdown of the events in the timeout streams are shown in Figure 4.5(b). It is seen that timeouts in the trigger were to a good approximation all found in the muon algorithm chains, which mainly occurre in the segment finder and track builder muon EF algorithms. The bin labelled other refers to timeouts in non-muon related algorithms. The muon EF timeouts seen in the debug stream were seen earlier in the 2009 cosmic data, and in busy simulation events, but at much smaller rates.

4.2 Inspecting Busy Events

To better understand the structure of events with long processing times and find methods of reducing the timing, TrigMuonEF was implemented with code to produce event-by-event information for the timing of the different processing steps and the characteristics of the event (e.g. number of hits in the muon spectrometer). This was done for both segment finding and track building algorithms by the author, where the majority of the processing time was being spent. This allows detailed studies of the source of the long processing time in both the segment finder and track builder by rerunning the trigger offline using the raw data for both data and simulation. Figure 4.6 shows the processing time in the segment finder verses the number of hits in the muon stations. The increase in the number of hits results in more fits per road performed by the segment finder which explains the positive correlation. Figure 4.7

shows the distribution of the time per RoI in the segment finder and track builder. The time in the track builder is found to be an order of magnitude larger than the segment finder. The time spent performing the track fitting is expected to be correlated with the combinatorics of the segments available to the fitter, which is observed in Figure 4.8. Figure 4.9 shows the total number of hits in the RoI (summed over MDT, RPC, TGC and CSC) as a function of the track building time. Looking into the cosmic stream we found the number of hits in the MDT detector was found to be a correlated to the track builder time.

Figure 4.10 shows the $\Delta R = \sqrt{\Delta\phi^2 + \Delta\eta^2}$ distribution for RoIs processed by TrigMuonEF, where $\Delta\phi$ and $\Delta\eta$ are the differences between RoIs in an event for the azimuthal angle and pseudo-rapidity respectively. RoIs can regularly overlap in the detector. As a result the hits in the detector are processed twice. This happens when the η-ϕ coordinates of two LVL1 RoIs are separated by less than $\Delta R = 0.2$. The distribution in Figure 4.10 shows the separation between RoIs that are processed by TrigMuonEF. The fraction of time spent processing overlapping RoIs in the track building compared to the total time in the track building is shown in Figure 4.11 and shows a significant fraction of time can be saved.

In addition multiple trigger chains were found to be processing the same RoI, rerunning the segment finding code. The trigger steering was unaware of the duplication because the input trigger elements are different for the different trigger chains.

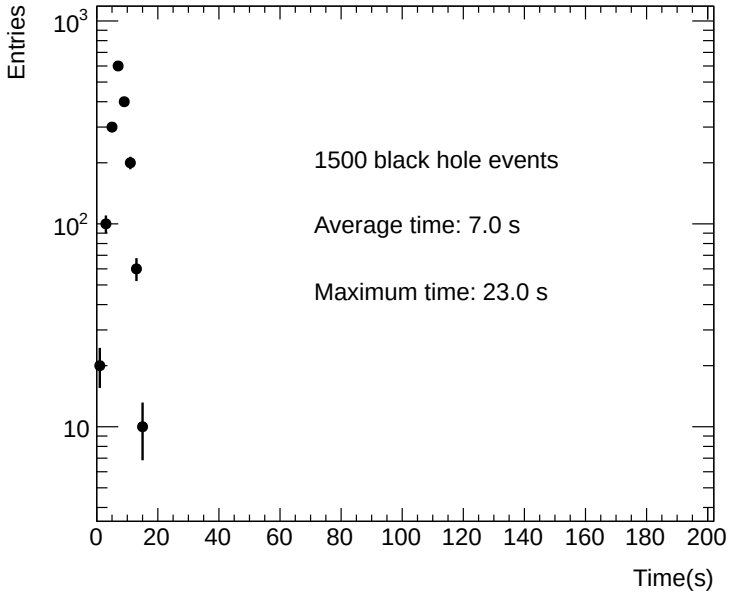

(a)

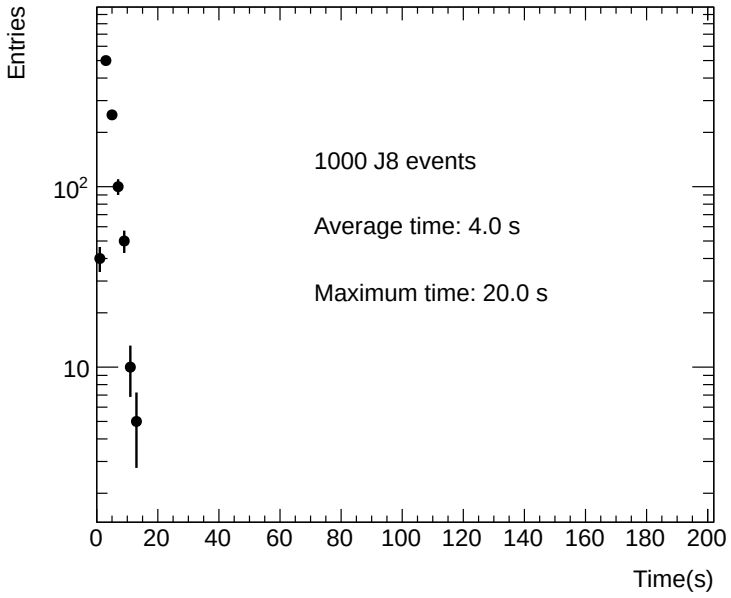

(b)

Figure 4.3: Trigger processing times with no TrigMuonEF processing for a) black-hole events and b) J8 events.

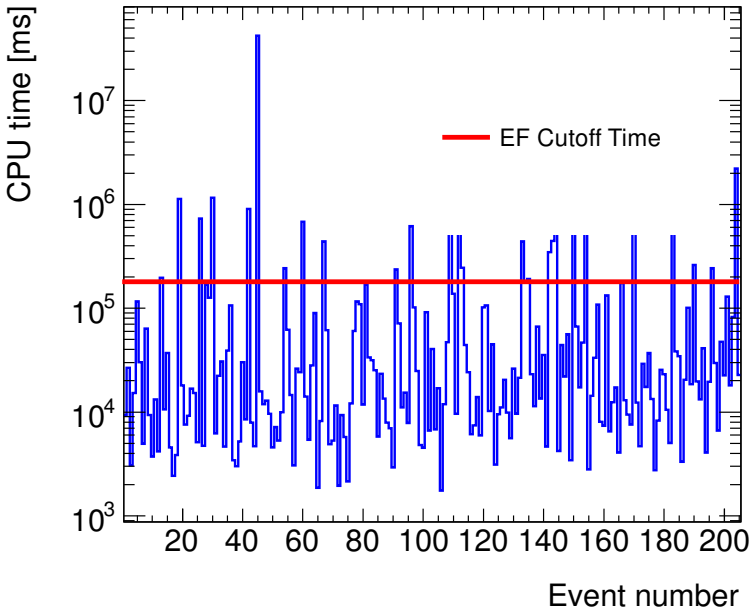

(a)

Figure 4.4: Trigger processing time per event (with TrigMuonEF) for J8 events.

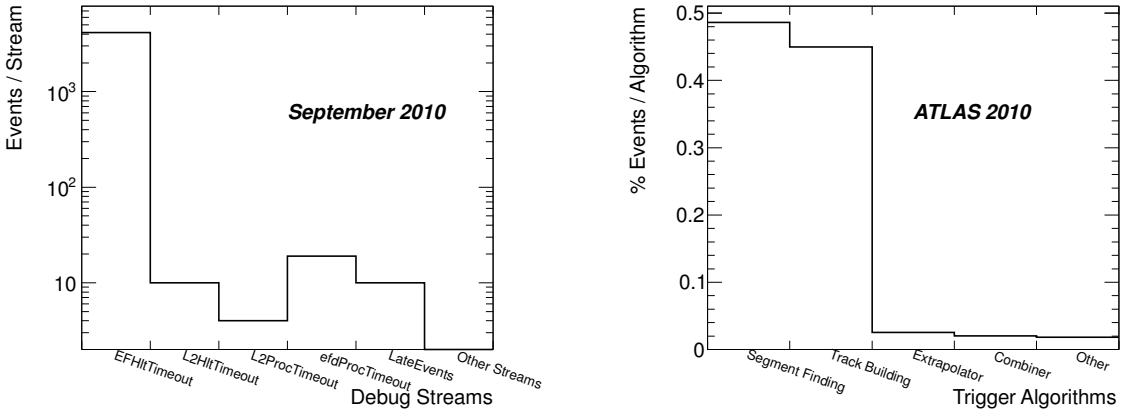

(a) (b)

Figure 4.5: Break down of debug stream events during 2010 operations, (a) shows the split of events in separate streams during September 2010 while (b) shows the breakdown of events in the soft timeout debug stream.

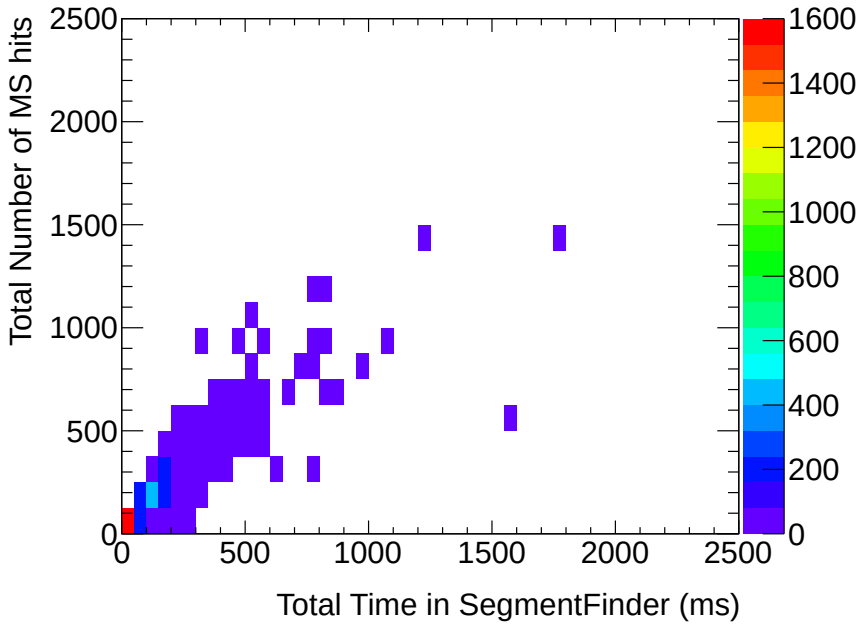

(a)

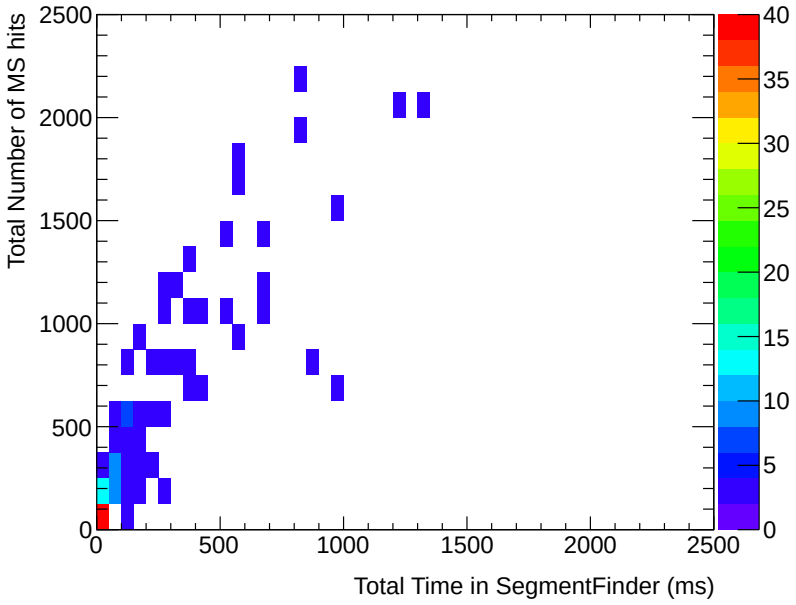

(b)

Figure 4.6: Relationship between the total segment finder processing time and the number of muon detector hits for a) $t\bar{t}$ events and b) black-hole events. The coloured bar on the right-hand side can be used to relate the bin colour to the number of bin entries.

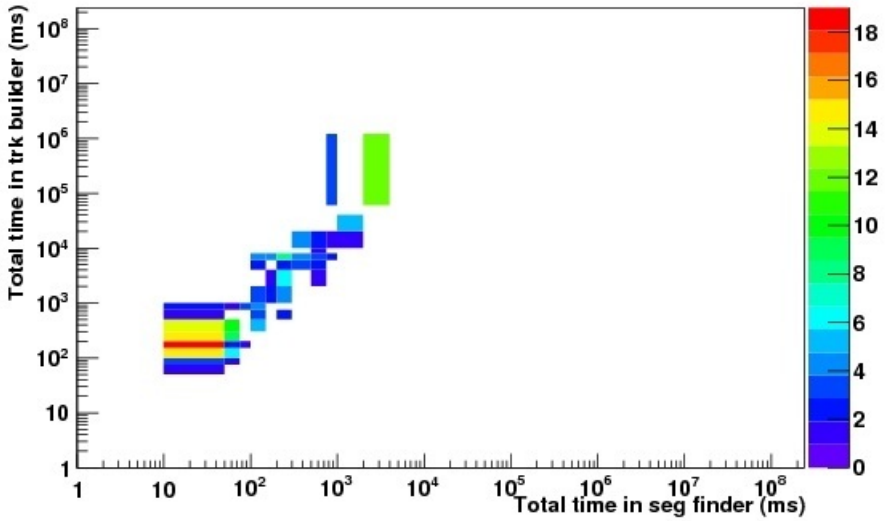

(a)

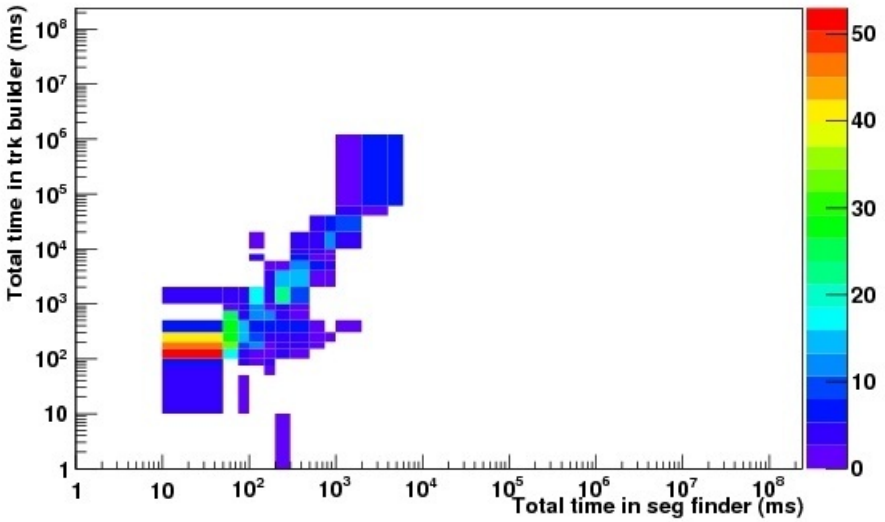

(b)

Figure 4.7: Distribution of time per RoI in the segment finder vs time spent in the track builder, for a) J6 events and b) black-hole events.

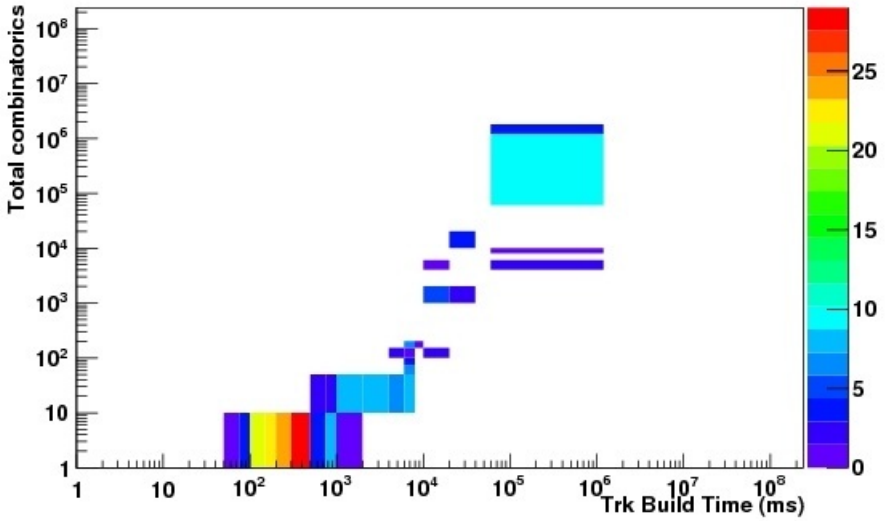

(a)

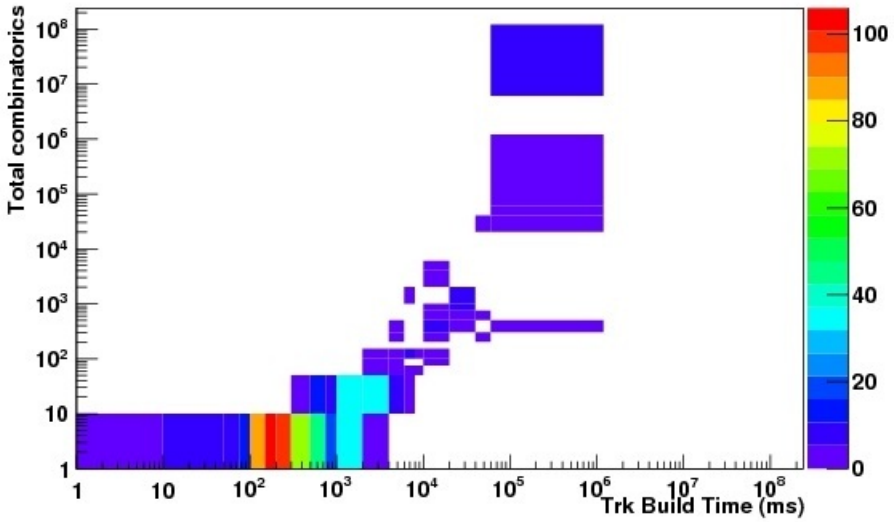

(b)

Figure 4.8: Distribution of time per RoI in the track builder as a function of the combinatorics of the segments for a) J6 events and b) black-hole events.

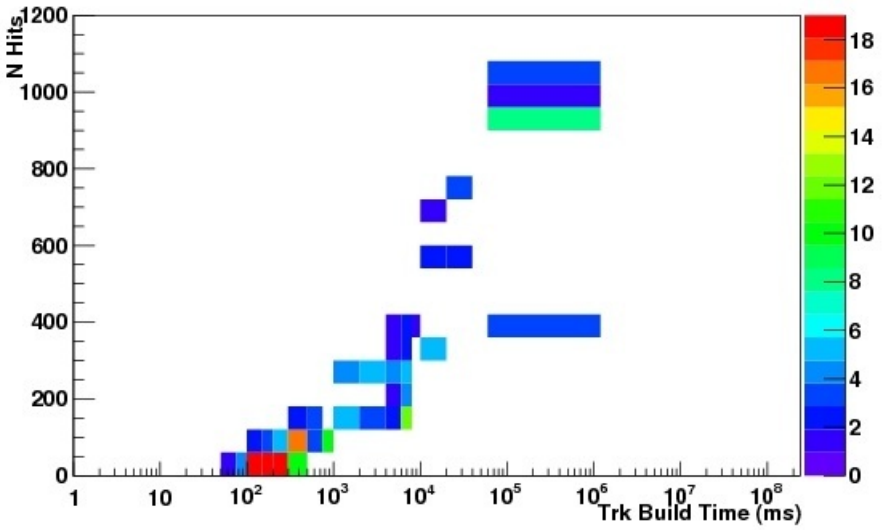

(a)

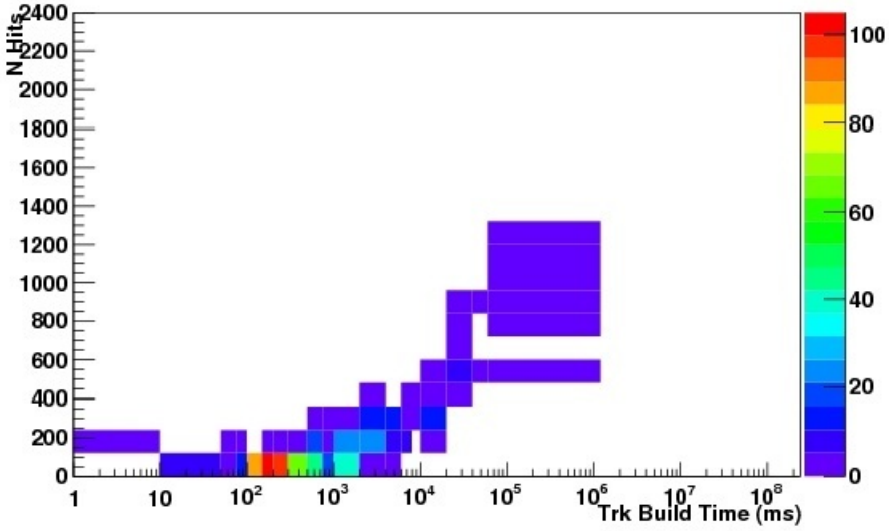

(b)

Figure 4.9: Distribution of time per RoI in the track builder as a function of the number of hits in the muon detectors within the RoI, for a) J6 events and b) black-hole events.

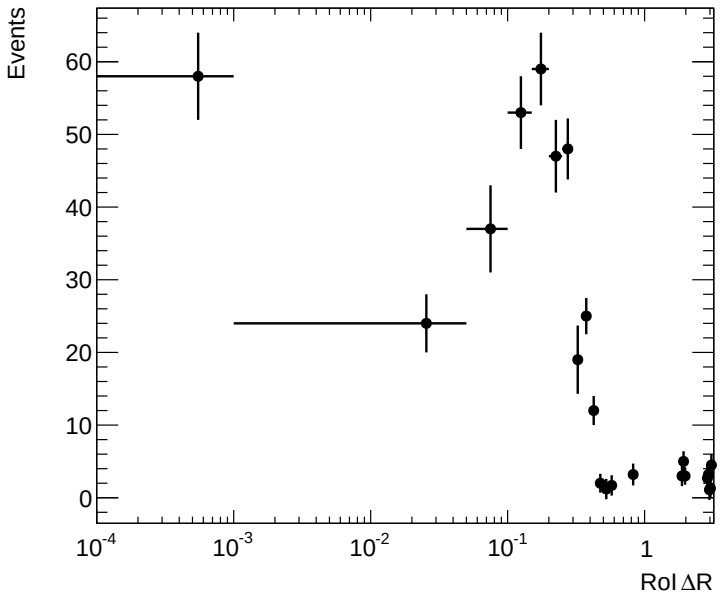

(a)

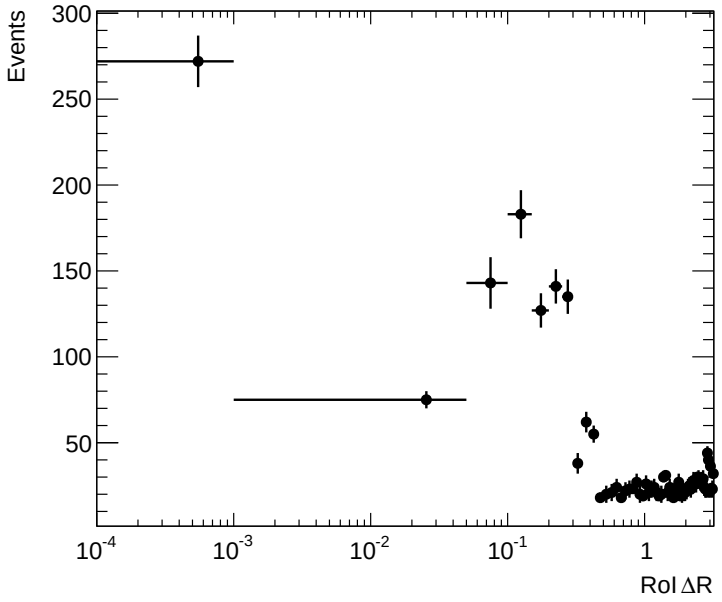

(b)

Figure 4.10: ΔR distribution between RoIs in events, for a) J6 events and b) black-hole events.

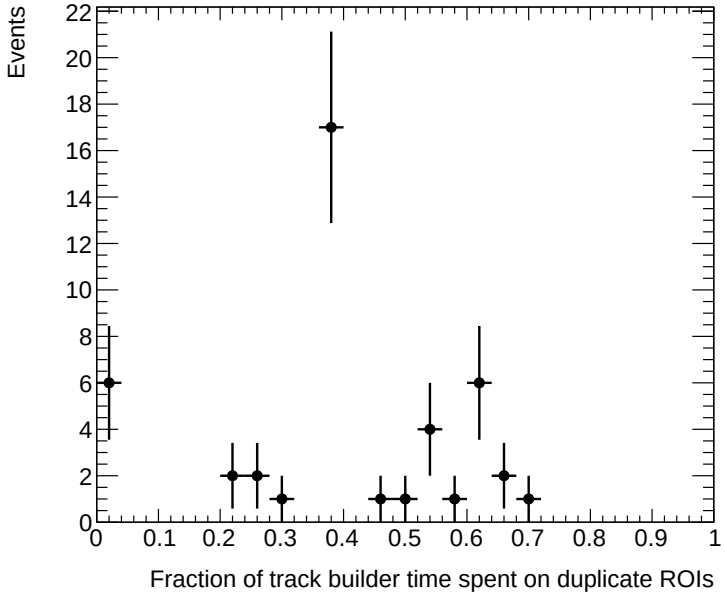

(a)

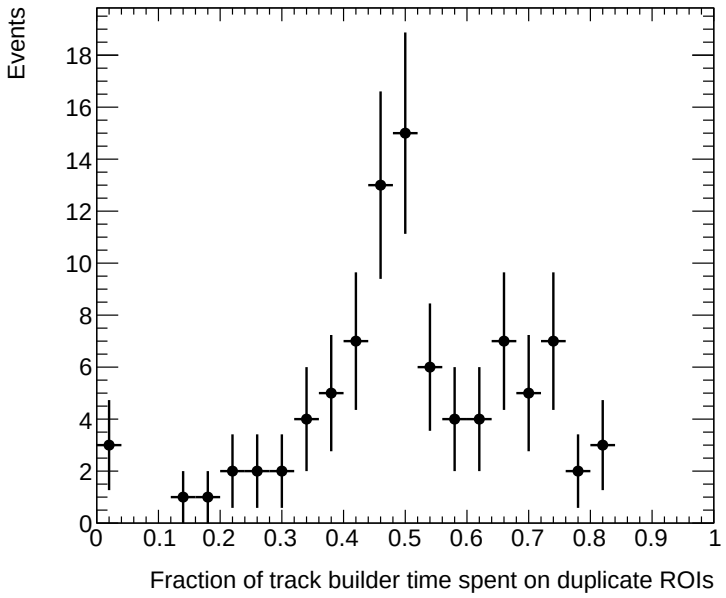

(b)

Figure 4.11: Distribution of the fraction of timing spent in the track builder processing duplicate RoIs, for a) J6 events and b) black-hole events.

4.3 Optimisation of Processing Time

Considering the points mentioned in the last section this section describes the methods used to reduce the processing time of both the segment finder and track builder algorithms. An investigation of the busy events in data and Monte Carlo show the following characteristics describe a typical timeout event:

- Locally very high track multiplicity in the muon system.
- Large number of hits in the MDT detector.
- High number of combinatorics in the segment matching.
- Multiple overlapping RoIs.

These events were found to be either cosmic showers or hadronic punch through jets. An event display for such an event can be seen in Figure 4.12, that took over 29 hours to be processed by the muon algorithms.

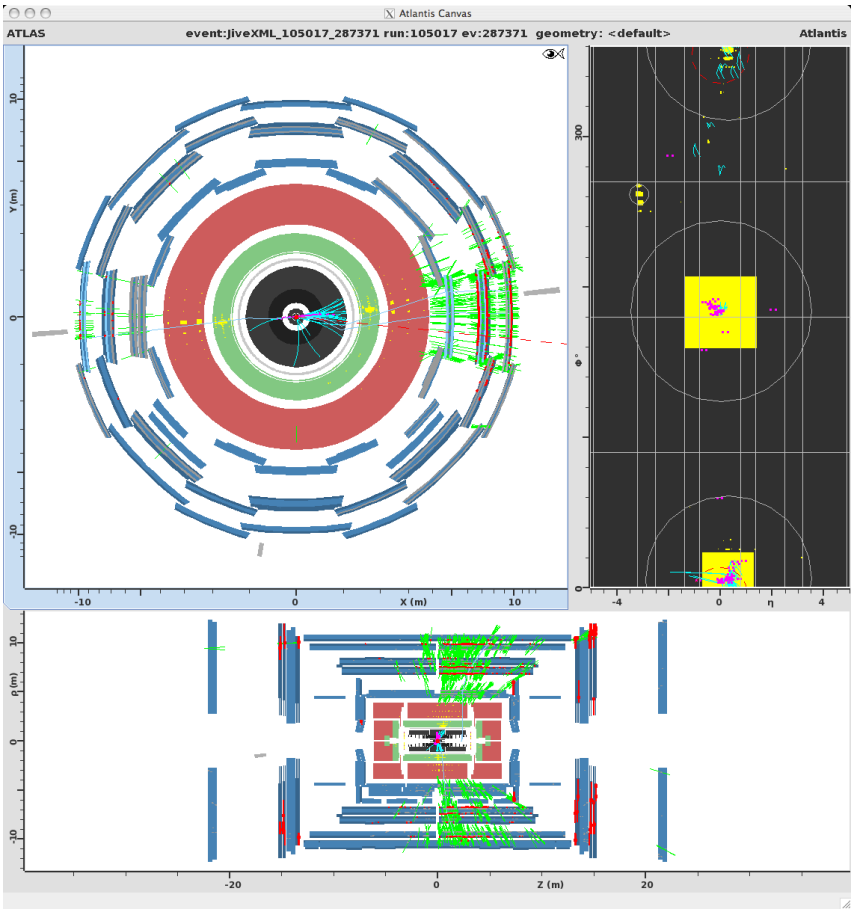

Figure 4.12: Event display for a timeout J8 event, event number 287371 with a processing time of 29 hours.

Feature Caching

To prevent the case where the segment finder reprocessed the same hit information, an RoI level caching was implemented. A trigger element is used to pass information from one trigger algorithm to another. Each algorithm in a chain uses the information stored by the trigger element, processes the information in some manner and produces a new trigger element to be used in the next step of the chain. This is how the segment finder accesses the LVL2 information and how the track finding algorithms gains access to the segments reconstructed by the segment finder.

In the segment finder a region selector is called for each RoI, taking the η, ϕ values passed from LVL2 and constructing the RoI trajectory with $\Delta R < 0.1$. As illustrated in Figure 4.13, the detector is split up into detector elements. Only detector elements that contain MDT/CSC hits that overlap with the RoI are processed by the segment finder. It is possible that multiple RoIs, with different trajectories will process the same set of detector elements, as seen schematically in Figures 4.13(a) and Figures 4.13(b).

A new class was added to the TrigMuonEF package that stores the segments and tracks created by the two algorithms and stores the list of detector elements processed by each new RoI. All preceding RoIs are compared to those stored, with two possible outcomes. Either the RoIs are well separated and therefore the segment finding code runs as usual or the RoI is a duplicate and the segment finding algorithm calls the stored results. This new caching benefits the processing time in two ways. First of all any overlapping RoI, containing the same hits as an already processed RoI will no longer be reprocessed. Additionally the reprocessing of multiple chains is removed.

The effect of this caching on a sample of 125 black-hole Monte Carlo events can be seen in Figure 4.14. The result is a 60% improvement in the processing time.

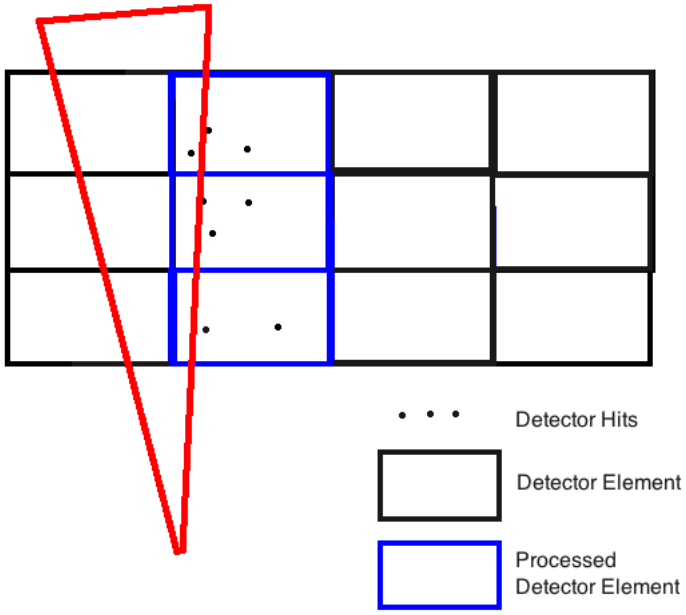

(a)

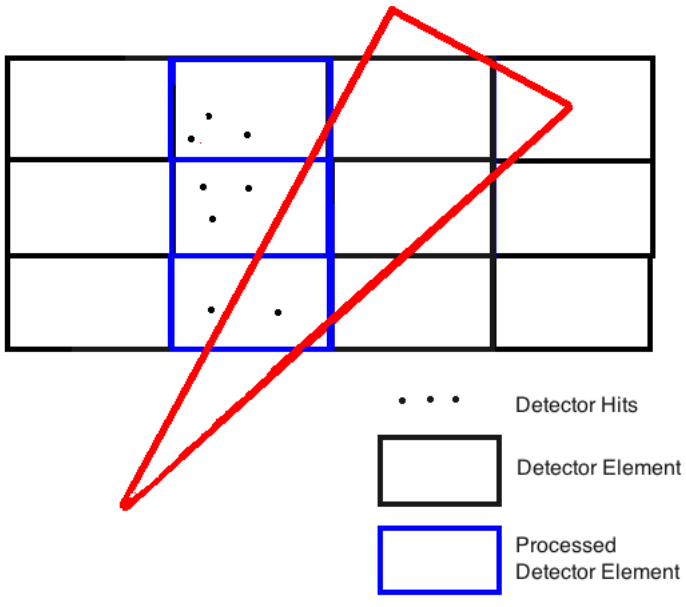

(b)

Figure 4.13: (a) and (b) show two possible RoIs (the red cones) overlapping a section of the muon spectrometer. The blue rectangles show the detector elements that contain muon hits and are therefore processed by the segment finder.

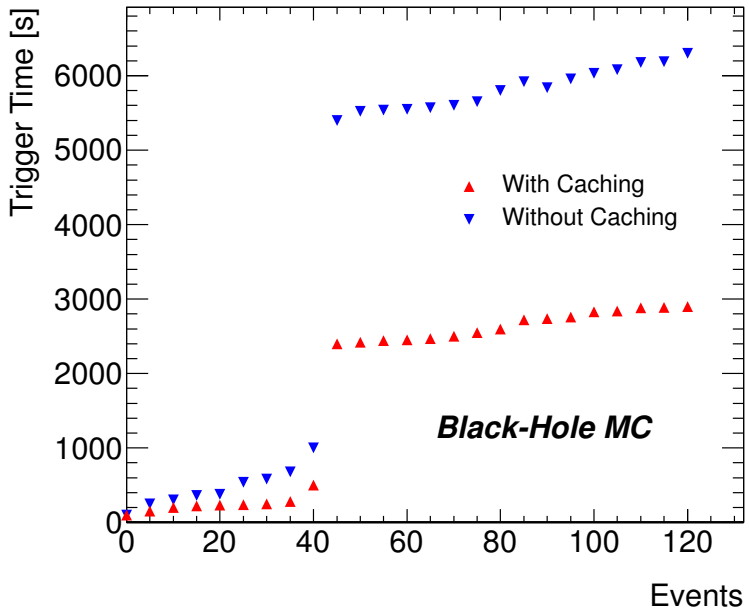

Figure 4.14: Total cumulative processing time of the segment finder and track builder for the black-hole MC sample.

Segment Matching

A segment matching tool was developed with the purpose of decreasing the number of track fits needed to reconstruct a muon. It has been shown in a detailed analysis [84] that 95% of the CPU consumption is spent on muon track reconstruction. Since the track fit is highly optimised, the biggest gain in CPU for the track reconstruction can be made by decreasing the total number of attempted fits. This can be achieved by determining prior to the fitting whether a segment is likely to belong to the same track as the seed.

Tracks in the muon spectrometer are found using a combinatorial search algorithm. A seed segment is selected within a road in the muon spectrometer which is combined with another segment in the road by the track fitter. The pair of segments are kept as a track candidate if the fit is successful. Additional segments are added one at a time to this track candidate, with the track fit performed with each additional segment.

The segments are selected by the segment matching algorithm based on their relative position and direction. From this requirement segments that are unlikely to belong to the same muon are removed before the CPU intensive fit is performed. This decreases the processing time of the track building algorithm. The selection requirements made on the matching are based on the position of the muon pairs due to the magnetic field and the amount of scattering from collisions with material that varies throughout the detector volume. The sample of muon segments are subdivided based on whether the segments are in the spectrometer barrel or end-cap, and based on whether a segment is in the inner, middle, or outer layer of MDT chambers.

The matching of segments in the precision plane (θ) have been studied in detail. The MDT hits provide a measurement in θ for segments in all layers of the muon spectrometer. The discriminating variables used for the segment matching are illustrated in Figure 4.15. The direction of the segments are compared to the direction of the line that connects them between points p_1 and p_2, in order to calculate the two angles α_1 and α_2. The sum of the angles $\alpha = \alpha_1 + \alpha_2$ between two muon segments that belong to the same muon track should be approximately zero. (Assuming a track of uniform curvature). Deviation from uniform curvature of the tracks are dependent on the detector region. The variable $\alpha = \alpha_1 + \alpha_2$ (also called $sumDeltaYZ$) is used as a selection variable. A comparison is made between the distribution of this variable for segments that appear in a successfully fitted muon track (signal muons) and segment pairs that are not associated with a muon (background muons). The distribution of the sum of the angles for segment pairs in different regions of the spectrometer for a $Z \rightarrow \mu\mu$ Monte Carlo is shown in Figure 4.16. A requirement is made that both segments are found in the same ϕ sector of the detector. The signal distribution (blue) is more sharply peaked than the background distribution (green), and has a more steeply falling tail. An upper limit can be placed on the sum of the angles such that background is

	BIBM	BIBO	BMBO	EIEM	EIEO	EMEO
loose	0.200	0.200	0.100	0.200	0.200	0.010
tight	0.100	0.100	0.060	0.100	0.100	0.005

Table 4.1: Cuts on *sumDeltaYZ* for segment pairs in different regions of the detector. Loose cuts are used as the default selection, while tight cuts are used for busy events. The stations are labeled as follows. B refers to barrel, E is end-cap and I,M,O refer to inner, middle and outer stations respectively.

removed with minimal efficiency loss.

The set of cuts used is given in Table 4.3. The sample is subdivided based on the location of the segments in the detector. As an example, "BIBM" indicates that one segment is in the barrel inner MDT station, and the second is found in the barrel middle MDT station. A loose selection has been developed as a default, with a tight selection for busy events.

Track Builder Cuts

In busy events the number of segments in the outer MDT stations used to seed the track candidates is large. This produces many track candidates and increases the number of fits performed by the track builder. A number of parameters were re-tuned in the offline tools to reduce the number of seeds allowed. For example, the number of seeds allowed in the event was reduced from 50 to 10 as well as the maximum number of combination attempts per event from 100 to 10. Here a seed is the segment found in the outer station, and the combinatorics is the number of possible combinations between the seed and segments found in the middle and inner stations. Additionally the segment matching used in the track building was given the option of rejecting segments in the fitting that are unlikely to be part of the track matching. The result of tightening these cuts can be see in Figure 4.17. A significant improvement in the processing time is observed.

MDT t_0 Fitting

The determination of the track position in the MDT tubes require an offset time to be determined using a complex fit. This is described in section 3.5. The fit is performed independently for all MDT tubes on an event by event basis. Studies into the processing time of this fit were performed and shown to be highly CPU intensive. After multiple validations by the author, both on the performance and timing, the t_0 fit for the MDT tubes was turned off in May 2011. This resulted in an improvement in the segment finding processing time by 80%.

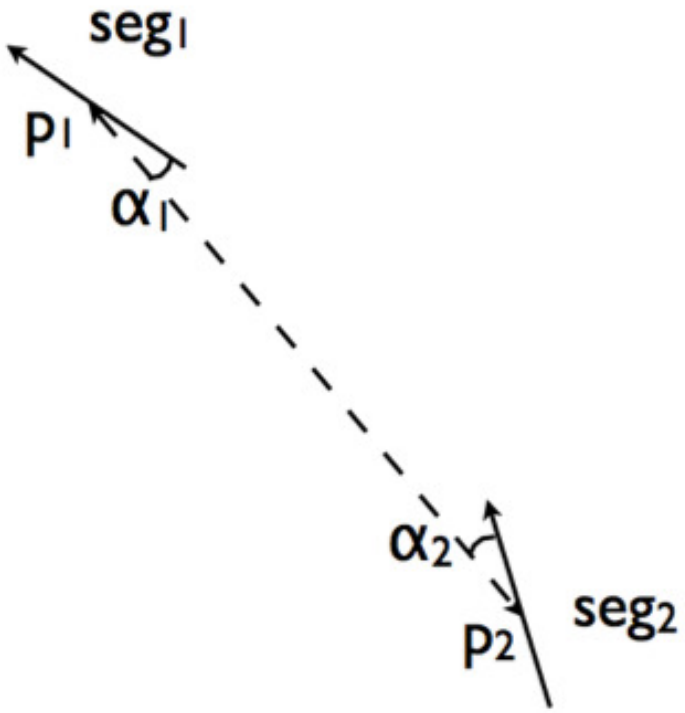

Figure 4.15: Schematic illustrating the discriminating variable used for segment matching: α_1 and α_2 are calculated from the directions of the segments in the precision plane and the direction of the line connecting the segments. The sum of the angles is zero for a uniformly curved track.

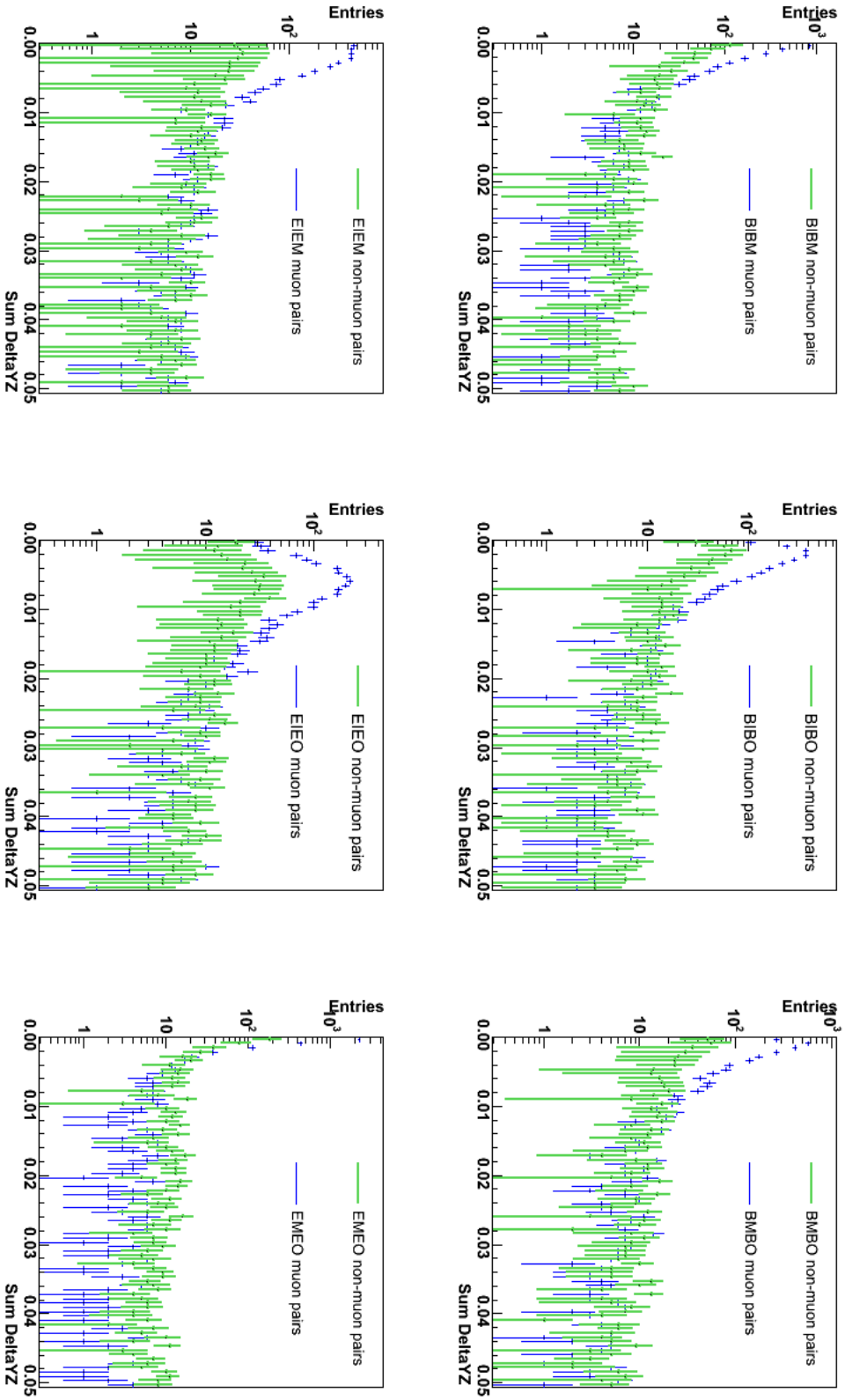

Figure 4.16: Comparison of segment pairs that are associated with a muon (blue) and pairs that are not associated with a muon (green), with *sumDeltaYZ* shown in radians.

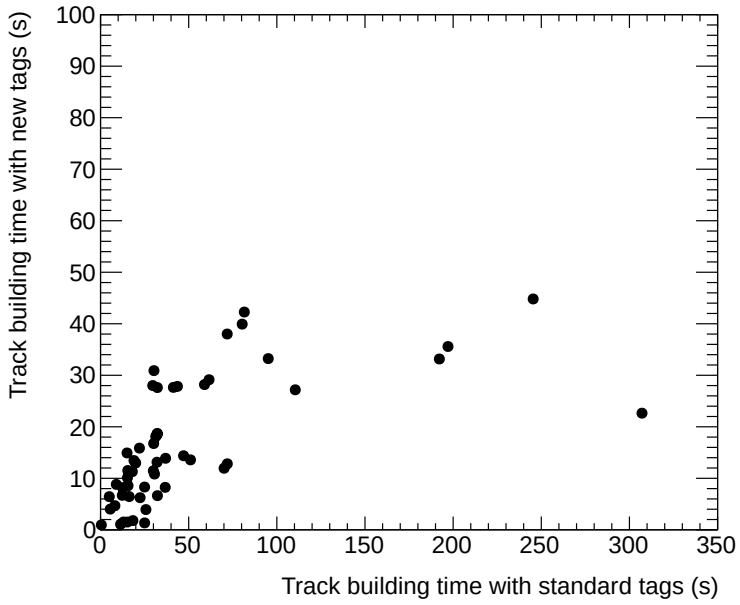

Figure 4.17: Time spent in the track building algorithm for events in debug stream run 158116, with tightened cuts in track combinations verses default track building times.

4.4 Improvement in Processing Time

To examine the effect of the improvements on different types of events, events are classed according to their original processing time. The classes are defined as:

- Normal events: < 4 seconds.
- Slow events: $4 - 20$ seconds.
- Very slow events: > 20 seconds.

The improvements are also sub-divided into four stages, and are named for simplicity stages one, two, three and four. Stage one contain the caching of the Trigger Elements in the segment finder. Stage two includes the cuts in the track builder with the improvement to the segment matching accounted for in stage 3. The last stage of improvements accounts for the switching off of the MDT t_0 fit.

Table 4.2 show the improvements (at stage 3) in the processing times for both offline and online modifications on Monte Carlo events. Here the online category refers to improvements specific to the trigger algorithms, while offline refers to improvements made to the offline tools that are used by both the trigger algorithms and the offline reconstruction algorithms. The improvements made to the online algorithms (i.e., caching) is consistent for all types of events, while the modifications to the offline algorithms (i.e., segment matching) has a larger

Sample	Online			Offline			Total		
Event Class	Norm	Slow	V.Slow	Norm	Slow	V.Slow	Norm	Slow	V.Slow
Black-Hole	46	38	33	11	44	64	51	65	78
SU4	48	45	47	8.6	44	7.9	51	68	66
J6	45	50	49	20	42	65	52	71	82
$t\bar{t}$	37	32	39	30	49	69	60	70	66

Table 4.2: Improvements in percent in the processing times for different classes of events for both online and offline algorithms and the total.

effect on the very slow events. The overall reduction in processing time for the Monte Carlo samples, not including stage four improvements, ranges from 50-82%.

The improvements up to stage three were added over the course of eleven months of data taking. The success of these changes can be seen in Figure 4.18 which shows the timeout rate per hour normalised to luminosity for a collection of runs in 2010. The x-axis lists runs chronologically. During the 2010 operations this rate dropped by a factor of 100. The drop is less pronounced in Figure 4.18 due to an increase in the trigger rates from LVL2 during the 2010 operations. Such rates could be handled by the trigger with instantaneous luminosity of order 10^{32} cm^{-2}s^{-1}, as seen at the end of the 2010 running, but extrapolating this to the run in 2011 the timeout rate would have reached 7000 per hour.

The overall improvements were obtained by rerunning the trigger for events in the debug stream from run 165732. The trigger was run with the online configuration present at each stage of improvement. The percentage reduction in the processing time of the trigger at each stage are shown in Table 4.4, with the reduction for the two segment finder and track builder algorithms shown separately in Figure 4.4.

Stage	$t < 180$ s	180s $< t <$ 300 s	$t >$ 300 s
One	36.1	57.0	68.4
Two	37.5	58.8	77.2
Three	48.3	69.0	77.2
Four	68.3	99.0	99.2

Table 4.3: Estimate of the improvement in percent for events in debug stream for run 165732 for different release setup relative to the start up conditions for 2010.

Stage	Segment Finder	Track Builder	% Time in Segment Finder	% Time in Track Builder
One	66.4	66.5	59.7	40.3
Two	66.5	80.8	80.1	29.9
Three	65.8	90.3	84.4	15.6
Four	90.4	97.3	64.4	35.6

Table 4.4: Estimate of the improvement in percent in TrigMuonEF algorithms after different stages of modification, relative to the start up conditions for 2010, using debug stream events.

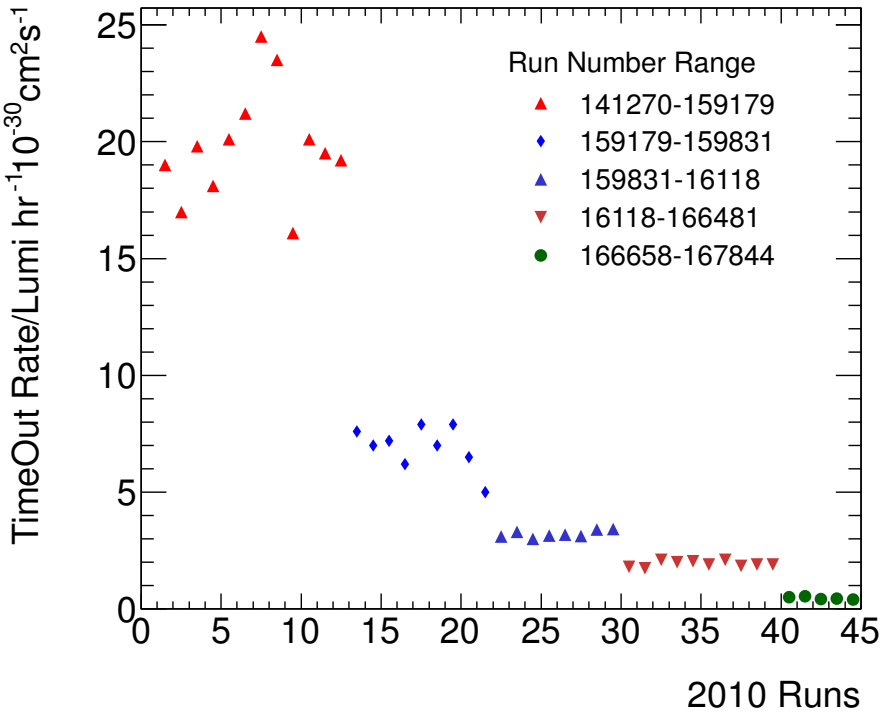

Figure 4.18: Rate of trigger timeouts for 2010 EF triggers, normalised to instantaneous luminosity, for several ranges of run number in 2010.

During the running of the detector in 2010 over 13000 timeouts occurred in the TrigMuonEF algorithms. All the improvements were made available online as of May 2011. By the end of the 2011 running, October 2011, ATLAS has delivered over 5 fb^{-1}of recorded luminosity, reaching as high as 3.5×10^{33} cm^{-2}s^{-1} of instantaneous luminosity. During the period between May and October 2011 not a single timeout was observed in the ATLAS muon EF trigger. The overall improvement due to the work presented here was over 98% in the segment finder and 97% in the track builder algorithms.

The MC samples (as listed in section 4.1) were reconstructed with the offline algorithms, with and without the updated software or the inclusion of the caching in TrigMuonEF, in order to validate the performance of the reconstruction. No loss of efficiency of resolution was seen as a result of these changes to the software [84].

Chapter 5

Monte Carlo Simulation

Monte Carlo event generators are used in particle physics to predict kinematic distributions and rates for signal and background processes. This chapter outlines the steps used to create these Monte Carlo events, which can be sub-divided into event generation, detector simulation and object reconstruction. Section 5.1 explains how the production rate and kinematics of the hard process in pp collisions are modelled. The ATLAS production chain for producing MC events is explained in section 5.2. The details of the event generation of heavy neutrino processes are discussed in section 5.3.

5.1 Monte Carlo Generators

The procedure for generating MC events can be split up into four stages. The stages involve the calculation of the hard scatter, evolution of the parton shower, hadronisation of the partons and the inclusion of multiple parton interactions. The hard scattering is the interaction of two partons from the incoming protons to produce one or more fundamental particles. This is determined using the matrix element method, which calculates cross sections from Feynman diagrams of the hard process, as discussed in section 2.5.2 for the calculation of the cross section of heavy neutrino production. The parton shower accounts for higher order corrections of the incoming (initial state) and outgoing (final state) partons. This is achieved by radiating soft or collinear partons from one of the partons in the hard scattering. This radiated parton in turn can radiate an additional parton and a shower of coloured partons is produced. The parton shower evolve the high energy partons down to a predefined cut-off scale. The evolution of the emitted partons can be ordered in terms of either the angle or p_{T} of the emitted partons, as illustrated in Figure 5.1. After the parton shower the event contains many coloured partons, while we know that partons must exist only in colourless states in a real world. To evolve the coloured partons into colourless hadrons the mechanism of hadronisation is used. Additionally multiple parton interactions can occur between spectator

partons in the pp collision. These multiple interactions are predominantly low momentum QCD processes. The affect of double-parton interacts, which is when two patron interactions occur in the same proton proton collision, are considered to be small and are not included in this thesis.

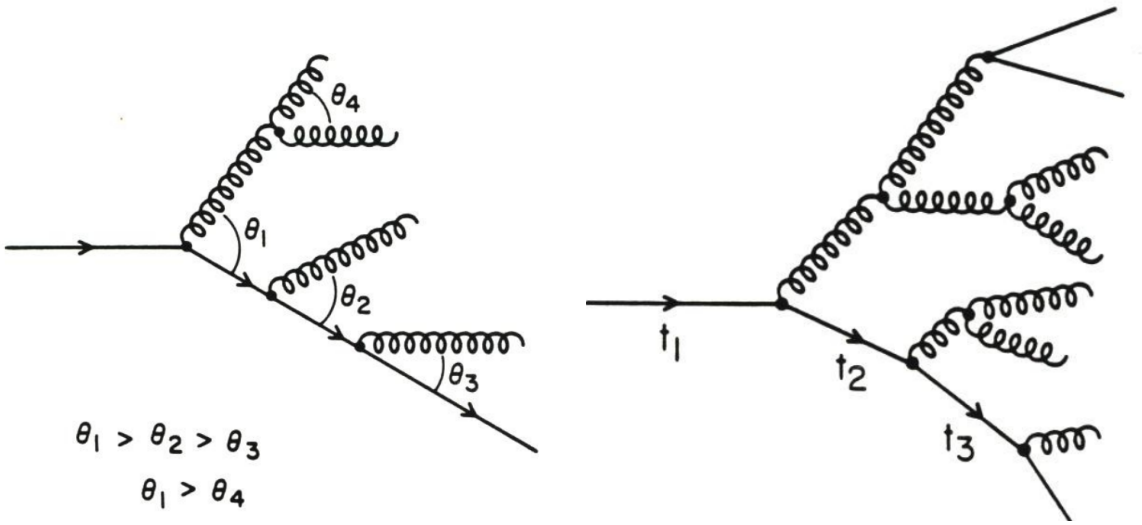

Figure 5.1: Evolution of the parton shower using angular ordering, $\theta_1 > \theta_2 > \theta_3$ (left), and p_{T} ordering, t1 > t2 > t3 (right).

The programs Pythia 6.4 [85] and Herwig 6.5 [86] match Leading-Order (LO) matrix elements to parton showers. The parton showers progression is p_{T} ordered for Pythia and angular ordered for Herwig. Models are included to implement hadronisation and the underlying event, which are tuned to describe experimental data. The Herwig generator uses the cluster model [87] for hadronisation, while Pythia uses the string model [88]. The programs Alpgen 2.14 [89], Madgraph 5.0 [90] and Sherpa 1.1 [91] all produce Leading-Order (LO) matrix elements including additional "legs" in the perturbative calculation. These are subsequently passed to a parton shower generator for Alpgen. The production of WZ events with the Alpgen generator produces separately the matrix element for $2 \to 2$, $2 \to 3$, $2 \to 4$ and $2 \to 5$ processes. The MLM and CKKM procedures [92] are used to perform the matching between the matrix element and the parton shower, in order to avoid double counting and to improve the description of multi-jet final states. The LO calculations of the cross section are missing significant physics which must be absorbed by model parameters. More recently, methods to match Next-to-Leading Order (NLO) matrix elements to parton showers have been introduced as implemented in the Powheg [93] and MC@NLO 4.03 [94] programs.

5.2 ATLAS Monte Carlo Production Chain

The simulation of events in ATLAS uses the procedure outlined in Figure 5.2. Firstly events are produced using a Monte Carlo generator, as discussed in the previous section. The events are then passed through a simulation of the detector, where the output is digitised into hits as discussed in section 5.2.1. These hits are overlaid with hits from events that simulate the effect of multiple parton interactions. The hits are then reconstructed into physics objects, using the same reconstruction software as the data to produce Analysis Object Data (AOD) used in analyses.

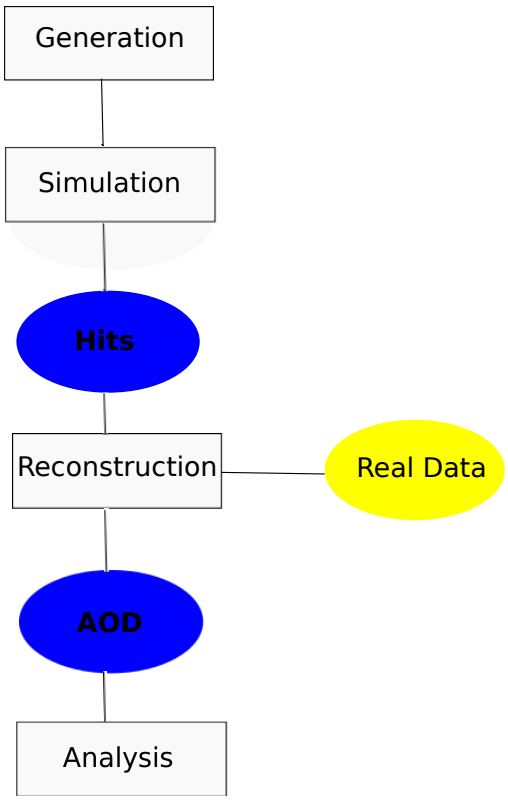

Figure 5.2: Schematic overview of the ATLAS MC production chain.

5.2.1 Event Simulation

As discussed above, the event generation calculates the interaction between two partons and produces events with high momentum final state particles. These stable particles are fed into the GEANT4 [95] software package. The GEANT4 software propagates the generated particles through the ATLAS detector and simulates the particles interactions with the detector material. The energy deposited into the detector by the particles is converted into detector signals with the same format as the actual detector read-out. The detector signals are digitised to produce hits which can be passed into the reconstruction software.

Run	Data period represented	Detector conditions	μ	% of total data
Run 1	B-D	Full ECal coverage	4-6	3.2%
Run 2	E-H	6 missing FEBs	5-10	17.4%
Run 3	I-K	2 missing FEBs	8-12	25.8%
Run 4	L-M	2 missing FEBs	10-15	53.5%

Table 5.1: Break down of the four runs used in the MC. The assigned run number of the MC sample is shown. Also shown are the data periods each run represents, any major detector malfunction modelled in the MC and the fraction of data during 2011 running represented by this run.

The full simulation of the detector is extremely computationally intensive. Some background processes may not need the full detector simulation offered by the GEANT4 software. In these cases a fast simulation of the ATLAS detector is used. This fast simulation is performed by AtlfastII [96]. This provides a combination of full and fast simulation of the detector response. The inner detector and muon system are both fully simulated in AtlfastII, using the GEANT4 software, while the calorimeter is simulated using FastCaloSim [97], which uses parameterised MC events with full simulation.

The effect of multiple proton-proton interactions per bunch crossing (pile-up) are generated with Pythia and simulated with GEANT4. The resulting hits are overlaid with the hits from the hard scattering process.

The number of additional interactions per bunch crossing, μ, varies with the running conditions of the machine. The simulation of the MC was developed to match the conditions of the online data taking during 2011. This was achieved by splitting the MC events into 4 separate samples, with each sample representing the online data taking for different data periods throughout 2011. The MC then simulates the conditions such as pile-up and detector malfunctions. The four different periods are shown in Table 5.1. During the 2011 operations a number of Front End Boards (FEB) in the calorimeter malfunctioned, resulting in a loss of detector coverage.

5.3 Seesaw type-I Signal MC Samples

Signal events are generated using the ALPGEN [76] MC generator with heavy neutrino production. ALPGEN evaluates tree level SM processes and provides unweighted events suitable for simulation. We generate events in the channel $pp \to W^* \to N\mu^\pm \to \mu^\pm\mu^\pm jj$, only considering same-sign di-muon production. Only diagrams with on-shell N are included as shown in Figure 5.3. No cuts on the lepton p_{T} but a very loose cut of $|\eta| < 10$ are applied at the generator level. The ALPGEN generator calculates the cross section using CTEQ5L PDFs and setting the factorisation scale Q^2 to the mass of the off-shell W. Nine signal samples are generated for heavy neutrino masses ranging from 100-300 GeV for muon channel as summarised in Table 5.2. The generated events are passed to HERWIG [86] to provide the showering and hadronisation.

The generation of the signal events was validated by checking the kinematic distributions of the two muons, the on-shell W boson from the heavy neutrino decay and the heavy neutrino particle (as shown in Figures 5.4 and 5.5) after hadronisation. The W is reconstructed from the two leading [1] jets. The heavy neutrino, N, can be reconstructed using the two leading jets, and one of the muons, depending on which combination has a mass closest to m_{N}.

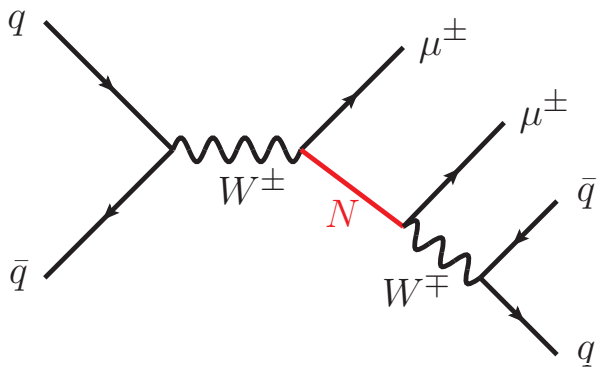

Figure 5.3: Feynman diagram for the leading order production of a heavy Majorana neutrino via an off-shell SM W boson decaying to two same-signed muons.

The simulation of the detector response for the signal MC events was performed using a fast simulation. A single signal mass point was fully simulated with GEANT4 in order to evaluate the systematic effect of using the fast simulation for modelling our signal. Figure 5.6 and 5.7 shows the comparison of the muon p_{T}, η and invariant mass of the di-muon pair for the full and fast simulation sample. These variables, where the calorimeter plays only a small role, are found to be in very good agreement. The isolation variables for the muons (as described in section 6.1.3) are shown in Figure 5.7(a) and 5.7(b), where small differences are

[1] In this thesis, physics objects such as muons and jets are ordered in terms of the transverse momentum (p_{T}). Objects with the largest p_{T} are named the leading objects. Objects with lowest p_{T} are named the trailing objects.

m_{N} [GeV]	cross-section [fb]
100	29.4
120	10.6
140	5.2
160	2.8
180	1.7
200	1.1
240	0.5
280	0.3
300	0.2

Table 5.2: List of seesaw type-I signal samples generated with $\sqrt{s} = 7$ TeV. Cross sections are leading order and assume $|V_{N\mu}|^2$=0.0096.

Event Selection Cuts	AtlfastII	GEANT4	Ratio
Data quality	4.9	4.9	1.0
Two muons	3.2	3.2	1.0
Two isolated muons	2.8	2.8	1.0
Third lepton veto	2.73	2.72	1.00
M($\mu\mu$) >15 GeV	2.72	2.72	1.00
N(jet) ≥ 2	1.93	1.95	0.99
$E_{\mathrm{T}}^{\mathrm{miss}} < 35$ GeV	1.68	1.72	0.98
$50 < M_{jj} < 120$	1.35	1.39	0.97

Table 5.3: Cut flow for signal with mass point $m_{\mathrm{N}} = 200$ GeV for a sample with full detector simulation and separately with fast simulation of the calorimeter.

seen in the calorimeter isolation variable. The $E_{\mathrm{T}}^{\mathrm{miss}}$, dijet mass of the leading two jets and the number of jets are shown in Figure 5.6(d) 5.7(c) 5.7(d), where small differences are seen between the full and fast simulation. The effect of these differences is quantified in Table 5.3, which shows the selection efficiency for different stages of the event selection. After all cuts, a 3% difference is seen between the efficiency of signal events to pass the selection criteria with fast and full simulation.

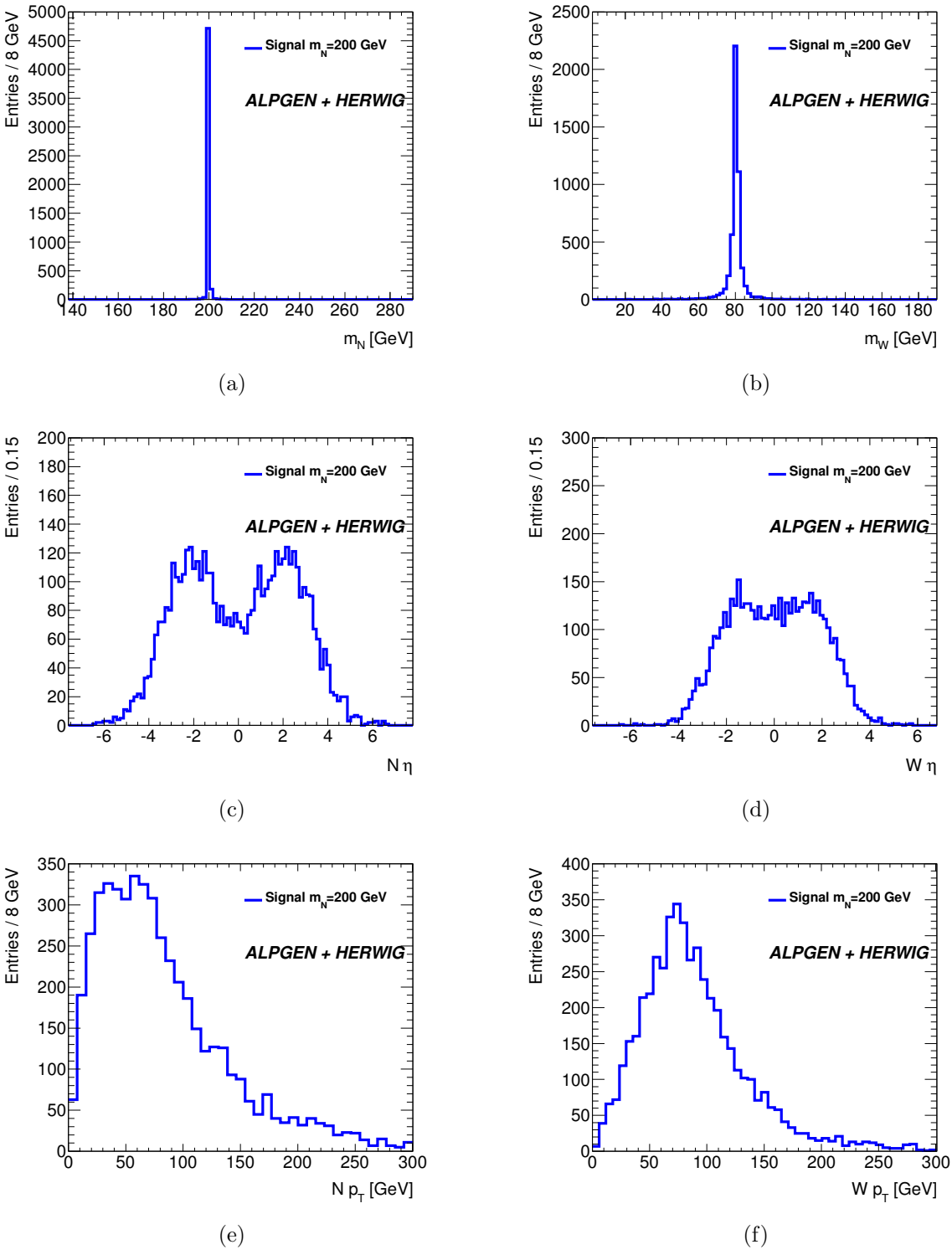

Figure 5.4: Validation plots for kinematic properties of W and N in signal MC events with heavy Majorana neutrino mass of 200 GeV showing (a) the mass of N, (b) mass of the reconstructed W (c) η of heavy neutrino, (d) η of reconstructed W boson, (e) p_{T} of reconstructed N and (f) p_{T} of the W boson.

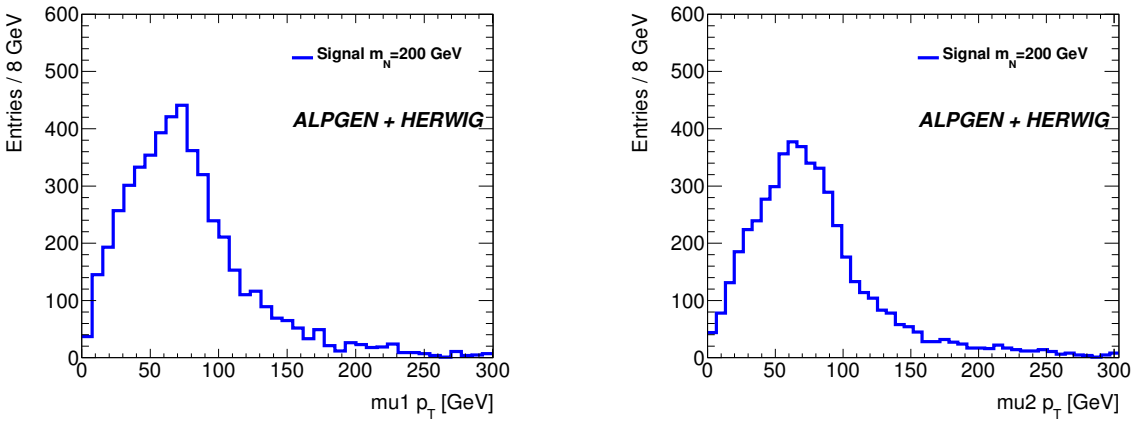

(a)

(b)

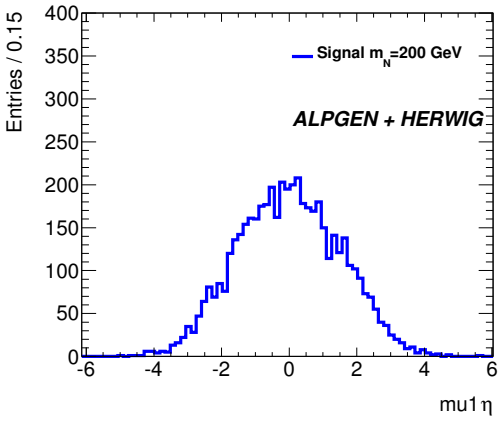

(c)

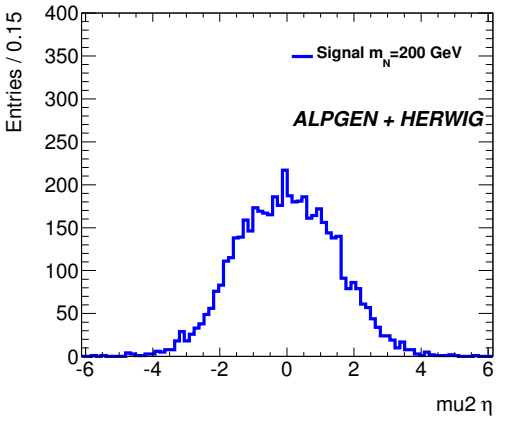

(d)

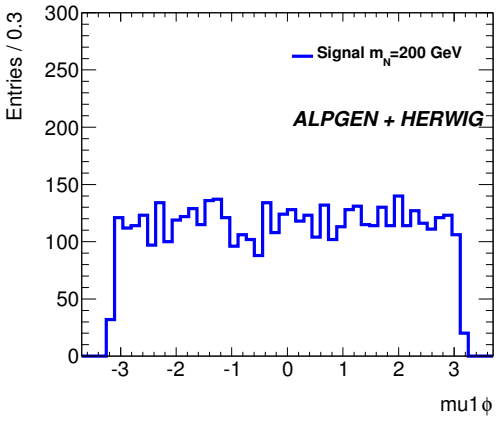

(e)

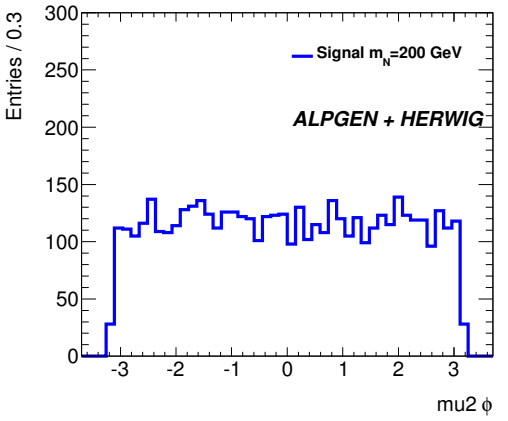

(f)

Figure 5.5: Validation plots for kinematic properties of muons in signal MC events with heavy Majorana neutrino mass of 200 GeV. Showing (a) p_{T} of muon from W decay, (b) p_{T} of muon from N decay, (c) η of muon from off-shell W, (d) η of muon from N, (e) ϕ of muon from off-shell W and (f) ϕ of muon from N.

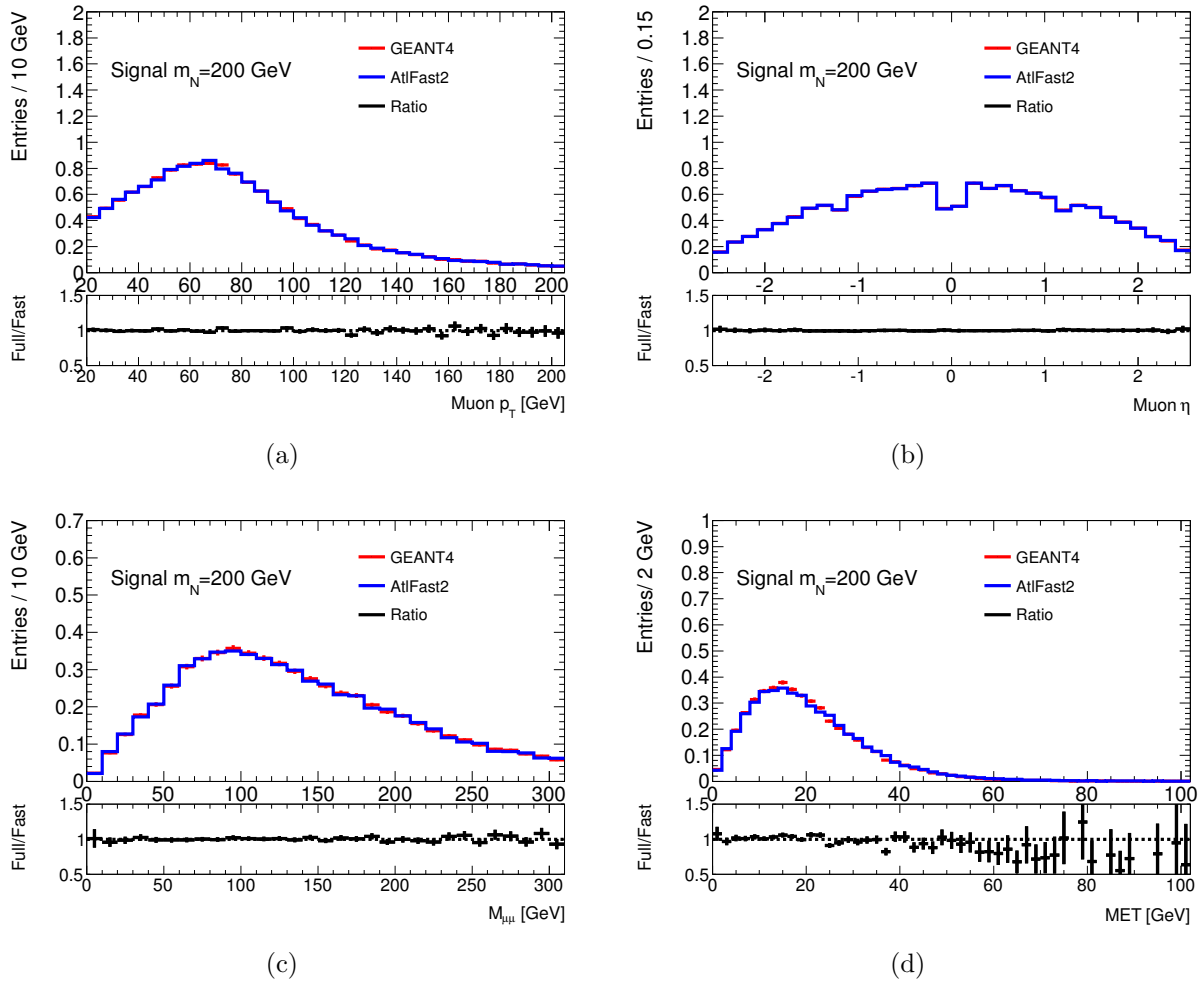

Figure 5.6: Comparison between GEANT4 and AtlfastII simulation in signal MC comparing (a) muon track p_{T}, (b) muon η, (c) the invariant mass of the two muons and (d) $E_{\mathrm{T}}^{\mathrm{miss}}$, for all same-sign di-muon events.

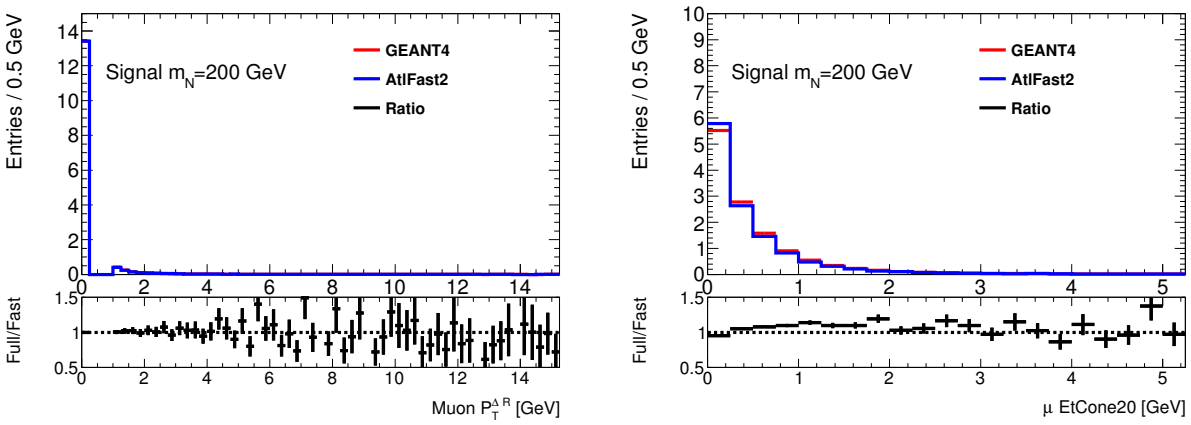

(a)

(b)

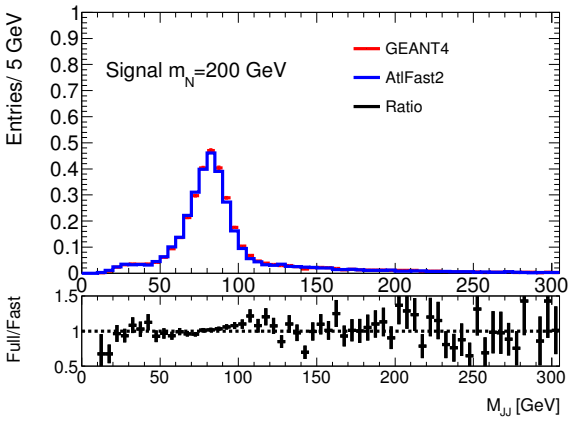

(c)

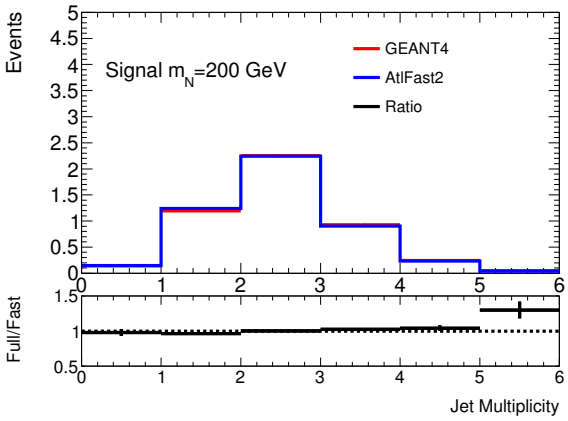

(d)

Figure 5.7: Comparison between GEANT4 and AtlfastII simulation in signal MC comparing (a) the muon track isolation, (b) the muon calorimeter isolation, (c) the invariant mass of the leading two jets and (d) the number of jets (with no analysis cuts applied) or all same-sign di-muon events.

5.4 Kinematics of Different Signal Models

As discussed in section 2.3.3 another model that can explain the neutrino mass problem is the LRSM model. This model has the same experimental signature to the search in this analysis. The difference between these models is the existence of a new TeV scale W_R boson in the LRSM model. This section outlines the kinematic differences observed between the generated signal samples in both these models, and demonstrates the need for different event selections for the two models.

As a benchmark, we examine two signal mass points for both models.
For the LRSM model the case is considered where $[m_{\mathrm{N}},\ m_{\mathrm{W_R}}]$ = [100 GeV, 1.8 TeV] and [500 GeV, 1.8 TeV], while for the seesaw type-I signal we consider m_{N} = 100 GeV and m_{N} = 200 GeV.

The high masses of the W_R bosons produce muons with much larger transverse momentum than seen in muons from W^* decays, which can be seen in Figure 5.8. For the LRSM signal the leading muon p_{T} is greater than 80 GeV in over 99% of events and over 75% of events for the sub-leading muon, while for the seesaw type-I model the leading muon p_{T} is less than 80 GeV in 75% of events and the trailing muon p_{T} is less than 80 GeV in 99% of events. Figure 5.8 also shows a comparison of the muon η and the missing transverse energy ($E_{\mathrm{T}}^{\mathrm{miss}}$). The muons in the LRSM are predicted to be more central than the muons from off-shell W decays, while the $E_{\mathrm{T}}^{\mathrm{miss}}$ distribution is much broader.

Figure 5.9 shows the expected number of reconstructed jets and the jet p_{T} expected in both models. The number of reconstructed jets per event is most commonly expected to be two for both models, resulting from the hadronic decay of either the W or the W_R^*. Additional jets result from initial and final state radiation. Some scenarios in the LRSM (where we have $m_{W_R} >> m_{\mathrm{N}}$) the neutrino is produced with very high p_{T}. In this case the heavy neutrino is boosted and the two jets from the W_R^* can be reconstructed as a single jet. In the scenario where N is produced via an off-shell W the jets tend to be softer, giving a lower selection efficiency.

Figure 5.9 also shows the reconstructed mass of the W and N, also including the invariant mass of the same-sign dimuon pair. The invariant mass of the two muons is used in the LRSM analysis as a discriminant to remove background, removing all events with masses below 110 GeV [52]. The lowest efficiency this cut has on events from LRSM scenarios is 88%, while in the seesaw type-I model the efficiency is as low as 25%. This demonstrates that the search for heavy neutrinos within the LRSM scenario [52] does not have sensitivity to the seesaw type-I model considered in this thesis.

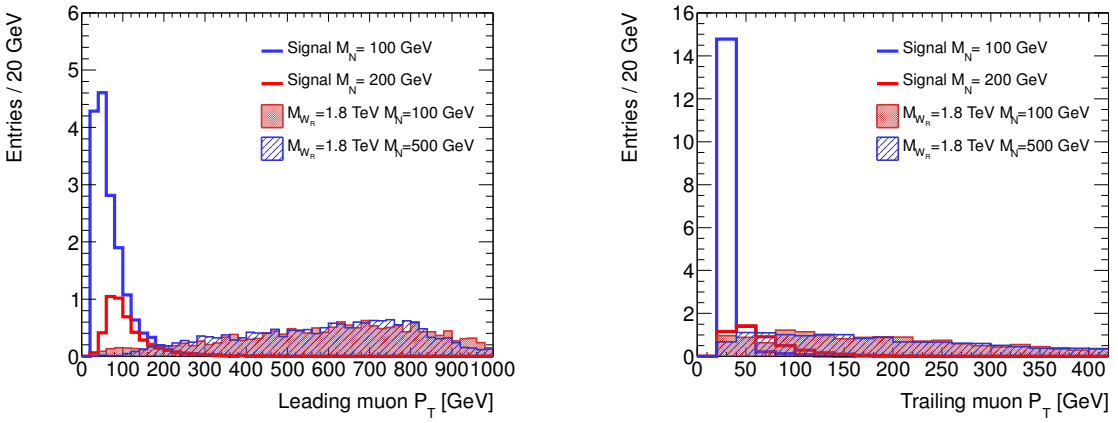

(a) (b)

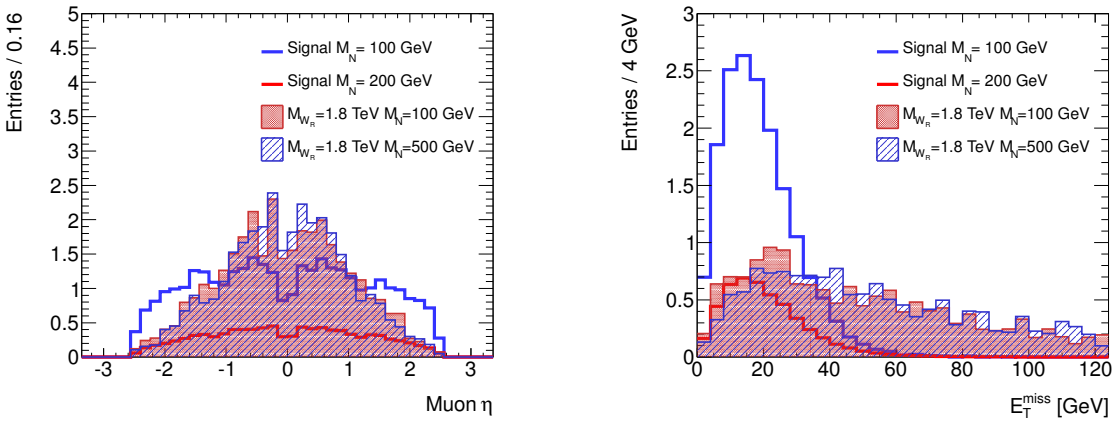

(c) (d)

Figure 5.8: Distributions of the p_{T} of (a) the leading and (b) trailing muons, (c) η of all muons and (d) the missing transverse energy for the benchmark LRSM and seesaw type-I samples, after requiring two muons with same-sign charge.

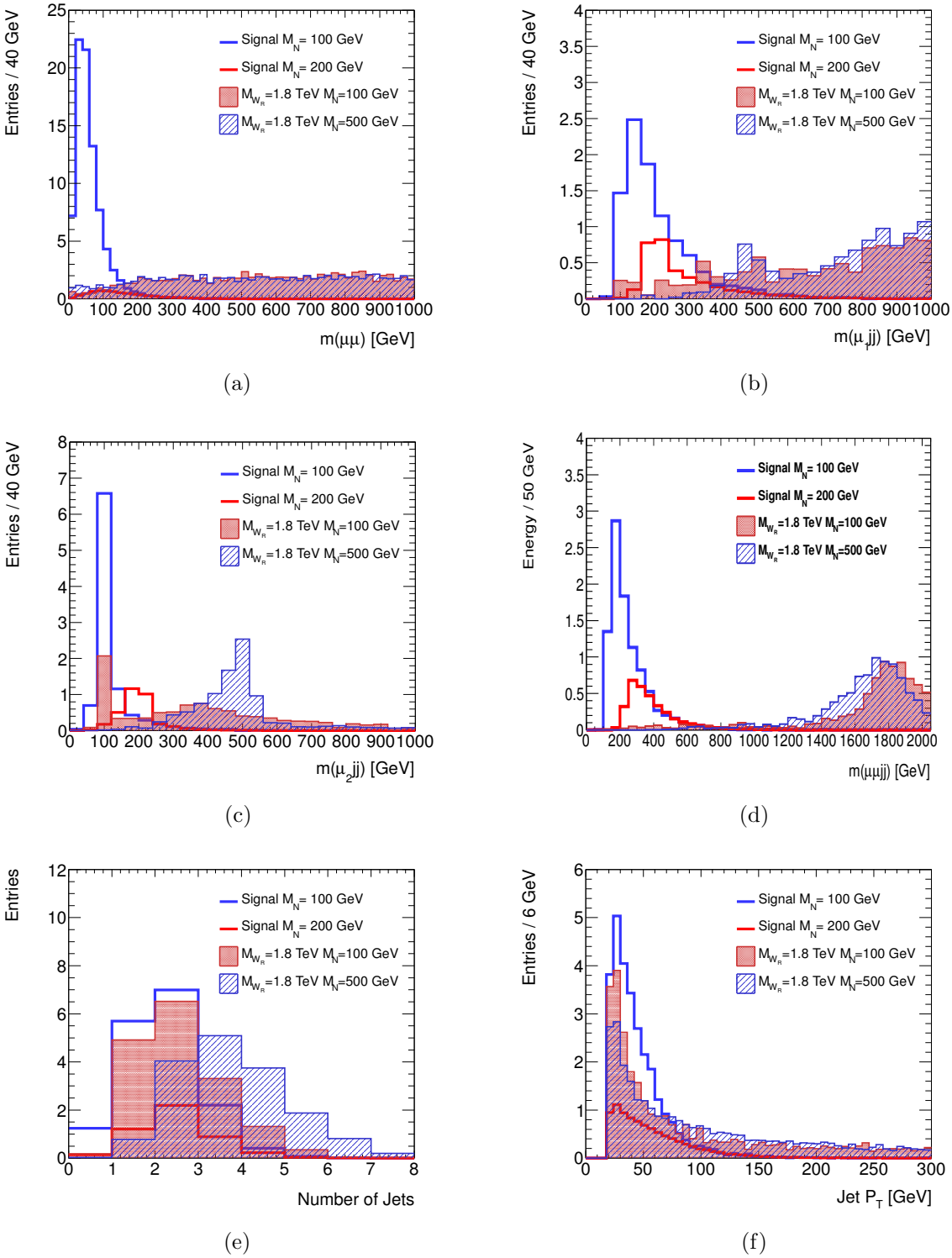

Figure 5.9: Distributions of (a) the invariant mass of the two muons, (b) the invariant mass of the two leading jets and the leading muon, (c) the invariant mass of the two leading jets and the trailing muon and (d) the invariant mass of the pair of muons and leading jets i.e., reconstructed W_R/W^*, (e) the jet multiplicity and (f) the jet transverse momentum. All the distributions are shown for the benchmark LRSM and seesaw type-I samples after requiring two muons with same-sign charge.

5.5 Background MC Samples

In order to estimate the contribution of background sources and validate data-driven backgrounds, a number of processes have been simulated. In this section we list the simulated MC samples used in this analysis. Samples that are used to estimate background processes include:

- Diboson samples for WZ and ZZ production have been produced with three separate generators. The generator used for the central value in the analysis is SHERPA. The SHERPA MC calculates the matrix element with 3 additional partons. These background processes are also studied with samples using the ALPGEN and HERWIG generators.

- Samples for the associated production of W and Z bosons with $t\bar{t}$ pairs are generated with MADGRAPH and interfaced to PYTHIA for showering and hadronisation.

- $W^{\pm}W^{\pm}jj$ events are generated with MADGRAPH which uses CTEQ6L1 PDFs and are interfaced with PYTHIA for showering and hadronisation.

Process	LO cross section [pb] $\times\epsilon_{\text{filter}}$	k-factor	N_{MC}	Generator
$W^{\pm}W^{\pm}+2p$	0.219	1.0	94998	MADGRAPH
$Wt\bar{t}$	0.124	1.36	100000	MADGRAPH
$Zt\bar{t}$	0.096	1.35	99997	MADGRAPH

Table 5.4: MC samples used to model the same-sign prompt backgrounds. The corresponding cross sections, k-factors and the total number of events are shown in the table.

The samples used in the validation of the background estimations include:

Process	Z/γ^* decay	W decay	$\sigma \times BR$ [pb]	N_{MC}	Generator
WZ	$[e,\mu,\tau]$	Inclusive	5.536	999896	ALPGEN + HERWIG
WZ	$[e,\mu,\tau]$	$l\nu$ $[e,\mu,\tau]$	6.30	999699	SHERPA
WZ+0p	$[e,\mu,\tau]$	$l\nu$ $[e,\mu,\tau]$	0.858	59900	ALPGEN + HERWIG
WZ+1p	$[e,\mu,\tau]$	$l\nu$ $[e,\mu,\tau]$	0.525	40000	ALPGEN + HERWIG
WZ+2p	$[e,\mu,\tau]$	$l\nu$ $[e,\mu,\tau]$	0.282	20000	ALPGEN + HERWIG
WZ+3p	$[e,\mu,\tau]$	$l\nu$ $[e,\mu,\tau]$	0.128	20000	ALPGEN + HERWIG
ZZ	$[e,\mu,\tau]$	-	1.176	249999	ALPGEN + HERWIG
ZZ	$[e,\mu,\tau]$	-	4.62	1999597	SHERPA
ZZ+0p	$[e,\mu,\tau]$	-	0.663	40000	ALPGEN + HERWIG
ZZ+1p	$[e,\mu,\tau]$	-	0.299	20000	ALPGEN + HERWIG
ZZ+2p	$[e,\mu,\tau]$	-	0.117	20000	ALPGEN + HERWIG
ZZ+3p	$[e,\mu,\tau]$	-	0.039	10000	ALPGEN + HERWIG

Table 5.5: MC samples used to model the diboson backgrounds and systematic checks. The $\sigma \times BR$ is shown at NLO and the number of generated events are shown in the table.

- Z+jets, covering the dilepton mass range $10 < m_{\mu\mu} < 2000$ GeV and including the $Zb\bar{b}$ contribution, were studied using the ALPGEN MC generator.
- W^+W^- events are generated with HERWIG, with a filter requiring at least one lepton.
- $t\bar{t}$ and single-top Wt background are generated using MC@NLO interfaced with HERWIG. The top mass is set to 172.5 GeV. A filter was applied at the generator level to retain only events where at least one lepton (e, μ or τ) is produced.
- QCD samples are generated with PYTHIA with a filter on two muons in the event each having minimum 10 GeV of transverse momentum.
- W+jets, $Wb\bar{b}$, $Wc\bar{c}$, Wc processes are generated with the ALPGEN.
- Single top Wt, t and s-channels are generated with MC@NLO and ACERMC [98].

These events were simulated and reconstructed as described in sections 5.3 and 6, using the same software algorithms that were used for the data. More sample details are given in tables 5.4- 5.5, which show the number of generated events, the NLO cross section (or LO cross section and the k factor to account for NLO effects) for the process and the generator used. Each sample is normalised to the cross section, σ and the total luminosity of the dataset, $\mathcal{L}$, with events being assigned a weight w_{norm} given by

$$w_{\text{norm}} = \frac{\mathcal{L}}{N_{\text{events}}\sigma} \tag{5.1}$$

where N_{events} is equal to the number of generated events.

Process	NLO $\sigma \times BR$ [pb]	ϵ_{filter}	N_{MC}	Generator
single top t-channel [τ]	7.13	1	176501	MC@NLO
single top s-channel [μ]	0.47	1	253594	MC@NLO
single top s-channel [τ]	0.47	1	176501	MC@NLO
Wt	13.10	1	797024	MC@NLO
$t\bar{t}$	164.57	0.56	14981474	MC@NLO
single top t-channel [μ]	7.01	1	999948	ACERMC

Table 5.6: Table of processes simulated using MC to model the single top and $t\bar{t}$ backgrounds. The $\sigma \times BR$ (NLO), generator filter efficiency and the number of generated events are listed.

Process	$\sigma \times BR$ (pb)	N_{events}	Generator
Z$\to \mu\mu$ + 0p ($40 < m_{\mu\mu} < 2000$)	835.85	6615230	Alpgen + Herwig
Z$\to \mu\mu$ + 1p ($40 < m_{\mu\mu} < 2000$)	167.68	1334296	Alpgen + Herwig
Z$\to \mu\mu$ + 2p ($40 < m_{\mu\mu} < 2000$)	50.41	1999941	Alpgen + Herwig
Z$\to \mu\mu$ + 3p ($40 < m_{\mu\mu} < 2000$)	13.99	549896	Alpgen + Herwig
Z$\to \mu\mu$ + 4p ($40 < m_{\mu\mu} < 2000$)	3.60	150000	Alpgen + Herwig
Z$\to \mu\mu$ + 5p ($40 < m_{\mu\mu} < 2000$)	1.04	50000	Alpgen + Herwig
Z$\to \mu\mu[10 < m_{\mu\mu} < 40]$ + 0p	3722.98	6615230	Alpgen + Herwig
Z$\to \mu\mu[10 < m_{\mu\mu} < 40]$ + 1p	107.20	6615230	Alpgen + Herwig
Z$\to \mu\mu[10 < m_{\mu\mu} < 40]$ + 2p	49.96	6615230	Alpgen + Herwig
Z$\to \mu\mu[10 < m_{\mu\mu} < 40]$ + 3p	10.51	6615230	Alpgen + Herwig
Z$\to \mu\mu[10 < m_{\mu\mu} < 40]$ + 4p	2.26	6615230	Alpgen + Herwig
Z$\to \mu\mu[10 < m_{\mu\mu} < 40]$ + 5p	0.56	6615230	Alpgen + Herwig
Z$\to \mu\mu$[bb] + 0p	8.20	389949	Alpgen + Herwig
Z$\to \mu\mu$[bb] + 1p	3.11	155000	Alpgen + Herwig
Z$\to \mu\mu$[bb] + 2p	1.11	60000	Alpgen + Herwig
Z$\to \mu\mu$[bb] + 3p	0.49	29999	Alpgen + Herwig
Z$\to \tau\tau$	985.52	495347	Pythia
W$\to \mu\nu$ + 0p	8314.03	3462942	Alpgen + Herwig
W$\to \mu\nu$ + 1p	1566.59	1334296	Alpgen + Herwig
W$\to \mu\nu$ + 2p	455.06	1999941	Alpgen + Herwig
W$\to \mu\nu$ + 3p	122.56	549896	Alpgen + Herwig
W$\to \mu\nu$ + 4p	31.44	150000	Alpgen + Herwig
W$\to \mu\nu$ + 5p	8.63	50000	Alpgen + Herwig
W$\to \tau\nu$ + 0p	8371.51	3418296	Alpgen + Herwig
W$\to \tau\nu$ + 1p	1576.87	2499194	Alpgen + Herwig
W$\to \tau\nu$ + 2p	457.60	3750986	Alpgen + Herwig
W$\to \tau\nu$ + 3p	122.82	1009946	Alpgen + Herwig
W$\to \tau\nu$ + 4p	31.02	249998	Alpgen + Herwig
W$\to \tau\nu$ + 5p	8.52	65000	Alpgen + Herwig
W$\to \mu\nu$[bb] + 0p	57.29	474997	Alpgen + Herwig
W$\to \mu\nu$[bb] + 1p	43.28	205000	Alpgen + Herwig
W$\to \mu\nu$[bb] + 2p	20.97	174499	Alpgen + Herwig
W$\to \mu\nu$[bb] + 3p	9.21	69999	Alpgen + Herwig
W$\to \mu\nu$[cc] + 0p	154.31	1274846	Alpgen + Herwig
W$\to \mu\nu$[cc] + 1p	126.66	1049847	Alpgen + Herwig
W$\to \mu\nu$[cc] + 2p	63.02	524947	Alpgen + Herwig
W$\to \mu\nu$[cc] + 3p	20.52	17000	Alpgen + Herwig

Table 5.7: Table of processes simulated using MC to model the Z/W backgrounds. The $\sigma \times BR$ (NLO), and the number of generated events are listed. As a note Np refers to N additional partons in the final state.

5.5.1 Diboson Production

The dominant source of events producing two same-sign muons is diboson production involving at least one Z/γ^*. The Feynman diagrams for WZ and ZZ production modes at the LHC are shown in Figure 5.10. In addition to the process mentioned above the produc-

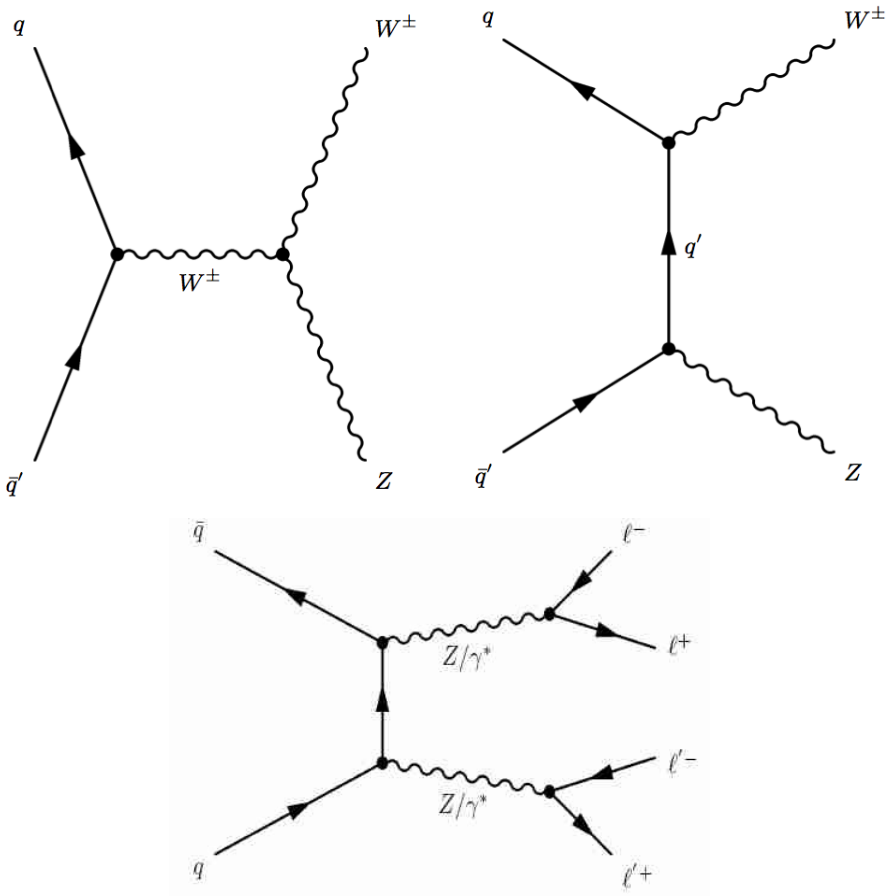

Figure 5.10: Example diagrams for s-channel and t-channel WZ production and ZZ production at the LHC.

tion of $W^{\pm}W^{\pm}jj$ is possible, which proceeds via the t-channel exchange of a gluon with an additional production of two jets in the final state. This is shown in Figure 5.11.

5.5.2 Top Pair Productions Associated with *W or Z*

The cross section for these processes are small, however as Figure 5.12 shows these are both SM sources of same-sign muon pairs that produce multiple jet final states. It is for this reason these processes are an important background to consider. In both these processes the final state contains jets containing b mesons from $t \to W^+b$ and $\bar{t} \to W^+\bar{b}$ and neutrinos from the process $W \to \mu\nu_\mu$, resulting in missing transverse energy in the event.

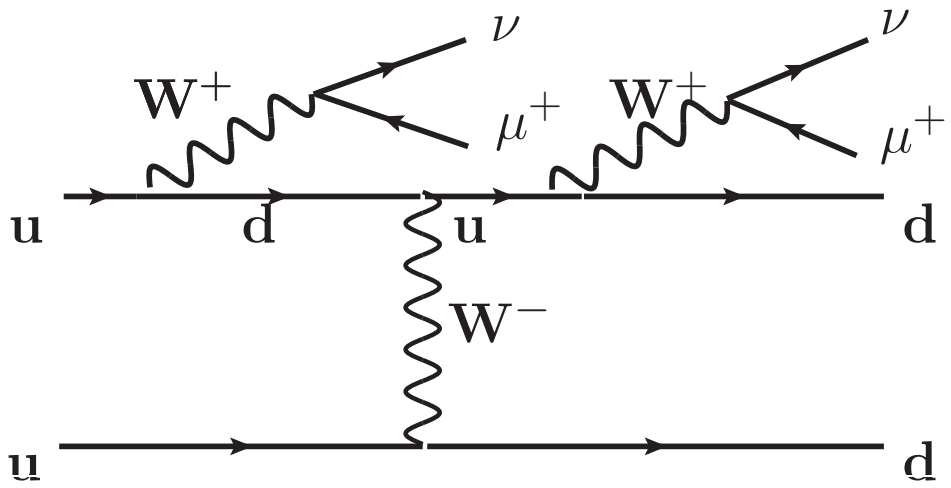

Figure 5.11: A possible leading order Feynman diagram for the production of two same-sign muons, from the decay of two same-sign W vector bosons.

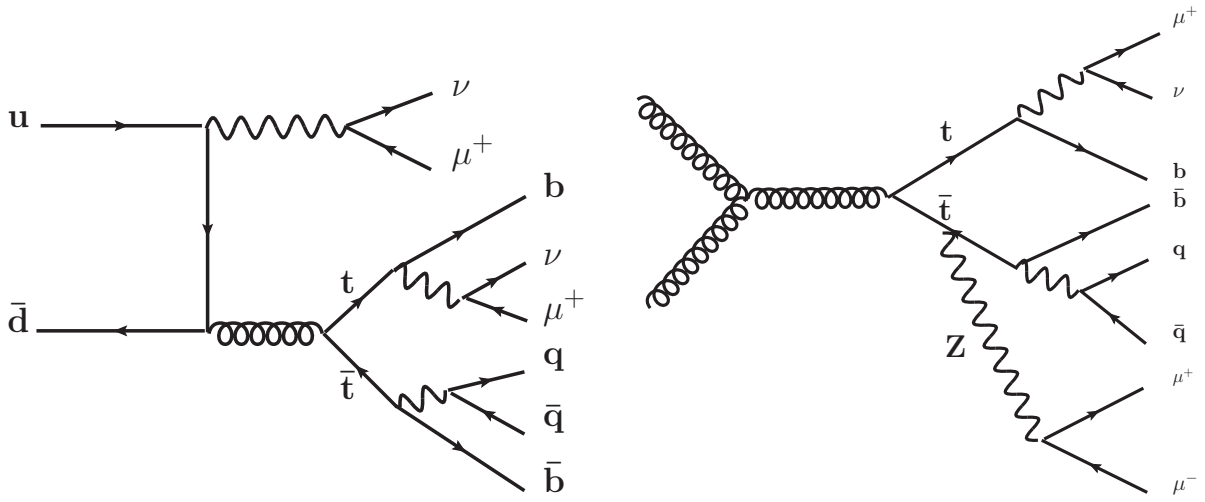

Figure 5.12: Possible leading order Feynman diagrams for the production of (a) $t\bar{t}W$ and (b) $t\bar{t}Z$, decaying to produce two same-sign muons in the final state. The red fermion lines represent the top and anti top particles, blue fermion lines represent b quarks, while all other fermions are in black.

Normalisation of diboson samples

The backgrounds for WZ and ZZ are estimated using MC events generated with SHERPA. At the generation stage the SHERPA samples include both the Z contribution and the γ^* contribution, with a cut on the invariant mass on $Z/\gamma^* > 0.5$ GeV and with an additional cuts on the lepton $p_{\mathrm{T}} > 5$ GeV and $|\eta| < 2.7$. From this point on in the thesis, the term WZ refers to the production of a W boson with either a Z or an off-shell photon, and the term ZZ includes the contribution of both Z and off-shell photons. The cross sections used are shown in Table 5.5. To account for higher order effects the normalisation is validated in a diboson control region with the uncertainty assigned by comparing the observed and predicted contribution in the one and two jet bin (more details in section 10.1.2).

The predictions from SHERPA are compared to that of MCFM [99]. The ratio of the cross section in MCFM and SHERPA for WZ and ZZ production as a function of same-sign dimuon mass is shown in Figure 5.13. Linear fits parameterising the correction factor between the two generators are also shown. It will be shown in section 9.1 that events with small masses of same-sign muon pairs are important, and the data driven uncertainty (discussed in section 10.2.2) applied to the WZ and ZZ SHERPA is larger than the correction factor for all same-sign masses below 450 GeV.

Normalisation of $V + t\bar{t}$ samples

The backgrounds for $Wt\bar{t}$ and $Zt\bar{t}$ are estimated using MC events generated with MADGRAPH. The LO cross sections and k-factors are shown in Table 5.4. The k-factors for these processes are taken from recently calculated NLO cross sections. For $Zt\bar{t}$ production the k-factor of 1.35 is taken from [100]. The cross section for the production of $Wt\bar{t}$ at NLO was calculated in [101]. This NLO cross section was used to normalise this background process for this analysis. This cross section is a factor of 1.36 higher than that obtained by the MADGRAPH generator.

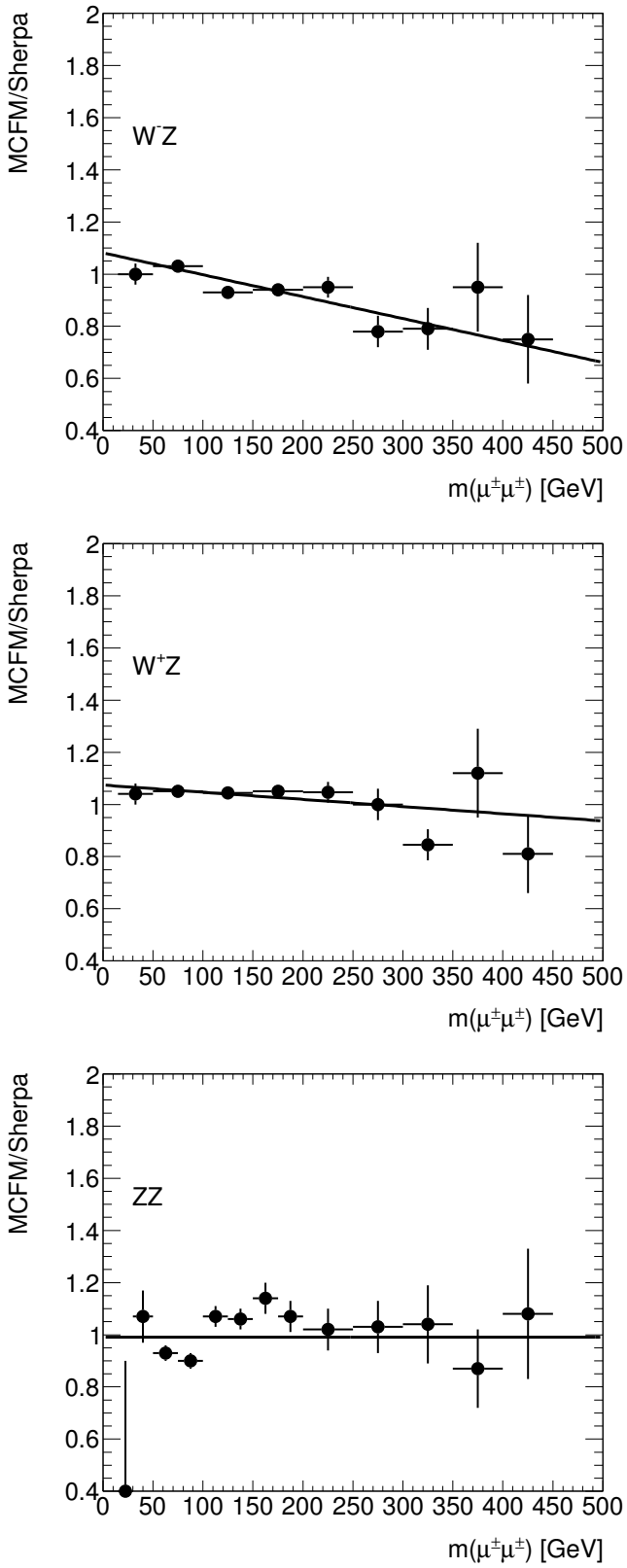

Figure 5.13: Ratio of cross section derived with MCFM to those derived with SHERPA for W^+Z, W^-Z, and ZZ production. The x-axis is shown in units of GeV.

Chapter 6

Experimental Techniques

This chapter outlines the techniques used by experimental particle physics to perform physics searches at a hadron collider. This includes the methods of reconstructing particles in the detector for use in analytical studies and the statistical methods used to set limits on theoretical models.

6.1 Object Reconstruction

Once an event is selected by the trigger, the information from the sub-detectors are read out and stored as hits. The hits are then processed by the offline reconstruction algorithms to reconstruct physics objects, used for various analyses.

6.1.1 Charged Tracks

The inner detector is important for measuring the momentum and position of charged tracks passing through the ATLAS detector (see section 3.3 for more details). Reconstruction of a charged track begins with silicon clusters deduced from raw hits in the pixel and SCT detectors. Using these clusters three dimensional space points are formed. Tracks are then formed using the inside-out pattern recognition algorithm, starting from space points closest to the beam line and fitting outwards towards the TRT detectors. Tracks seeds are found by joining three space points and searching for nearby hits that can be associated to the track. These track candidates are then extended to the TRT detectors using a road defined from the silicon tracks and combined to hits in the TRT.

A track is approximated as a helix and is parametrised with respect to the primary reconstructed vertex using the *perigee* representation (d_0, z_0, ϕ, θ, q/p). These variables are defined as:

- d_0: transverse impact parameter, the closest distance to the z-axis in the transverse

plane,

- z_0: longitudinal impact parameter, the z coordinate along the track at the closest distance in the transverse plane,
- ϕ: azimuthal angle of the track at the perigee,
- θ: polar angle of the track at the perigee,
- q/p: charge of the track divided by the track momentum.

The tracks charge, q (determined from the curvature of the track in the solenoid magnetic field) and position are measured with respect to the interaction point (primary vertex). The sign of the parameter d_0 is signed using the following convention. It is positive if the vector $\overrightarrow{OP}$ in Figure 6.1 points along the positive x-axis, and negative if $\overrightarrow{OP}$ points along the negative x-axis.

6.1.2 Primary Vertex Reconstruction

The knowledge of the position of the primary vertex is important in most analyses to help reduce tracks associated with pile-up vertices. The reconstruction of the primary vertex is performed in two stages. First the primary vertex finding algorithm associates reconstructed tracks to a vertex candidate. Secondly the vertex fitting algorithms reconstruct the position of the vertex and the corresponding error matrix. When more than one reconstructed vertex are present in an event the vertex with the largest summed track momentum, $\sum_{p_{\mathrm{T}}}$, is referred to as the primary vertex. Reconstructed vertices that are not the primary vertex are called pile-up vertices.

6.1.3 Muons

The reconstruction of muon objects is performed using the combined data from the inner detector, calorimeters and muon spectrometer. The pattern recognition algorithms use the following steps:

- Identification of a region of activity within the muon system, through the muon chambers.
- Pattern finding algorithms incorporate the initial road finding in the bending and non-bending plane of the spectrometer, and combine them to form three dimensional roads.
- Segment finding is achieved with local reconstruction of segments in the three layers of the precision detectors.

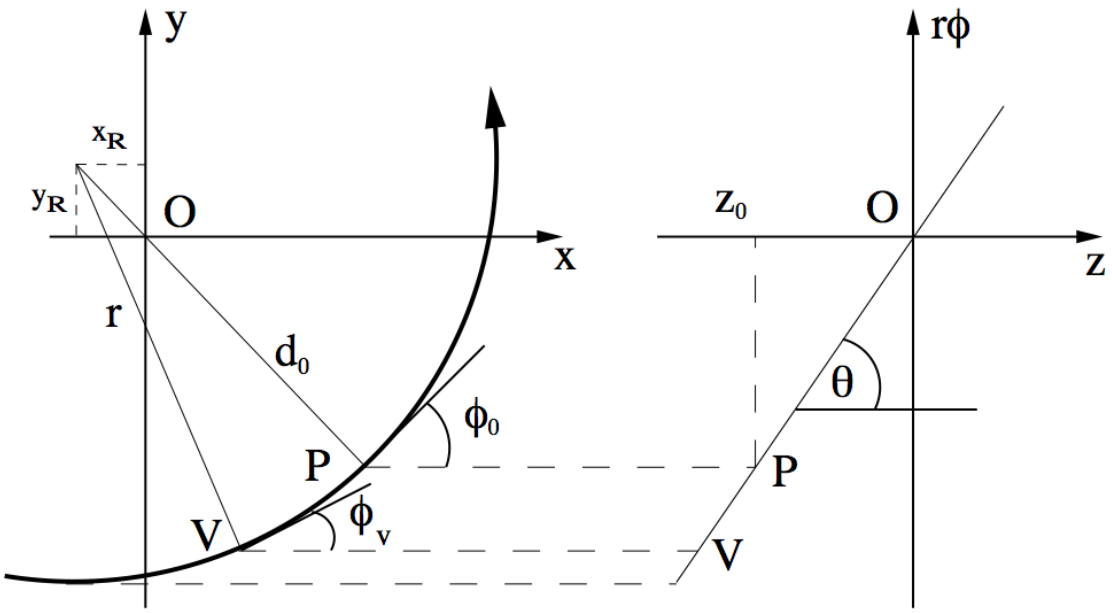

Figure 6.1: Schematic view of the ATLAS Perigee Parameters.

- Formation of tracks in the muon spectrometer using a combinatorial search of the muon segments, and a fit with the hits. This is referred to as a muon spectrometer standalone track.

There are three classifications of reconstructed muons:

- Combined Muon (CB): Track reconstruction is performed independently in the ID and MS. A statistical combination is made with the two independent track measurements.
- Extrapolated Muon (EX): Hits in the MS produce standalone tracks. These tracks are extrapolated back to the Interaction point.
- Muon Tagged (MT): A track in the ID is identified as a muon if the track extrapolated to the MS is associated with straight track segments in one of the spectrometer precision chambers.

There are benefits to all three types. The extrapolated tracks do not require the use of the inner detector. These tracks can therefore be reconstructed within $|\eta| < 2.8$, while a combined track is limited by the coverage of the inner detector and can only be reconstructed within $|\eta| < 2.5$. The muon tagged tracks have a higher efficiency in regions with poor MS coverage. The combined tracks however have a better momentum resolution, especially at low p_{T}, dominated by the inner detector measurement. This is shown in the comparison of Figures 6.2(a) and 6.2(b). Combined tracks are used in this thesis.

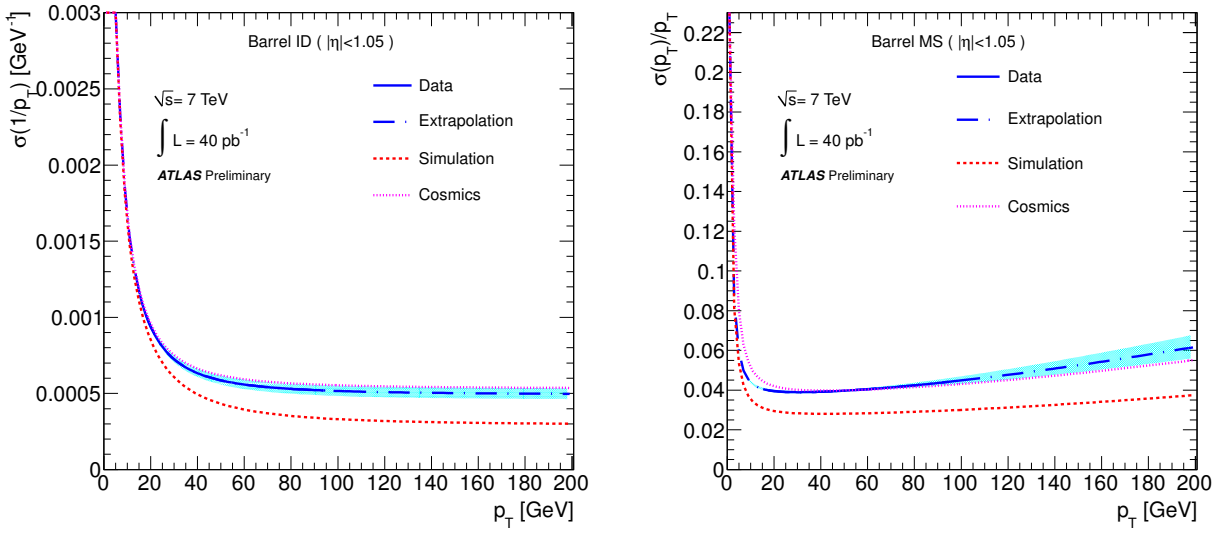

(a) (b)

Figure 6.2: Resolution curve for tracks reconstructed in the ID (left) and in the MS (right), in the region $0 < |\eta| < 1.05$.

The momentum and charge of the combined track is taken from a weighted average of the ID and MS track momenta. This is dependent on the η of the muon track due to the separate track momentum resolutions. The ID tracks are required to pass the following selection cuts to remove background from mesons in the tails of the track distributions (see section 3.3 for information on the ID):

- At least one b-layer hit is required if the track crosses an active region of the b-layer.
- The number of pixel hits added to the number of crossed dead pixel sensors must be > 1.
- The number of SCT hits added to the number of crossed dead SCT sensors must be ≥ 6.
- The number of pixel holes added to the number of SCT holes should be < 3.
- For tracks with $|\eta| < 1.9$, we require that in the TRT, $(N_{\text{hits}} + N_{\text{outliers}}) > 5$ and $N_{\text{outliers}} < 0.9 \times (N_{\text{hits}} + N_{\text{outliers}})$. Here N_{hits} refers to the number of hits in the TRT and N_{outliers} is the number of outliers, where an outlier appears in two forms, either as a straw tube in the TRT with a signal but not crossed by the nearby track, or as a set of TRT measurements in the prolongation of a track which, however, failed to form a smooth trajectory together with the pixel and SCT measurements.

- For tracks with $|\eta| \geq 1.9$, if $(N_{\text{hits}} + N_{\text{outliers}}) > 5$, the track must satisfy $N_{\text{outliers}} < 0.9 \times (N_{\text{hits}} + N_{\text{outliers}})$.

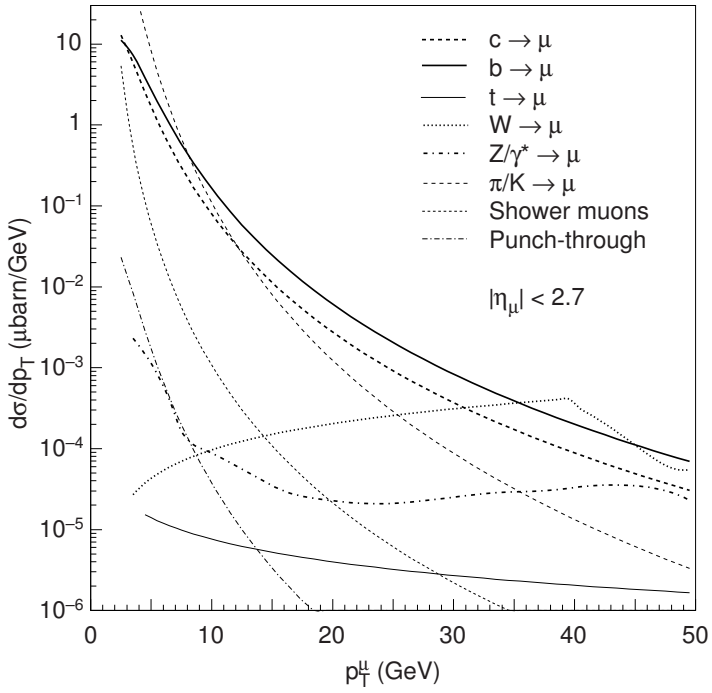

Figure 6.3: Inclusive muon production cross sections as a function of transverse momentum [78].

There are a large number of processes that contribute to the muon background. The inclusive muon cross sections for the various backgrounds are shown in Figure 6.3. In order to discriminate between prompt and background muons we use the following discriminators

- **Calorimeter Isolation**
  The calorimeter isolation, $E_{\text{T}}^{\Delta\text{R}}$, is the summed energy deposited in the calorimeter cells within a cone of size ΔR around the muon axis, removing the deposited energy by the muon.

- **Track Isolation**
  The track isolation, $p_{\text{T}}^{\Delta\text{R}}$, is the scalar sum of the transverse momenta of all the tracks with $p_{\text{T}} > 1.0$ GeV within a cone ΔR around the muon axis.

- **Track χ^2**
  Light mesons, such as $\pi^{\pm}, K^{\pm}$, can decay within the ATLAS detector tracking system. These light mesons can decay semi-leptonically to produce a muon and a muon neutrino, and are the most dominant source of low p_{T} muons backgrounds. The decay of the meson tends to cause a change in the trajectory and as a result will lead to a poor

quality combined muon track with a large χ^2 fit.

- **Impact Parameter Significance**

  The heavy-flavour b/c hadrons can decay semi-leptonically, producing a real muon. These muons from semi-leptonic decays are usually surrounded by additional jet activity from high p_{T} partons. They are not isolated and have high values of $p_{\mathrm{T}}^{\Delta\mathrm{R}}$ and $E_{\mathrm{T}}^{\Delta\mathrm{R}}$.

  Due to the lifetime of the B meson, the muon from the B decay is associated with a secondary vertex. The transverse impact parameter, d_0, for these muons with respect to the primary vertex is generally large. The impact parameter significance, $|d_0|/\sigma\,(d_0)$, where $\sigma\,(d_0)$ is the error on the measured transverse impact parameter, is typically used to discriminate background muons from these secondary vertices from signal muons. This variable gives more weight to accurately measured impact parameters. There are distinct differences in the shape of this distribution for prompt muons (from Z or W decays) and muons from b-hadron decays. Figure 6.4 shows the transverse impact parameter significance for muons from b decays, muons from π/K decays, and prompt muons from Z decays.

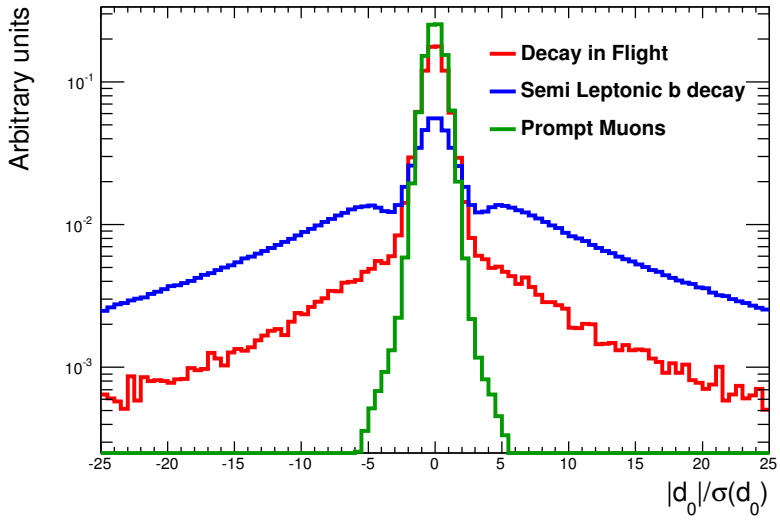

Figure 6.4: Impact parameter significance for difference muon sources.

- **Heavy-Flavour b-Tagging**

  There are a number of methods deployed by ATLAS to attempt to tag muons from a b-hadron decay. This technique is referred to as b-tagging and can be a strong tool in physics analyses. The recommended algorithm for b-tagging on ATLAS is MV1 [102]. MV1 is a neural network based b-tagger. The efficiency for correctly tagging a muon from a b-hadron is shown in Figure 6.5.

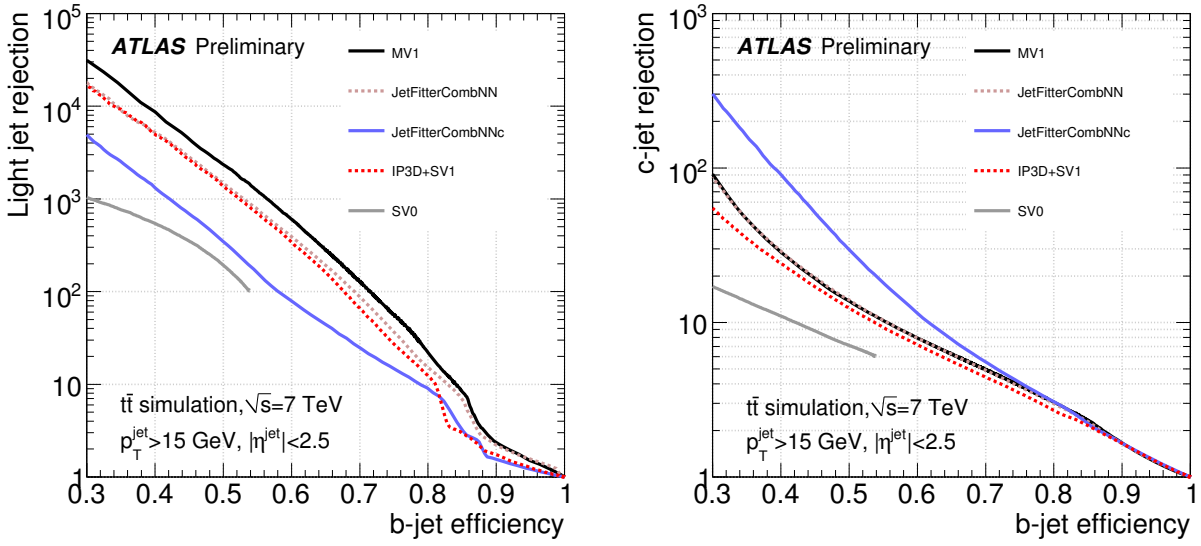

(a) (b)

Figure 6.5: Distribution of (a) light-jet rejection and (b) c-jet rejection as a function of the b-tag efficiency for various ATLAS b-taggers, based on simulated $t\bar{t}$ events.

- **Cosmic Ray Muons**

  Cosmic rays are continuously passing through the muon spectrometer. These muons are uncorrelated with the ATLAS collisions and can be vetoed with timing information of the muon trigger chambers. In the events that a cosmic ray muon passes through both hemispheres of the detector, two tracks may be formed. These tracks tend to have large transverse impact parameters with respect to the primary vertex and appear back-to-back in the detector. To remove these muons a requirement can be made on the angle between the two tracks, removing muon pairs that are back-to-back with large transverse impact parameters.

6.1.4 Jets

A jet can be considered as a bunch of collimated particles originating from the parton parton interactions that are hardonised and are either detected through energy deposition in the calorimeters or formed by tracks found in the inner detector. Jets used in this thesis are reconstructed using topoclusters. Topoclusters are built up of calorimeter cells that have not been associated with a reconstructed electron or photon and are not removed by noise suppression. The formation of a topocluster is seeded by calorimeter cells that have a signal-to-noise ratio, σ_{noise}, of at least 4. The seed is added to by any surrounding cells with a threshold above 2 σ_{noise}. Finally all cells directly neighbouring the cluster are added. The topocluster is then defined as having energy equal to the summed energy of the consisting

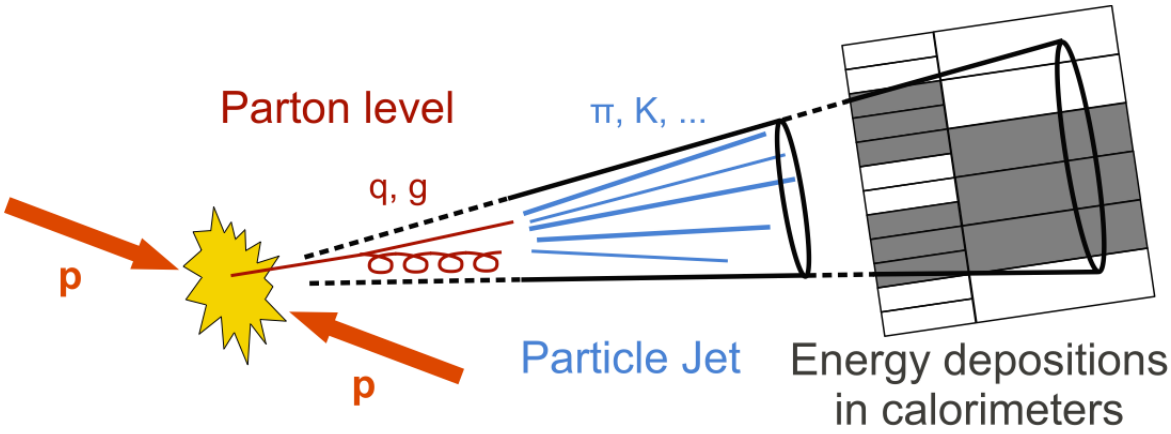

Figure 6.6: Development of a jet, collimated particles, from the hadronisation of quarks and gluons.

cells, with the direction taken from the vector connecting the centre of the ATLAS coordinate system to the energy weighted centre of the topocluster.

The energies of the calorimeter cells are measured at the electromagnetic scale (EM scale), and no correction is made due to the difference in the response of the calorimeter to hadrons compared to electrons. After forming calorimeter clusters a jet finder algorithm is used. All jets are defined by the choice of this algorithm. The jet finding algorithm used to reconstruct jets in this thesis is the anti-k_t algorithm [103]. This is a recombination algorithm that combines the closest pair of clusters according to the distance d_{ij} defined as:

$$d_{ij} = \min(k_{t,i}^{-2}, k_{t,j}^{-2}) \frac{(\Delta R)_{ij}^2}{R^2}$$

where

$$(\Delta R)_{ij}^2 = (y_i - y_j)^2 + (\phi_i - \phi_j)^2$$

up to a distance R=0.4, where y_i is the rapidity of cluster i. All softer clusters, in the vicinity $\Delta R < R$ of a hard cluster, are merged to form a jet.

A correction is needed to account for the response of the calorimeter to hadrons in order to obtain the correct energy of the jets (jet energy scale), as well as additional corrections relating to the detector, such as

- energy deposited outside of the calorimeter,
- energy deposited in inactive regions of the detector,
- out of cone energy of particles not included in the reconstructed jet,
- inefficiencies in the clustering and jet reconstruction.

These corrections are applied as a function of the jet energy and the jet pseudo-rapidity to jets that are reconstructed at the jet EM scale. First of all a pile-up correction is applied to the jet energy to remove energy from cells that are not associated with the interaction from the primary vertex. The kinematics of the topoclusters are then corrected to point back to the primary vertex, and the jet kinematics are recalculated. Finally an energy response, derived from MC is applied to the jets to match the jet energy back to the true jet energy.

To remove jets, originating from additional *pp* interactions, within the coverage of the inner detector, we require the jet vertex fraction to be at least 75%. This means that at least 75% of the total transverse momentum of tracks belonging to the jet must be associated to the primary vertex. The jet vertex fraction is shown in Figure 6.7 for four different levels of pile-up in data. Each histogram is normalised to unity for comparison. Jets in events with a low number of interactions per bunch crossing are shown to have on average larger values of jet vertex fraction than jets in high pile-up events. In addition each jet must pass quality requirements based on their shower shape, and their calorimeter signal timing must be consistent with the timing of the beam crossing [104]. An event containing a jet that fails this quality requirement is rejected.

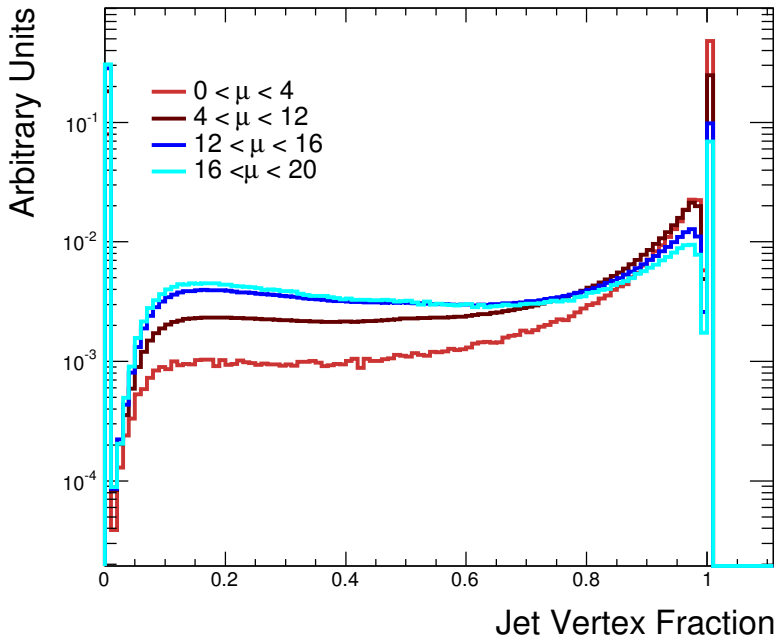

Figure 6.7: Jet vertex fraction for jets in events with different levels of pile-up.

6.1.5 Electrons

Electron reconstruction

Electron are charged particles, similar to muons but with a mass of 0.5 MeV. They are expected to deposit almost all their energy in the EM calorimeter system. The reconstruction is seeded by an electromagnetic cluster, which is reconstructed using energy deposits in the electromagnetic calorimeter. The deposited energy in the calorimeter is stored per cell, with a calibration applied. The cell energies are then formed into a matrix of granularity $\Delta\eta \times \Delta\phi = 0.025 \times 0.025$, and preliminary clusters are created corresponding to 3×5 cells in the middle layer of the EM calorimeter. A sliding window algorithm with a 5×5 cell window is then applied over the full acceptance of the EM calorimeter and an electron is seeded if the summed cluster energy exceeds 2.5 GeV. The ϕ position is measured in the central component and the η position is measured in the first two longitudinal components (the energies are corrected for the η and ϕ modulations and the calibration is adjusted to account for the finite cluster size). Electrons are reconstructed using the sliding window algorithms if there is an ID track found with $p_{\mathrm{T}} > 0.5$ GeV pointing towards the cluster. The optimum size of clusters reconstructed in the barrel are 3×7 cells in $\eta \times \phi$ and 5×5 cells for the end-cap. The cluster energy is calculated by summing the energy deposited in front of the calorimeters, the energy deposited in the cluster cells, the energy deposited outside the cluster and the energy deposited after the EM calorimeter. The last two are referred to as lateral and longitudinal leakage respectively. The transition region between the barrel and end-cap has a poorer performance due to the limited coverage of the calorimeters. As a consequence this region is excluded for reconstruction of electrons.

Electron identification

The electron identification algorithms concentrate on variables that are well suited in separating isolated electrons from QCD jets. The probability of a QCD jet being identified as an electron is small, but is still a major background due to the large QCD cross section. The dominant process here is when a high p_{T} track in the inner detector coincides with a $\pi \to \gamma\gamma$ decay.

Three definitions of electrons are available, with different sets of cuts namely *loose*, *medium* and *tight*. These take advantage of the following discriminating variables:

- **Track quality cuts,** A set of cuts are applied to the ID tracks.
- **Inner Detector and Calorimeter consistency,** Consistency checks are made on the $\Delta\eta$ and $\Delta\phi$ between the track and the cluster. For real electrons the momentum of the

ID track is similar to the energy of the EM cluster. The fraction E_{cal}/p_{trk} is therefore a good discriminator.

- **Track Isolation,** The track isolation, $p_{\mathrm{T}}^{\Delta \mathrm{R}}$, is defined as the summed momentum of inner detector tracks within a cone of size R, with momentum above 0.4 GeV.

- **Calorimeter Isolation,** The calorimeter isolation, $E_{\mathrm{T}}^{\Delta \mathrm{R}}$, is defined as the sum of calorimeter cell energies inside a cone of radius ΔR, excluding the electron energy. This includes cells from cells from both EM and hadronic calorimeters. Corrections to this energy are applied due to energy leakage of the electron as well as pile-up corrections, which is dependent on the number of reconstructed vertices.

6.1.6 Missing Transverse Energy

The presence of neutrinos or any other particles that are too weakly interacting with the detector are inferred by calculating the missing transverse energy. Since at hadron colliders, the longitudinal momenta of two scattered partons are not known but the transverse momenta are known to be zero, the missing energy can only be calculated in the transverse plane. This is referred to as *missing transverse energy*, ($E_{\mathrm{T}}^{\mathrm{miss}}$). The $E_{\mathrm{T}}^{\mathrm{miss}}$ is the negative sum of all the transverse energy in the event. The $E_{\mathrm{T}}^{\mathrm{miss}}$ definition consists of two separate terms. These include contributions from the calorimeter cells and muons terms, given by [105]:

$$E_{\mathrm{x,y}}^{\mathrm{miss}} = E_{\mathrm{x,y}}^{\mathrm{miss\ Calo}} + E_{\mathrm{x,y}}^{\mathrm{miss\ Muon}} \tag{6.1}$$

The first term relates to the calorimeter cells. Only cells that belong to three dimensional topoclusters are used in the calculation of this term, in order to suppress the electronic noise contribution. Each cell is either assigned to one particle or to no particles. Cells that are associated with a high p_{T} reconstructed object use the re-calibrated energies of the object, which are known to higher accuracy than the general cell energies, which use a global calibration. For cells that are occupied by multiple physics objects the assigned object is chosen that appears first in the order of: electrons, photons, hadronically decaying taus, jets and muons. Once the cells are assigned to physics objects the term for the $E_{\mathrm{T}}^{\mathrm{miss}}$ in the calorimeter is calculated using:

$$E_{\mathrm{x,y}}^{\mathrm{miss\ Calo}} = E_{\mathrm{x,y}}^{\mathrm{miss\ e}} + E_{\mathrm{x,y}}^{\mathrm{miss}\ \gamma} + E_{\mathrm{x,y}}^{\mathrm{miss}\ \tau} + E_{\mathrm{x,y}}^{\mathrm{miss\ jets}} + E_{\mathrm{x,y}}^{\mathrm{miss\ softjets}} + E_{\mathrm{x,y}}^{\mathrm{miss\ Calo}\mu} + E_{\mathrm{x,y}}^{\mathrm{miss\ Cellout}} \tag{6.2}$$

where each term is the negative sum of the calibrated energy in the cells assigned to each object. The electrons, photon's and tau leptons used in this definition are required to be reconstructed with $p_{\mathrm{T}} > 10$ GeV, with the electrons using the default electron calibration

and the photons energy measured at the EM scale. The term $E_{\mathrm{x,y}}^{\mathrm{miss\ jets}}$ is calculated from jets with $p_{\mathrm{T}} > 20$ GeV, while the $E_{\mathrm{x,y}}^{\mathrm{miss\ softjets}}$ is taken from jets with $7 < p_{\mathrm{T}} < 20$ GeV. The $E_{\mathrm{x,y}}^{\mathrm{miss\ Cellout}}$ term in equation 6.2 is taken from the cells with no assigned physics object.

The second term in the $E_{\mathrm{T}}^{\mathrm{miss}}$ is calculated by summing the energy of muons measured in the muon spectrometer, with $p_{\mathrm{T}} > 6$ GeV and $|\eta| < 2.7$. For muons with $|\eta| < 2.5$ a matched inner detector track is required to reduce the level of false muons candidates in the muon spectrometer, relating to high energy jets that escape the hadronic calorimeter. The energy lost by the muon in the calorimeter is not included in this term, as this is already accounted for in $E_{\mathrm{x,y}}^{\mathrm{miss\ Calo}}$. Muons that are not reconstructed in the regions with low coverage of the muon spectrometer are accounted for by using muons seeded by an inner detector track.

The value of the $E_{\mathrm{T}}^{\mathrm{miss}}$ and the azimuthal position of the missing transverse energy, ϕ^{miss} are calculated as

$$E_{\mathrm{T}}^{\mathrm{miss}} = \sqrt{(E_x^{miss})^2 + \left(E_y^{miss}\right)^2}, \phi^{miss} = \arctan(E_y^{miss}/E_x^{miss}). \tag{6.3}$$

6.2 Muon Isolation in Heavy Neutrino Processes

The search discussed in this thesis looks for events with two muons with the same charge. In such analyses the muon isolation plays a very important role. The expected SM background from di-muon events with two prompt same-sign muons is less than 100 events (seen in Table 11.1). In comparison the observed number of events that contain two same-sign muons (where all selection criteria apart from isolation are applied) is over 30000. This gives a required rejection rate of 99.8% in order to reduce the non-prompt background to the same level as the prompt muon backgrounds of the SM.

In order to achieve this goal we have to make use of the track and calorimeter isolation as mentioned previously. There are three important criteria that need to be considered when optimising the isolation requirements. These are:

- The isolation should have minimal dependence on pile-up.
- The isolation should be efficient at reducing the level of background from non-prompt muons.
- The isolation should have a high efficiency for signal-like muons.

Pile-up Dependence on Isolation

The track isolation variables have little dependence on pile-up compared to the calorimeter isolation, this is because the track isolation only considers tracks originating from the primary vertex, while the calorimeter isolation can be affected by both in-time and out-of-time pile-up due to the long drift times in the calorimeter. The isolation efficiency is studied as a function of the number of reconstructed vertices, where the vertex is required to have a minimum of two tracks. Figure 6.8 shows the isolation efficiencies of the track and calorimeter isolation separately for di-muon events from ALPGEN $Z \to \mu\mu$ MC. The events are selected by requiring two opposite-charge muons in a mass window of 10 GeV to the Z mass. The isolation efficiencies were also studied in $b\bar{b}$ QCD MC events, which are shown in Figure 6.9.

The significant effect of pile-up on the calorimeter isolation can be seen in Figure 6.8. A loss of $4 - 25\%$ (as we increase the cone size from 0.2-0.4) in efficiency is seen for prompt muons with $N_{\text{vtx}} = 8$, while the loss for the track isolation ranges only from $1 - 2\%$. The track isolation algorithm with 0.2 and 0.3 angular cone sizes performs similarly with regards to pile-up. Cone sizes of 0.2 are generally 1.5% more efficient than the 0.3 cone for prompt muons. However Figure 6.9 shows the 0.3 cone track isolation has a factor of 2 higher rejection rate for non-prompt muons. A combination of calorimeter and track isolation is chosen for this analysis, using the least pile-up dependent $E_{\text{T}}^{\Delta\text{R}=0.2}$ and $p_{\text{T}}^{\Delta\text{R}=0.3}$ variables.

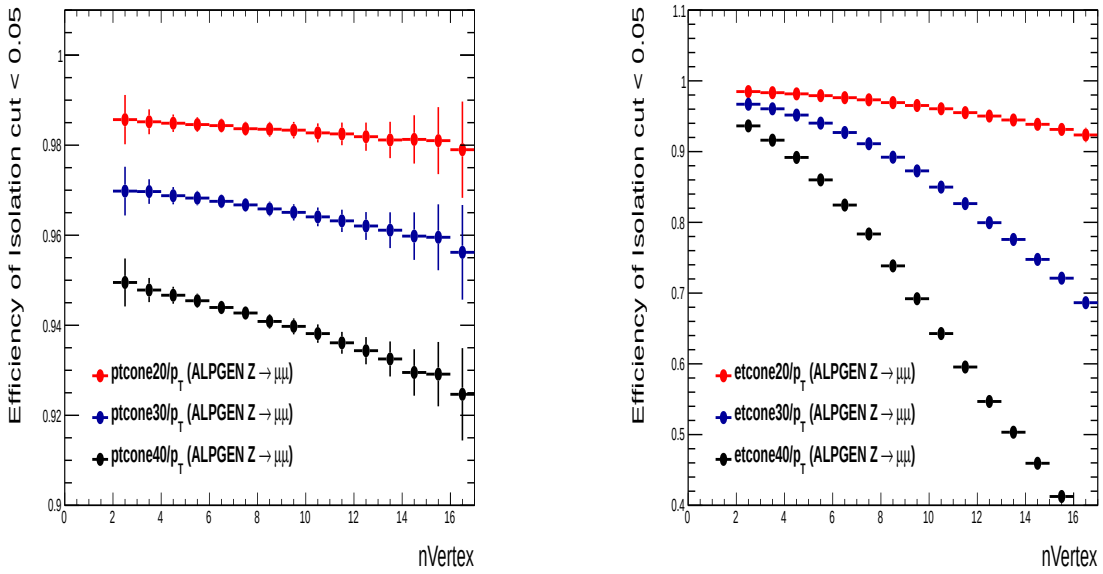

(a) (b)

Figure 6.8: Average efficiency of isolation criteria for (a) $p_{\mathrm{T}}^{\Delta \mathrm{R}}$ and (b) $E_{\mathrm{T}}^{\Delta \mathrm{R}}$ isolation variables as a function of the number of reconstructed vertices for muons in $Z \to \mu\mu$ MC.

Although this thesis only presents results for neutrino searches in the minimal extension to the SM, the isolation study is also performed for events in the LRSM model, as discussed in section 2.3.3. The isolation is therefore optimised for neutrino production in both regimes and the studies described below refer to both models.

There is a complication when considering the isolation for the muons in the LRSM model. For some phase space of the LRSM signal, where m_{N} is relatively small compared to $m_{\mathrm{W_R}}$, the neutrino is produced with large transverse momentum (boosted). The lepton and jets from the N decay are produced in the same direction, meaning that the lepton from the N decay is less isolated than the lepton from the decay of the real W_R. The isolation studies were performed to partially recover acceptance losses for such mass points, while keeping the signal efficiency high for the minimal model. Using the same LRSM MC samples as discussed in section 5.4 it was found that signal muons from N decays have a large p_{T} compared to muons from semi-leptonic heavy meson decays. Which are the dominant contribution to the fake-muon background. In events with boosted decay products, the muon from the decay of N has large p_{T}. However, in more than 90% of the time it is within $\Delta R < 0.4$ of a reconstructed jet. The "standard" track and calorimeter isolation selection criteria used to reduce the background from heavy meson decays also reject the LRSM signal when the N is boosted. As a result, separate isolation requirements are applied to muons away from jets ($\Delta R > 0.4$) compared to muons close to jets ($\Delta R \leq 0.4$).

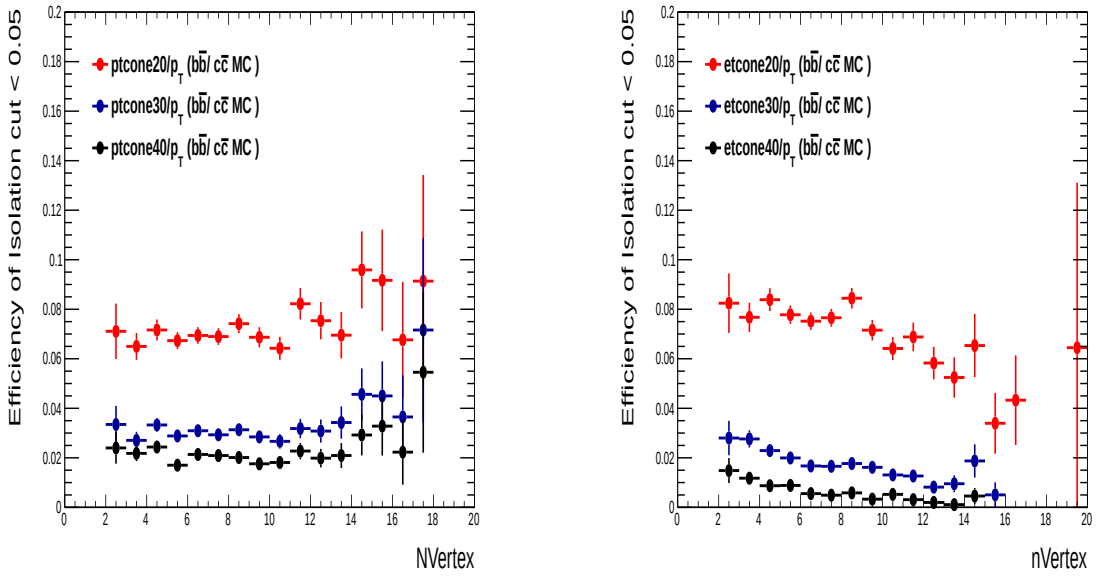

(a) (b)

Figure 6.9: Average efficiency of isolation cut for (a) $p_{\mathrm{T}}^{\Delta\mathrm{R}}$ and (b) $E_{\mathrm{T}}^{\Delta\mathrm{R}}$ isolation variables as a function of the number of reconstructed vertices for muons in $b\bar{b}$ and $c\bar{c}$ MC.

Efficiency [%]	m_N =200 GeV		m_N =100 GeV	
	leading μ	sub-leading μ	leading μ	sub-leading μ
$p_{\mathrm{T}}^{\Delta\mathrm{R}=0.3}/p_{\mathrm{T}}^{\mu}$	99.8	97.3	99.9	95.0
$(E_{\mathrm{T}}^{\Delta\mathrm{R}=0.2}$-1)$/p_{\mathrm{T}}^{\mu}$ wrt pass $p_{\mathrm{T}}^{\Delta\mathrm{R}=0.3}/p_{\mathrm{T}}^{\mu}$	99.6	97.3	99.3	97.6
$(E_{\mathrm{T}}^{\Delta\mathrm{R}=0.2}$-1)$/p_{\mathrm{T}}^{\mu}$	99.6	99.0	99.1	95.0
Combined	98.7	96.2	99.0	88.5

Table 6.1: Efficiency in percentage, for the individual isolation criteria and their combination for muons that have no jet within a cone of ΔR=0.4. The efficiencies are quoted for the lead and sub-leading muons in the LRSM and seesaw type-I benchmark samples, m_{N} = 100, 200 GeV with $m_{\mathrm{W_R}}$ = 1800 GeV.

Muons away from jets

A cut on both the calorimeter isolation and track isolation is applied to muons that are not close to a jet. In both cases the cuts are chosen to be relative to the muon transverse momentum, p_{T}^{μ}, rather than an absolute value. This allows the isolation to be tighter at low p_{T}^{μ}, where the background from fake muons is highest, but looser at high p_{T}^{μ} so as to retain high signal efficiency. The calorimeter isolation is required to satisfy $E_{\mathrm{T}}^{\Delta\mathrm{R}=0.2} <$ (0.05 p_{T}^{μ}+1 GeV) and for the track isolation requirement is $p_{\mathrm{T}}^{\Delta\mathrm{R}=0.3} < 0.05\ p_{\mathrm{T}}^{\mu}$. The efficiency of the isolation cut for muons away from jets can be seen in Table 6.1 for signal muons and Table 6.2 for background.

Efficiency [%]	Z+jets	$t\bar{t}$	bb	CR
	prompt μ	fake μ	fake μ	fake μ
$p_{\mathrm{T}}^{\Delta\mathrm{R}=0.3}/p_{\mathrm{T}}^{\mu}$	93.3	24.4	11.9	17.8
$(E_{\mathrm{T}}^{\Delta\mathrm{R}=0.2}\text{-}1)/p_{\mathrm{T}}^{\mu}$ wrt pass $p_{\mathrm{T}}^{\Delta\mathrm{R}=0.3}/p_{\mathrm{T}}^{\mu}$	99.3	74.7	76.9	72.7
$(E_{\mathrm{T}}^{\Delta\mathrm{R}=0.2}\text{-}1)/p_{\mathrm{T}}^{\mu}$	95.4	47.0	58.8	43.3
Combined	92.6	21.7	8.5	12.5

Table 6.2: Efficiency in percentage, of the individual isolation criteria and their combination for muons that have no jet within a cone of ΔR=0.4. The efficiencies are quoted for the combination of the leading and sub-leading muons.

Muons close to jets

To remove the majority of fake muons that are close to jets in the detector we apply a cut on the transverse momentum of the muon, p_{T}^{μ}, requiring these muons to have $p_{\mathrm{T}} > 80$ GeV. Considering only muons close to jets, this removes 99% of muons in the fake control sample, while only removing 10% of the boosted LRSM signal and 45% of the muons in the minimal model.

For muons found close to a jet with $p_{\mathrm{T}}^{\mu} > 80$ GeV we apply the same relative calorimeter isolation cut applied to muons away from jets. This retains over 75% of signal for these muons while removing 75% of muons from a boosted N. To discriminate muons in processes such as $N \to W\mu \to \mu jj$ where the N is boosted, from non-prompt muons we use a method used in jet substructure analyses [106]. This uses the difference in mass between the overlapping muon+jet pair and the mass of the closest jet to discriminate between the boosted signal and the background. We define this mass difference as the mass-drop, such that:

$$\texttt{mass-drop} = m(\mu j) - m(j) \tag{6.4}$$

where $m(\mu j)$ is the invariant mass of the muon and closest jet to the muon while $m(j)$ is the mass of the jet closest to the muon.

Figure 6.10 shows the mass-drop variable for muons that are close to an analysis jet in an LRSM sample, a seesaw type-I signal sample, $b\bar{b}$ MC sample and in a fake dominated data sample. A cut on the mass-drop of 10 GeV is applied which removes over 99% muons in the $b\bar{b}$ MC and 98% of muons in the fake dominated data sample, while retaining approximately 75 and 10 % of the LRSM and minimal model signal muons close to jets, respectively. The efficiency of the isolation cut for muons close to jets can be seen in Table 6.3 for signal muons and Table 6.4 for backgrounds.

The correlation between the mass-drop variable and the calorimeter isolation requirement is shown in Figure 6.11. By applying an "OR" between the mass-drop cut and the calorimeter isolation requirement the signal efficiency for muons close to jets increases to 40% for the seesaw type-I sample ($m_{\mathrm{N}} = 200$ GeV) and 80% for the LRSM sample ($m_{\mathrm{W_R}} = 1800$ GeV,

Efficiency [%]	m_{N} =200 GeV		m_N =100 GeV	
	leading μ	sub-leading μ	leading μ	sub-leading μ
$p_{\mathrm{T}}^{\mu} > 80$ GeV	67.2	29.3	98.8	85.3
$(E_{\mathrm{T}}^{\Delta\mathrm{R}=0.2}\text{-}1)/p_{\mathrm{T}}^{\mu}$ wrt $p_{\mathrm{T}}^{\mu} > 80$ GeV	88.0	86.0	98.0	26.8
mass-drop wrt $p_{\mathrm{T}}^{\mu} > 80$ GeV	29.3	40.0	32.3	97.3
Combined	59.6	25.2	96.7	82.1

Table 6.3: Efficiency in percentage, of the individual isolation criteria and their combination for muons that have a jet within a cone of ΔR=0.4. The efficiencies are quoted for the lead and sub-leading muons in the LRSM and seesaw type-I benchmark samples, m_{N} = 100, 200 GeV with $m_{\mathrm{W_R}}$ = 1800 GeV.

Efficiency [%]	Z+jets	$t\bar{t}$	$b\bar{b}$	CR
	prompt μ	fake μ	fake μ	fake μ
$p_{\mathrm{T}}^{\mu} > 80$ GeV	4.5	1.4	0.14	1.8
$(E_{\mathrm{T}}^{\Delta\mathrm{R}=0.2}\text{-}1)/p_{\mathrm{T}}^{\mu}$ wrt $p_{\mathrm{T}}^{\mu} > 80$ GeV	82.6	2.1	3.2	4.7
mass-drop wrt $p_{\mathrm{T}}^{\mu} > 80$ GeV	33.2	5.7	3.1	3.7
Combined	4.0	0.1	0.008	0.01

Table 6.4: Efficiency in percentage, of the individual isolation criteria and their combination for muons that have a jet within a cone of ΔR=0.4. The efficiencies are quoted for the combination of the leading and sub-leading muons.

$m_{\mathrm{N}} = 100$ GeV), while the efficiency in the fake-dominated data sample is 3%.

Isolation Criteria

To summarise, separate isolation requirements are used for muons close to jets and muons away from jets. The purpose was to retain muons from event topologies with boosted neutrinos. Muons that have no jet within a cone of $\Delta R = 0.4$ are required to have:

- $p_{\mathrm{T}}^{\Delta\mathrm{R}=0.3} < 0.05 p_{\mathrm{T}}^{\mu}$ for $p_{\mathrm{T}}^{\mu} < 80$ GeV;
- $E_{\mathrm{T}}^{\Delta\mathrm{R}=0.2} < (0.05 p_{\mathrm{T}}^{\mu} + 1$ GeV),

where p_{T}^{μ} is the transverse momentum of the muon. Muons that have a jet within a cone of $\Delta R = 0.4$ are required to have:

- $p_{\mathrm{T}}^{\mu} > 80$ GeV;
- $E_{\mathrm{T}}^{\Delta\mathrm{R}=0.2} < (0.05 p_{\mathrm{T}}^{\mu} + 1$ GeV) or $|m(\mu j)$ - $m(j)| > 10$ GeV.

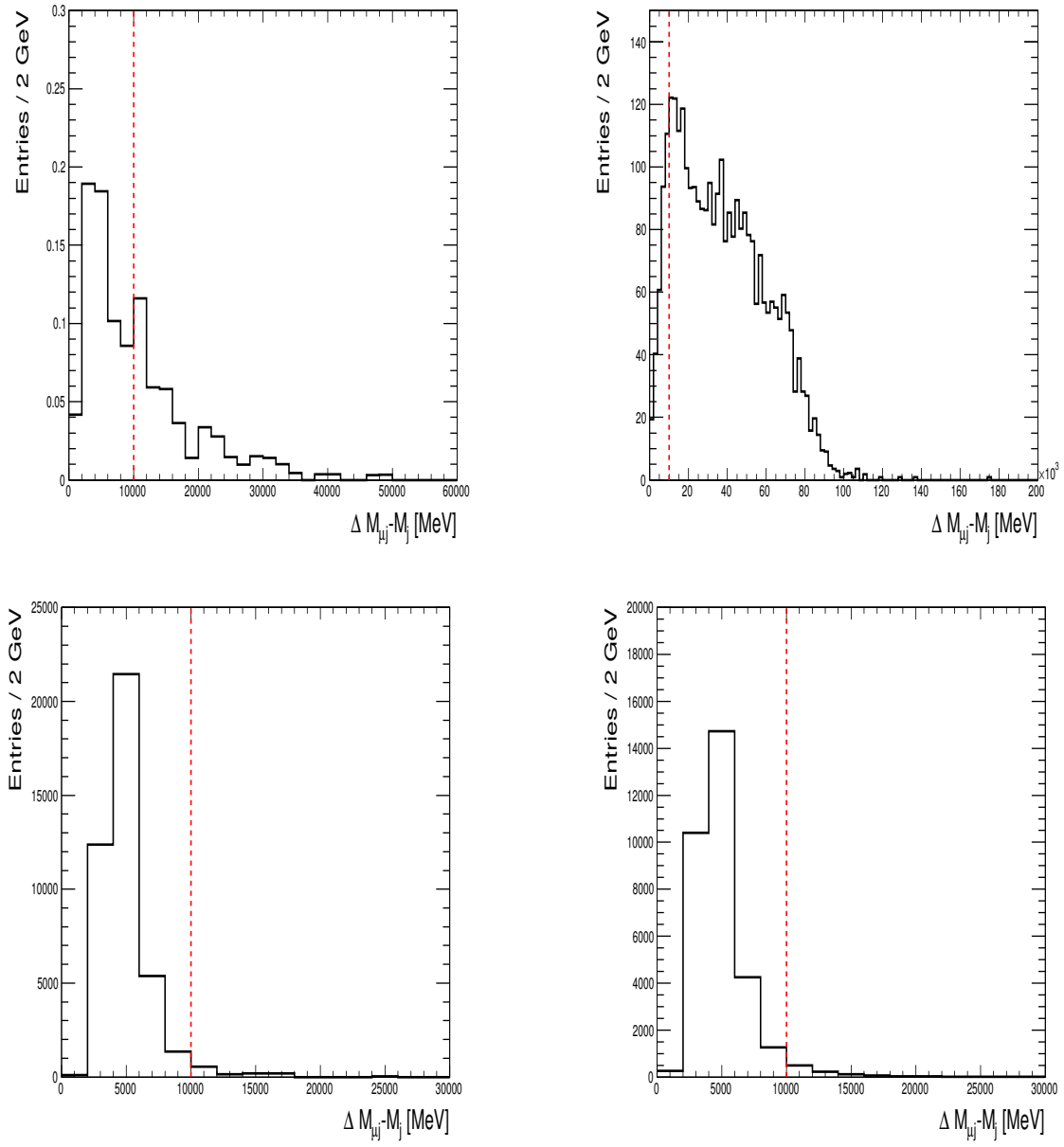

0

Figure 6.10: Mass-drop of muons with a nearby jet with $p_{\mathrm{T}}^{\mu} > 80$ GeV. Top left is for muons in a seesaw type-I signal sample, top right is for a LRSM sample where the N is boosted ($\mathrm{m}_N = 100$, $\mathrm{m}_{W_R} = 1800$), bottom left is $b\bar{b}$ and $c\bar{c}$ MC and bottom right is for a fake dominated data sample. The cut is shown by the red-dashed line.

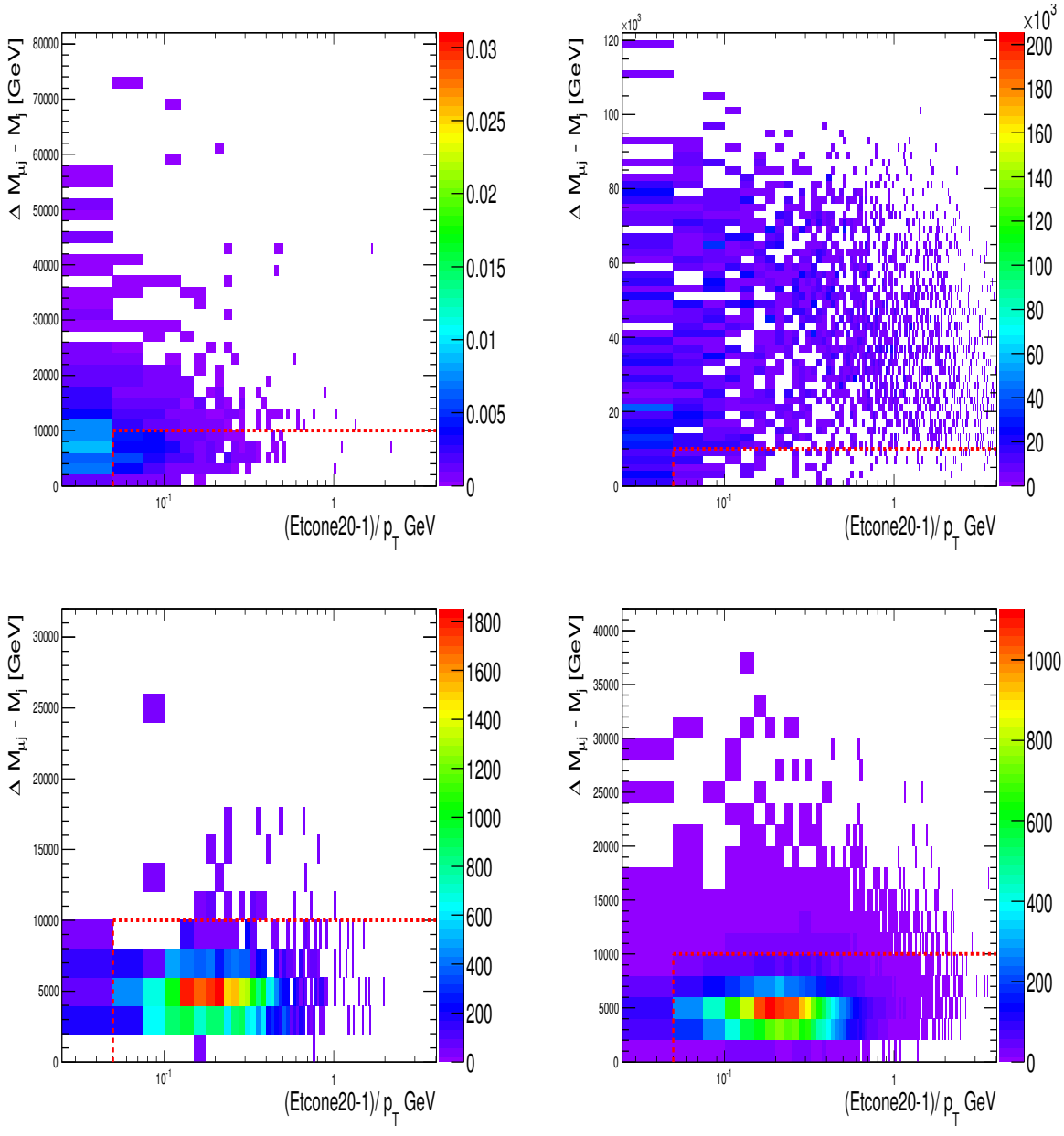

Figure 6.11: Mass-drop vs relative calorimeter isolation for muons with a nearby jet with $p_{\mathrm{T}}^{\mu} > 80$ GeV. Top left is for muons in seesaw type-I signal sample, top right is for a LRSM sample where N is boosted ($\mathrm{m}_{W_R} = 1800$ GeV, $\mathrm{m}_N = 100$ GeV), bottom left is $b\bar{b}$ and $c\bar{c}$ MC and bottom left is for a fake dominated data control sample. The cut is shown by the red-dashed line.

6.3 Limit Setting

When developing a search for a new particle it is essential to setup a robust statistical framework in which it is possible to define the significance of any observed signal. In the absence of a signal the same framework should be able to make a statement on the strength of signal that may exist and still be consistent with the observed data [107].

As an example consider a simple counting experiment that has n data events. It is possible to make a hypothesis on the outcome of this experiment by constructing a model that predicts the number of expected signal and background events. The consistency between the number of data events and the predicted signal plus background events can be used to set limits on the maximum number of signal events, n_{lim}, that are consistent with the number of data events at a given confidence level (CL). This is referred to as the "observed" limit. The expected exclusion can be predicted by setting the observed number of data events equal to the number of background events, which gives an "expected limit".

For the analysis presented in this thesis the test statistic is chosen as a profile likelihood ratio (PLR). This is determined using a likelihood function that for a given μ, where μ is the signal strength, describes the expected signal and background. The analysis must choose a kinematic variable for which the signal and background are input into the limit setting tool. These distributions are both normalised to the total luminosity of the dataset and combined to determine the expected number of signal + background events per bin for comparison with data. The likelihood function depends on both the signal strength and the systematic uncertainties α, and for the case where the input has only one bin is defined by

$$L(\mu, \alpha) = \frac{(\mu s + b)^n e^{-(\mu s+b)}}{n!} \prod_j \frac{1}{\sqrt{2\pi}} e^{-\frac{\alpha_j^2}{2}}, \tag{6.5}$$

where the number of events in the input distribution is given by n and the systematics sources are labeled with the index j. The number of events that are expected in bin i is $\mu s_i + b_i$. The effect of the systematics on the number of expected signal and background is:

$$b = b_0 \times \prod_j (\rho_{b_j(\alpha_j)}) \tag{6.6}$$

$$s = s_0 \times \prod_j (\rho_{s_j(\alpha_j)}) \tag{6.7}$$

where b_0 is the expected background and $\rho_{j(\alpha_j)}$ is the systematic uncertainty j, such that $\rho_{b_j(\alpha_j=1)}$ is $+1\sigma$.

A profile likelihood ratio can be defined such that

$$\lambda(\mu) = \begin{cases} \frac{L(\mu,\hat{\hat{\alpha}}(\mu))}{L(0,\hat{\hat{\alpha}}(0))} & \text{if } \hat{\mu} < 0 \\ \frac{L(\mu,\hat{\hat{\alpha}}(\mu))}{L(\hat{\mu},\hat{\alpha}(0))} & \text{if } 0 < \hat{\mu} < \mu \\ 0 & \text{if } \hat{\mu} > \mu \end{cases} \tag{6.8}$$

where $\hat{\alpha}$ and $\hat{\mu}$ are the maximum likelihood estimators (MLE) for the systematics and signal strengths and $\hat{\hat{\alpha}}(\mu)$ is the conditional MLE for the systematic uncertainties for a given signal strength. By performing the MLE fit the data can be used to constrain the effect of the different systematic uncertainties.
The test statistic, q_μ, is based on the profile likelihood ratio. This test statistic is given by

$$q_\mu = -2\ln\lambda(\mu). \tag{6.9}$$

Large values for the test statistic mean that the data is less compatible with the hypothesis. In order to determine at what level the data disagrees with the hypothesis a p-value is defined such that

$$p_\mu = \int_{q_{obs\ \mu}}^{\infty} f(q_\mu|\mu)dq_\mu \tag{6.10}$$

where the value of the test statistic observed in the data, $q_{\text{obs }\mu}$ and the probability density function for the signal is $f(q_\mu|\mu)$.
Using the input signal and background templates it is possible for any value of μ to produce the expected pdf distributions for the PLR test statistic. This can be done for both the background hypothesis and the signal plus background hypothesis. To find the expected background hypothesis distribution toy MC events are produced, where a poisson fluctuation of the SM templates is applied bin by bin around the expected values. These toy data events are now representative of a set of SM datasets that ATLAS could possibly record. The background pdf distribution can be produced by evaluating the test statistic for each of these pseudo data templates. In this distribution events that are signal-like tend toward zero while background-like events tend are evenly distributed. This allows a separation between the two hypotheses.

The p-value for a given set of data for the background only case is found, as shown in Figure 6.12, by integrating the afore mentioned background pdf. This is given by

$$p_b = \int_{q_{obs,\ \mu}}^{\infty} f(q_\mu|0,\hat{\hat{\alpha}}(0,\text{obs}))dq_\mu. \tag{6.11}$$

Similarly the p-value for a given signal strength μ of the observation (p_μ) is found by inte-

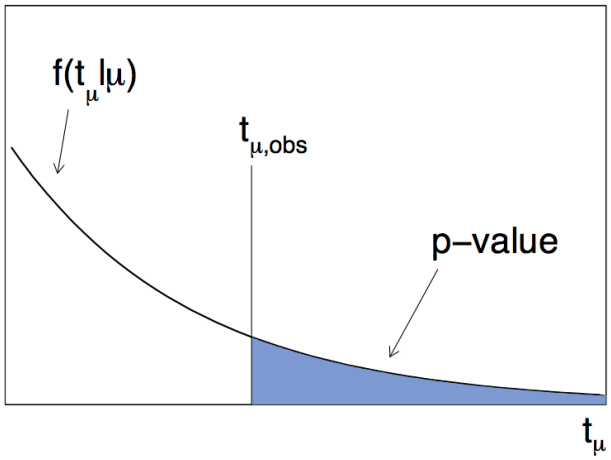

Figure 6.12: Illustration of the relation between the p-value obtained from an observed value of the test statistic t_μ [107]. The y-axis represents the probability distribution function $f(t_\mu|\mu)$.

grating the pdf for the signal strength μ:

$$p_b = \int_{q_{obs,\ \mu}}^{\infty} f(q_\mu|\mu, \hat{\hat{\alpha}}(0, \text{obs}))dq_\mu. \tag{6.12}$$

Different CL regions can be defined by integrating the expected distributions from the observed value of the test statistic. There are two CL regions, which are the background hypothesis CL_b, and the signal plus background hypothesis, CL_{s+b}. These are defined as

$$\begin{aligned} CL_b &= p_b(q \geq q_{obs}) \\ CL_{s+b} &= p_{s+b}(q \geq q_{obs}). \end{aligned} \tag{6.13}$$

In this equation $p_b(q \geq q_{obs})$ is the probability that the result of the test statistic is less signal-like that the observed data for the case of the background hypothesis. Similarly for $p_{s+b}(q \geq q_{obs})$, but when using the signal plus background hypothesis.

In the case that a signal is present in the data the background confidence level, 1-CL_b can be used to set the level of significance that the data is different from the background model. In particle physics for one to claim evidence of a new particle or process a statistically significant departure from the expected background is needed. Commonly for evidence of a new process a requirement is made that there is a 3σ departure from the background estimation. For a discovery this discrepancy has to reach 5σ. This can be expressed in terms of CL, which correspond to $CL_b = 2.7 \times 10^{-3}$ and $CL_b = 5.7 \times 10^{-7}$ respectively.

In the case that no signal is seen, upper limits on the level of signal that may be present in the data can be placed. If this is the case the expected CL_{s+b} is calculated for all signal

strengths considered.

It is possible that issues arise surrounding the power and sensitivity of the limit setting method. As an example, if the test statistic for the signal and background hypotheses are both alike the analysis will not have much discriminating power between the two. In this case the limit that is found on the signal process may be much lower than the limit that the experiment is sensitive to. The CL_s approach has been widely used in the past by the LEP and Tevatron collaborations and is now used on ATLAS. Here the background CL_b is used to protect against situations where the two hypotheses are poorly separated. CL_s is defined as:

$$CL_s = \frac{CL_{s+b}}{CL_b}. \tag{6.14}$$

CL_s is used in the same manner as CL_{s+b}, where the signal contributions is varied until the critical region is reached. With this approach the contribution from CL_b softens any limits gained. The effect of this is to increase, in a smooth fashion, the coverage of the test from the quoted 95% to 100%. In the case that there is good separation of the pdfs in the two hypotheses the softening of the limit will be minimal due to the small overlap. As the pdfs become less separated the contribution of CL_b will increase. Here the limit will be softened, which represents the loss in confidence in the power of the analysis to distinguish the two scenarios. An apparent failing of CL_s is that it is not itself a true probability, but a ratio of two probabilities. As a result it is difficult to infer the level of over coverage from 95%. The main limits on the cross section for heavy Majorana neutrino production quoted in this analysis will use the CL_s method as described here.

Chapter 7

Event Selection for Heavy Neutrino Searches

This chapter outlines the event selection for heavy Majorana neutrino searches in the minimal extension to the SM in the channel $pp \to N\mu^{\pm} \to \mu^{\pm}\mu^{\pm}$jj. The details of the dataset are outlined in section 7.1. section 7.2 details the preselection of the physics objects and the event selection requirements [108].

7.1 Dataset

The dataset used in this analysis was collected by the ATLAS detector between March 2011 and October 2011. It corresponds to a total recorded luminosity of 5.25 fb^{-1} (Figure 7.1). The ATLAS Data Quality framework [81] is used to assure data events are recorded with no detector *defects*. A defect is defined as a problem with a detector sub-system that affects the quality of the data acquisition. In the event of an intolerable defect in one of the ATLAS sub-detector systems the data is marked as bad and all LBs associated with the defect are removed before analysis. The analysis selects events that have been accepted by the single muon trigger. The two single muon trigger chains used to select events in this analysis can be found in Table 7.1, both requiring that a muon with $p_{\mathrm{T}} > 18$ GeV was found by the trigger. For data periods B to I (March to July 2011) the single muon trigger chain, EF_mu18_MG was used, while for all subsequent periods EF_mu18_MG_medium is used. After data quality selection and trigger pre-scales are considered the dataset statistics correspond to an integrated luminosity of 4.7 fb^{-1}, with an uncertainty of 1.8% [83]. To assure the event is from a pp collision events are required to have at least one primary vertex, consistent with the beam spot. The dataset is sub-divided into four periods, as shown in Table 7.2, reflecting key changes to the running conditions.

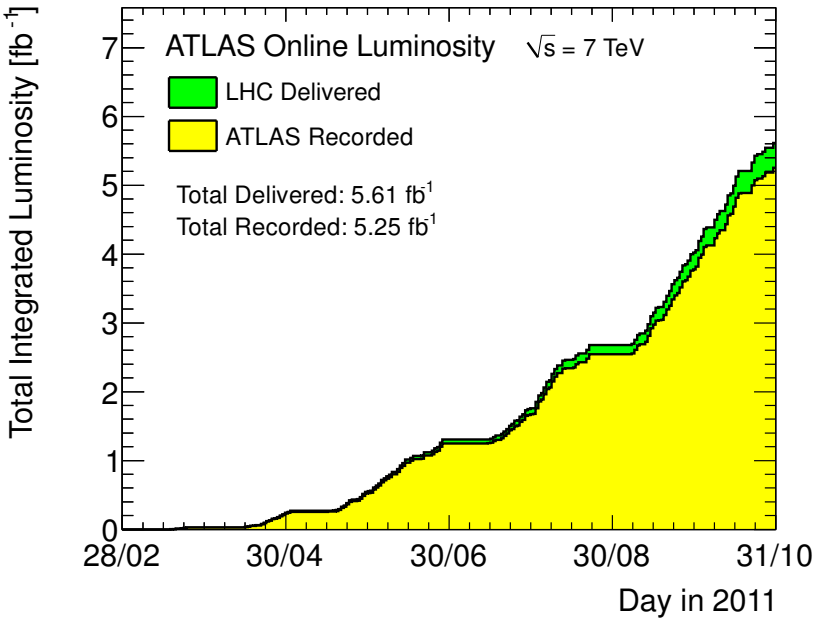

Figure 7.1: Cumulative luminosity versus day delivered to (green), and recorded by ATLAS (yellow) during stable beams and for pp collisions at 7 TeV centre-of-mass energy in 2011.

Event Cleaning

In order to remove poor quality events in data and MC certain cleaning cuts are applied. These are summarised below:

- To account for the loss of six front end boards of the electromagnetic calorimeter during periods E to H, events are removed in the data and MC simulation if a jet with $p_{\mathrm{T}} > 25$ GeV is found in the area of the detector affected by the missing front end boards.
- Events are removed that contain any jet that does not overlap with an electron, that has $p_{\mathrm{T}} > 20$ GeV and is classified as a *bad* jet according to *looser* bad jet definition [104].
- Events with noise bursts in the calorimeter or data integrity issues are removed.

Trigger Chain	Station Coincidence	Luminosity [pb^{-1}]
EF_mu18_MG	2	1500
EF_mu18_MG_medium	3	3250

Table 7.1: Luminosity for the 2011 primary muon triggers used in this analysis.

Data Periods	Luminosity [pb^{-1}]	Running conditions
B-D	180	Initial run conditions
E-H	980	Hole in the EM calorimeter coverage
I	340	Hole in EM calorimeter fixed
J-M	3250	Change in muon trigger

Table 7.2: Table of 2011 running conditions.

7.2 Selection Criteria

This section discusses the selection of data events used to keep signal-like events with high efficiency, while rejecting events from background sources.

7.2.1 Muon Preselection Criteria

Muons are required to be combined (see section 6.1.3) and have transverse momentum $p_{\mathrm{T}} > 20$ GeV. The muons must be found within the coverage of the inner detector, in the pseudo-rapidity range $|\eta| < 2.5$. The measured charge of both the inner detector and muon spectrometer tracks are required to be the same to reduce the rate of charge mis-measurement of the combined muon tracks. To reduce backgrounds due to muons from decays of hadrons produced in jets, muons are required to be isolated from hadronic activity (discussed in detail in section 6.2). In order to ensure that the muons used in this thesis are consistent with the primary vertex, the transverse (d_0) and longitudinal (z_0) impact parameters with respect to the primary vertex must be small, $|d_0| < 0.2$ mm and $|z_0| < 5.0$ mm, and the transverse impact parameter significance is required to be $|d_0|/\sigma\,(d_0) < 3.0$, where $\sigma\,(d_0)$ is the error on the measurement of d_0.

7.2.2 Electron Preselection Criteria

The transverse energy of the calorimeter cluster associated with the electron is required to satisfy $p_{\mathrm{T}} > 20$ GeV. In order to ensure that electrons are consistent with the primary vertex, the transverse (d_0) and longitudinal (z_0) impact parameters with respect to the primary vertex must be small, $|d_0| < 0.2$ mm and $|z_0| < 5.0$ mm, and the transverse impact parameter significance is required to be $|d_0|/\sigma\,(d_0) < 5.0$. The inner detector track associated with an electron must not have an associated track in the muon spectrometer. Electron tracks are required to be isolated in the calorimeter, and have few tracks close by in the tracking system. An electron is said to be isolated if $(p_{\mathrm{T}}^{\Delta\mathrm{R}} + 1)\ /\ E_T < 0.10$ and $E_{\mathrm{T}}^{\Delta\mathrm{R}}/E_T < 0.1$.

7.2.3 Selection Requirements

Events in this dataset are preselected to contain two muons. The two muons are required to be of equal charge. This reduces the signal by 50% but removes the biggest background of Z+jet events almost entirely as shown in Figure 7.2(a). At least one muon must have $p_{\mathrm{T}} > 25$ GeV. This p_{T} requirement is not made on both muons due to the trailing muons in the signal, which tends to be low for neutrino masses below 120 GeV. This is shown in Figure 7.2(b). All events must contain two jets, where jets are required to have $p_{\mathrm{T}} > 20$ GeV and $|\eta| < 2.8$. Events are rejected if they contain an electron. To further reduce backgrounds and increase signal significance additional selection criteria are applied. The invariant mass of the two muons, $m(\mu\mu)$, is required to be larger than 15 GeV to exclude any contribution from low energy mesons such as the J/ψ or the Υ. A series of additional selection cuts are used to reduce the background from $W^{\pm}Z$, ZZ, W + jets, $t\bar{t}$ and multi-jet events.

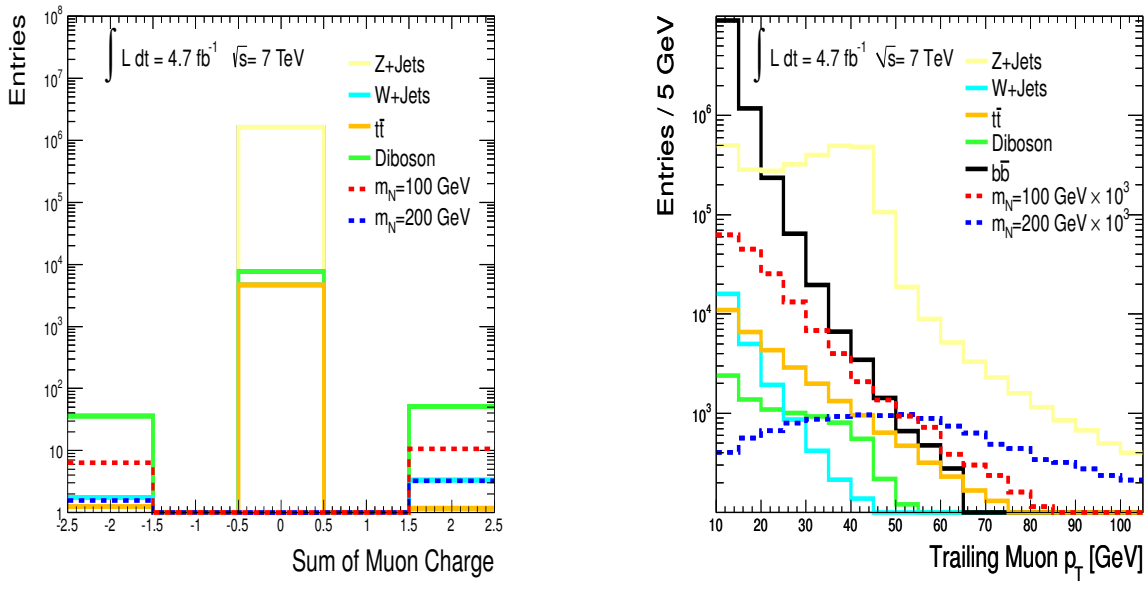

(a) (b)

Figure 7.2: (a) Sum of muon charge in events with two isolated muon and (b) the trailing muon p_{T} in events with two muons with no p_{T} requirement.

Additional Muons

A dominant source of backgrounds are events from $WZ \to \mu^{\pm}\mu^{\mp}\nu\mu^{\pm}$ and $ZZ \to \mu^{\pm}\mu^{\mp}\mu^{\pm}\mu^{\mp}$, where one or two of the muons fails the events selection. This is likely to happen in decays of $W\gamma^{*}$, where the muons from γ^{*} are soft and have transverse momentum below 20 GeV (as required in the analysis). To maximise the rejection of these backgrounds a separate muon selection is chosen that has very high efficiency, classified as "Looser" muons in this thesis.

Events are required to contain no additional "Looser" muons. These muon differs from a muon object by the following criteria:

- The muon is of loose quality.
- The muon is not required to pass the isolation.
- The transverse momentum is loosened. The muon must satisfy $p_{\mathrm{T}} > 10$ GeV.

The number of "Looser" muons per event predicted by MC simulation for backgrounds of this analysis are shown in Figure 7.3. The plot shows that the signal events are expected to have only two "Looser" muons per event, while cutting on events with greater than two "Looser" muons should remove 40% of the background.

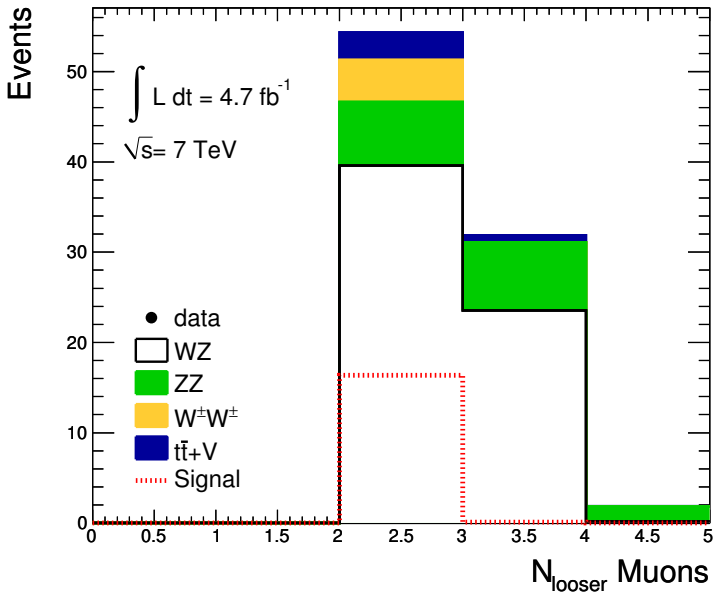

Figure 7.3: The number of looser muons per event in MC simulation for same-sign backgrounds.

Low Missing Transverse Energy

Signal events have no intrinsic $E_{\mathrm{T}}^{\mathrm{miss}}$. Requiring events to have low $E_{\mathrm{T}}^{\mathrm{miss}}$ reduces backgrounds containing $W \to \mu\nu$ decays and backgrounds with semi-leptonic top quark decays, as seen in Figure 7.4(a). The selection was optimised using a sliding cut on both signal and background estimates in order to optimise the signal significance defined as $s/\sqrt{s+b}$. The optimisation of the $E_{\mathrm{T}}^{\mathrm{miss}}$ requirement is shown in Figure 7.4 for three separate signal mass points. Requiring events to have $E_{\mathrm{T}}^{\mathrm{miss}} < 35$ GeV was optimal for this analysis.

W Boson Mass Window

Since the signal process is expected to have a peak in the dijet mass spectrum around m_{W}, the invariant mass of the two leading jets are required to be within a mass window centred around $m(\mathrm{jj}) = 80.4$ GeV. Figure 7.5(a) shows this is a good discriminator against diboson and backgrounds containing leptonically decaying top pairs. Similar to the $E_{\mathrm{T}}^{\mathrm{miss}}$ selection, the window was optimised by maximising the signal significance. Both window window edges were allowed to slide independently, with the signal significance shown in Figure 7.5. The selection is found to be optimal using a lower window edge between 50 and 70 GeV and an upper window edge between 90 and 120 GeV. A window of $55 < m(\mathrm{jj}) < 120$ GeV is used to select events containing $W \to jj$.

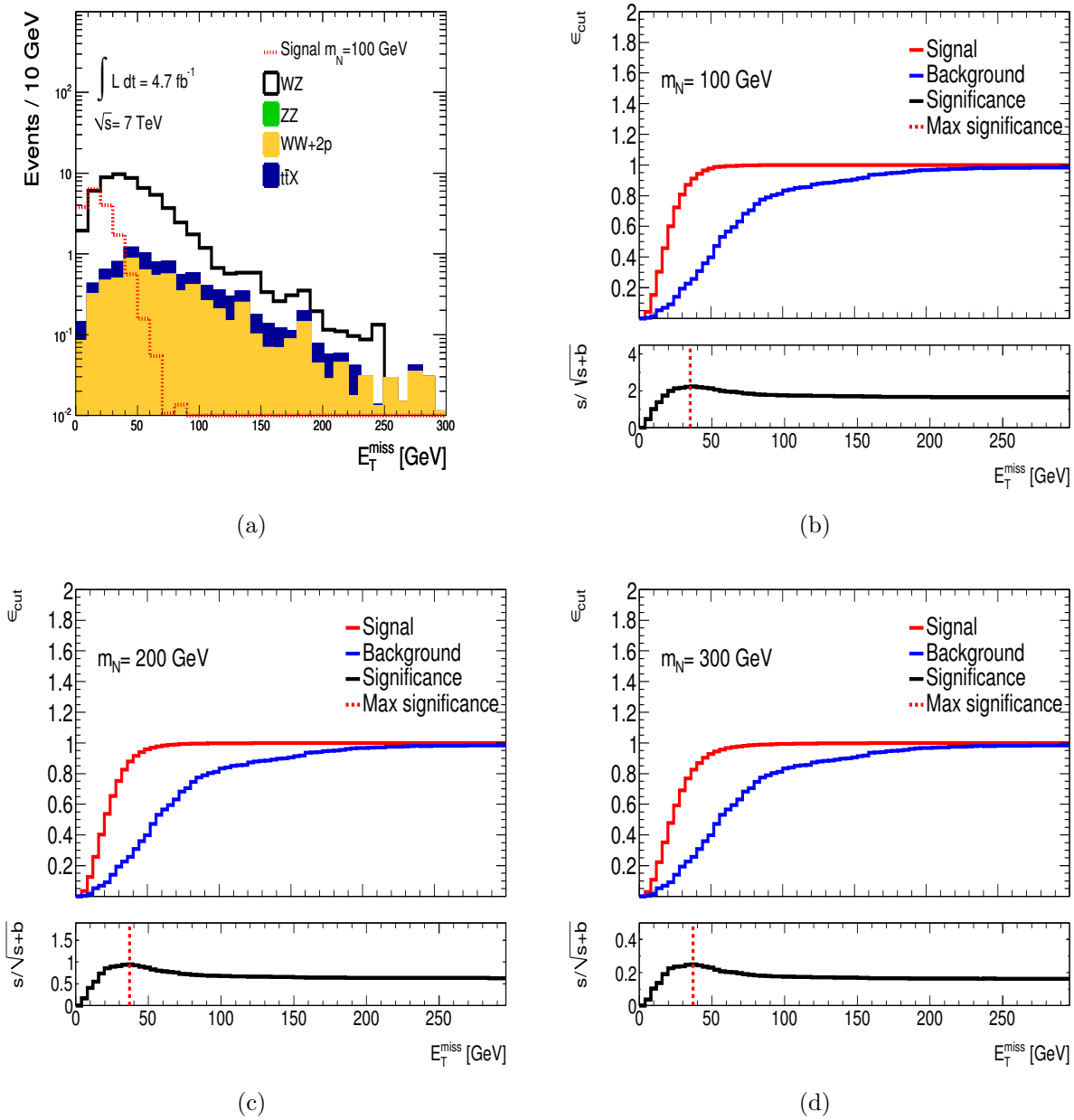

Figure 7.4: Distribution of (a) $E_{\mathrm{T}}^{\mathrm{miss}}$, plus the significance of signal to background as a function of the cut made on the $E_{\mathrm{T}}^{\mathrm{miss}}$ for three mass points (b) 100 GeV, (c) 200 GeV and (d) 300 GeV respectively using expected background in signal region in 4.7 fb^{-1} of data.

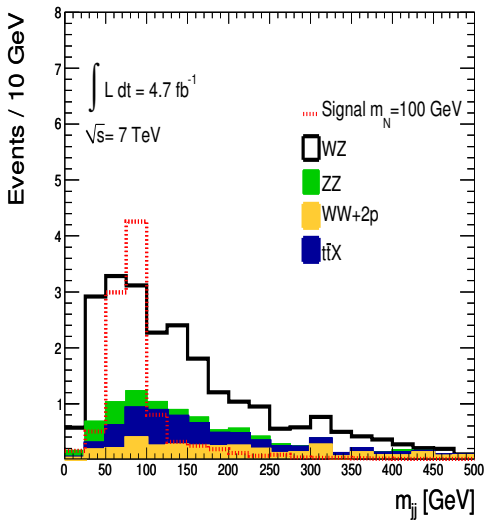

(a)

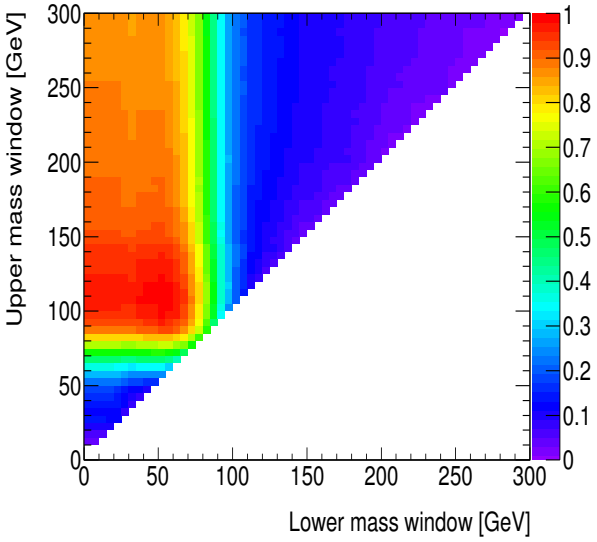

(b)

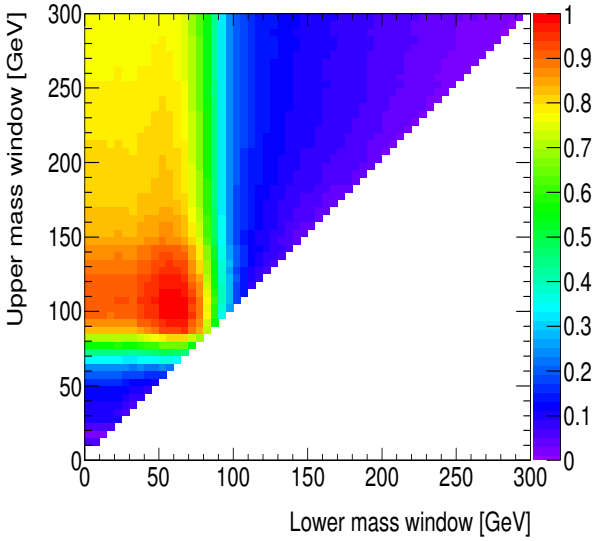

(c)

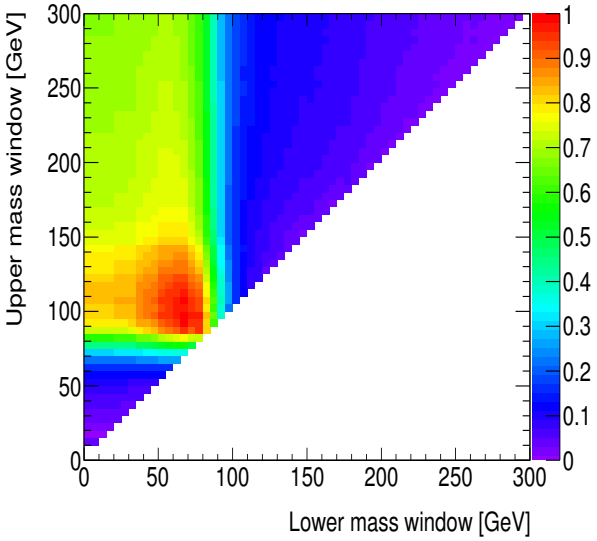

(d)

Figure 7.5: Distribution of (a) the invariant mass of the leading two jets in same-sign dimuon background events in signal and background MC simulation. The significance of signal to background as a function of a cut on the invariant mass of the reconstructed W for m_{N} of (b) 100 GeV, (c) 200 GeV and (d) 300 GeV, using expected background in signal region in 4.7 fb^{-1} of data.

7.3 Signal Acceptance

The efficiency for signal events to pass the event selection is shown Table 7.3 and illustrated in Figure 7.6. The efficiency is broken down further in Figure 7.7. The order of selection requirements applied is; trigger, two muons, isolation requirement, two or more jets, $E_{\mathrm{T}}^{\mathrm{miss}} <$ 35 GeV and $50 < m_{\mathrm{jj}} < 120$ GeV. The efficiencies shown in Figure 7.7 are all relative to the previous selection requirement. The signal efficiency for heavy neutrino masses below 120 GeV is dominated by the requirement of two same-sign muons and the p_{T} requirement on the two muons. This efficiency rises as the neutrino mass increases and plateaus off at mass above 250 GeV. This can be seen in Figure 7.7(b). The trigger and isolation criteria have a similar dependence on the neutrino mass as shown in Figures 7.7(a) and 7.7(c). Figure 7.7(e) and 7.7(f) show the efficiency for signal events to pass the W window and $E_{\mathrm{T}}^{\mathrm{miss}}$ criteria have little mass dependence.

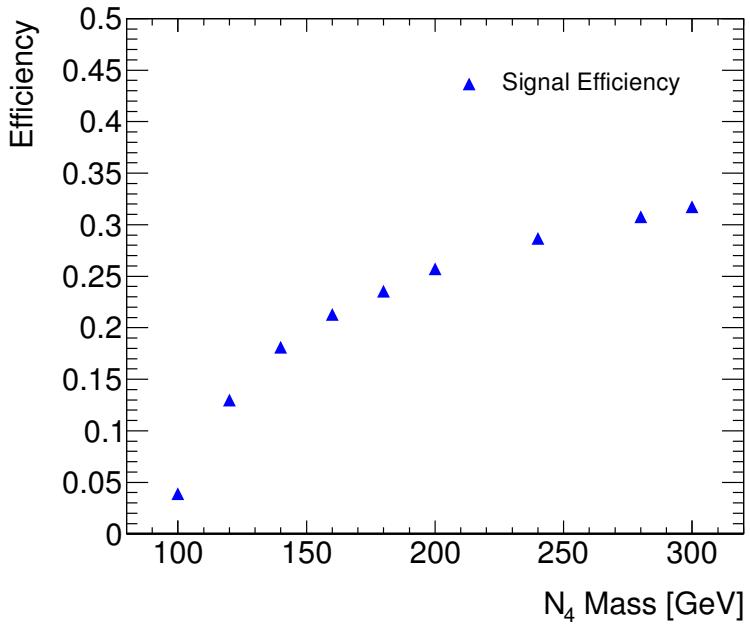

Figure 7.6: Efficiency for signal events to pass the event selection as a function of the heavy neutrino mass.

m_{N} [GeV]	100	120	140	160	180	200	240	280	300
Overall Efficiency	3.9%	13.0%	18.1%	21.3%	23.9%	25.7%	28.7%	30.8%	31.7%

Table 7.3: Efficiency of signal events expected to pass all analysis cut.

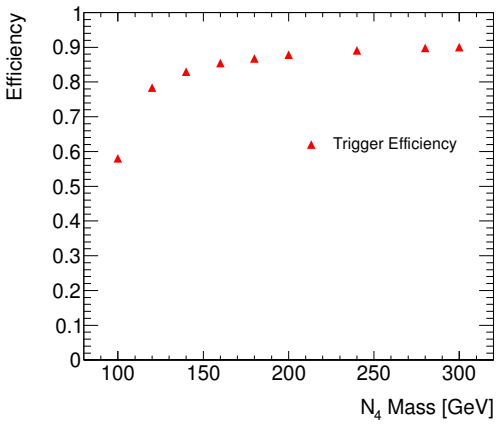

(a)

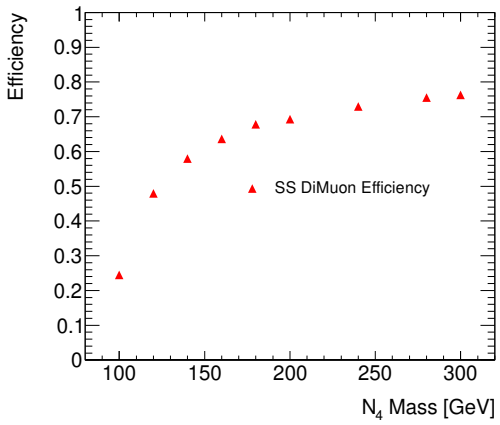

(b)

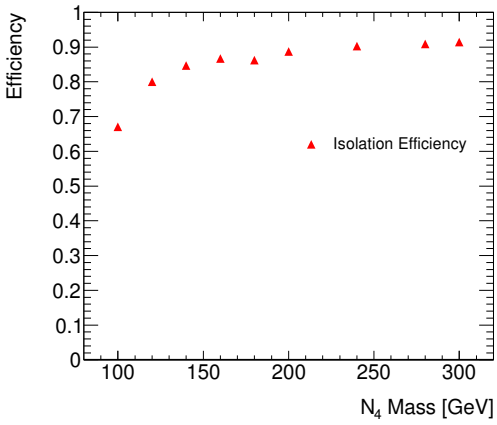

(c)

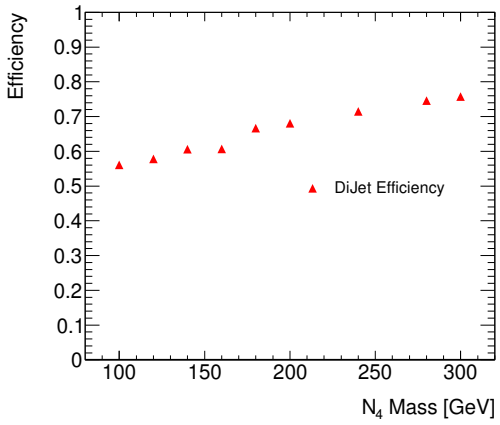

(d)

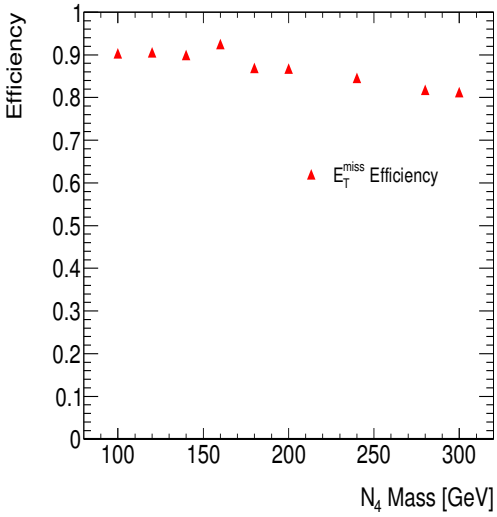

(e)

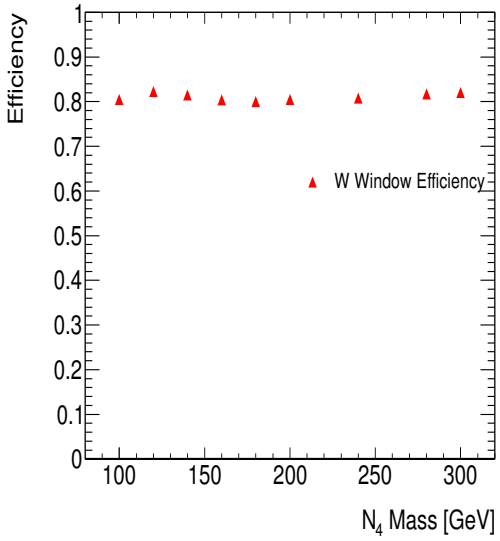

(f)

Figure 7.7: Efficiency for signal events to pass (a) trigger selection, (b) contain two same-sign muons, (c) pass the isolation criteria, (d) contain two or more jets, (e) pass $E_{\mathrm{T}}^{\mathrm{miss}}$ cut and (f) have invariant mass of two leading jets in the W window, as a function of neutrino mass.

Chapter 8

Corrections to Monte Carlo Simulation

The simulation of signal and background processes cannot be expected to fully describe the data. The MC simulations used in this thesis were produced to best reflect the online data taking conditions. However inefficiencies in the hardware or changes in the pile-up conditions can lead to the inaccurate modelling of the data. This section outlines the corrections applied to MC to account for these issues.

8.1 Muon Efficiency Corrections

The efficiency of the reconstruction, identification and trigger selection for muon in MC events are compared to data. Corrections are applied by measuring the efficiencies in data and MC using the tag-and-probe method.

8.1.1 The Tag-and-Probe Method

The tag-and-probe method is used to measure muon efficiencies. As illustrated in Figure 8.1 it makes use of the leptonic decay of the Z boson, $pp \to Z \to \mu^+\mu^-$. This process has a large cross-section, so a pure sample of events can be selected. Since these events have two leptons in the final state one lepton can be used to tag the event, while the second can be used to probe the efficiency.

Events are selected with two leptons of opposite charge with an invariant mass within a predefined window around the Z mass. One of the leptons is then required to pass strict selection criteria. This lepton is then referred to as the *tag* lepton. The number of events that contain at least one tag lepton is n_{T}. The second lepton is then referred to as the *probe* lepton as it is used to probe the efficiency. The efficiency is calculated by counting

the number of probe leptons that pass the selection requirement. The number of events that contain a probe lepton that passes the selection is n_{p}. Since in the case that the probe passes the selection, it is also considered as a tag, and so the efficiency ϵ, is then given by

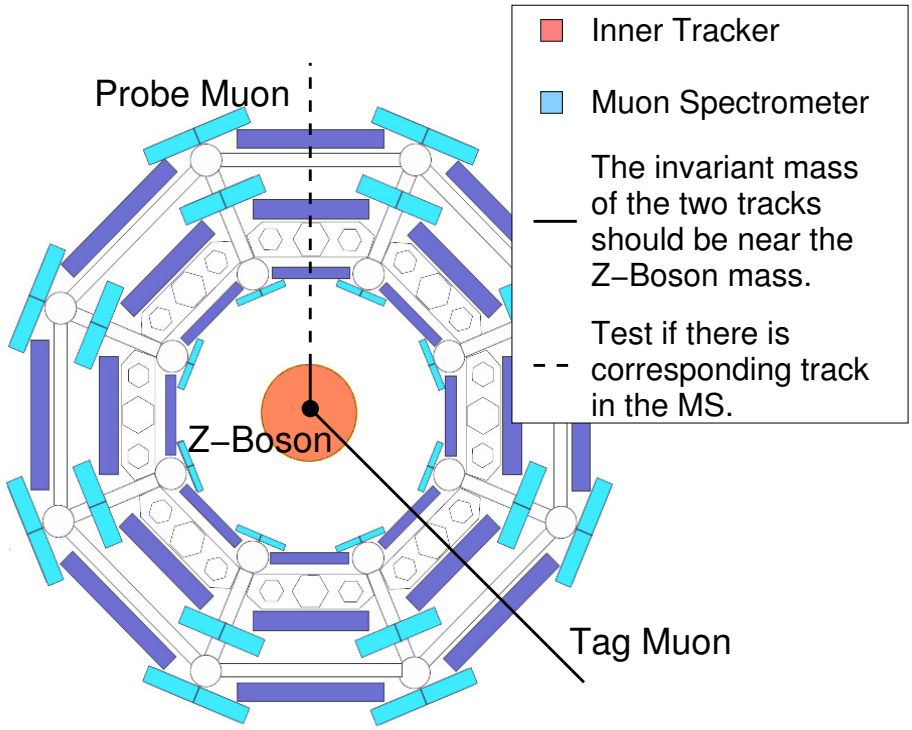

Figure 8.1: Illustration of the Tag-and-Probe method as used in the ATLAS detector.

$$\epsilon = \frac{2n_{\mathrm{p}}}{n_{\mathrm{p}} + n_{\mathrm{T}}}. \tag{8.1}$$

The efficiency can be parameterised in terms of the most useful variable (e.g p_{T} or η).

8.1.2 Muon Reconstruction

The Muon Combined Performance group provide scale factors to correct for the deviations in the reconstruction and identification efficiencies of combined-muons. The efficiency of the muon reconstruction is dominated by the detector coverage. The efficiency is measured using the tag-and-probe method. The tag is selected using a muon that passes the muon selection and is required to be matched to a trigger object, while the probe is taken as a charged track measured in the inner detector. The reconstruction efficiency for combined-muons used in this thesis can be seen in Figure 8.2. The efficiency is seen to be flat in p_{T} and η, except for values near $\eta = 0$. Correction factors are applied to the simulation, using the ratio of the efficiencies in data and MC for different geometric and kinematic regions.

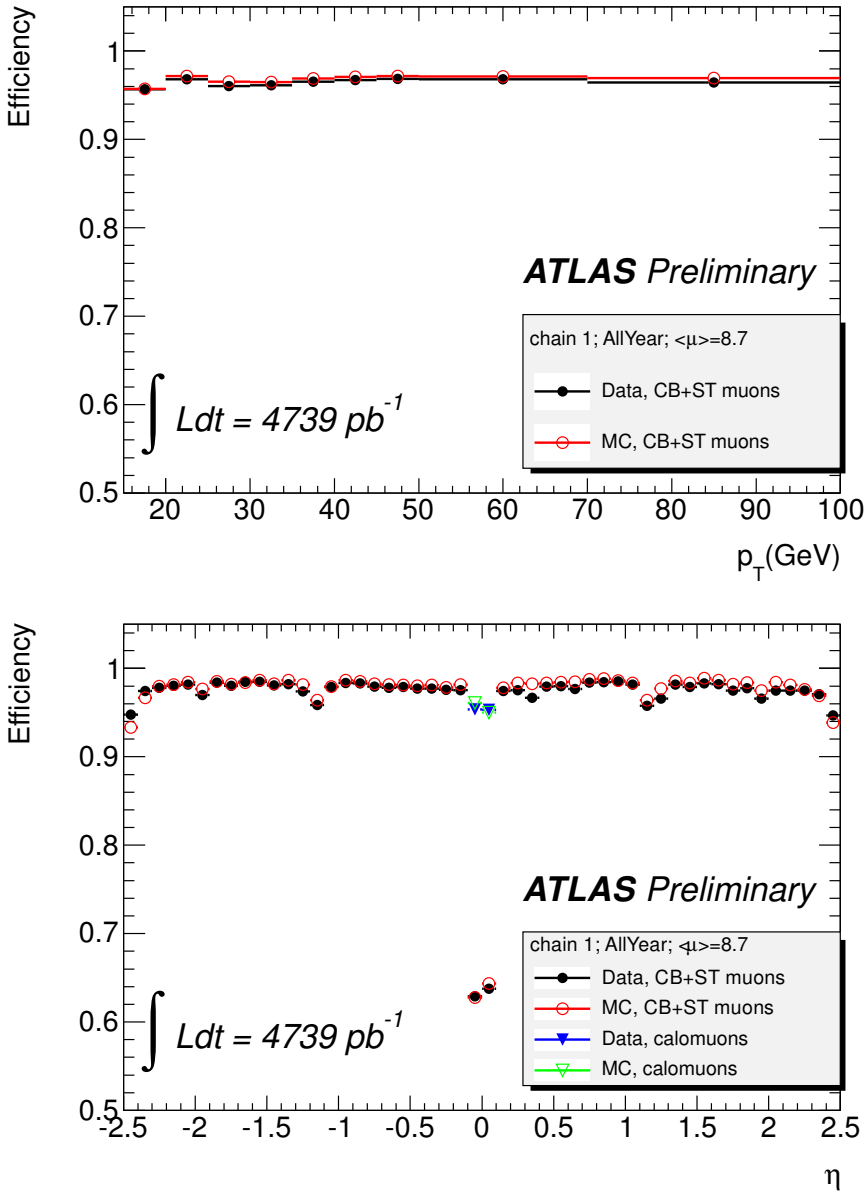

Figure 8.2: Muon reconstruction efficiency as measured with Z boson decays as a function of the pseudo-rapidity of the muon in data taking periods B to M of the 2011 ATLAS data. Chain 1 refers to combined-muons used in this thesis.

8.1.3 Muon Identification

For muon used in this thesis, several additional selection requirements are applied on top of standard combined-muons including:

- $Q_{ID} == Q_{MS}$.
- Isolation requirement on muons.
- Impact parameter requirements: $|d_0| < 0.2\,\text{mm}$, $|z_0| < 5\,\text{mm}$ and $|d_0/\sigma(d_0)| < 3$.
- Muons must originate from same vertex.

Events are selected using two opposite charged combined-muons with $p_{\text{T}} > 20$, $|\eta| < 2.5$ and having passed the ID hit requirements only. The invariant mass of the two opposite charged muons is required to be within 10 GeV of the Z mass. A tagged muon is chosen that passes all the additional selection cuts, and the other probe muon is used to measure the efficiency of the requirements.

Figure 8.3 show the measured isolation efficiencies as a function of muon p_{T}, η and number of primary vertices. The ratio of the data and MC as a function of muon p_{T} for events with different numbers of additional jets are shown in Figure 8.4. The overall scale factor is found to be 0.998, which is sufficiently close to one to neglect this correction factor. Since a small dependence on muon p_{T} and $n(\text{jets})$ is observed, an uncertainty of $^{-1.4}_{+2.4}\%$ is assigned to account for these variations.

Both muons passing the baseline selection criteria have to share the same primary vertex. This requirement reflects the signature of signal events and provides an additional background suppression. Scale factors for Data/MC are measured using events with two opposite signed muons with that have an invariant mass around the Z peak, $80 < M_{\mu\mu} < 100$ GeV. The measured efficiencies and scale factors are shown as a function of p_{T}, number of jets and number of reconstructed vertices in Figure 8.5, with the estimated scale factor for the common primary vertex requirement consistent with one.

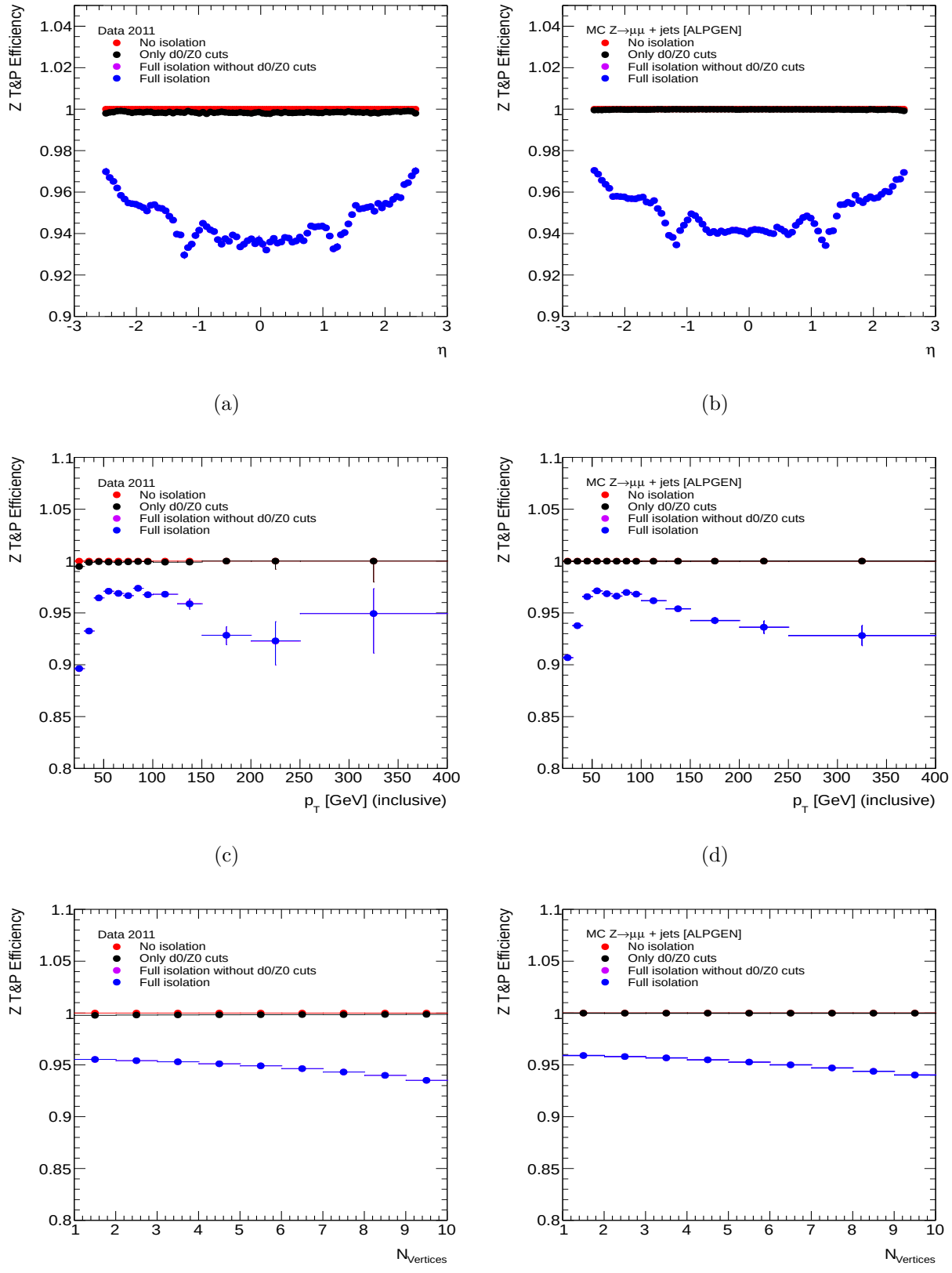

Figure 8.3: Muon isolation efficiencies for (left) data and (right) MC as a function of the muon η, muon p_{T} and the number of primary vertices. The histogram labelled "Full isolation" includes the impact parameter selection criteria.

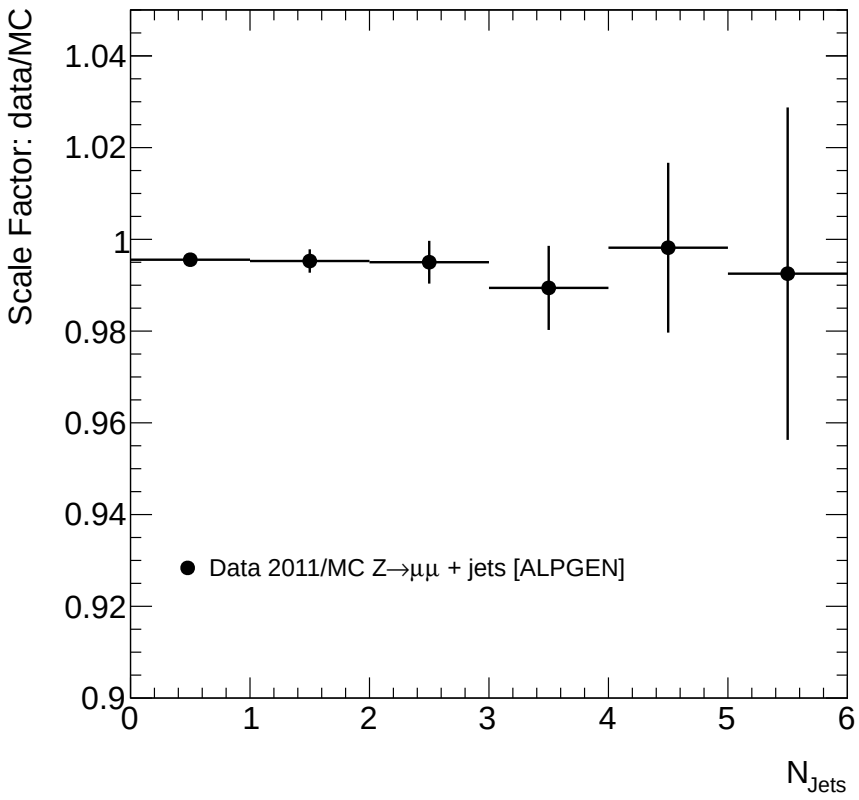

Figure 8.4: Muon isolation efficiency scale factor between data and MC as a function of jet multiplicity.

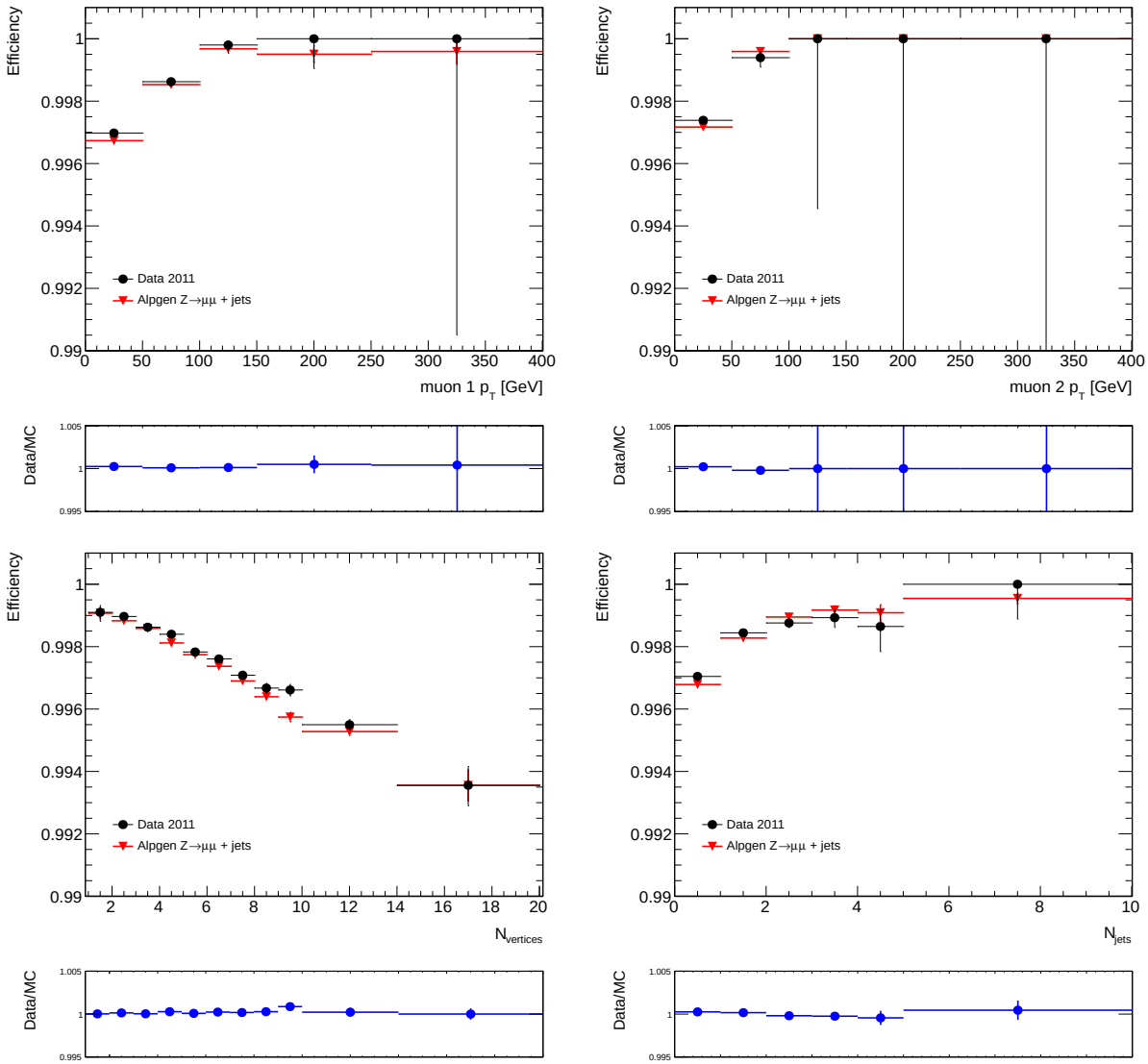

Figure 8.5: Selection efficiency and Data/MC scale factors for the common primary vertex requirement for two selected muons, for transverse momentum of the leading muon (top left), transverse momentum of the trailing muon (top right), number of jets (bottom left) and number of primary vertices (bottom right).

The mass-drop variable used in the isolation for muons close to jets is shown for muons with $p_{\mathrm{T}}^{\mu} > 80$ GeV between events in a Z dominated sample from data and Z MC simulation in Figure 8.6. The variable peaks at low values which is expected for non boosted events. The MC simulation models this variable well.

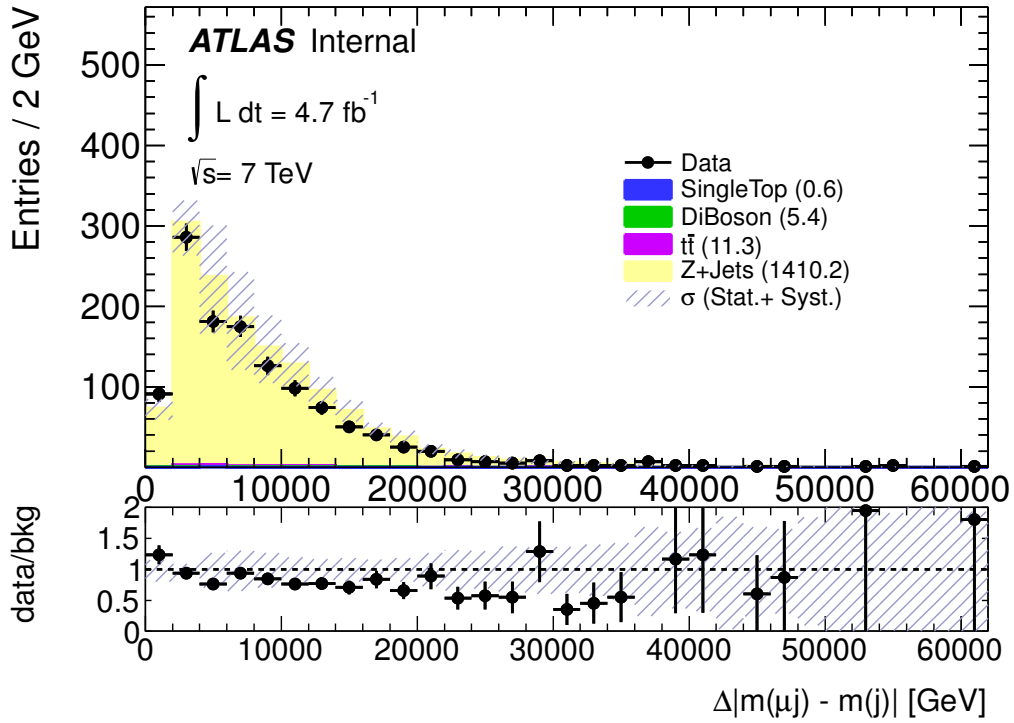

Figure 8.6: Distributions of mass-drop in Z window for MC and data for muons with $p_{\mathrm{T}}^{\mu} > 80$ GeV and with $\Delta R(\mu, j) < 0.4$.

8.1.4 Muon Momentum Resolution

The muon momentum resolution of the muon spectrometer is discussed in Section 3.5. combined-muons rely on the presence of a reconstructed track in the ID and MS detectors, which are combined to form a single trajectory. This improves the resolution of the muon spectrometer or inner detector alone. Due to the detector coverage there are four distinct η regions in which we expect to see a difference in the momentum resolutions:

- Barrel - covering $0 < |\eta| < 1.05$,
- Transition region - covering $1.05 < |\eta| < 1.7$,
- End-caps - covering $1.7 < |\eta| < 2.0$,
- Barrel - covering $2.0 < |\eta| < 1.5$.

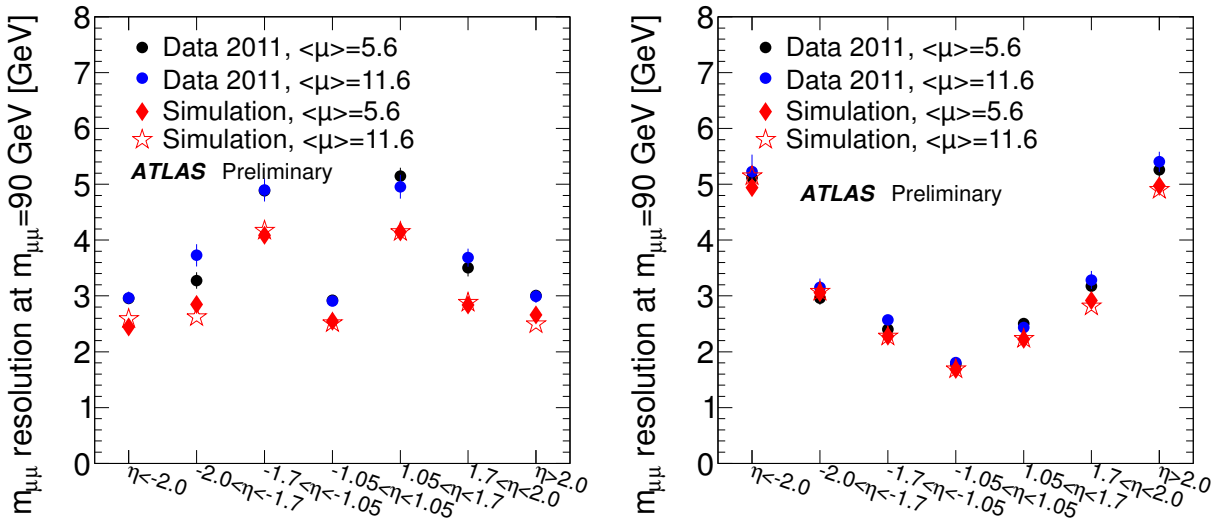

(a) (b)

Figure 8.7: Resolution contribution $\sigma(M)$ to the relative di-muon invariant mass width in data (circles) and simulation (open triangles) as a function of track η region, for (a) the Muon Spectrometer part and (b) the Inner Detector part of combined muon pairs.

The momentum resolution in data and simulation is measured separately for each of these η regions (Figure 8.7), using a fit to the di-muon invariant mass distributions that are obtained separately from ID and MS track parameters, where events are selected specifying that both muons are found in the same η region. Discrepancies between the simulation and data is seen in all η bins. This is understood as a limited understanding of the calibration and alignment constants of the two detectors, prior to the reconstruction. An additional uncertainty is present in the MS resolution related to the material distribution and the knowledge of the toroidal magnetic fields. Using the measured resolutions, corrections to the muon track momentum are derived and applied at the analysis level. Figure 8.8 shows that good agreement in the resolution for combined tracks between data and simulation is achieved, after the corrections are applied.

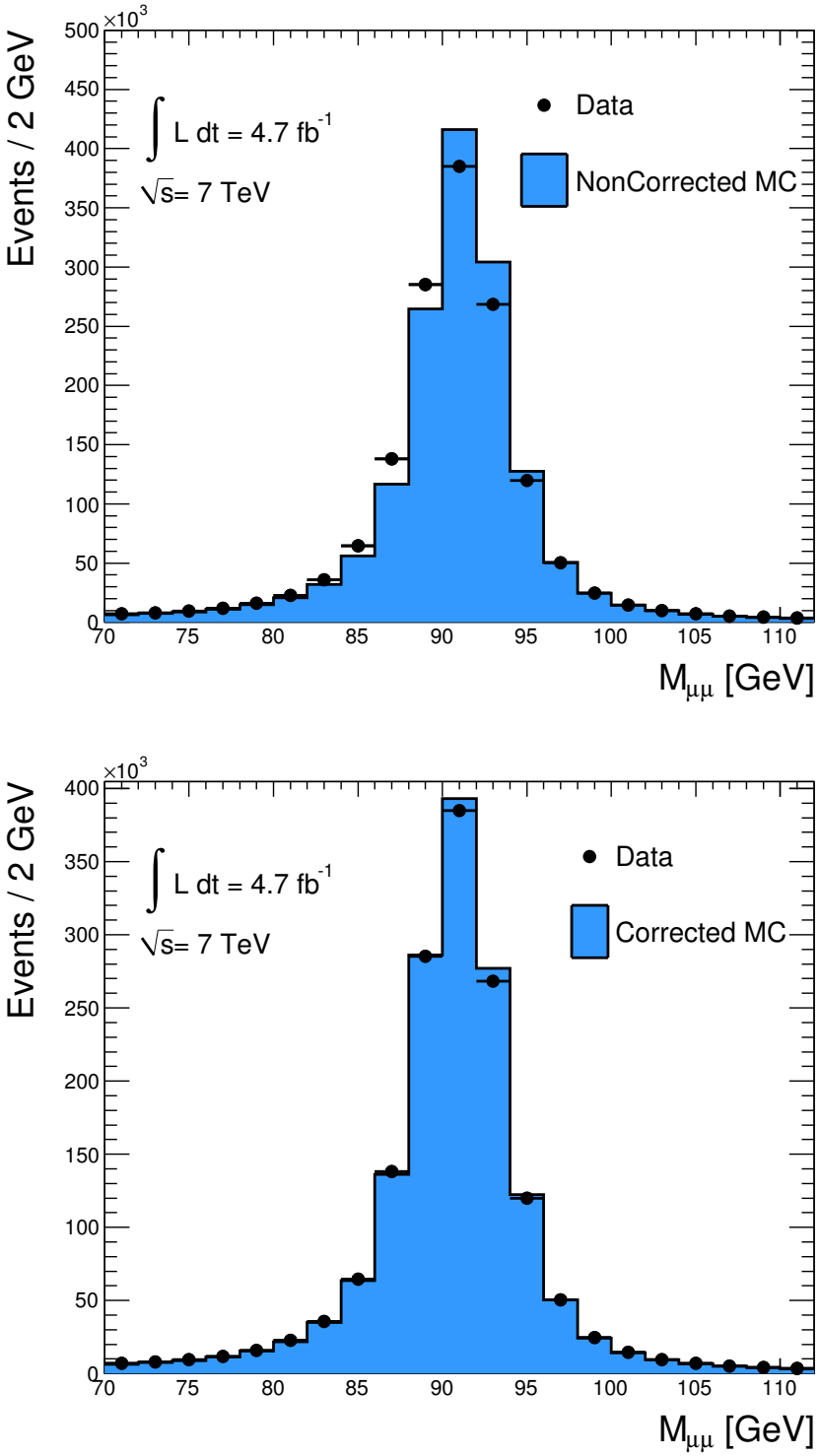

Figure 8.8: Di-muon invariant mass comparison in the Z boson mass range between collision data (dots) and simulation (full histogram). The distribution is shown for combined-muons and is integrated over the full range of η

Barrel	Data	MC	SF
B-I	$85.00 \pm 0.07\%$	$82.43 \pm 0.14\%$	1.031 ± 0.002
J-M wo l3,L4	$77.77 \pm 0.06\%$	$78.91 \pm 0.15\%$	0.986 ± 0.002
L3,L4	$61.87 \pm 0.17\%$	$78.43 \pm 0.15\%$	0.784 ± 0.003

Table 8.1: Trigger efficiencies in the barrel for data and MC as measured by the ATLAS trigger group, with the assigned scale factors. Period B-I correspond to EF_mu18_MG and J-K corresponds to EF_mu18_MG_medium.

Endcap	Data Efficiency	MC Efficiency	Scale Factor
B-I	$86.13 \pm 0.07\%$	$86.68 \pm 0.14\%$	1.017 ± 0.002
J-M wo l3,L4	$85.58 \pm 0.06\%$	$84.63 \pm 0.15\%$	1.011 ± 0.002
L3,L4	$85.48 \pm 0.13\%$	$84.63 \pm 0.15\%$	1.010 ± 0.002

Table 8.2: Trigger efficiencies in the end-cap for data and MC as measured by the ATLAS trigger group, with the assigned scale factors. Period B-I correspond to EF_mu18_MG and J-K corresponds to EF_mu18_MG_medium.

8.2 Trigger Efficiencies

The trigger system is used by ATLAS to select events of interest. The trigger is simulated in the MC, however the efficiency seen in the simulation usually differs from that seen in the data. It is therefore necessary to correct the MC simulation for the triggers used in physics analyses. To select events used in this thesis the primary single muon trigger with the lowest p_{T} threshold was used. The trigger varied during the 2011 running due to the increase in the luminosity and the need for a steady trigger rate. The event triggers used for each run period in the 2011 are

- Runs 177986-184169: EF_mu18_MG.
- Runs 186516-191933: EF_mu18_MG_medium.

As seen in Table 5.1 the MC samples have been simulated with four periods, each of which represents different detector/operational conditions for portions of the 2011 data sample. The different MC periods use the same triggers used online to trigger the events in our dataset. Trigger efficiencies in MC and data are measured by the muon combined performance group. The efficiencies can be seen in Table 8.1 for the barrel and Table 8.2 for the end-cap. Single muon Scale Factors (SFs) are taken by the ratio of the efficiencies in data and simulation. Event level Scale Factors ($\mathrm{SF}_{\mathrm{event}}$) are applied to correctly account for differences between the trigger rates in data and the rates modelled in simulation using

$$\mathrm{SF}_{\mathrm{event}} = \frac{1 - (1 - SF_1 \times \epsilon_{\mathrm{MC}_1})(1 - SF_2 \times \epsilon_{\mathrm{MC}_2})}{1 - (1 - \epsilon_{\mathrm{MC}_1})(1 - \epsilon_{\mathrm{MC}_2})} \tag{8.2}$$

, where ϵ_{MC_i} and SF_i are the single muon efficiencies and scale factors in Monte Carlo for the i^{th} muon in the event. The importance of these scale factors can be seen in the muon triggers for period L3 and L4 where the data efficiency was reduced by 17% due to problems with the RPC detectors in the muon spectrometer. This effect is not simulated in the MC.

The change in the muon trigger efficiency seen in Table 8.1 for the step between EF_mu18_MG and EF_mu18_MG_medium at the end of period I was due to the requirement of a three muon trigger station coincidence in EF_mu18_MG_medium, compared to two in the EF_mu18_MG, and was needed to maintain an acceptable LVL1 trigger rate. This change results in a loss of trigger efficiency for the muons in the barrel of the detector by $5 - 10\%$, which is modelled in the MC.

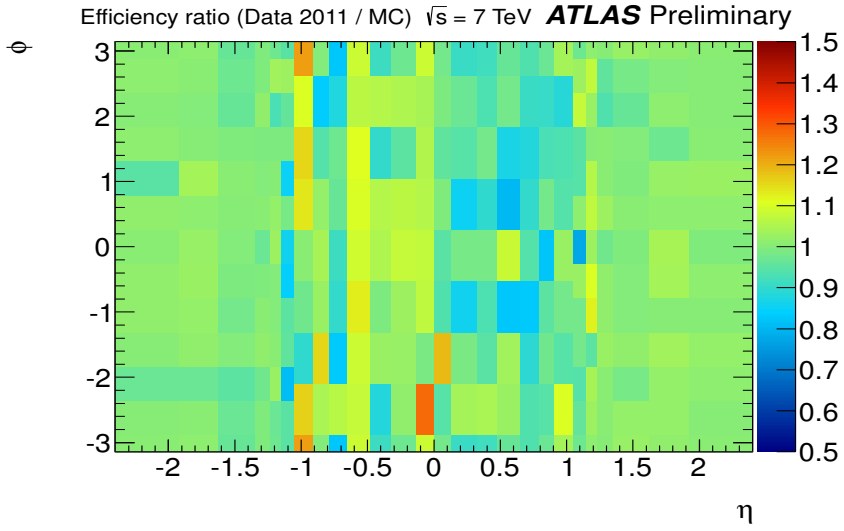

Figure 8.9: The $\eta - \phi$ dependence of the efficiency ratios between data and MC for the mu18_medium trigger with inner detector track based algorithm at EF.

8.3 Pile-up Corrections

For the 2011 data taking, the bunches in the LHC are grouped in bunch trains with an in-train bunch separation of 50 ns. Due to this configuration, out-of-time pile-up from overlapping signals from different bunch crossings plays an important role. In order to emulate the pile-up appropriately, the average number of interactions per luminosity block and bunch crossing, $\langle\mu\rangle$, is used. Monte Carlo samples have been generated with a nominal distribution of $\langle\mu\rangle$ and therefore need to be re weighted to correspond to the observed $\langle\mu\rangle$ in the data. Figure 8.10 shows the distribution of $\langle\mu\rangle$ in MC before and after applying the reweighting as well as $\langle\mu\rangle$ in the full dataset. The corrected distribution agrees well with the data.

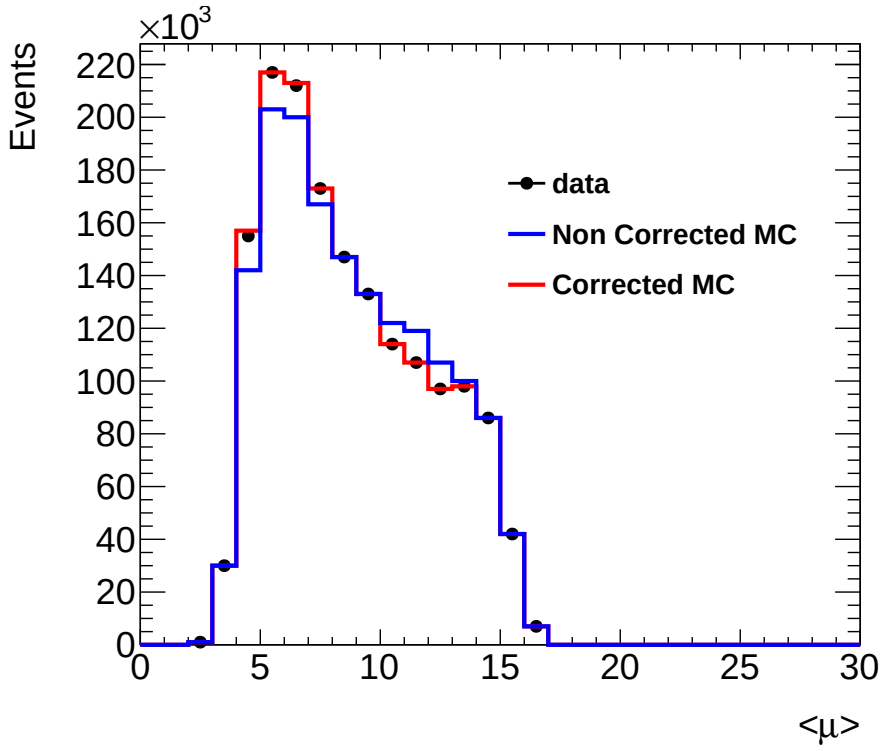

(a)

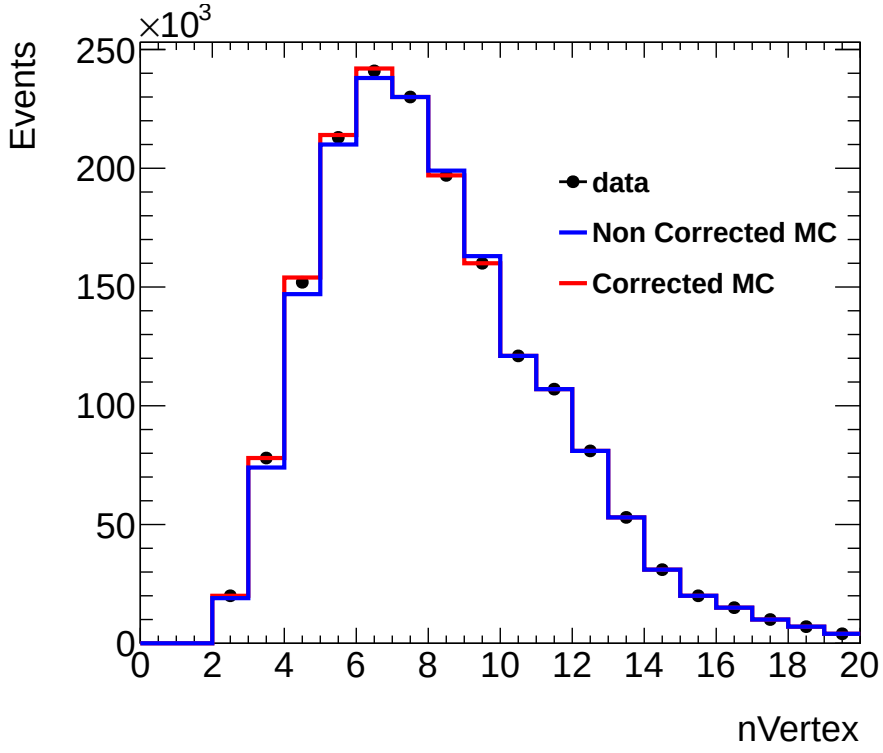

(b)

Figure 8.10: Distribution in data and MC, before and after re-weighting for (a) $\langle\mu\rangle$ and (b) number of good vertices in the event.

Chapter 9

Background Estimation

There are very few processes in the SM that can produce two same-sign muons. Of these processes we can sub-divide them up into three categories. The first category are processes which contain two prompt muons, where prompt means that the muon has decayed from either a W or Z boson or from a τ decay from a W or Z decay. The second include processes where at least one muon is non-prompt, these are typically muons from b hadrons or light meson decays. The final category are processes that produce two opposite sign prompt muons where one of the two muons has its charge incorrectly measured. The contribution from same-sign prompt muons are estimated using MC and validated in a control region in the data. The non-prompt backgrounds are estimated using a data driven technique, and validated using different control regions. The rate of charge mis-identification is measured in the data and is used in concert with the MC to estimate the background from charge mis-identification. The methods used to estimate the contributions of these backgrounds are described below in detail.

9.1 Backgrounds from Prompt Muons

The dominant SM background containing two prompt muons with equal charge comes from the diboson production processes WZ and ZZ. Other rare SM processes which become important when requiring jets include $W^{\pm}W^{\pm}jj \rightarrow \mu^{\pm}\mu^{\pm}\nu\nu jj$ and $t\bar{t}$ production in association with either a W or Z boson.

The backgrounds from diboson production with leptonic decays are estimated using samples generated with Sherpa. These processes can result in same-sign di-muon events in two ways. The first case is where both bosons decay into muons, $WZ \rightarrow \mu\nu\mu\mu$ and $ZZ \rightarrow \mu\mu\mu\mu$, and one or two muons are outside the detector acceptance or fail the muon object selection. The second case involves the τ decays of the Z boson such as $WZ \rightarrow \mu^{\pm}\nu\tau^{\pm}\tau^{\mp}$ where the τ with the same-sign charge to the muon decays leptonically and the second tau decays

into hadrons. The SHERPA samples, described in section 5.5, are used as they contain both additional jets in the matrix element and the contributions from virtual photons (γ^*). The prediction of these samples is validated in the data in a control region of three or more muons as described in section 10.

Backgrounds from triple vector boson production with leptonic decays are also possible. The NLO cross sections for the leptonic decays of ZZZ, WWZ and WWW have been recently calculated [109] [110] with cross sections orders of magnitude smaller than diboson production. These processes are considered negligible due to the small production rate.

Contribution from γ^* in same-sign events

The relative contribution of events from $W\gamma^*$ and WZ in the signal region was compared in events from the SHERPA MC generator. Events with $WZ(\gamma^*) \to e\nu_e\mu^{\pm}\mu^{\mp}$ were selected by requiring one isolated electron and two opposite sign muons in the sample. The was done to remove any ambiguity in the selection of the opposite sign muon pair from the Z with the muon from the W. For this study on-shell Z production is considered if the invariant mass of the two muons are within the mass window 81-101 GeV. The fraction of events in this sample that contained an on-shell Z boson is 92%. This is repeated but now requiring the muons to pass the object selection and selecting events where only one of the muons passes the selection. In this sample the fraction of events that contain an on-shell Z boson is now 71%. This shows there is a greater contribution of events from $W\gamma^*$ in the signal region. The invariant masses of the two muons in these samples, taken from truth information is shown in Figure 9.1.

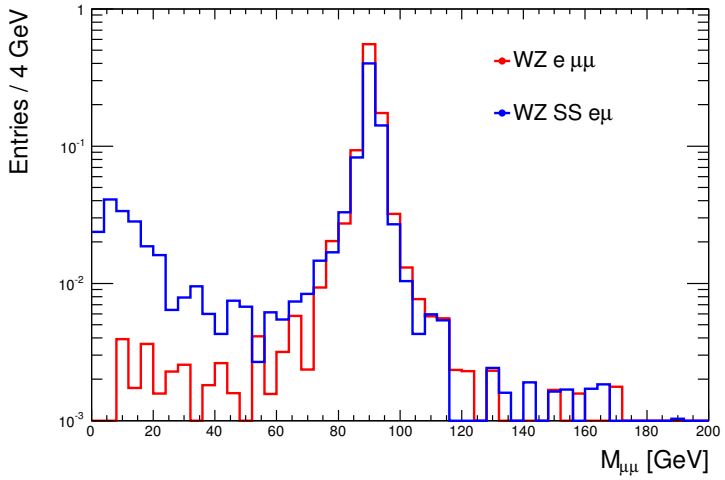

Figure 9.1: Invariant mass of di-muon pair in events with two reconstructed muons and one reconstructed electron passing selection criteria and the case of a same-sign electron muon pair passing the selection criteria. Both histograms are normalised to unity.

Source	Inclusive (SS)	3rd Muon Veto	$n(jet) \geq 2$	$E_{\mathrm{T}}^{\mathrm{miss}}$ Cut	m_W Window
WZ	65 ± 1	40 ± 1	8 ± 1	2.4 ± 0.3	1.0 ± 0.2
ZZ	17 ± 1	7.0 ± 0.3	0.7 ± 0.1	0.5 ± 0.1	0.22 ± 0.05
$W^{\pm}W^{\pm}$+2p	4.8 ± 0.2	4.6 ± 0.2	3.9 ± 0.2	0.7 ± 0.1	0.15 ± 0.04
$Zt\bar{t}, Wt\bar{t}$	4.1 ± 0.2	3.0 ± 0.2	3.0 ± 0.2	0.5 ± 0.1	0.23 ± 0.04
Total	90 ± 2	54 ± 1	16 ± 1	4.0 ± 0.3	1.6 ± 0.2

Table 9.1: Predicted background for events with two same-sign charge muons and observed data for a total integrated luminosity of 4.7 fb^{-1}.

9.1.1 Prompt Background Distributions

The predicted backgrounds for events containing two same-sign muons, normalised to 4.7 fb^{-1} of data are shown in Figure 9.2. All distributions used to discriminate signal and background are shown. As seen in Figure 9.2(d) the backgrounds with low jet multiplicity are almost entirely from diboson decays, while backgrounds with associated top pair production contribute more in events with two or more jets. The $E_{\mathrm{T}}^{\mathrm{miss}}$ distribution shown in Figure 9.2(c) peaks at about 30 GeV. Processes that produce $t\bar{t}$ pairs are found mostly in the upper tail of the $E_{\mathrm{T}}^{\mathrm{miss}}$ distribution, due to the neutrinos in the final state, while backgrounds with no neutrinos in the final state such as fully leptonic ZZ decays have dominantly low $E_{\mathrm{T}}^{\mathrm{miss}}$. The charge of the muon pairs are seen in Figure 9.2(b) to be mostly positive, which is expected with pp collisions. The only contribution with no asymmetry in the charge are backgrounds from ZZ decays, which is expected since the reconstruction or muon selection does not favour either charge. The invariant mass of the two leading jets is shown in Figure 9.3(a) to peak at 50 GeV with a broad tail. The shape is dominated by the WZ background. The jet p_{T} is seen to peak at low low momentum, as expected in processes like leptonic WZ decays, where the jets are produced from initial and final state radiation.

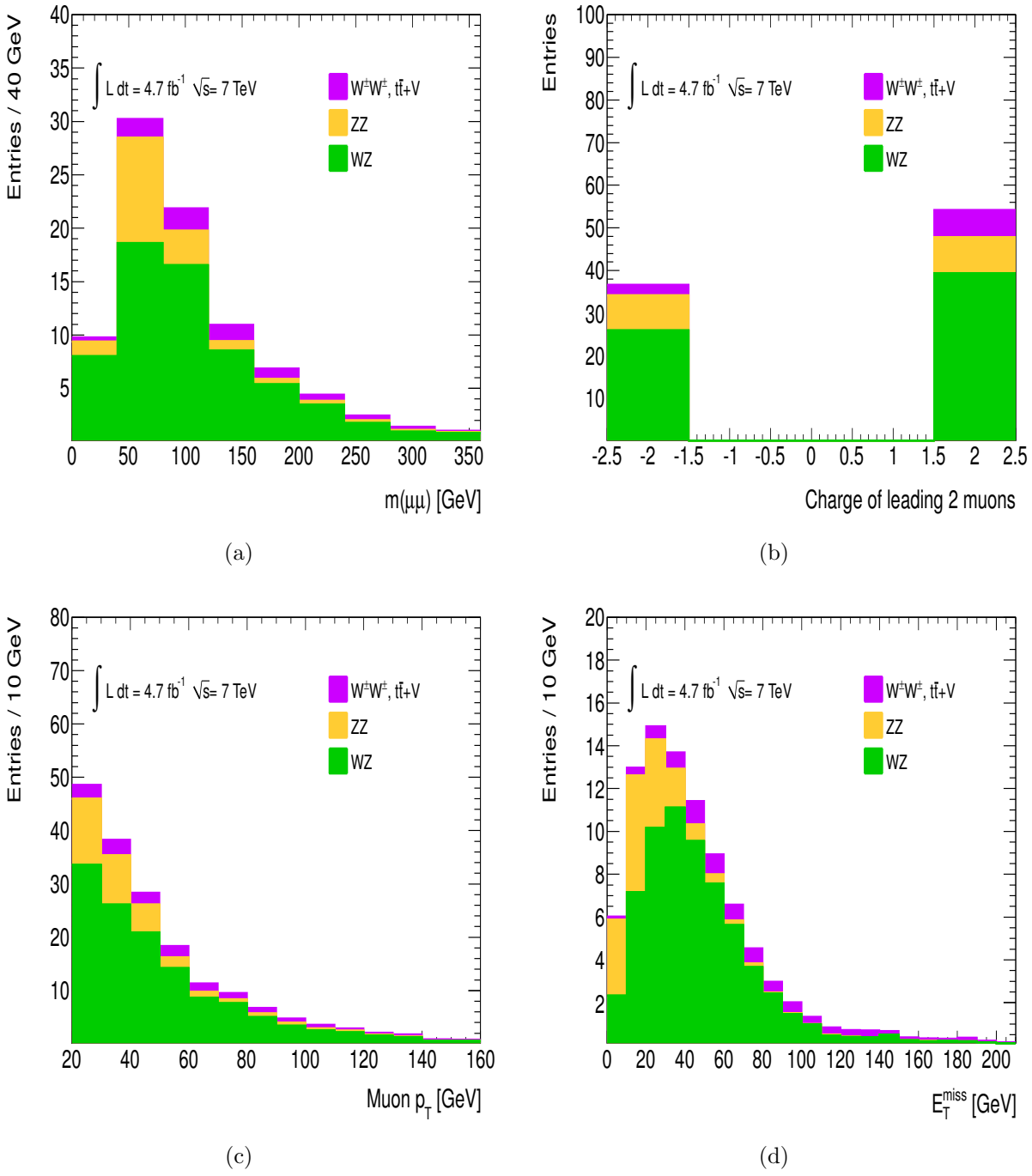

Figure 9.2: Prompt background predictions for events containing same-sign isolated muons normalised to 4.7 fb^{-1}. (a) The invariant mass, (b) the summed charge, (c) the p_{T} of the muons, (d) the missing transverse energy.

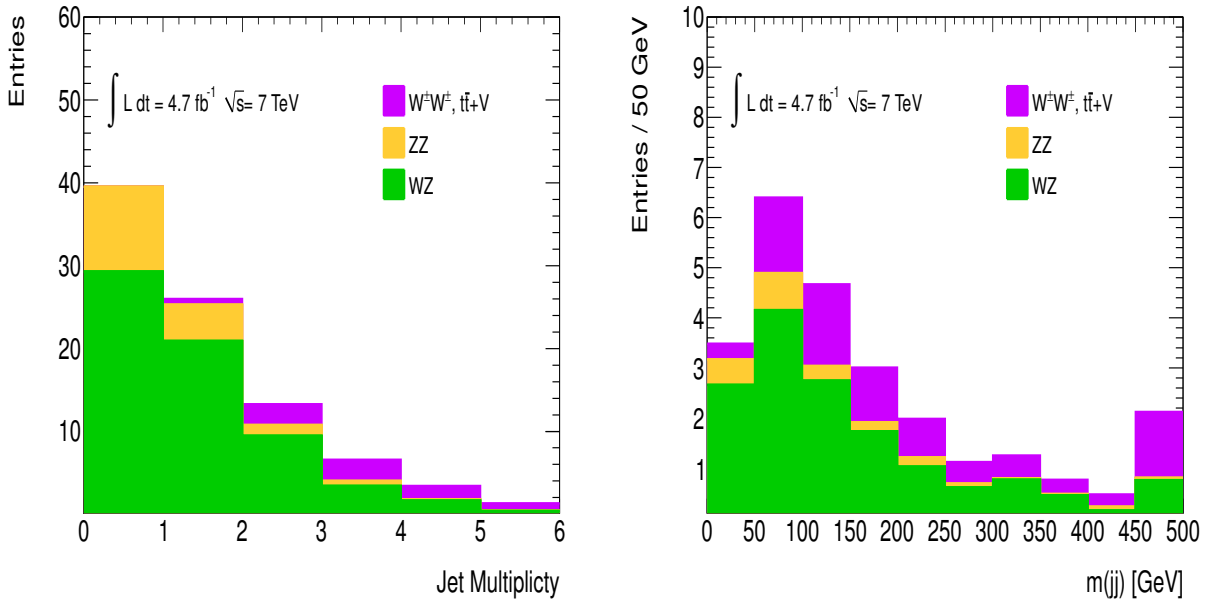

(a)

(b)

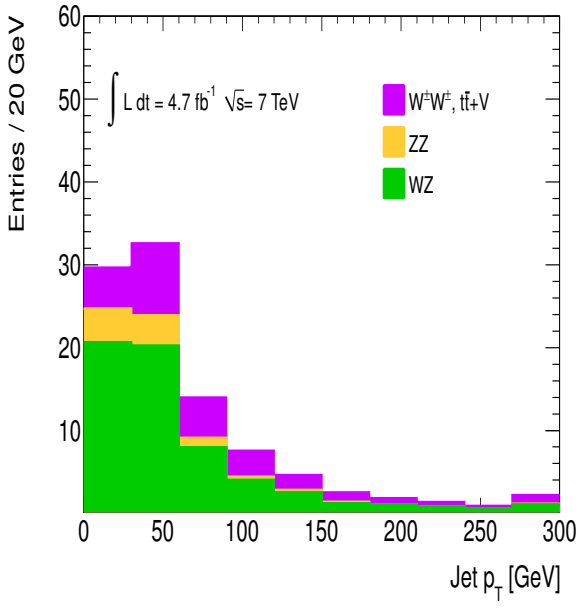

(c)

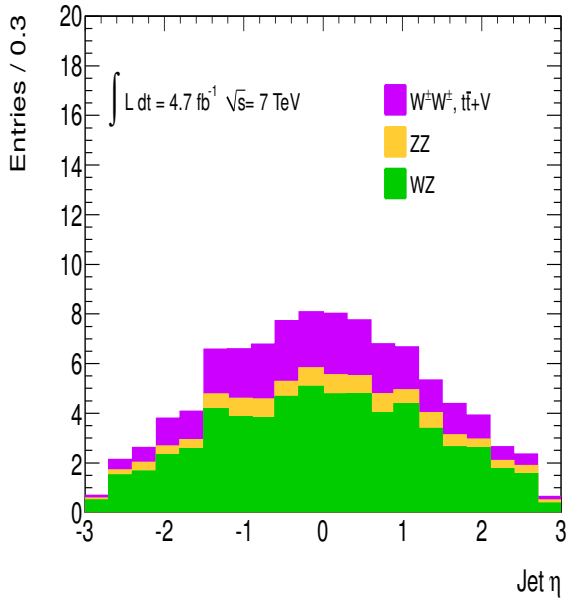

(d)

Figure 9.3: Prompt background predictions for events containing same-sign isolated muons normalised to 4.7 fb^{-1}. (a) The number of jets, (b) the invariant mass of the leading two jets, (c) the jet p_{T} and (d) the η.

9.2 Backgrounds with Non-Prompt Muons

This section describes the method used to estimate the contribution of background events with one or more non-prompt leptons in our signal region. These include muons from:

- semi-leptonic decay of a b or c jet,
- decay-in-flight of a $\pi^{\pm}$ or $K^{\pm}$ meson,
- jets that penetrate the muon system, referred to as punch through jets.

The primary processes containing at least one non-prompt muon are processes where one muon originates from a W or Z boson (which is a prompt muon) and a second muon is non-prompt. This category includes processes such as single vector boson production in association with jets, $t\bar{t}$ and single top production. A smaller contribution arrises when both muons are non-prompt, for example $b\bar{b}$ production. To estimate these backgrounds in the search discussed in this thesis the data-driven matrix method is used.

9.2.1 Overview of the Matrix Method

The matrix method starts with a data sample with looser requirements than the main analysis sample and is referred to as the "loose" sample here. Muons in the loose sample are defined to pass all object cuts used for the analysis muons (as described in section 7.2.1) except the isolation cut is removed and muons that have $p_{\mathrm{T}}^{\mu} < 80$ GeV and $\Delta R(\mu, j) < 0.4$ are removed in order to correctly account for the isolation dependence on $\Delta R(\mu, j)$. The loose sample is required to contain two muons with the veto on a third lepton applied. We then define two types of muons referred to be either "Loose" (L) or "Tight" (T). Here "Tight" refers to a muon in the loose sample that passes the muon isolation requirements, while "Loose" is defined as a muon in the loose sample that fails the isolation requirements. It is therefore possible in this definition that a muon is Tight, but not Loose. The loose sample is then split into four categories (TT, TL, LT and LL) where the first label refers to the type describing the leading muon and the second label refers to the type describing the trailing muon, i.e., a LL event is an event with two Loose muons, while TL refers to an event with two muons where the leading muon is Tight and the trailing muon is Loose. Additional contributions from three muon events such such as TLL and LLT do not contribute as a result of the additional lepton cuts applied.

The matrix shown in equation 9.1 relates the four categories of TT, TL, LT and LL to the true composition of prompt and non-prompt muons (noted as R and F in the matrix). The additional index ll in equation 9.1 refers to pairs of muons in the loose sample. The real efficiency, r, is defined as the probability that a prompt muon in the loose sample passes

the isolation requirements and the fake efficiency, f, is defined as the probability that a non-prompt muon in the loose sample passes the isolation requirements. If the real and fake efficiencies are measured in the data then the matrix can be inverted to give the estimated background in the signal region, $N_b = N_{FF} + N_{RF} + N_{FR}$. These contributions are related to the relative components in the loose sample : by $N_{FF} = f_1 f_2 N^{ll}_{FF}$, $N_{RF} = r_1 f_2 N^{ll}_{RF}$ and $N_{FR} = f_1 r_2 N^{ll}_{FR}$. The measurements of the real and fake efficiencies are discussed in the following two sub-sections.

$$\begin{bmatrix} N_{TT} \\ N_{TL} \\ N_{LT} \\ N_{LL} \end{bmatrix} = \begin{bmatrix} rr & rf & fr & ff \\ r(1-r) & r(1-f) & f(1-r) & f(1-f) \\ (1-r)r & (1-r)f & (1-f)r & (1-f)f \\ (1-r)(1-r) & (1-r)(1-f) & (1-f)(1-r) & (1-f)(1-f) \end{bmatrix} \begin{bmatrix} N^{ll}_{RR} \\ N^{ll}_{RF} \\ N^{ll}_{FR} \\ N^{ll}_{FF} \end{bmatrix} \quad (9.1)$$

9.2.2 Real Efficiencies

To measure the tight lepton efficiency of prompt muons found in the loose sample, a prompt muon control region is defined that is dominated by prompt muons. This prompt muon control region requires events with two muon, where both muons are required to pass the loose requirements, have opposite sign charge and have dilepton mass close to the Z boson mass i.e., $86 < m(\mu\mu) < 96$ GeV. A tag-and-probe method is used to measure the efficiency for these prompt muons to pass the isolation requirements. Tag muons are required to pass the isolation requirements and be matched to the single muon trigger. The events are required to have at least one tag muon and the second (probe) muon is then used to measure the efficiency of the isolation requirements. If both muons pass the tight requirements, then both are considered as tags and so both muons are used to measure the efficiency. For more details on the method see section 8.1.1.

Since the real control region may not be completely representative of the kinematics in the signal sample, the real efficiencies are measured and parameterised in terms of the muon p^{μ}_{T}, η and jet multiplicity in order to eliminate any possible biases. In addition, the dependencies on ϕ_{μ}, $E^{\mathrm{miss}}_{\mathrm{T}}$, $\Delta R(\mu, jet)$ are also checked, where ϕ_{μ} is the azimuthal angle of the muon track and $\Delta R(\mu, jet)$ is the angular separation in η-ϕ space between the muon and closest jet. The largest dependence was seen in p^{μ}_{T}, with an efficiency of 90% at $p^{\mu}_{\mathrm{T}} = 20$ GeV and an efficiency above 99% for $p^{\mu}_{\mathrm{T}} > 80$ GeV, shown in Figure 9.2.2. It was also noted that there was some dependence on the muon η. Muons in the real control region traversing the ATLAS detector at high $|\eta|$ were more likely to pass the tight selection than muons with an $\eta \sim 0$ (Figure 9.2.2). There is also a dependence on the jet multiplicity where the prompt lepton efficiency is largest in events with no hard jet actively (where prompt lepton efficiency is typically 96%) and steadily decreases with increasing jet multiplicity, which is shown in

Figure 9.2.2. The real efficiencies are parametrised in bins of p_{T}^{μ} and the number of jets in the event for three separate η bins of $|\eta| \leq 1.05$, $1.05 < |\eta| \leq 1.6$ and $1.6 < |\eta| \leq 2.5$. Any dependence on $E_{\mathrm{T}}^{\mathrm{miss}}$, $\Delta R(\mu, jet)$ and ϕ not covered by this parametrisation are covered by an appropriate systematic as discussed below.

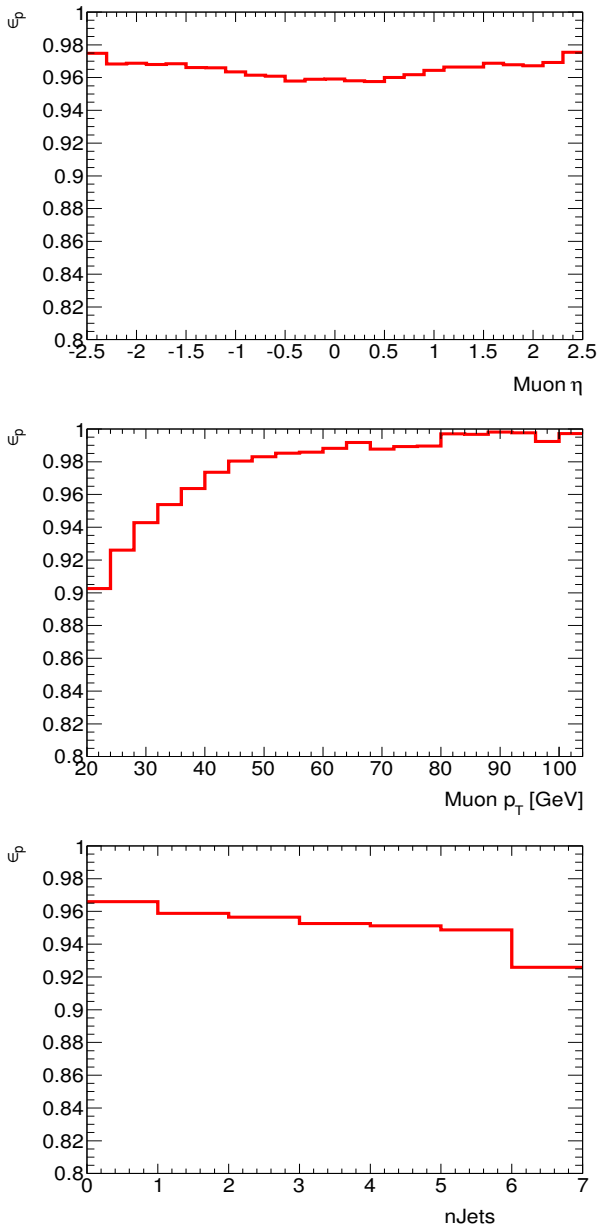

Figure 9.4: Probability for a prompt loose muon to pass the tight requirements as a function of muon (top) pseudo-rapidity, (middle) muon transverse momentum and (bottom) number of analysis jets.

The efficiency maps used in the analysis can be seen in Figure 9.5. The efficiencies range from 84% at low momentum and high jet multiplicity to approximately 100% for high momentum muons with low jet activity.

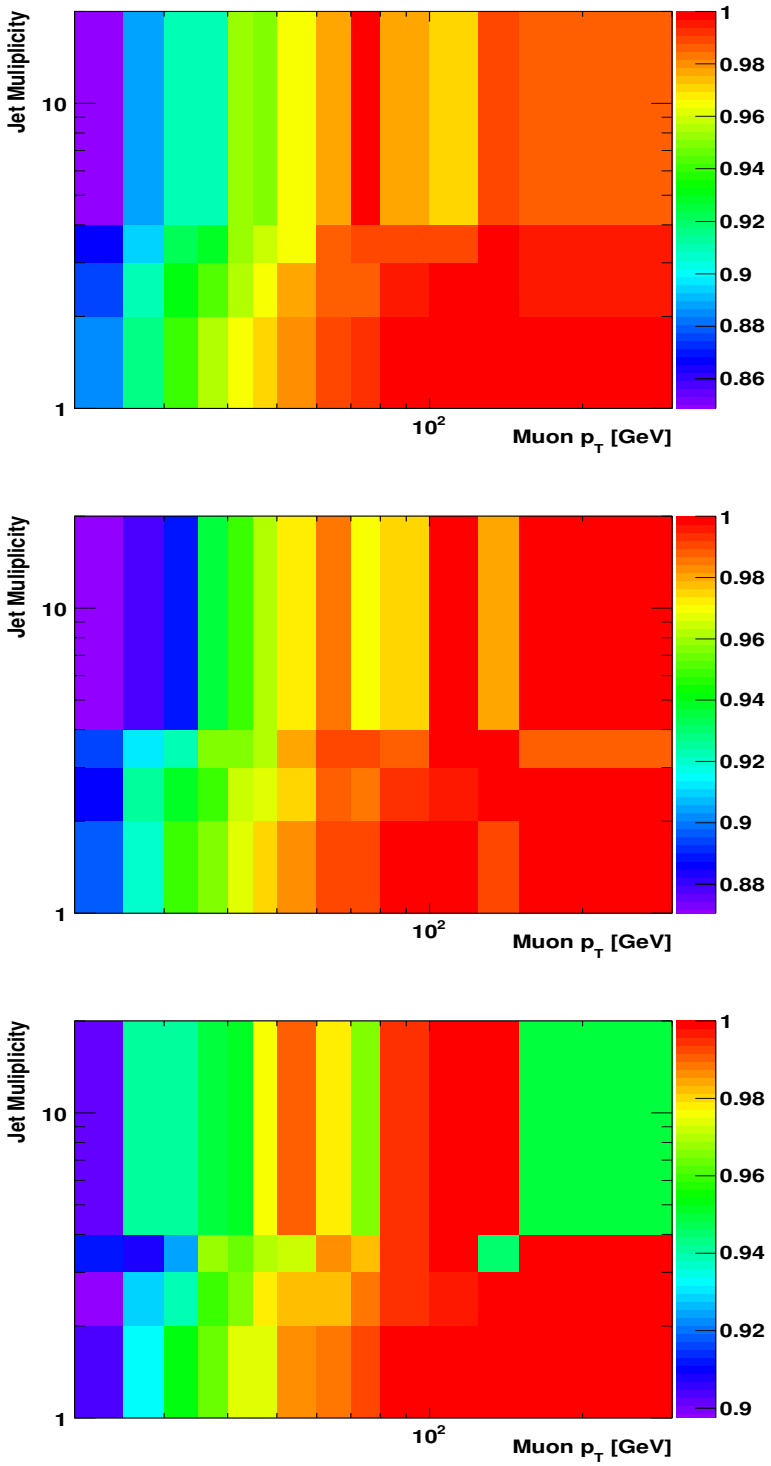

Figure 9.5: Probability for a prompt loose muon to pass the tight requirements as a function of muon transverse momentum (x-axis) and number of analysis jets (y-axis) in the detector for three separate $|\eta|$ regions - (top) $|\eta| \leq 1.05$, (middle) $1.05 < |\eta| \leq 1.6$ and (bottom) $1.6 < |\eta| \leq 2.5$.

Uncertainty on real efficiency

The statistics used in the sample to obtain the prompt lepton efficiency are large with over 2×10^6 $Z \to \mu\mu$ events in the data. The control sample is split into three separate regions in η, comprising $|\eta| \leq 1.05$, $1.05 < |\eta| \leq 1.6$ and $1.6 < |\eta| \leq 2.5$, which contain approximately 1×10^6, 0.4×10^6 and 0.6×10^6 events respectively. The statistical uncertainty for bins with low momentum and low number of jets is approximately 0.5% and only in bins with $p_{\mathrm{T}}^{\mu} > 100$ GeV or with large jet multiplicities does the statistical uncertainty contribute, where it reaches between $5 - 10\%$.

To obtain the systematic uncertainty in the parametrized efficiency r, the effect of loosening the mass requirement used to select the Z dominated data sample in the tag-and-probe method is considered by varying the window from 86-96 GeV to 81-101 GeV. The effect seen on the prompt lepton efficiency is checked bin by bin. This effect can be seen in Figure 9.6 to be small in most bins with the largest effect at the level of 3%. The time dependence on the prompt lepton efficiency is checked by averaging the efficiency over entire data periods. This is to ensure no detector issues were present that would affect small periods of data. The result of this check is shown in Figure 9.7, where the prompt lepton efficiency is seen to be to be consistent across all data periods to within 1%.

Half Sample Test

With finite statistics in the control sample, the parametrisation of the efficiency can only account for the key kinematics variables that show the most dependence on the efficiency. To account for systematic uncertainties relating to non parametrised variables the half sample test technique can be used. As an example the uncertainty on the efficiency as a function of $E_{\mathrm{T}}^{\mathrm{miss}}$ is explained.

The procedure for this test is to first separate the control sample into two equal datasets, based on a random number generator. The efficiencies are then measured in the first of these datasets, as a function of p_{T}, η and n(jets), as used in the analysis. The efficiencies are measured in the second dataset as a function of $E_{\mathrm{T}}^{\mathrm{miss}}$, that is not used in the analysis, which are referred to as the "measured" efficiencies. A histogram of $E_{\mathrm{T}}^{\mathrm{miss}}$ is then filled with events in the second dataset that are weighted with the efficiency measured in the first dataset. Each bin is then divided by the number of bin entries. The corresponding histogram is now the "predicted efficiency" as a function of $E_{\mathrm{T}}^{\mathrm{miss}}$. A comparison of the measured and predicted is then used to assign a systematic uncertainty on the method. The predicted and observed efficiencies measured with the half sample test as a function of the parametrized muon η and the non parametrised $E_{\mathrm{T}}^{\mathrm{miss}}$ are shown in Figure 9.8. The observed and expected efficiencies agree well within the systematic band, which is taken as a 3% symmetrical uncertainty on the expected efficiency.

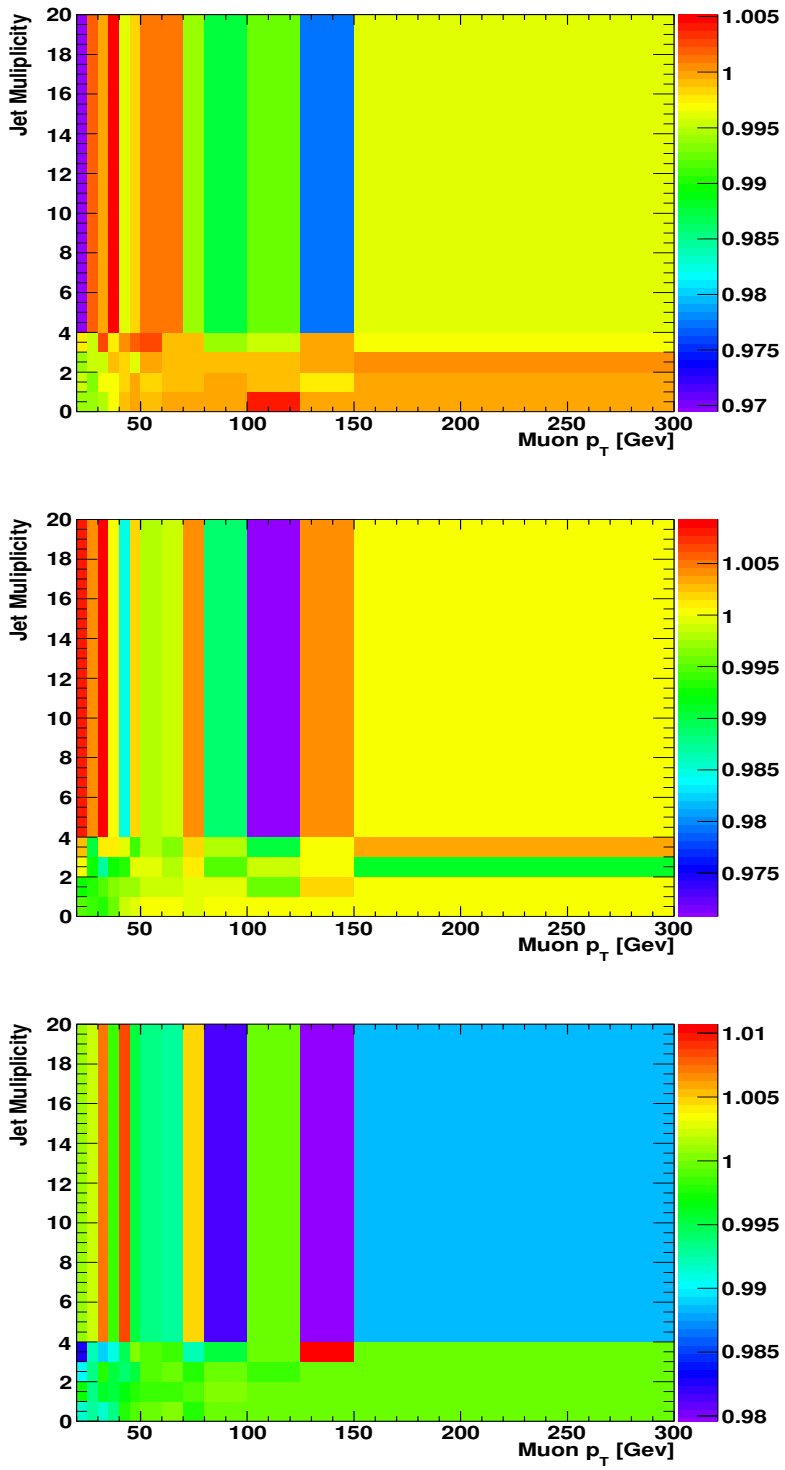

Figure 9.6: Fractional change in prompt lepton efficiency by widening the Z mass window to $|M_Z - 10|$ GeV compared to the nominal Z window of $|M_Z - 5|$ GeV for three separate eta regions - (top) $|\eta| \leq 1.05$, (middle) $1.05 < |\eta| \leq 1.6$ and (bottom) $1.6 < |\eta| \leq 2.5$..

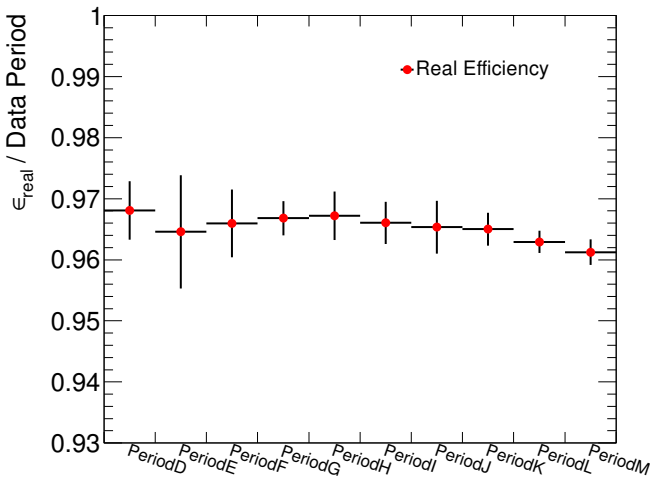

Figure 9.7: Data period dependence on the measured real efficiency. The plot shows the average prompt lepton efficiency measured in each data period.

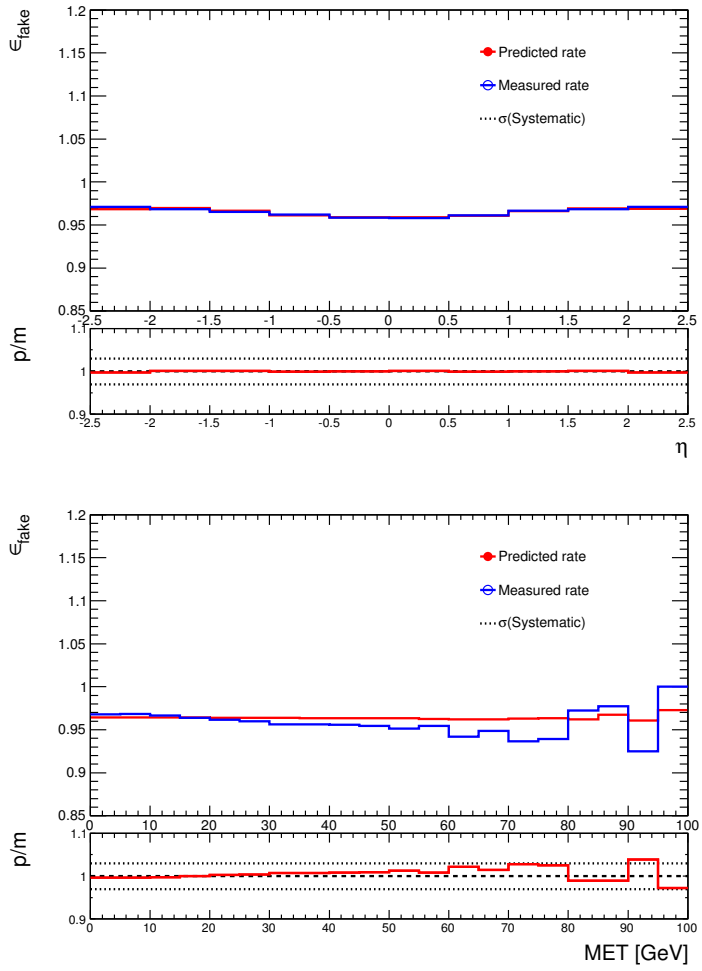

Figure 9.8: Rates for observed and predicted real efficiencies using the half sample test including a 3% systematic band as a function of muon η and $E_{\mathrm{T}}^{\mathrm{miss}}$.

9.2.3 Fake Efficiencies

To measure the fake rate for muons found in the loose sample a region dominated by non-prompt muons is selected. The fake rate is expected to depend on the source of the non-prompt muons, such as semi-leptonic b-decays, decays-in-flight of pions/kaons and jet punch-through. Since the sample composition is unknown in the signal region, two separate fake dominated regions are selected. These are selected to have different fake compositions and allow the dependence of the fake rate on the sample composition to be examined.

In the first control sample muons are selected where the significance of the impact parameter d_0 is large (this either means a large displacement from the primary vertex or a large error on the distance from the primary vertex). This sample is expected to have a significant fraction of muons originating from the semi-leptonic decays of b-quarks. Efficiencies measured in this control sample are used as the central values for the fake rates. Events in this sample are selected that satisfy the condition:

- exactly 1 loose muon with $|d_0/\sigma(d_0)| > 5.0$ and $|d_0| < 1.0$ mm.

The second control sample is used to assign a systematic uncertainty on the central efficiencies, using muons in events with small transverse missing energy. This sample is expected to have a smaller fraction of muons originating from semi-leptonic decays of b-quarks. The following requirements are applied to the second fake control region:

- exactly 1 loose muon.
- at least 1 analysis jet.
- $\Delta\phi(\mu, E_{\mathrm{T}}^{\mathrm{miss}}) < 0.5$.
- $(M_T + E_{\mathrm{T}}^{\mathrm{miss}}) < 30$ GeV.

Both control regions have contamination from W+jets and Z+jets (and to a lesser effect from $t\bar{t}$) and the expected contribution from Z, W and $t\bar{t}$ is subtracted using the MC simulation. The prompt contamination is larger in the second region than the first. The fake rate is then measured by counting the fraction of muons that pass the isolation requirements.

Since the central fake rates are measured using muons with a different impact parameter requirement to the muons in the loose sample, the effect is studied in $b\bar{b}$ MC events to account for any bias on the fake rates. The muon isolation variables in the MC simulation are compared between muons with large and small impact parameter significance and are shown in Figure 9.9. The relative difference in efficiencies to pass the isolation cut when comparing muons with $|d_0/\sigma(d_0)| > 5$ and $|d_0| < 1$ mm to muons with $|d_0/\sigma(d_0)| < 3$ and $|d_0| < 0.2$ mm in $b\bar{b}$ MC events is shown in Table 9.2, varying between $33-37\%$, and are shown

	$\lvert d_0/\sigma(d_0)\rvert < 3.0$, $\lvert d_0\rvert < 0.2$ mm	$\lvert d_0/\sigma(d_0)\rvert > 5.0$, $\lvert d_0\rvert < 1.0$ mm	correction factor
barrel	7.69±0.33	5.61±0.44	1.37 ± 0.02
end-cap	10.16±0.28	7.64±0.28	1.33 ± 0.01

Table 9.2: Fake rates (in percentage for b-jets) derived from MC for muons with low and high impact parameter significance, shown separately for barrel and end-cap. The last column shows the resulting correction factor.

as a function of muon p_{T} in Figure 9.10, where the MC predicts the isolation efficiency to be higher in regions with low impact parameter significance. This difference is applied as a scale factor to the fake rates obtained from the control region using muons with $|d_0/\sigma(d_0)| > 5$ and $|d_0| < 1$. A systematic uncertainty equal to the scale factor is applied to account for the fact that this correction relies on the MC simulation.

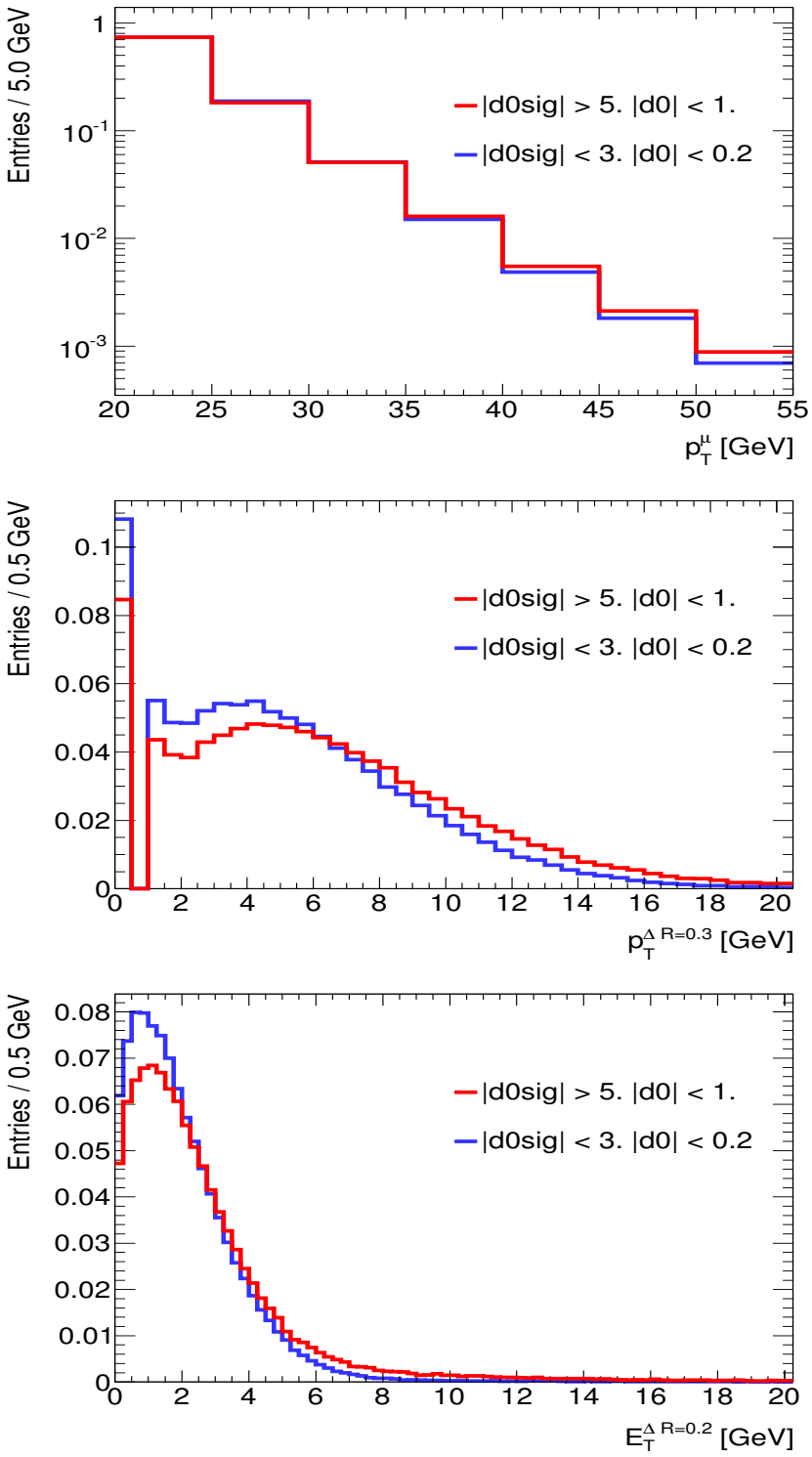

Figure 9.9: Difference in isolation properties between region used to estimate fake rates and the region used for our analysis selection for - (top) transverse momentum of muons and (middle) track isolation variable $p_{\mathrm{T}}^{\Delta\mathrm{R}=0.3}$ and (bottom) calorimeter isolation $E_{\mathrm{T}}^{\Delta\mathrm{R}=0.2}$.

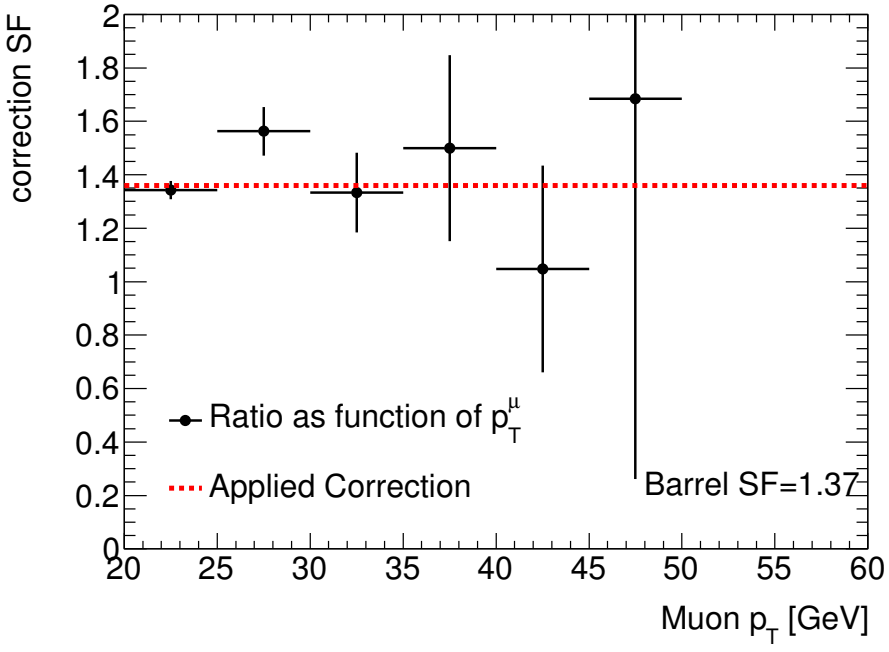

(a)

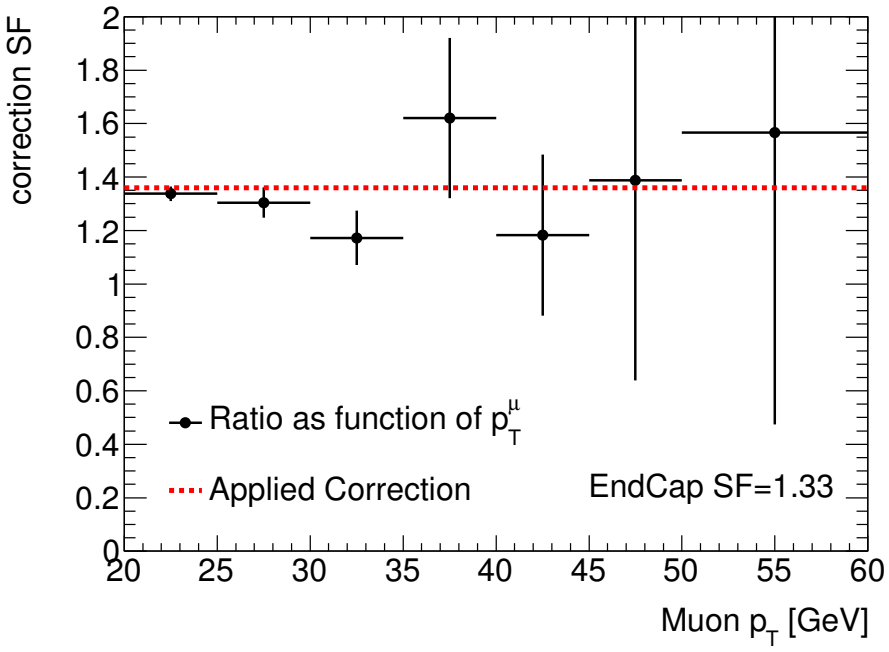

(b)

Figure 9.10: The ratio of efficiencies for muons in $b\bar{b}$ Monte Carlo that pass the isolation requirement for muons used to measure the fake rates and for muons with analysis cuts applied for - (a) barrel and (b) end-cap muons.

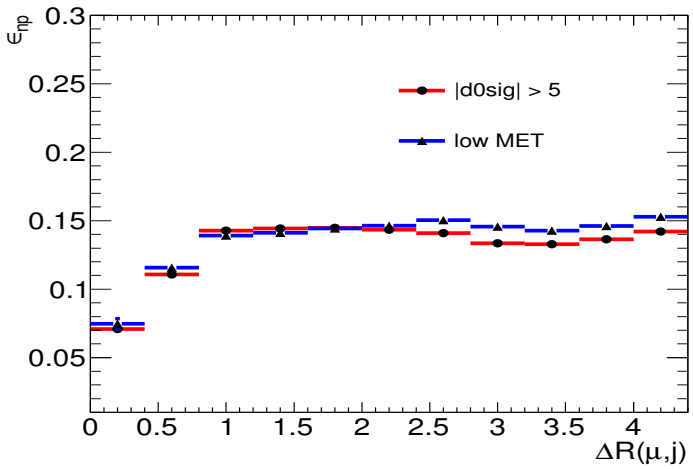

Figure 9.11: Fake muon probabilities derived from the two different control samples as a function of the angular separation between the muon and the closest jet, $\Delta R(\mu, j)$, for events with at least one analysis jet.

Parametrization of Fake Efficiency As described in section 6.2 the isolation is significantly different for muons close to jets ($\Delta R(\mu, j) \leq 0.4$) than for those away from jets ($\Delta R(\mu, j) > 0.4$). The fake rate is therefore evaluated separately for the two regions. The dependence of the fake rate as measured in both control regions on the angular separation between the muon and closest jet, $\Delta R(\mu, j)$ can be seen in Figure 9.11, This shows the fake rate is fairly constant for muons with $\Delta R(\mu, j) > 0.8$, but is significantly lower for muons with $\Delta R(\mu, j) < 0.4$.

Muons from heavy-flavour sources, such as b hadrons are selected by requiring the muon have an overlapping jet (within $\Delta R(\mu, j)$ of 0.4) or an away jet (where $\Delta R(\mu, j)$ is greater than 2.5) that has an MV1 tag weight > 0.901 (see Figure 6.5). Muons not satisfying this requirement are classified as light-flavour muons. The fake rates are measured separately for these two flavours. As seen in Figure 9.12, muons from light-flavour quarks are more likely to pass the isolation selection than heavy-flavour muons. This is largely due to the definition of heavy and light-flavour muons used. Since a heavy-flavour muon requires a close by jet, these muons will tend to be less isolated than light-flavour tagged muons. There is also a large dependence on the probability for a non-prompt muons from light-flavour quarks to pass the isolation requirements on the muon p_{T}. In addition the fake rates are also found to depend on the number of jets in the event and the pseudo-rapidity of the muon. The fake rate is therefore parameterised as a function of muon p_{T} and the number of jets, separately for the barrel and end-cap regions of the muon spectrometer.

The effect of the non-prompt subtraction can be seen in Figure 9.13, as a function of p_T^{μ}. The dependence of the fake rate on the data period is shown in Figure 9.14, which shows the rate is stable as a function of time.

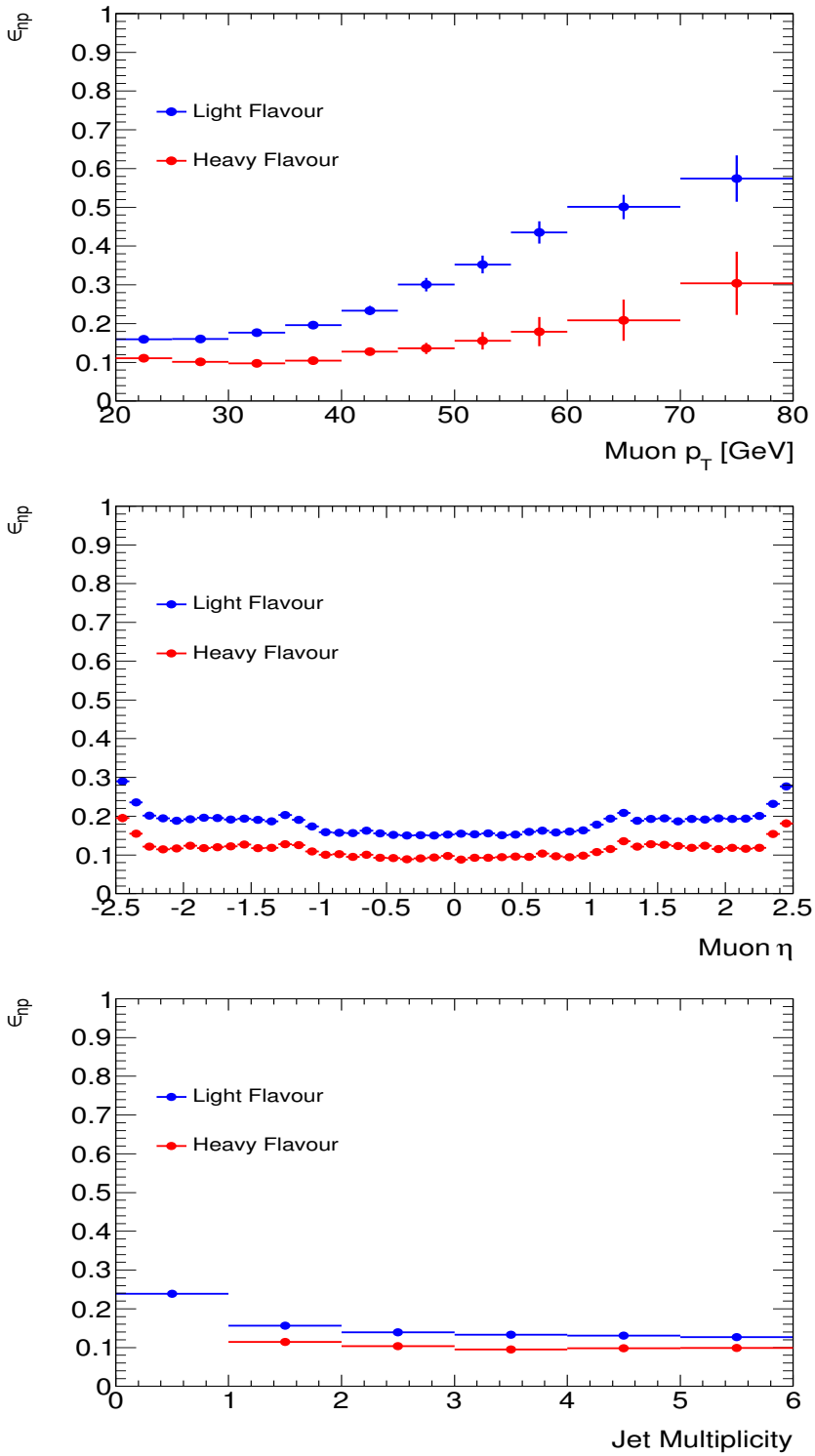

Figure 9.12: Probability for non-prompt muons to pass the isolation requirement as a function of (top) muon p_{T}, (middle) muon η and (bottom) the number of jets in the event.

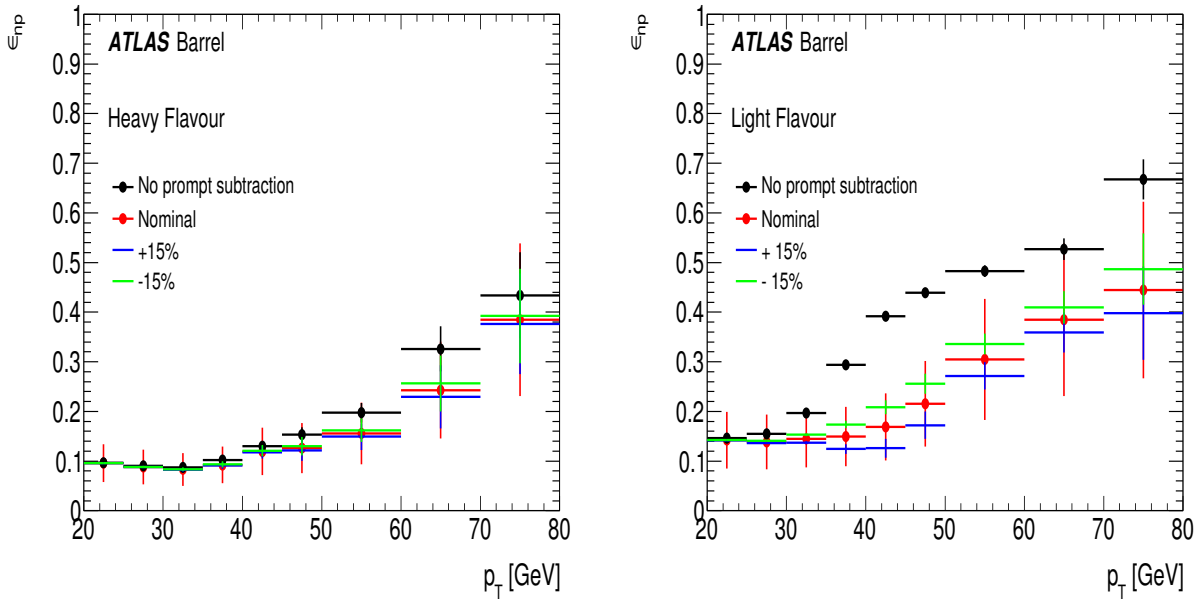

(a) (b)

Figure 9.13: Effect of prompt subtraction on muon fake rates, measured in the barrel region, as a function of muon p_{T} and heavy/light-flavour.

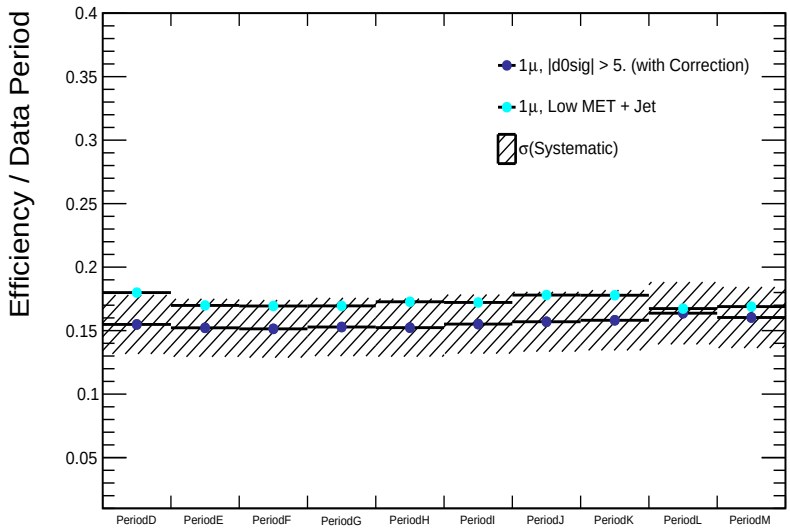

Figure 9.14: Time dependence of the fake rate measured in the two control regions. The control region using high d_0 significance has been corrected for the difference in isolation efficiency between low and high d_0 significance muons (using the MC). The shaded band is the $\pm 15\%$ uncertainty assigned to cover the difference between the two control regions.

Uncertainty on fake efficiency

Several aspects of obtaining the fake rate introduce systematic uncertainties in the measurement. These are:

- Uncertainty assigned to the correction factor used to correct for fake rates measured for muons with low impact parameters and fake rates measured with high impact parameters. The full correction factor is taken as the systematic error in this case.
- The statistical uncertainty associated with the data sample used to evaluate the fake rates. This varies from 0.1% at low momentum to $10-15\%$ for $p_{\mathrm{T}}^{\mu} > 100$ GeV.
- Uncertainty on the subtraction of prompt muons from W, Z and $t\bar{t}$ events. This is estimated by varying the predicted contribution by $\pm 15\%$, to account for uncertainties in the normalisation of the MC predictions.
- An uncertainty of $\pm 15\%$ is assigned to cover the difference between the two different samples used to measure the fake rate.

The typical uncertainty assigned to the fake rates taking into account all the uncertainties mentioned above is $\pm 40\%$.

The effect of only parametrizing the fake rate with a limited number of variables was checked by using the half sample test. In this test the fake rate is measured in half the data sample and then the parameterised fake rate is compared to the measured fake rate in the second half of the data sample. Figures 9.15 shows this comparison as a function of $E_{\mathrm{T}}^{\mathrm{miss}}$, the transverse mass, the $\Delta\phi$ between the muon and the closest jet and H_T, where H_T is the summed momentum of the jets. Since the uncertainty on the fake rate was found to cover any discrepancies in variables not included in the parametrisation, no further systematic uncertainty was assigned for the parametrisation chosen.

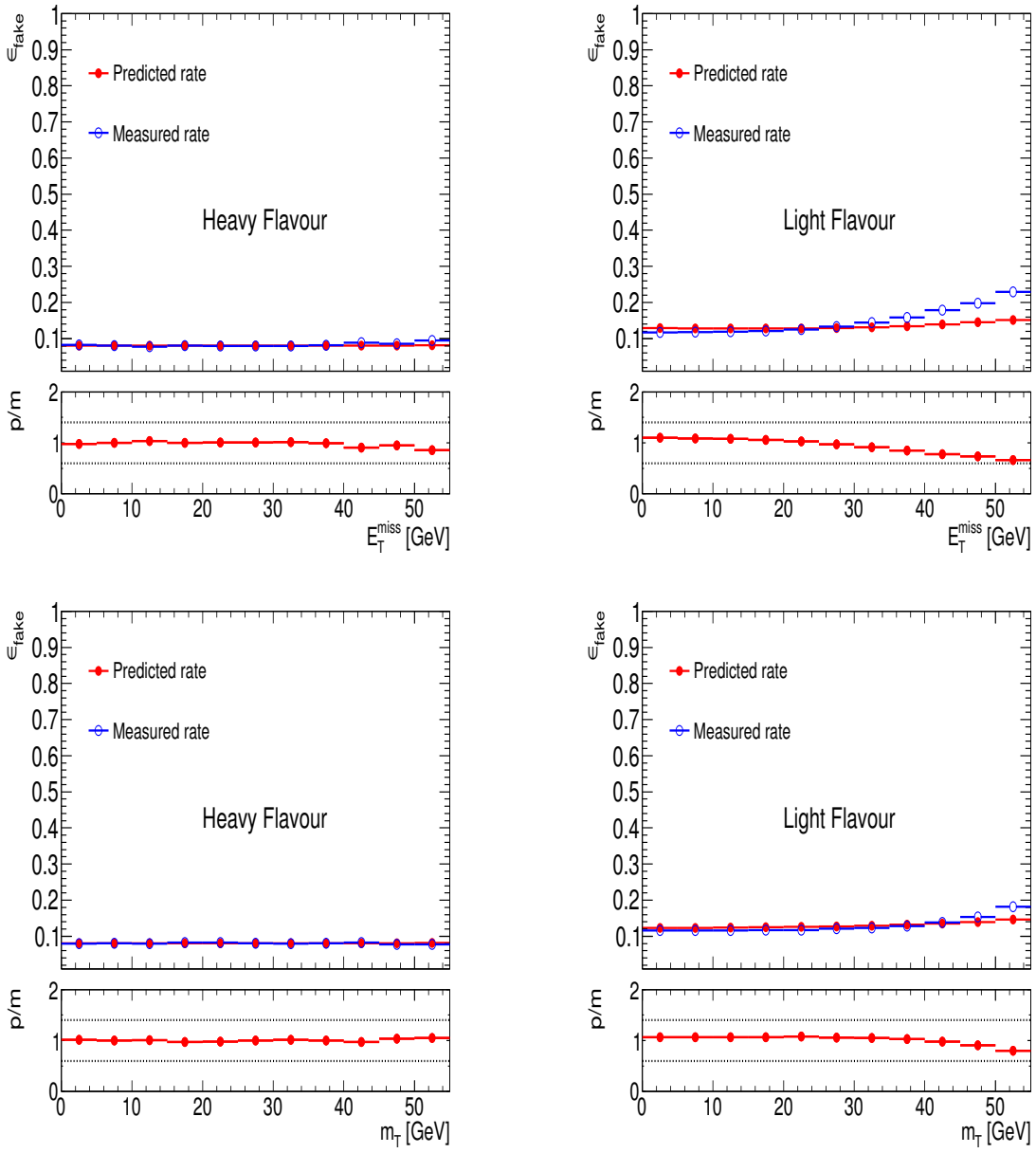

Figure 9.15: Rates for observed and predicted fake efficiencies using the half sample test, showing a 40% systematic band in p/m as a function of the $E_{\mathrm{T}}^{\mathrm{miss}}$ (top row), the transverse mass of the muon (bottom row) for muons tagged as heavy-flavour (left) and light-flavour (right).

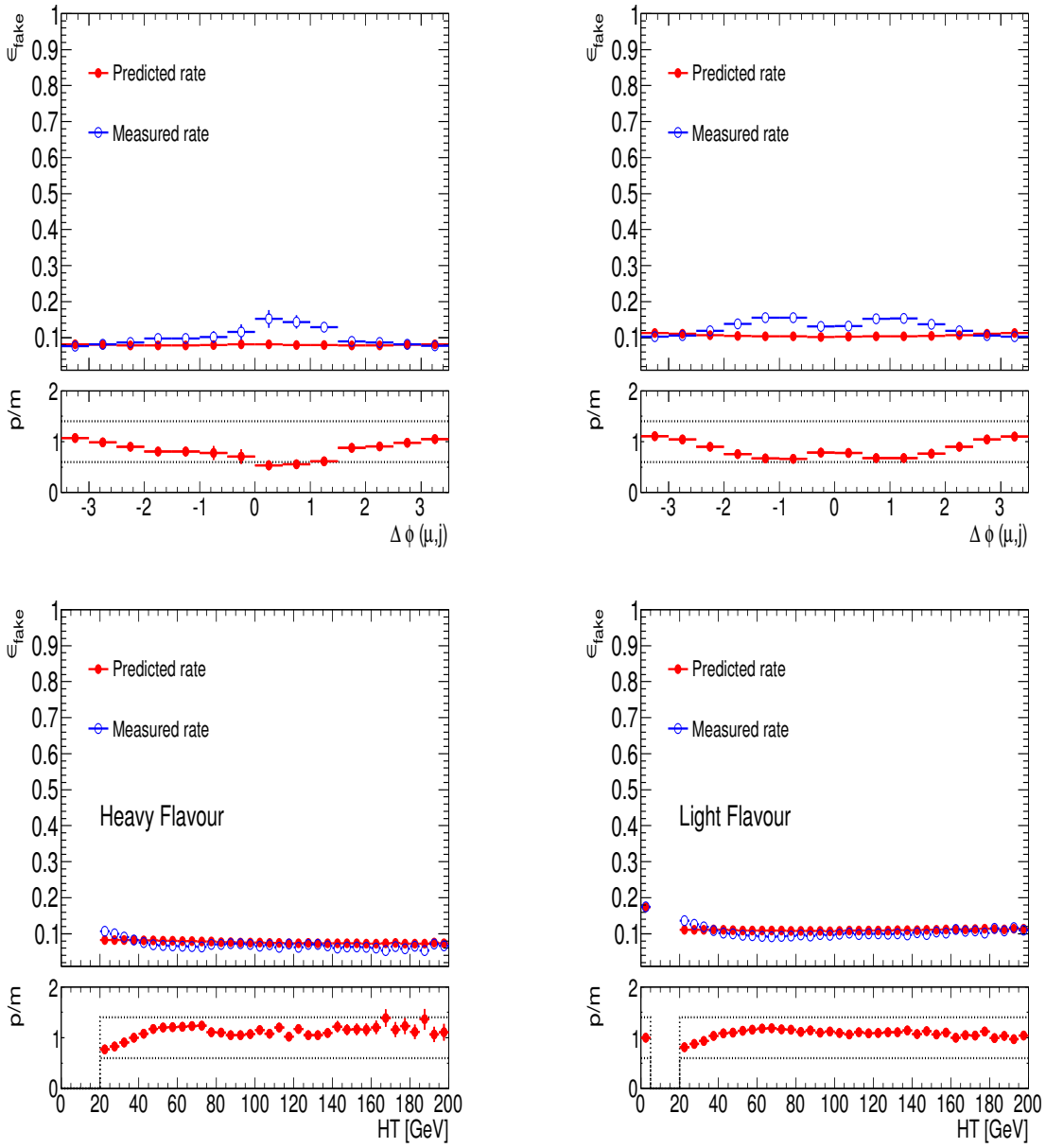

Figure 9.16: Rates for observed and predicted fake efficiencies using the half sample test including a 40% systematic band in ± as a function of the angle ϕ between the muon and closest jet (top row) and the summed momentum of jets (bottom row) for muons tagged as heavy-flavour (left) and light-flavour (right).

The fake rates are applied using 8 two dimensional maps of p_{T} vs n(jets). These are shown in Figure 9.17, as a function of muon p_{T} only (summed over jet bins).

Monte Carlo Closure Test

The application of the matrix was tested in MC using $t\bar{t}$ events. The observed number of same-sign events passing the isolation requirement was compared with the expected number predicted from the matrix method. For this closure test the real efficiencies were calculated using the ALPGEN $Z \to \mu\mu$ samples whilst the fake rates were determined using the non-prompt muons in a $b\bar{b}$ sample. The measured fake rates can be seen in Table 9.3. Table 9.4 shows the number of events predicted by the matrix method and observed to contain two same-sign muons from two different $t\bar{t}$ MC generator samples. In both cases the observed number of events agree well with the number of events expected from the matrix method.

	$\Delta R(\mu, j) \leq 0.4$	$\Delta R(\mu, j) > 0.4$
Barrel HF	0.04±0.01	0.07±0.01
End-Cap HF	0.03±0.00	0.06±0.01
Barrel LF	0.06±0.01	0.07±0.01
End-Cap LF	0.05±0.01	0.08±0.01

Table 9.3: Average fake rates measured in a $b\bar{b}$ Monte Carlo from the Monte Carlo closure test.

	Expected	Observed
ACERMC $t\bar{t}$	$4.3 \pm 0.6 \pm 0.9$	4.5 ± 0.8
MC@NLO $t\bar{t}$	$3.4 \pm 0.5^{+0.8}_{-0.7}$	2.8 ± 0.6

Table 9.4: Observed number of same-sign di-muon events in MC and the predicted number using the matrix method normalised to 4.7 fb^{-1} of data.

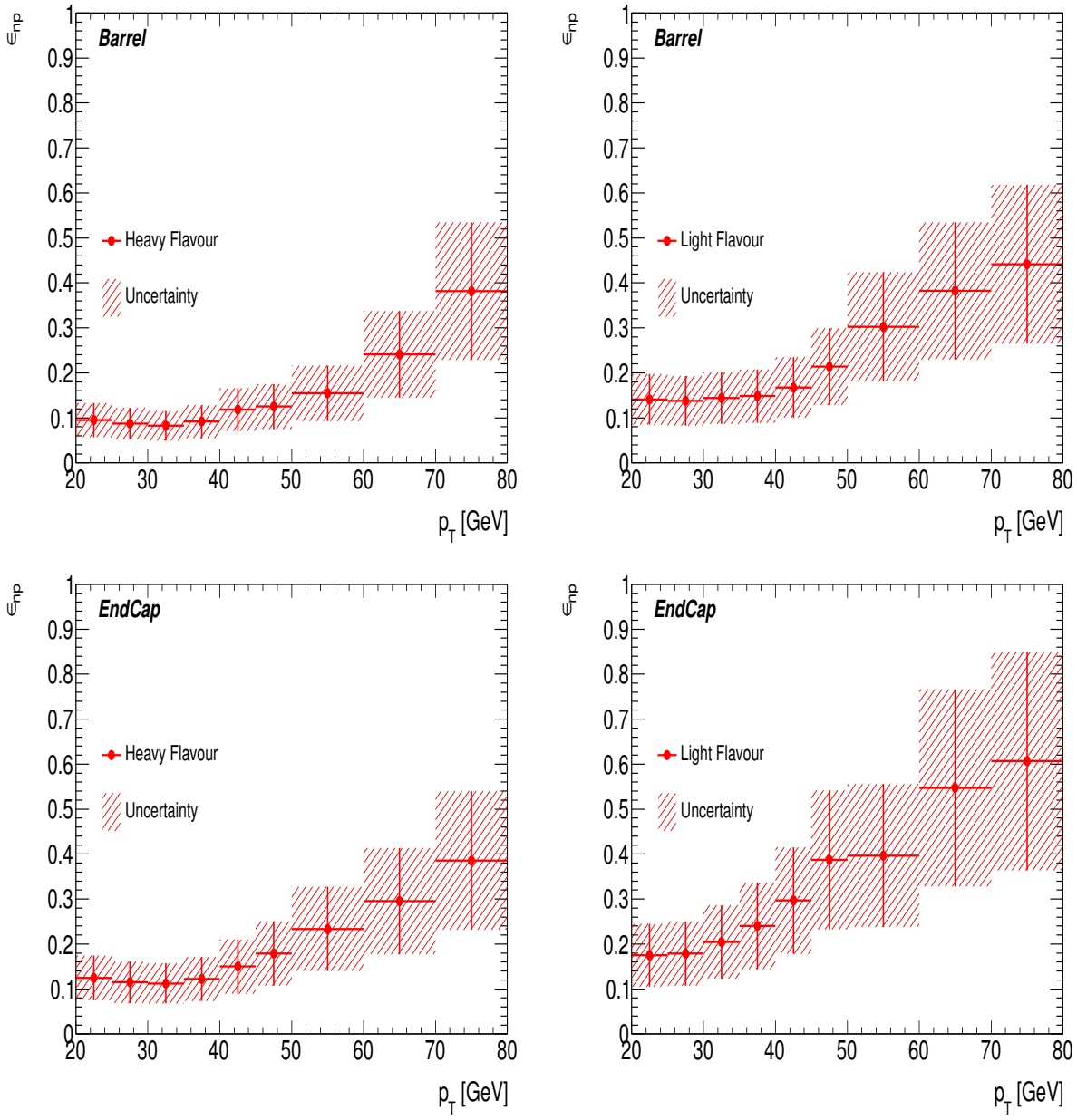

Figure 9.17: Probability for non-prompt muons to pass the isolation requirement that have a jet within $\Delta R > 0.4$ in the detector as a function of muon p_{T} for muons in the barrel (top row) and end-cap (bottom row) further separated into heavy-flavour (left) and light-flavour (right).

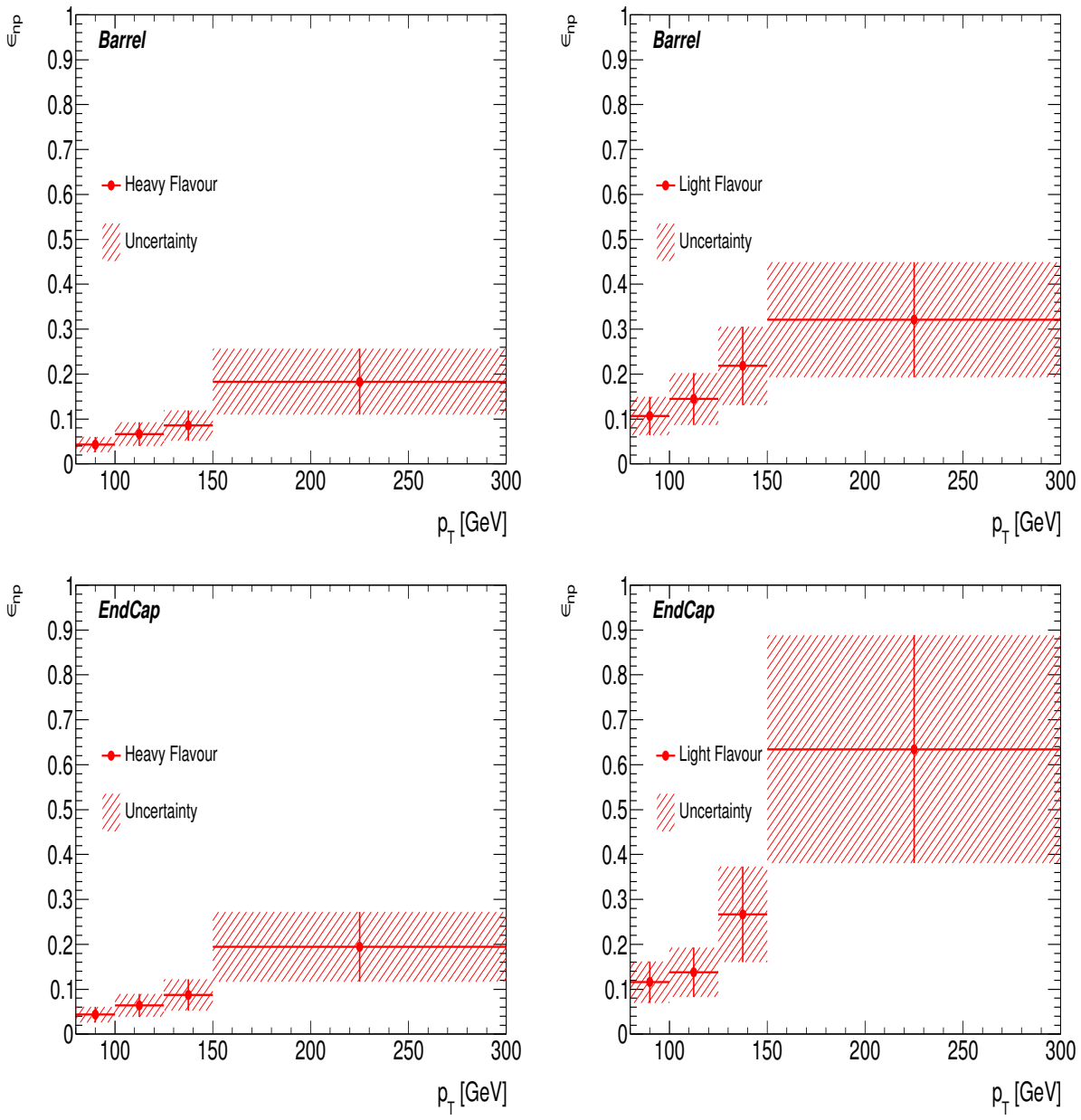

Figure 9.18: Probability for non-prompt muons to pass the isolation requirement that do not have a jet within $\Delta R > 0.4$ in the detector as a function of muon p_{T} for muons in the barrel (top row) and end-cap (bottom row) further separated into heavy-flavour (left) and light-flavour (right).

9.2.4 Event Weights using Fake Matrix Method

It has been explained that the matrix method is used to estimate the contribution of non-prompt muon sources in the signal region and how the real and fake rates needed for this method are obtained. Here details on the application of the method are discussed. As explained two types of muons, loose and tight are defined. The number of fake-fake and real-fake events in a sample of di-muon events is then estimated using the matrix in 9.1, which is constructed using he real efficiencies (r1,r2) and fake rates (f1,f2) of the two muons. The matrix relates the number of tight-tight (TT), tight-loose (TL), loose-tight (LT) and loose-loose (LL) events passing our analysis criteria (N_{TT},N_{TL},N_{LT},N_{LL}) to the number of real-real (RR), real-fake (RF), fake-real (FR) and fake-fake (FF) events that pass our analysis criteria (N_{RR},N_{RF},N_{FR},N_{FF}). In order for an event to pass our analysis selection criteria, both muons must be reconstructed as Tight. Therefore the estimated number of fake events that are reconstructed as TT is given by :

$$\begin{aligned} N_{fake\to TT} &= N_{RF,FR\to TT} + N_{FF\to TT} \\ &= (r_1 f_2 N_{RF} + f_1 r_2 N_{FF}) + f_1 f_2 N_{FF} \end{aligned} \tag{9.2}$$

The matrix 9.1 can be inverted to solve for the unknown real and fake contributions:

$$\begin{bmatrix} N^{ll}_{RR} \\ N^{ll}_{RF} \\ N^{ll}_{FR} \\ N^{ll}_{FF} \end{bmatrix} = M^{-1} \begin{bmatrix} N_{TT} \\ N_{TL} \\ N_{LT} \\ N_{LL} \end{bmatrix} \tag{9.3}$$

$$M^{-1} = \frac{1}{(r_1 - f_1)(r_2 - f_2)} \begin{bmatrix} (1-f_1)(1-f_2) & (f_1-1)f_2 & f_1(f_2-1) & f_1 f_2 \\ (f_1-1)(1-r_2) & (1-f_1)r_2 & f_1(1-r_2 & -f_1 r_2 \\ (r_1-1)(1-f_2) & (1-r_1)f_2 & r_1(1-f_2) & -r_1 f_2 \\ (1-r_1)(1-r_2) & (r_1-1)r_2 & r_1(r_2-1) & r_1 r_2 \end{bmatrix} \tag{9.4}$$

Below the expression for $N_{RF,FR\to TT}$ and $N_{FF\to TT}$ are expanded :

$$
\begin{aligned}
N_{fake\to TT} &= N_{RF,FR\to TT} + N_{FF\to TT} \\
&= (r_1 f_2 N_{RF} + f_1 r_2 N_{FF}) + f_1 f_2 N_{FF} \\
&= \alpha r_1 f_2[(f_1-1)(1-r_2)N_{TT} + (1-f_1)r_2 N_{TL} + f_1(1-r_2)N_{LT} - f_1 r_2 N_{LL}] \\
&= +\alpha r_2 f_1[(r_1-1)(1-f_2)N_{TT} + (1-r_1)f_2 N_{TL} + r_!(1-f_2)N_{LT} - r_1 f_2 N_{LL}] \\
&= +\alpha f_1 f_2[(1-r_1)(1-r_2)N_{TT} + (r_1-1)r_2 N_{TL} + r_1(r_2-1)N_{LT} + r_1 r_2 N_{LL}]
\end{aligned}
\tag{9.5}
$$

where

$$
\alpha = \frac{1}{(r_1 - f_1)(r_2 - f_2)}. \tag{9.6}
$$

The input for f_1, f_2, r_1 and r_2 are given by the parameterised real and fake values, which results in a weight dependent on the muons kinematics, which are different per event. The sum of (N_{TT}, N_{TL}, N_{LT}, N_{LL}) is not correct, and one must instead apply the fake matrix to each event separately to obtain $N_{fake\to TT}$. Each di-muon event attains a weight using the matrix where N_{TT}, N_{TL}, N_{LT}, N_{LL} are either 0 or 1 depending on the muon's characteristics. The two muons are then treated as tight leptons and are used to fill all kinematic plots as if they were actually reconstructed as tight.

As an example, if both leptons are loose (and not tight), meaning the muon has failed the isolation, (N_{TT},N_{TL},N_{LT},N_{LL}) = (0,0,0,1) the event would obtain a weight equal to:

$$
\begin{aligned}
N_{fake\to LL} &= N_{RF,FR\to TT} + N_{FF\to TT} \\
&= -\alpha 2 r_1 f_1 r_2 f_2 + \alpha r_1 f_1 r_2 f_2 \\
&= -r_1 f_1 r_2 f_2 \alpha
\end{aligned}
\tag{9.7}
$$

while if the lead muon is tight (and not loose), which means that the muon has passed the isolation, and the second muon is loose (and not tight), meaning the muon has failed the isolation, (N_{TT},N_{TL},N_{LT},N_{LL}) = (0,1,0,0) the event would obtain a weight equal to:

$$
\begin{aligned}
N_{fake\to TL} &= N_{RF,FR\to TT} + N_{FF\to TT} \\
&= \alpha(f_1 + r_1 + 2 f_1 r_1) r_2 f_2 + -\alpha(1-r_1) f_1 r_2 f_2 \\
&= (r_1 - f_1 r_1) f_2 r_2 \alpha
\end{aligned}
\tag{9.8}
$$

Note that for loose-loose events the weight is always negative. The same is true for tight-tight events, while tight-loose and loose-tight events always have positive weights. The negative weights assigned to the tight-tight are to remove the contribution from real-real events in the

Source	Inclusive (SS)	3rd Muon Veto	$n(\text{jet}) \geq 2$	$E_{\text{T}}^{\text{miss}}$ Cut	m_W Window
Non-prompt	29 ± 4	24 ± 3	9 ± 1	2.1 ± 0.7	1.1 ± 0.5

Table 9.5: Predicted background for events with two same-sign charge muons for a total integrated luminosity of 4.7 fb^{-1}.

loose-tight and tight-loose samples.

9.2.5 Non-Prompt Background Distributions

Using the matrix method the following distributions are obtained for backgrounds with one or two non-prompt muon. Figure 9.19 presents the inclusive same-sign muon background, with no event cuts applied, showing the shapes and normalisation of the key variables used in the analysis. The bands shown are a combination of the systematic and statistical uncertainties, added in quadrature.

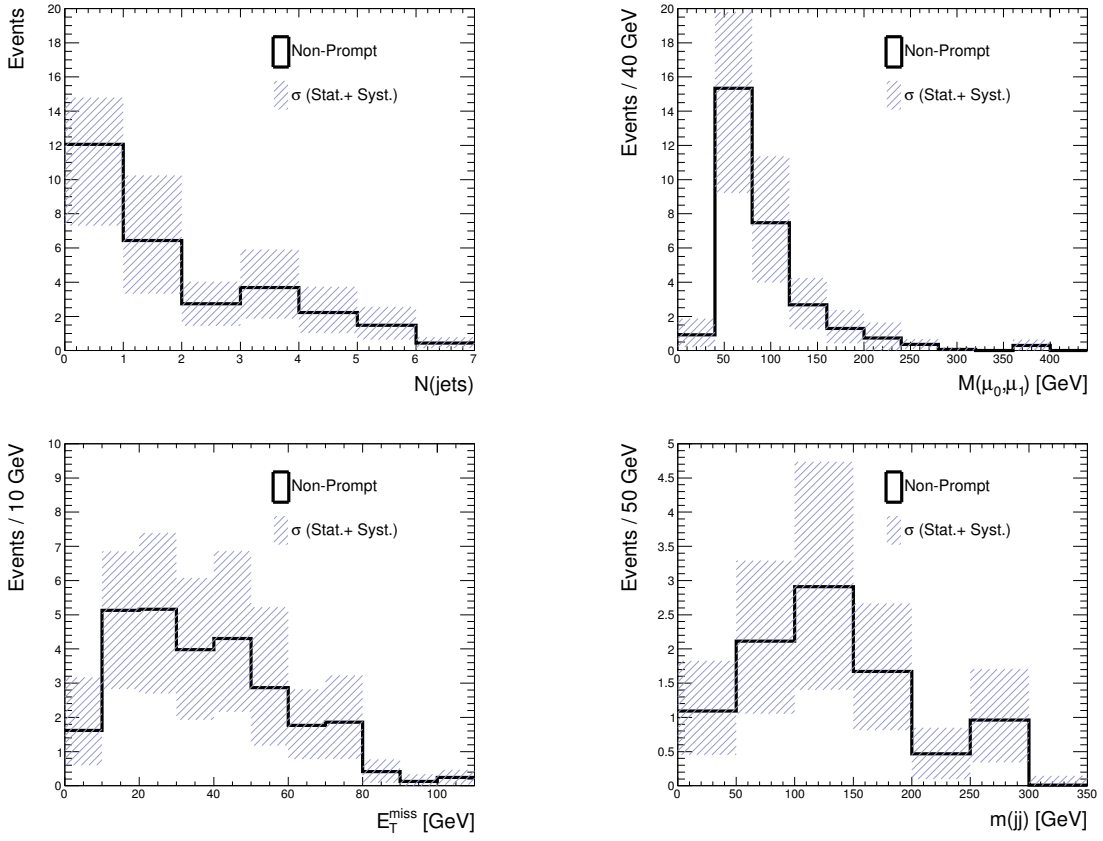

Figure 9.19: Predicted non-prompt backgrounds with same-sign muons. Distributions show (a) number of jets in the event, (b) invariant mass of the two muons, (c) the missing transverse energy and (d) the invariant mass of the lead two jets.

9.3 Backgrounds from Muon Charge Mis-identification

Background contributions from SM sources with two opposite-charge prompt muons can occur through lepton charge mis-identification. These sources are completely dominated by Z+jets events and so only this source of background from charge mis-identification is considered. The procedure for calculating the mis-identification rate for muons is discussed in the following section.

The charge of the muon can be wrongly reconstructed if the curvature is wrongly measured. This can happen in regions of the detector with poorer momentum resolution, for example at high momentum or regions with less detector coverage.

Muons in this analysis use a combination between a track in the Inner Detector (ID) and a track in the Muon Spectrometer (MS), requiring in addition the charge of both tracks to be the same. As a result if the curvature was to be mis-measured for either the MS or ID track, the muon would not pass the selection. For muons in this analysis to have the charge mis-measured both ID and MS tracks are required to be simultaneously incorrectly reconstructed.

We measure the charge mis-identification rate using $Z \to \mu^+\mu^-$ data candidates. The rates are measured independently for ID and MS tracks and combined. To measure the mis-identification rate for ID(MS) tracks, di-muon events with an invariant mass within 10 GeV of the Z boson mass are selected based on the MS(ID) kinematics. It is important that the ID(MS) charge mis-identification rate is measured with respect to the kinematics of the MS(ID) track, so that the kinematics are not biased by the charge mis-identification. Muons with matching ID and MS charge are selected as a 'tag' muon and this charge is matched to the MS(ID) charge measurements of the second muon. If these charges are opposite then the second muon becomes the 'probe'. The probes can then be directly used to obtain the mis-identification rate.

The resolution of the combined muon is dominated by the ID tracks (shown in Section 6.1.3). In the entire control region, no charge flips are observed in the ID track of muons and the result is therefore statistically limited. The mis-identification rate in MS tracks is observed to be less than 0.1% for muons with $p_{\mathrm{T}} < 100$ GeV and 68% confidence limits (CL) have been set on the combined muon mis-identification rate using the product of the separate MS and ID rates with a central value of zero, as shown in Figure 9.20. The data can be seen to have larger charge mis-identification rate than the MC due to the poorer resolution in data compared to MC, which is shown in Figure 9.21.

To obtain an upper limit on the background from charge mis-identification opposite-sign

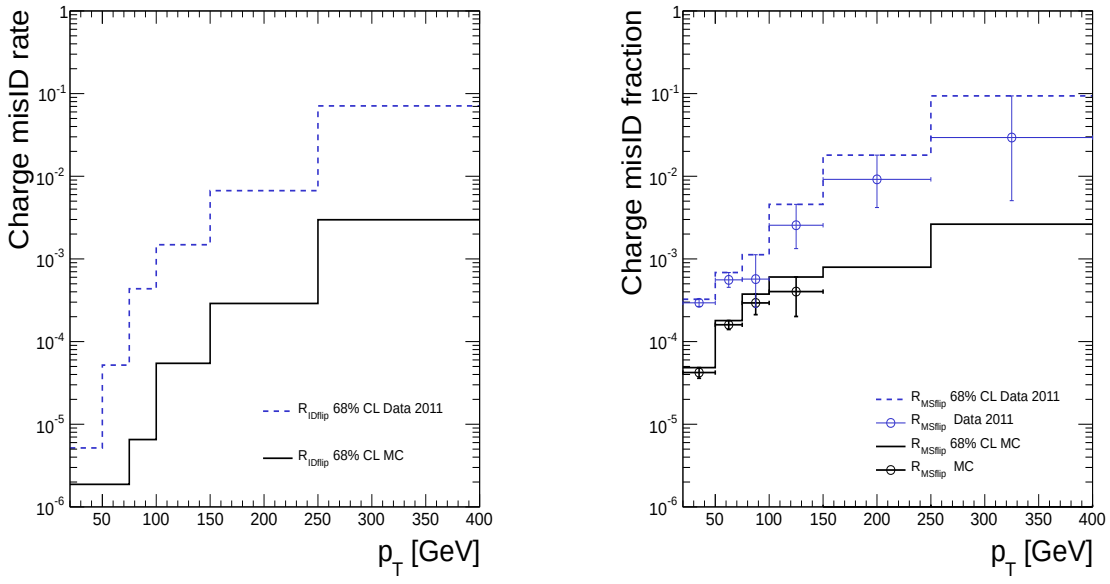

Figure 9.20: Muon charge mis-identification rates in data and MC events as a function of p_{T} for (left) ID tracks and (right) MS tracks. Circular points indicate measured rates and solid lines indicate 68% confidence limits with a central value of zero based on the data statistics.

Source	Inclusive (SS)	3rd Muon Veto	$n(jet) \geq 2$	$E_{\mathrm{T}}^{\mathrm{miss}}$ Cut	m_W Window
Charge Flip	< 0.3	< 0.3	< 0.2	< 0.1	< 0.03

Table 9.6: Predicted number of events in the signal region due to charge mis-identification of the combined muon tracks in 4.7 fb^{-1} of data.

Z MC events and weight using [111]

$$\frac{w_1^k \times w_2^l}{(1 - w_1^k)(1 - w_2^l)} \tag{9.9}$$

where w_i^m is the combined flip rate for muon i in p_{T} bin m. The denominator is a result of the fact we are only applying the weights to opposite signed muons. The number of predicted events passing our selection cuts are shown in Table 9.6.

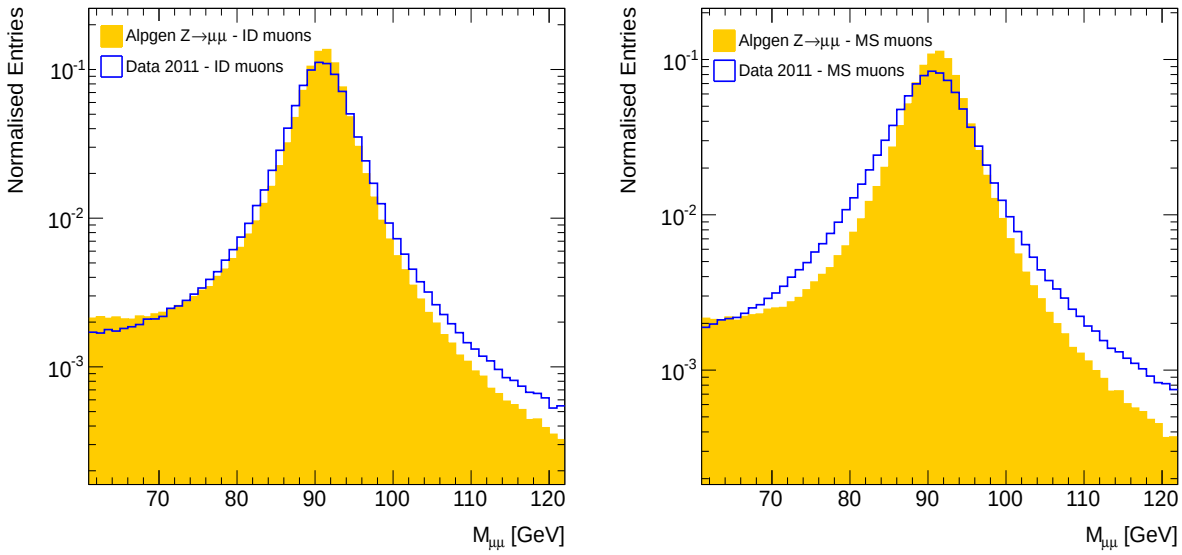

Figure 9.21: Dimuon mass normalised to unit area for ID-only muons (left) and MS-only muons (centre), in data and MC. ID-only muons and MS-only muons in data are shown on the right.

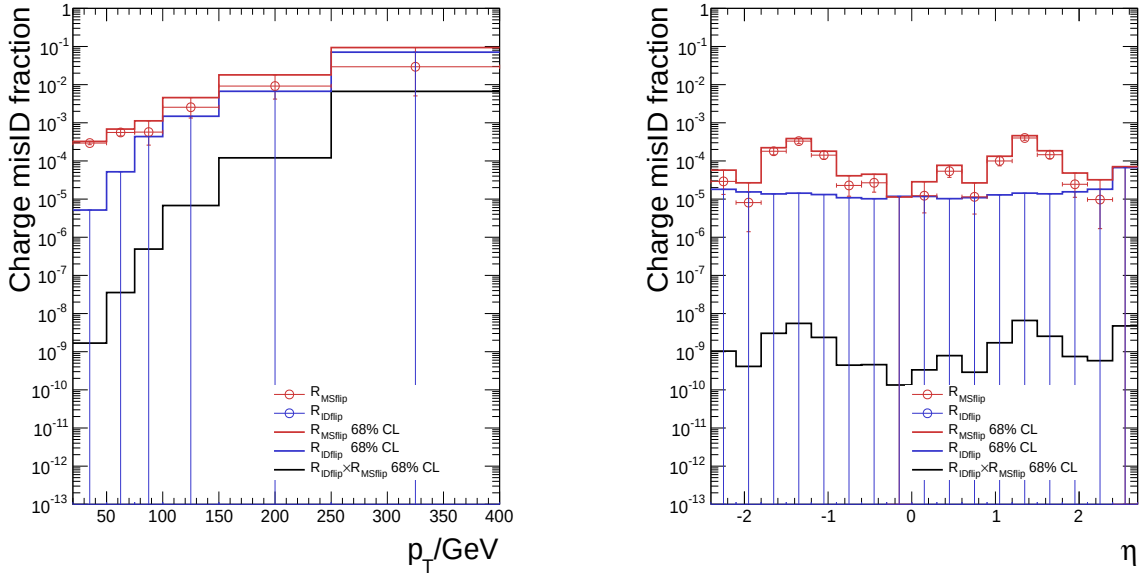

Figure 9.22: Muon charge mis-identification rates for data binned in (left) p_{T} and (right) η. Circular points indicate measured rates and solid lines indicate 68% confidence limits with a central value of zero based on the data statistics. No charge mis-measurements are observed for inner detector tracks.

9.4 Final Background Estimates

The final backgrounds are presented in Table 9.7. The errors shown are statistical only. The dominant backgrounds in the inclusive sample of events with same-sign muon pairs are from diboson production. WZ and non-prompt sources contribute equally, with the statistical uncertainty dominated by the data driven non-prompt background, and is at the level of 20%.

Source	Inclusive (SS)	3rd Muon Veto	$n(\text{jet}) \geq 2$	$E_{\text{T}}^{\text{miss}} \leq 35$ GeV	W Window
WZ	65 ± 1	40 ± 1	8 ± 1	2.4 ± 0.3	1.0 ± 0.2
ZZ	17 ± 1	7.0 ± 0.3	0.7 ± 0.1	0.5 ± 0.1	0.22 ± 0.05
$W^{\pm}W^{\pm}$+2p	4.8 ± 0.2	4.6 ± 0.2	3.9 ± 0.2	0.7 ± 0.1	0.15 ± 0.04
$Zt\bar{t}, Wt\bar{t}$	4.1 ± 0.2	3.0 ± 0.2	3.0 ± 0.2	0.5 ± 0.1	0.23 ± 0.04
Non-prompt	29 ± 4	24 ± 3	9 ± 1	2.1 ± 0.7	1.1 ± 0.5
CMM	< 0.3	< 0.3	< 0.2	< 0.1	< 0.1
Total	120 ± 4	78 ± 3	24 ± 1	6 ± 1	2.7 ± 0.5

Table 9.7: Expected number of events containing two same-sign isolated muons for different event selection cuts. The uncertainties are stated as statistical.

Chapter 10

Systematics for Backgrounds and Signal estimations

10.1 Validation of Background Estimates

Before performing the search it is necessary to verify that the background estimated provide a good modelling of the data in a variety of *control regions*. A control region is chosen to have similar event kinematics to the signal region, but containing a negligible number of signal events. A number of control regions are used in this analysis. These control regions have different background contributions and together verify that the background estimates correctly model the observed data. The regions are:

- Region 1: Opposite-sign di-muon events. These events are dominated by $Z \to \mu\mu$ events and verify the basic modelling of the di-muon events regarding triggers and muon and jet reconstruction. In addition, this region tests the MC modelling of the $E_{\mathrm{T}}^{\mathrm{miss}}$ distribution in a kinematic regime similar to the signal events.

- Region 2: Events with three or four muons. These events are dominated by diboson events and verify that the Sherpa MC samples provide a good description of the diboson events observed in the data.

- Region 3: Events with a single muon and low $E_{\mathrm{T}}^{\mathrm{miss}}$. This region has a significant contribution from non-prompt muons. Thus it helps to verify the modelling of the non-prompt background.

- Region 4: Events with same-sign muons with 0 or 1 additional jet. This region is similar to the signal region but with less jet activity. The expected background is dominated by diboson events and backgrounds from non-prompt muon events.

For all plots in this chapter the final bin contains the overflow events.

10.1.1 Control Regions with Opposite-Sign Muon Pairs

To validate the performance of the leptons, jets and $E_{\mathrm{T}}^{\mathrm{miss}}$ and the correct implementation of scale factors for the trigger and reconstruction, events are used with two muons of opposite-sign charge. The region is split into two sets, the first includes events with 0 or 1 jet and the second includes events with ≥ 2 jets. The first region has the largest statistics, while the second is kinematically quite similar to the signal region and is used to check the MC modelling of jets and $E_{\mathrm{T}}^{\mathrm{miss}}$.

Opposite-Sign Di-muon Events with 0 and 1 Jets

In the first validation sample events with two opposite-sign isolated muons are considered that have passed the muon object selection and contain 0 or 1 additional jet. A cut is applied on the invariant mass of the two opposite-sign muons $m_{\mu\mu} < 110$ GeV to remove any contamination of the LRSM signal in the one jet bin. The observed data are compared with the background estimates in Table 10.1. The dominant process in this sample is Z+jet events, in which the normalisation agrees well. Figures 10.1 and 10.2 show a number of distributions including the p_{T} and η of the muons. The muon p_{T} peaks at half the Z mass for both the leading muon as expected and the muon η maps the coverage of the muon system in the ATLAS detector. The jet p_{T} and η distributions are shown. The number of events in bins of jet momentum falls with increasing p_{T} as expected for initial and final state radiation. The invariant mass of the opposite-sign muon pairs and the summed momentum of the muon and jets, H_T, are seen to peak at 90 GeV since it is dominated by Z events with no jets, while $t\bar{t}$ events that contain many additional jets have larger values of H_T.

Source	$N_{\mathrm{Jet}} < 2, M_{\mu\mu} < 110$ GeV	$N_{\mathrm{Jet}} \geq 2, M_{\mu\mathrm{jj}} < 350$ GeV
Z	$1450000 \pm 1000 \pm 70000$	$89000 \pm 200 \pm {}^{46000}_{12000}$
WZ	$191 \pm 1 \pm 57$	$41 \pm 1 \pm {}^{13}_{12}$
ZZ	$113 \pm 2 \pm 33$	$22 \pm 1 \pm 7$
Top	$410 \pm 10 \pm 60$	$2800 \pm 40 \pm 290$
Non-prompt	$7500 \pm 220 \pm {}^{2000}_{2600}$	$260 \pm 30 \pm {}^{120}_{90}$
Total	$1460000 \pm 1000 \pm 70000$	$92000 \pm 160 \pm {}^{46000}_{12000}$
Data	1445051	85822

Table 10.1: Expected and observed number of events containing two oppositely charged muons. The uncertainties are stated as statistical followed by systematic.

Opposite-sign Dimuon Events with at Least Two Jets

This control region is defined by two opposite-signed muons with two or more jets; with an additional cut on the invariant mass of the two jets and a leading muon of $m_{\mu jj} < 350$ GeV to

remove any signal from the LRSM model. This control region is selected as it is similar to the signal region, with the difference that the leptons are opposite-sign rather than same-sign. Figure 10.3 shows distributions of some variables in this sample. The $E_{\mathrm{T}}^{\mathrm{miss}}$ peaks at low values for the Z+jet background, while $t\bar{t}$ events generally have $E_{\mathrm{T}}^{\mathrm{miss}} > 60$ GeV. This is expected from the presence of high momentum neutrinos in top decays, while the Z decays to muons which are measured in the detector. Also shown in this sample are the invariant mass combinations between the selected muons and jets, where the data events are well modelled in the MC simulation.

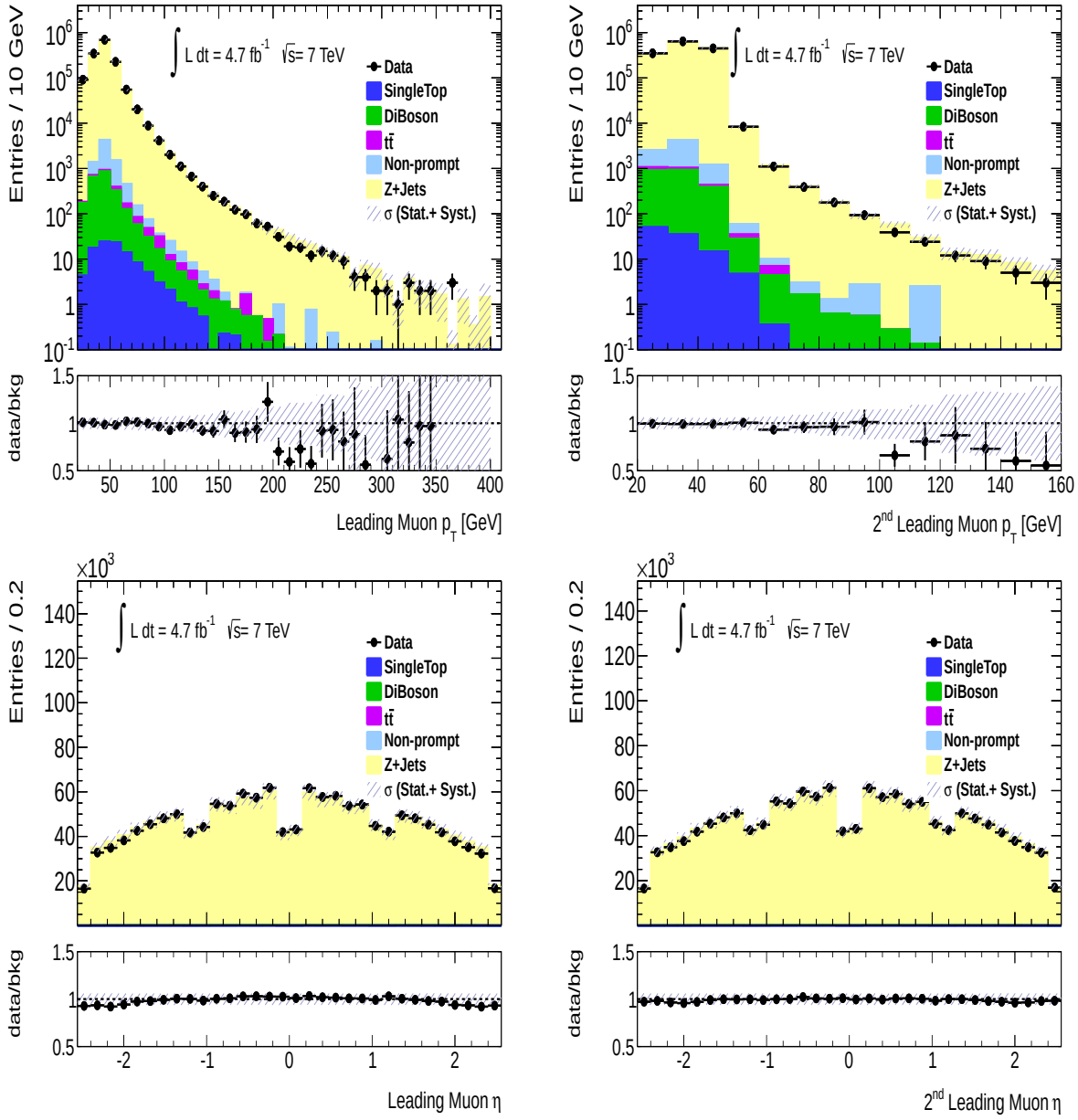

Figure 10.1: Distributions of leading and sub leading muon p_{T} (top row) and η (bottom row). The blue hatched area is the combined systematic and statistical uncertainty.

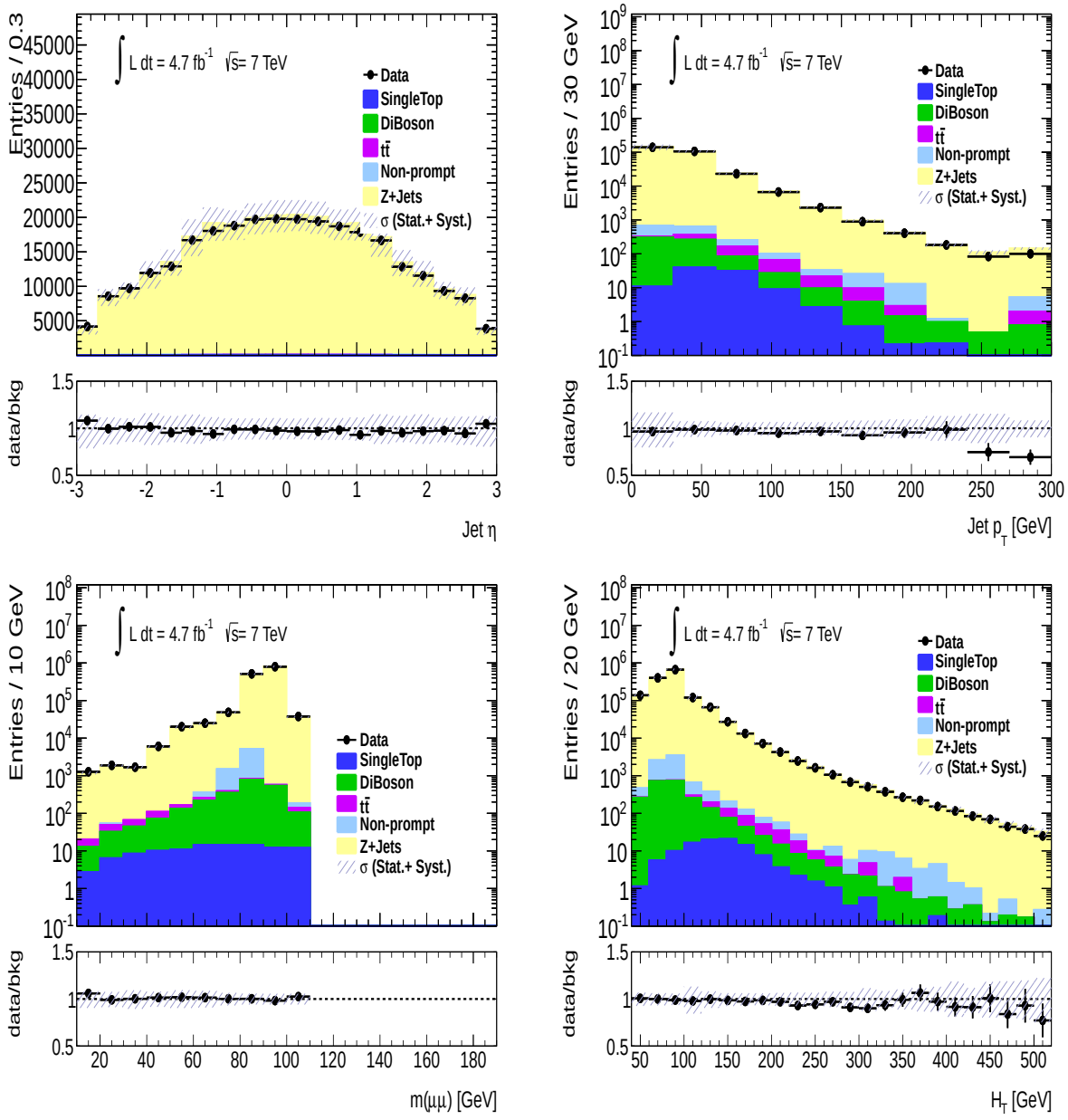

Figure 10.2: Distributions of jet p_{T} and η (top row) and the invariant mass of two muons and summed transverse momentum of all muons and jets (bottom row). The blue hatched area is the combined systematic and statistical uncertainty.

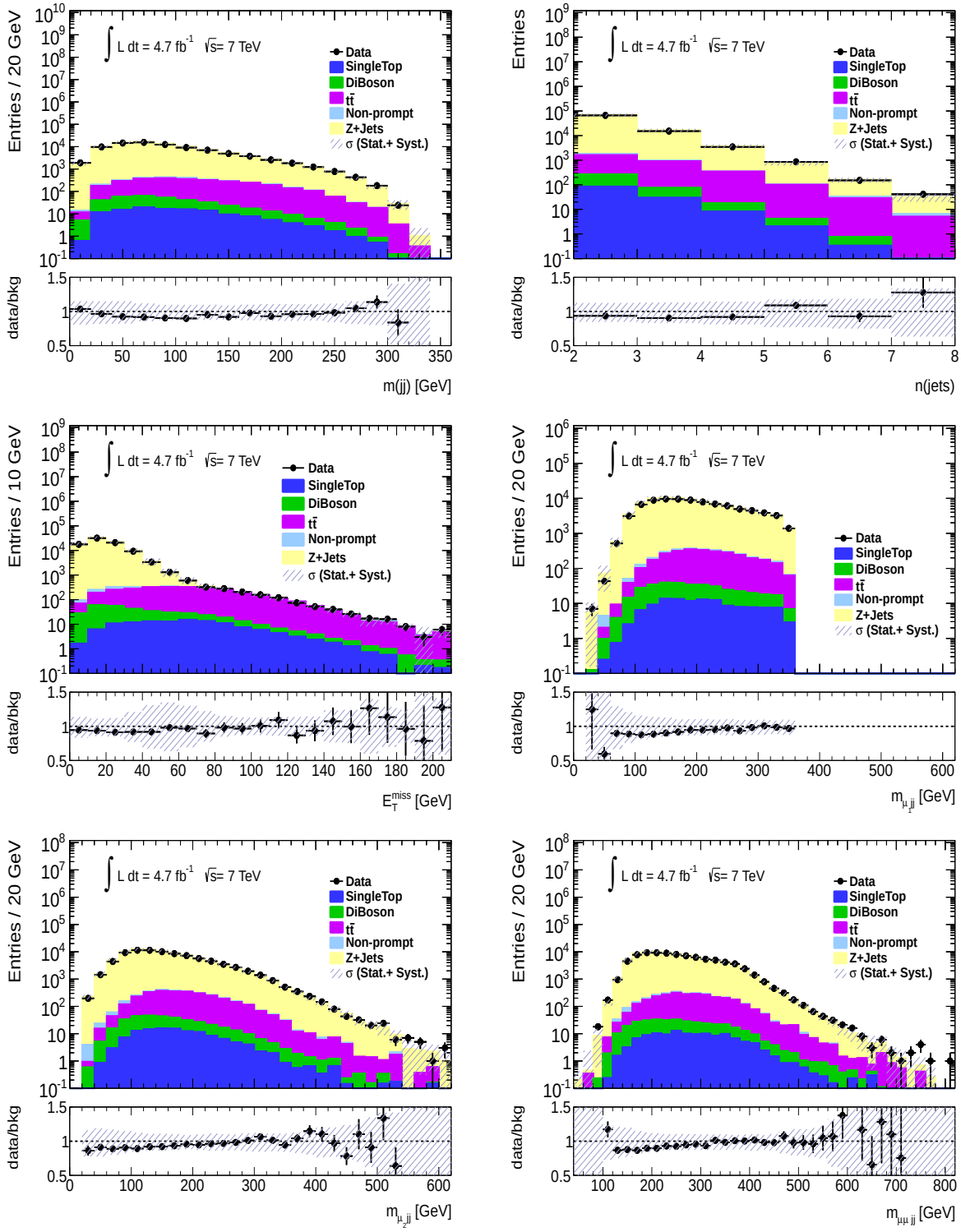

Figure 10.3: Distributions of the invariant mass of the two leading jets plus leading muon $m_{\mu 1jj}$ (top), the invariant mass of the two leading jets plus sub-leading muon $m_{\mu 2jj}$ (centre) and the invariant mass of the two leading jets plus leading muons $m_{\mu 1\mu 2jj}$ (bottom) for events with two opposite-sign muons, two or more jets and $m_{\mu jj} < 350$ GeV for 4.7 fb^{-1} of data. The blue hatched area is the combined systematic and statistical uncertainty.

10.1.2 Control Regions with Three or Four Muons

Two control regions are defined to test the modelling of the WZ and ZZ background estimates. In the first region, dominated by WZ events, exactly three muons are required and in the second region, dominated by ZZ events, exactly four muons are required. No requirements are made on the number of jets or missing transverse energy. The predicted background and observed data in the two regions are shown in Table 10.2 with good agreement in the overall normalisation. The backgrounds from non-prompt sources are estimated using MC, with contributions from $Z \to \mu\mu$, $W^+W^- \to \nu\mu\nu\mu$ and $t\bar{t}$ events included. Figure 10.4 shows a range of kinematic distributions in events with three muons used to validate these backgrounds (specifically the SHERPA MC samples are validated). The $E_{\mathrm{T}}^{\mathrm{miss}}$ for these events is broad between 10 and 50 GeV with a tail after 50 GeV. This is a combination of a peak in the $E_{\mathrm{T}}^{\mathrm{miss}}$ at half the W mass from WZ events, and the ZZ events predominantly having low $E_{\mathrm{T}}^{\mathrm{miss}}$. The summed charge of the three muons is shown to be positive in more cases than negative. This is expected from the shape of the up and down valence quark parton distribution function of the proton. The ratio between the number of $\mu^{\pm}\mu^{\pm}\mu^{\mp}$ to $\mu^{\pm}\mu^{\mp}\mu^{\mp}$ is approximately 1.5. The number of jets, the jet p_{T} and the invariant mass distributions of the two leading jets in the three muon events are shown. These distributions demonstrate the SHERPA simulation is providing a good model of events in Figure 10.4.

	Number of events with	
Source	three muons	four muons
WZ	$95 \pm 2 \pm 27$	< 0.03
ZZ	$24 \pm 1 \pm 7$	$7.6 \pm 0.3 \pm 2.1$
Z	$3 \pm 1 \pm 3$	< 0.6
$t\bar{t}$	$2.2 \pm 0.4 \pm 1.1$	< 0.01
Total expected	$124 \pm 2 \pm 28$	$7.6 \pm 0.3 \pm 2.1$
Data	120	11

Table 10.2: Expected and observed number of events containing three and four isolated muons. The uncertainties are stated as statistical followed by systematic.

Comparisons of Different Generators for Diboson Productions

The WZ background is compared using three different MC generators: ALPGEN, HERWIG and SHERPA. The ALPGEN sample does not include the γ^* contribution, which is important when looking at same-sign events and the HERWIG sample relies exclusively on the parton shower to generate additional jets in the events. These limitations can be seen in the three muon control region. Figure 10.6(a) 10.6(c) 10.6(e) show the distribution of the di-muon mass for the opposite-sign muon pair. A deficit of MC events is seen at high and

Process	Three Muons	SS di-muon	looser muon veto	$N_{jet} \geq 2$	$E_{\mathrm{T}}^{\mathrm{miss}}$	m_W window
SHERPA	96.1 ± 1.7	66.5 ± 1.4	40.2 ± 1.1	8.1 ± 0.5	2.5 ± 0.3	1.0 ± 0.2
HERWIG	96.5 ± 1.6	50.5 ± 1.2	30.8 ± 0.9	4.1 ± 0.3	1.3 ± 0.2	0.7 ± 0.1
ALPGEN	93.3 ± 2.6	46.8 ± 1.7	34.0 ± 1.4	8.1 ± 0.7	2.3 ± 0.4	0.9 ± 0.2

Table 10.3: Predicted event yield for WZ background using three different MC generators. Errors are statistical.

low mass for the ALPGEN sample because of the missing γ^* contributions. The jet multiplicity in the three muon events is shown in Figure 10.6(b) 10.6(d) 10.6(f). The ALPGEN and SHERPA samples provide a good description of the observed data, which is expected because they include the matrix elements for the additional jet radiation. The HERWIG sample is seen to underestimate the data at high jet multiplicities.

Table 10.3 shows the number of predicted events with three isolated muons and after the event selection, for the three different generators. Using HERWIG or ALPGEN underestimates the background contribution by up to 60 %.

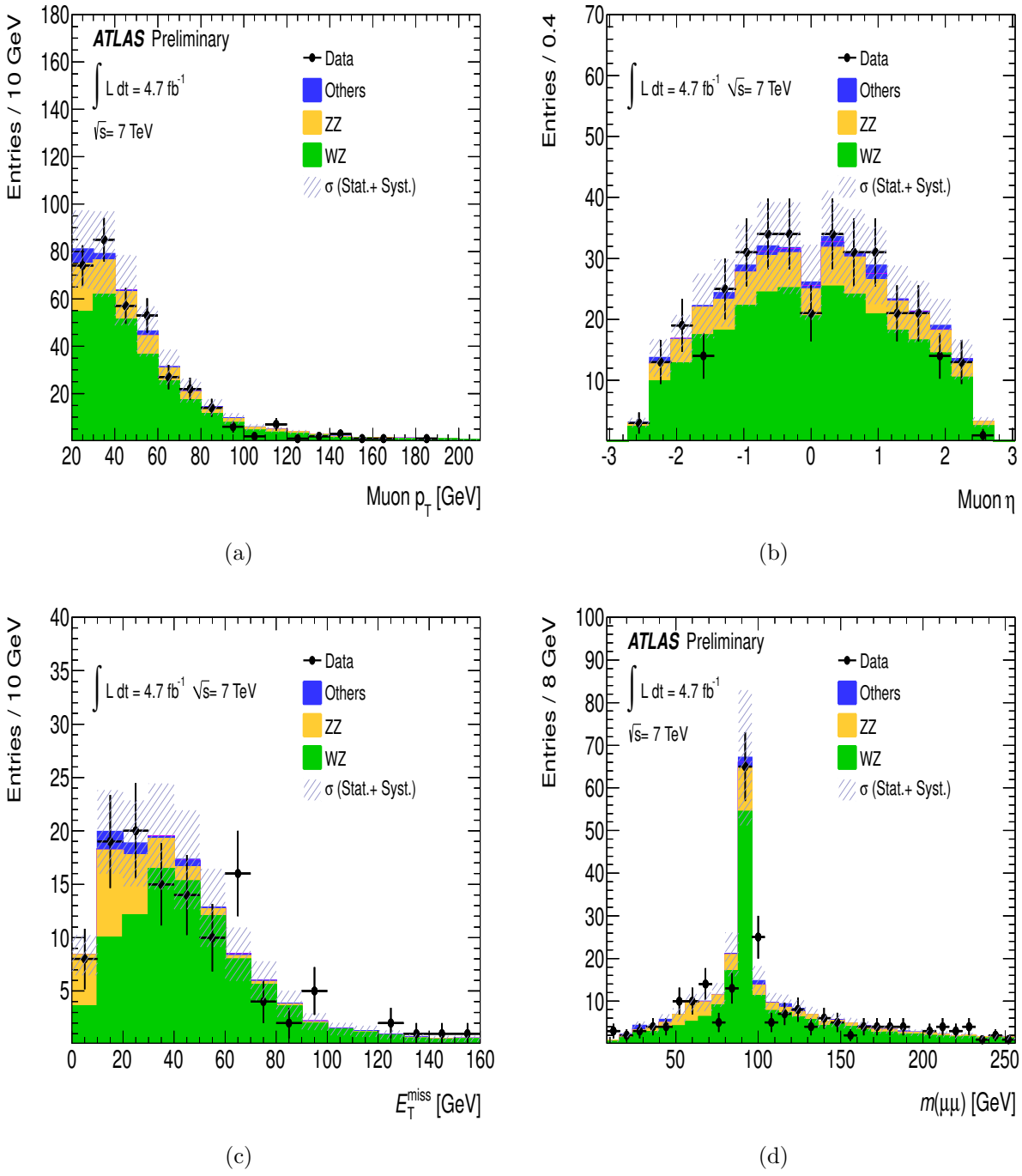

Figure 10.4: Distributions in the sample of events containing three muons of (a) the muon p_{T}, (b) the muon η, (c) $E_{\mathrm{T}}^{\mathrm{miss}}$ and (d) the invariant mass of the opposite-sign muons. The blue hatched area is the combined systematic and statistical uncertainty.

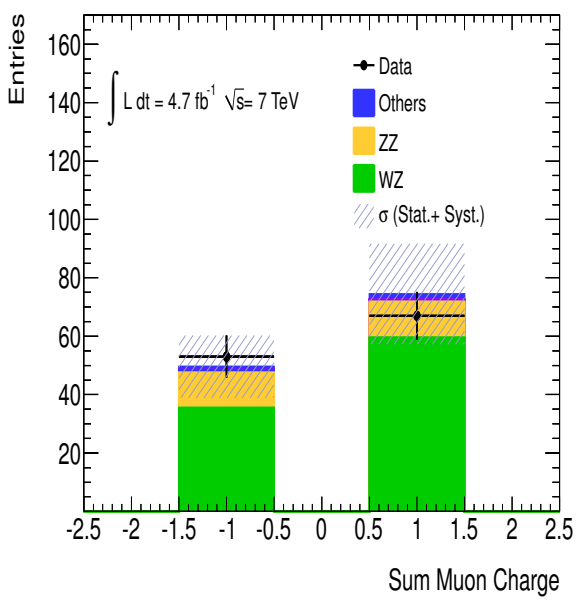

(a)

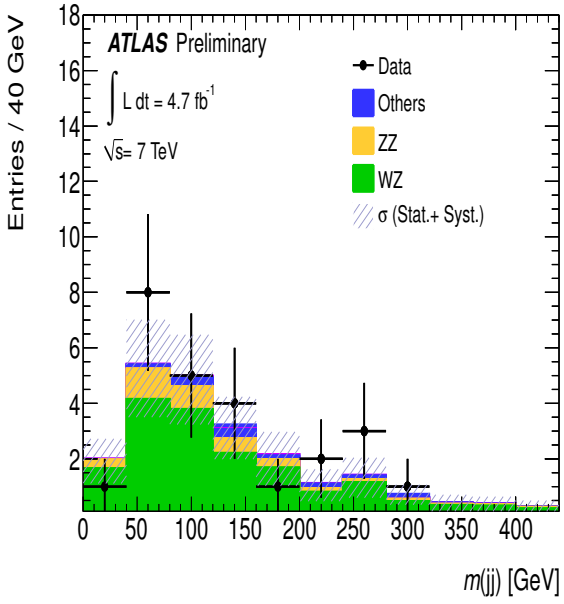

(b)

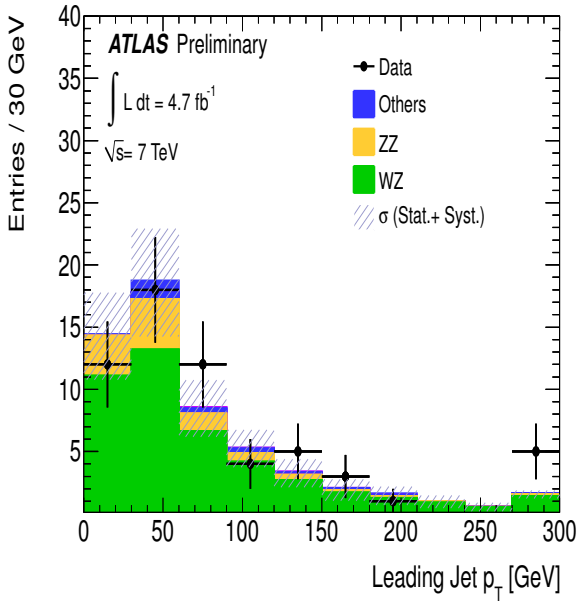

(c)

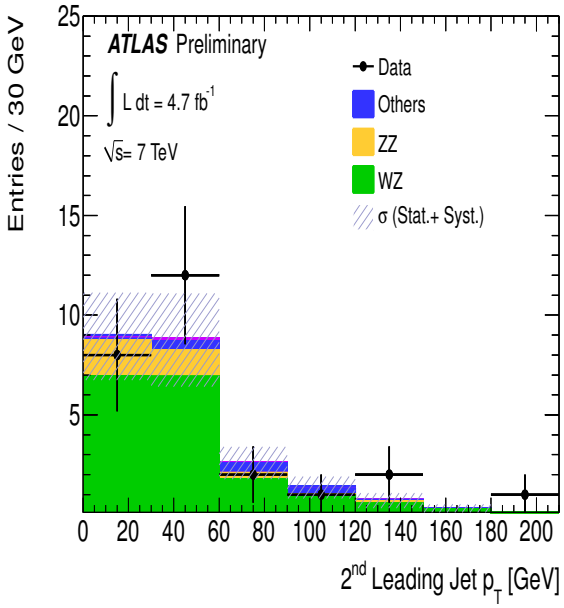

(d)

Figure 10.5: Distributions in the sample of events containing three muons of (a) the summed muon charge, (b) the invariant mass of the two leading jets, and the (c) leading and (d) subleading jet p_{T}. The blue hatched area is the combined systematic and statistical uncertainty.

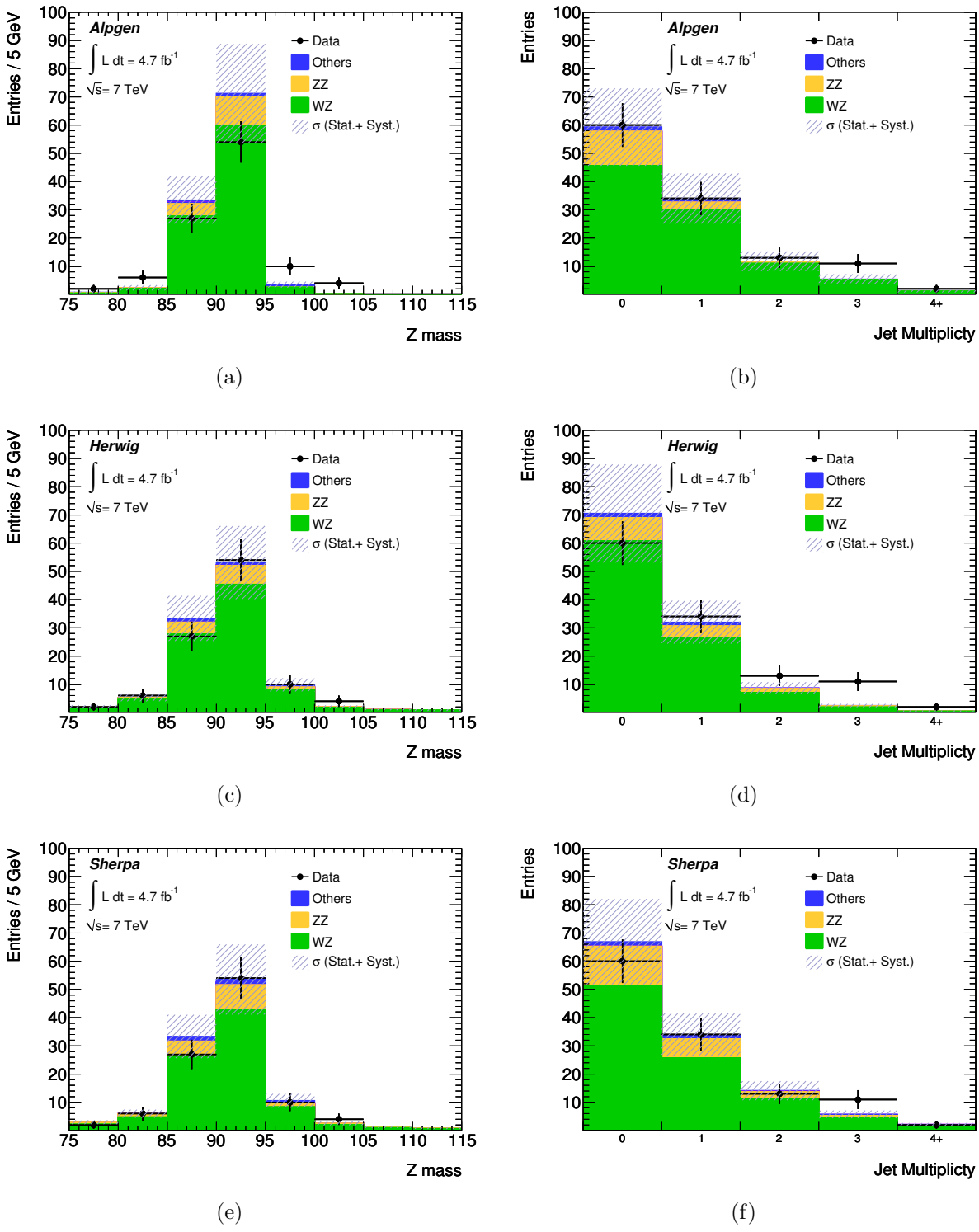

Figure 10.6: Distribution of the invariant mass of the opposite-sign muon pair closest to the Z mass (left) and jet multiplicity (right) for events with three muons. The diboson events are simulated with (top) ALPGEN, (middle) HERWIG and (bottom) SHERPA. The blue hatched area is the combined systematic and statistical uncertainty.

10.1.3 Control Regions with Single Muon and Low Missing Transverse Energy

Events containing a single muon with low missing transverse energy ($E_{\mathrm{T}}^{\mathrm{miss}} < 20$ GeV) and at least one jet are used to validate the estimate of the non-prompt muon backgrounds. The matrix method in the single muon events is more sensitive to the correct knowledge of the efficiency for non-prompt muons to pass the isolation than in the multi muon case. This sample can validate that the non-prompt and real efficiencies measured in section 9.2.3 are reasonable.

The muons are split further into cases where the muons are close to a jet that has been tagged as a heavy-flavour jet or not. This is done using the `MV1` tagger, which has a 60 % efficiency of correctly tagging a b-hadron. This is to test the modelling of the non-prompt background in both events with light- and heavy-flavour jets. The angular separation between the muon and closest jet are shown for this control sample in Figure 10.7. The separation peaks at a value of π. This is expected by momentum conservation. For events with a heavy-flavour jet, muons from top decays are more pronounced. Muons from top decays tend to have a smaller angular separation from the jet. Although the top anti-top pair are produced back-to-back, the muon and b-jet ($t \to W^{\pm}b \to \mu^{\pm}\nu b$) are not.

Distributions of the muon p_{T} and η for different jet multiplicities can be seen in Figures 10.8, 10.9, 10.10 and 10.10 for events which contain a b-jet and all events respectively. The muon p_{T} from the non-prompt sources tend to be low, with the majority of these processes producing a muon with $p_{\mathrm{T}} < 40$ GeV. The shape of the p_{T} changes as we require more jets in the event, most noticeably the peak in the distribution shifts to higher momentum as the non-prompt background becomes less dominant and muons from $t\bar{t}$ and W+jets contribute more.

In summary the data are well described by the non-prompt estimates.

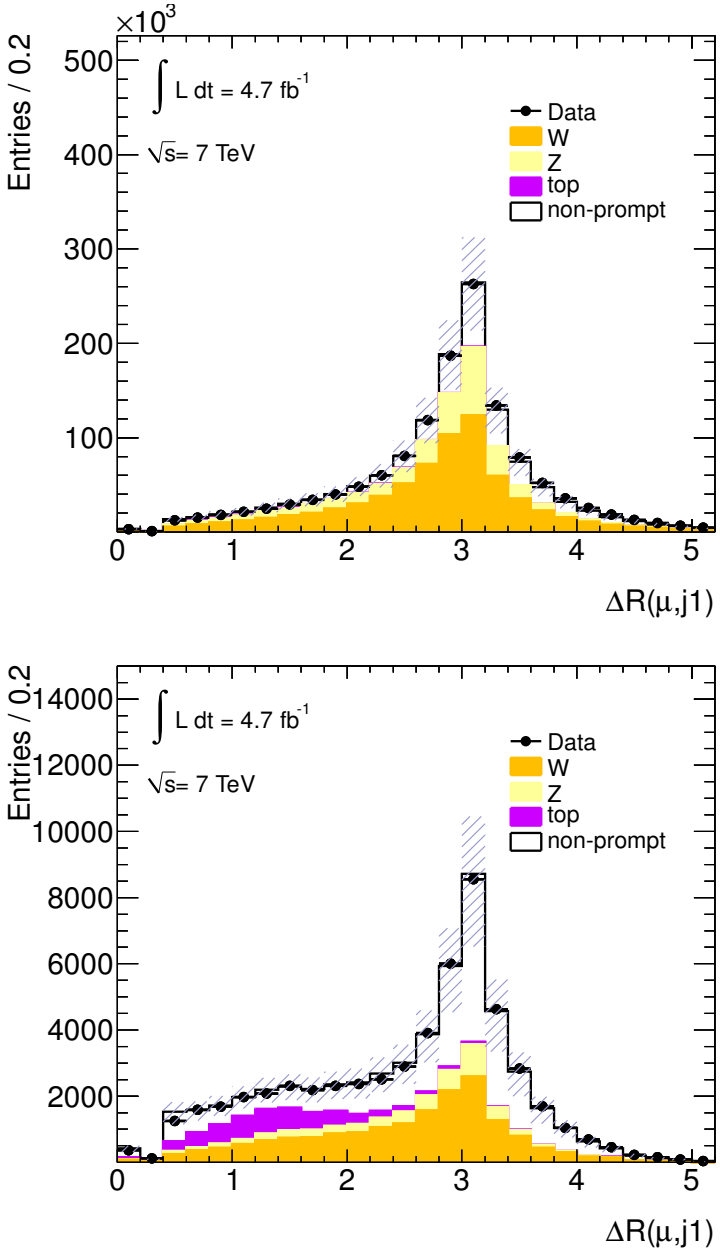

Figure 10.7: Distribution of ΔR between isolated muons and the closest jet in events with only one muon, low missing transverse energy and at least one jet (top) and at least one b-tagged jet (bottom). The uncertainty shown is both statistical and systematic.

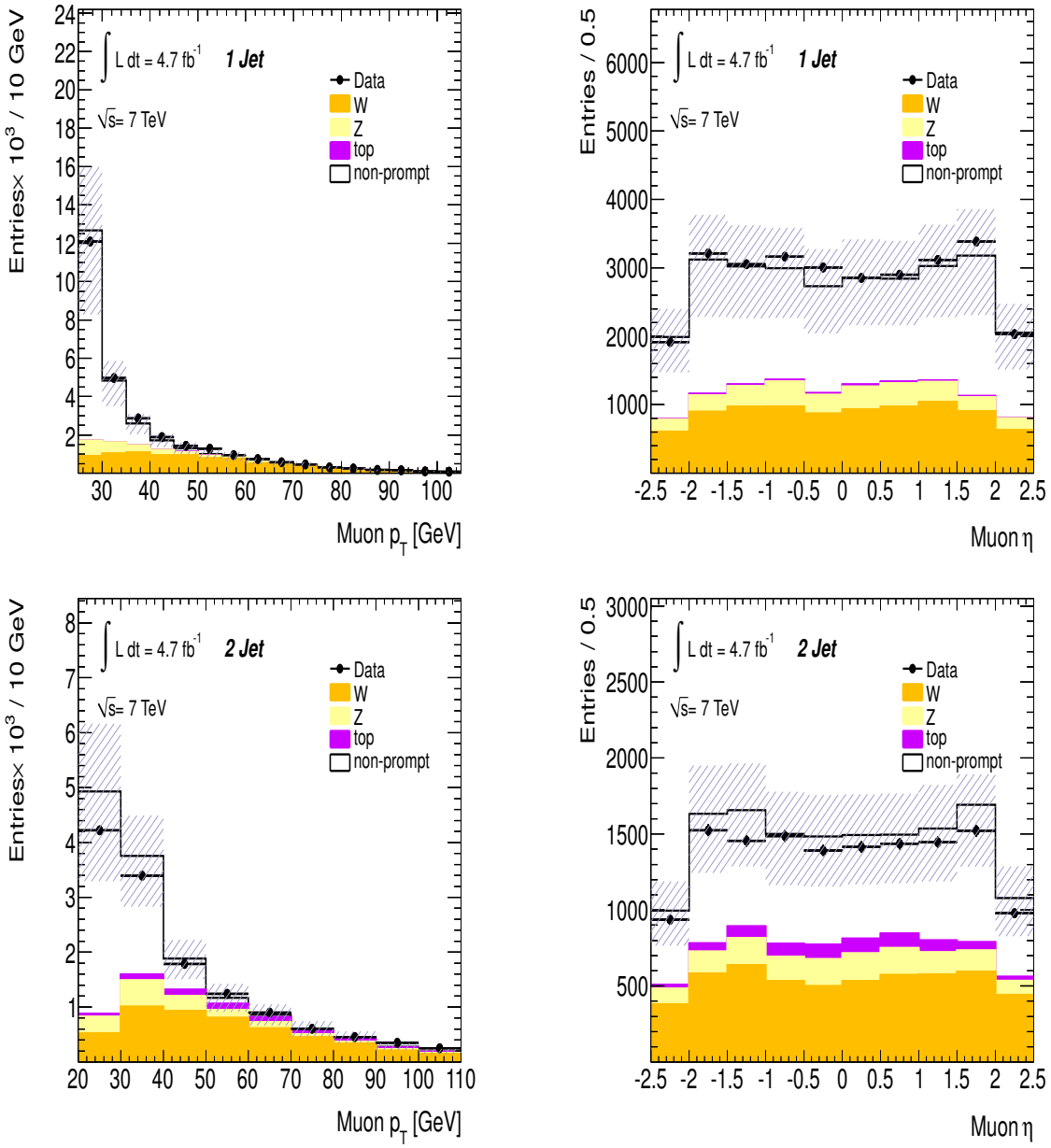

Figure 10.8: Distributions of p_{T} (left) and η (right) of isolated muons in events with only one muon, low missing transverse energy and at least one b-tagged jet. The top row shows events with one jet while the second row shows events with two jets. The uncertainty shown is both statistical and systematic.

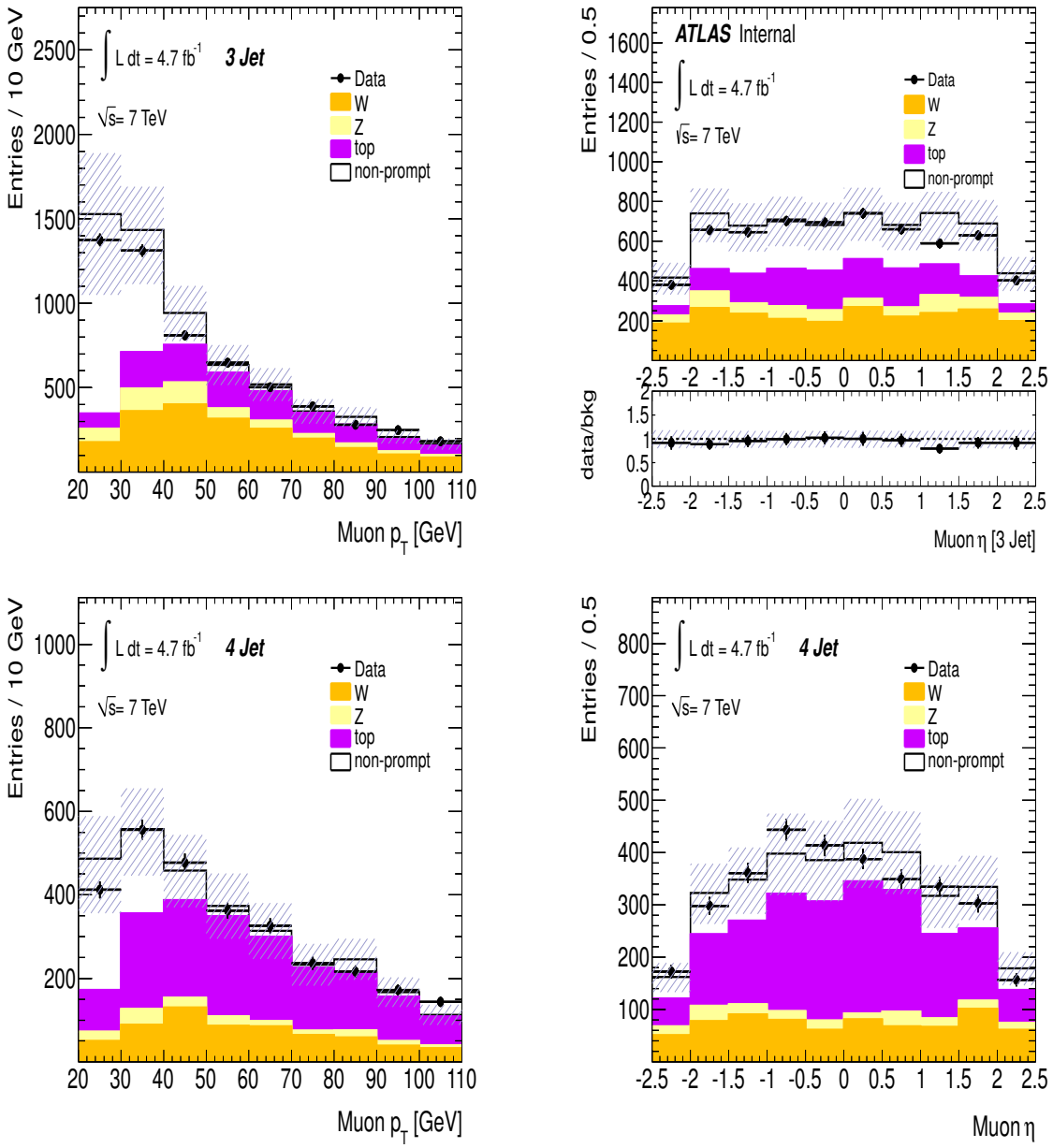

Figure 10.9: Distributions of p_{T} (left) and η (right) of isolated muons in events with only one muon, low missing transverse energy and at least one b-tagged jet. The top row shows events with three jets and the bottom row shows events with four jets. The uncertainty shown is both statistical and systematic.

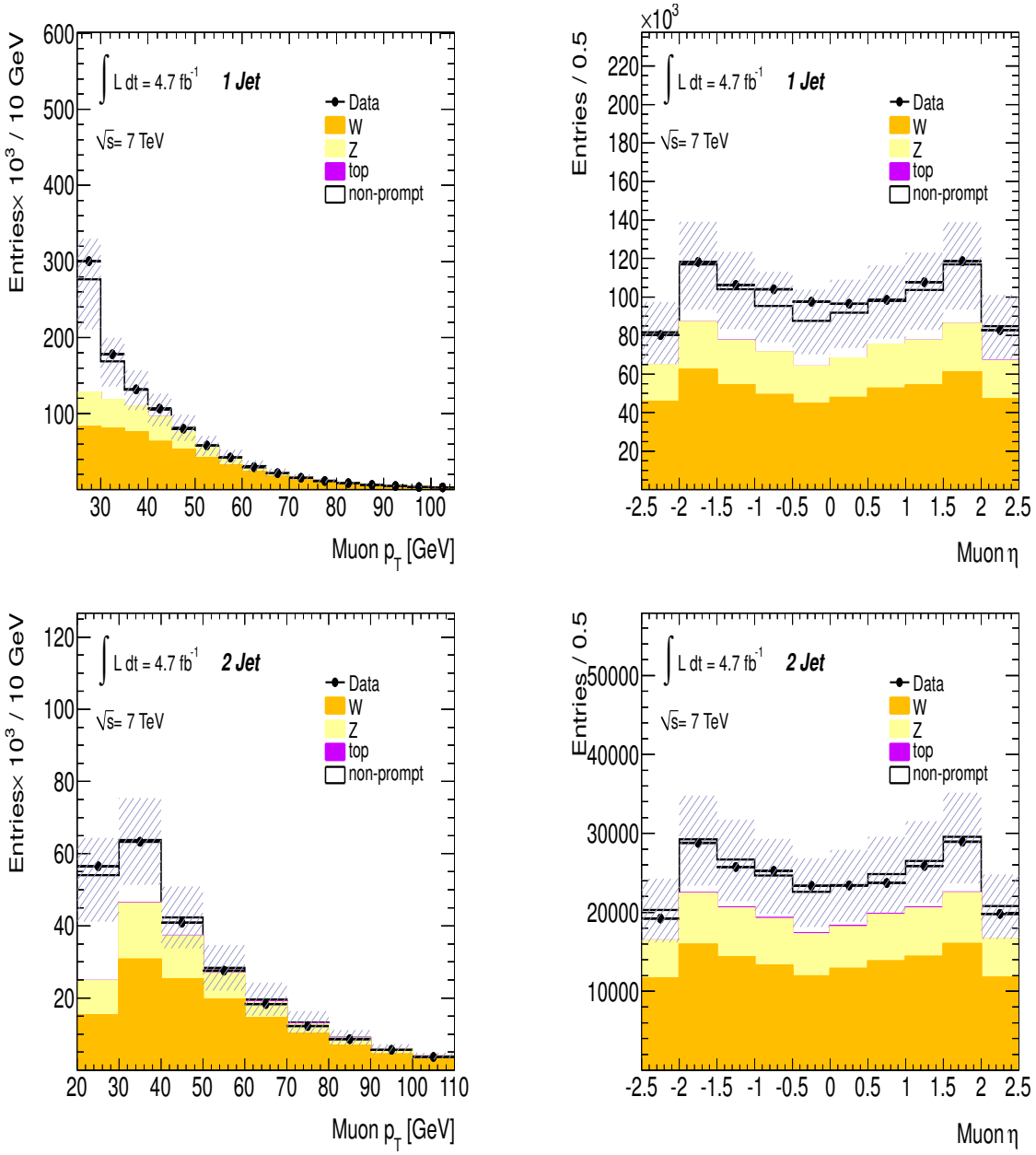

Figure 10.10: Distributions of p_{T} (left) and η (right) of isolated muons in events with only one muon, low missing transverse energy and no b-tagged jets. The top row shows events with one jet and the second row shows events with two jets. The uncertainty shown is both statistical and systematic.

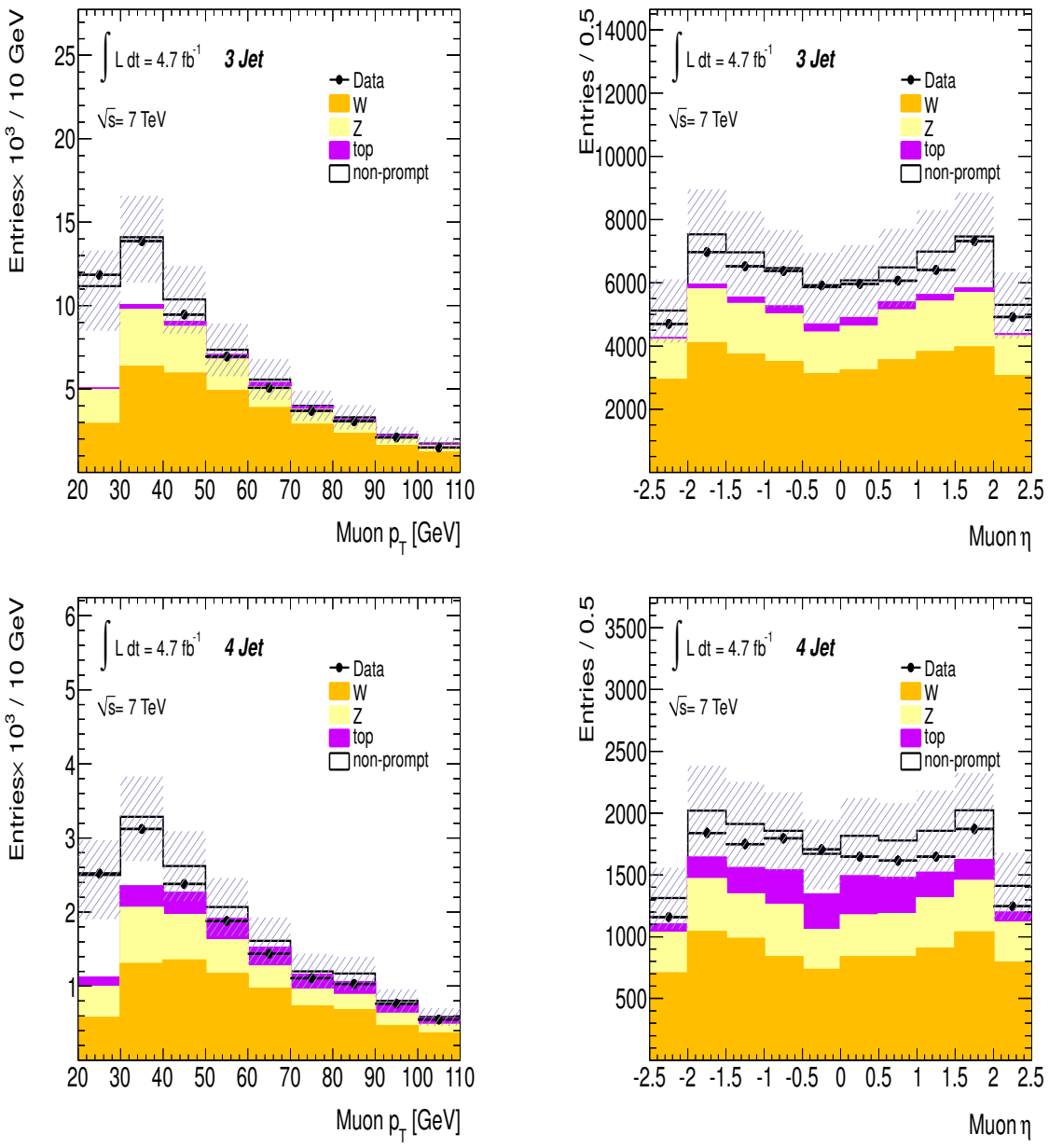

Figure 10.11: Distributions of p_{T} (left) and η (right) of isolated muons in events with only one muon, low missing transverse energy and no b-tagged jets. The top row shows events with three jets and the second row shows events with four jets. The uncertainty shown is both statistical and systematic.

Process	$N_{Jets} = 0$	$N_{Jets} < 2$, $m_{\mu\mu} < 110$ GeV
WZ	$18 \pm 1 \pm 5$	$20 \pm 1 \pm 6$
ZZ	$4.6 \pm 0.2 \pm 1.3$	$5.7 \pm 0.2 \pm 1.6$
$W^{\pm}W^{\pm}$+2p	$0.05 \pm 0.02 \pm 0.03$	$0.27 \pm 0.05 \pm 0.14$
$Zt\bar{t}, Wt\bar{t}$	$0.02 \pm 0.01 \pm 0.01$	$0.02 \pm 0.01^{+0.01}_{-0.02}$
Fake	$10 \pm 2^{+1}_{-3}$	$14 \pm 3^{+2}_{-5}$
Total	$33 \pm 3^{+5}_{-6}$	$40 \pm 3^{+6}_{-8}$
Data	33	33

Table 10.4: Predicted background for events with two same-sign charge muons and observed data for a total integrated luminosity of 4.7 fb^{-1}.

10.1.4 Control Region with Same-Sign Muon Pairs with 0 or 1 jet.

To validate the modelling of events with exactly two muons with same electrical charge whilst not looking at events in the signal region, same-sign events are selected with less than two jets. To further suppress contribution from events in the LRSM with a boosted N (resulting in only 1 jet in the final state) events are removed where the invariant mass of the two leptons is greater than 110 GeV in only the 1 jet channel. This gives two independent control regions, one with exactly zero selected jets and one with exactly one selected jet and $m_{\mu\mu} < 110$ GeV. The control regions are dominated by diboson events and non-prompt muon backgrounds. Thus it probes the modelling of these dominant background channels. The predicted background and observed data for both control regions are found to be in good agreement as shown in Table 10.4. Figures 10.12 and 10.13 shows several kinematic distributions for events in this control region. The data events and background predictions are peaked both at low momentum for the trailing muon p_{T}, mostly with $p_{\mathrm{T}} < 30$ GeV. This suggests a contribution of both $b\bar{b}$ events, which have low $E_{\mathrm{T}}^{\mathrm{miss}}$, and $t\bar{t}$ or W+jets, which have large $E_{\mathrm{T}}^{\mathrm{miss}}$. The predicted background shape for this distribution agrees well with the data. The muon pairs in the background estimates are generally back-to-back in ϕ. This is also presumably the case for non-prompt muons from $b\bar{b}$, where one of the muons is found in the jet. Muon pairs in WZ events are generally not back-to-back in ϕ. This shape again agrees with the data. It can be seen that the background predictions in these events do a good job in modelling the data.

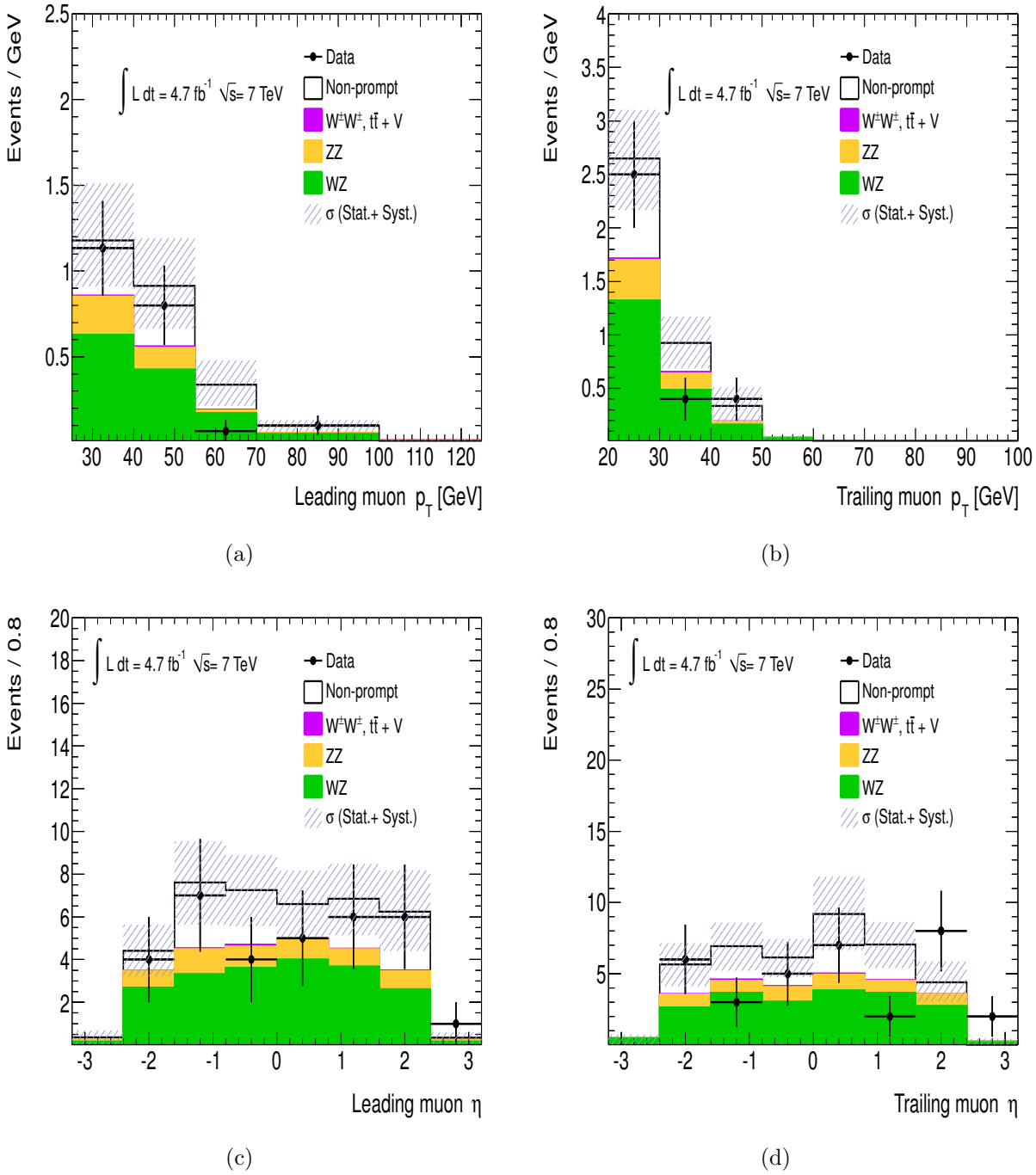

(a) (b)

(c) (d)

Figure 10.12: Distributions of the (a) trailing and (b) leading muon p_{T}, the (c) leading and (d) trailing muon η The hashed line is the combined systematic and statistical uncertainty band.

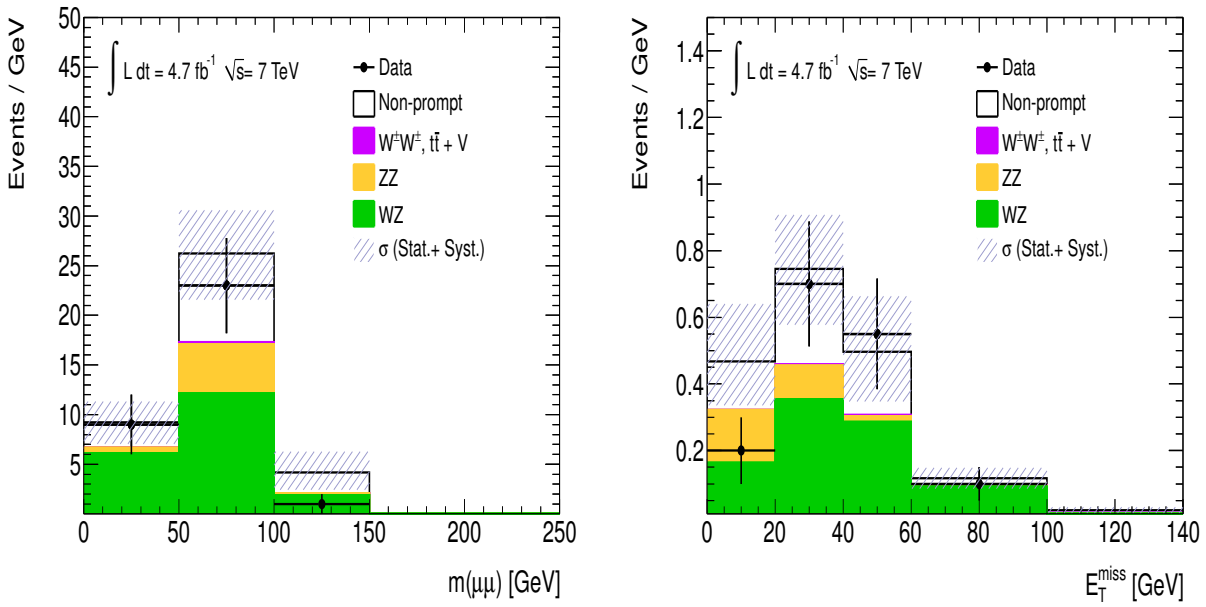

(a) (b)

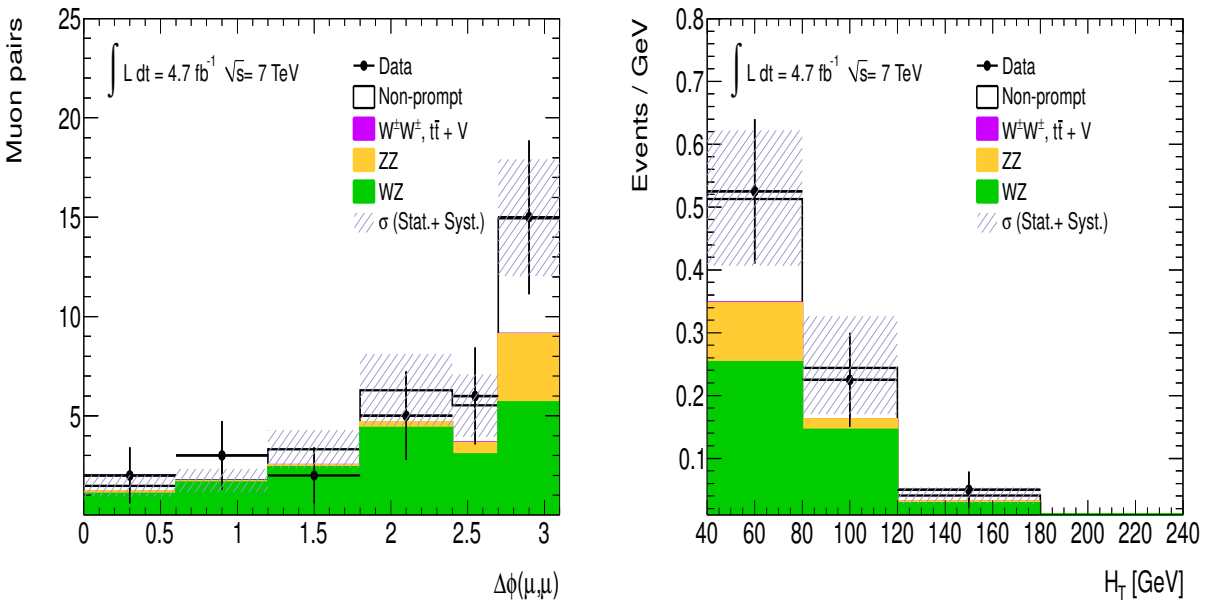

(c) (d)

Figure 10.13: Distributions of (a) the invariant mass of the two muons, (b) $E_{\mathrm{T}}^{\mathrm{miss}}$, (c) $\Delta\phi$ between muons and (d) the summed momentum of muons and jets.

Source of Uncertainty	WZ	ZZ	$W^{\pm}W^{\pm}+2p$	W+$t\bar{t}$	Z+$t\bar{t}$
Statistical	$\pm$17	$\pm$22	$\pm$27	$\pm$27	$\pm$71
JES$\uparrow$	10	8	1	$-$9	$-$57
JES$\downarrow$	$-$15	$-$6	0	1	0
JER	8	$-$14	$-$7	$-$22	50
MS$\uparrow$	2.0	0.0	0.0	3.2	0.0
MS$\downarrow$	0.0	0.0	0.0	0.0	0.0
ID$\uparrow$	0.0	0.0	0.0	0.0	0.0
ID$\downarrow$	0.0	0.0	0.0	0.0	0.0
Muon Reconstruction	1.0	2.0	1.0	1.0	1.0
Trigger SF	1.0	1.0	1.0	1.0	1.0
$E_{\mathrm{T}}^{\mathrm{miss}}$	1.0	1.0	1.0	1.0	1.0
Normalisation	28	28	50	50	50
Luminosity	1.8	1.8	1.8	1.8	1.8
Total	+35 / $-$37	+36 / $-$38	+58 / $-$59	+60 / $-$59	$\pm$100

Table 10.5: Assigned systematics to Monte Carlo derived backgrounds for events with two same-sign muons, two or more jets, $E_{\mathrm{T}}^{\mathrm{miss}} < 35$ GeV and m(jj) in the W mass window as a percentage of the central value.

10.2 Systematic Uncertainties

This section is an overview of the systematics effects that can result in a change in the yield of signal and background predictions in our signal region. The sources are listed below. Tables 10.5 to 10.8 summarise the impact of all the systematic and statistical uncertainties assigned to both signal and background in our signal region.

10.2.1 Signal Efficiency Uncertainties

Fast Simulation

The calorimeter response in the signal MC events was performed with a fast simulation unlike in the case of the MC background events which used the full detector simulation. The uncertainly in the signal acceptance due to the fast calorimeter simulation has been studied and a 3 % uncertainty is introduced to cover the discrepancies between the fast and full simulation. Detailed studies are shown in section 5.2.1.

Parton Distribution Function Uncertainties

Uncertainties in the parton distribution functions (PDF) lead to uncertainties in the efficiency to select signal events. Following the recommendations from the PDF4LHC group [112], the MSTW08NLO [113], CTEQ66 [114] and NNPDF2.0 [115] PDFs were considered and signal efficiencies were computed for each of their associated error sets (respectively 40, 44

Source of Uncertainty	m_{N} =100 GeV	m_{N} =120 GeV	m_{N} =140 GeV
Statistical	2.2	1.2	1.0
JES↑	4.5	5.2	3.3
JES↓	−5.6	−5.9	−4.7
JER	2.3	3.8	4.0
MS↑	−0.1	−0.0	−0.1
MS↓	0.1	0.1	0.1
ID↑	0.0	0.1	0.0
ID↓	0.0	0.1	0.0
Muon Reconstruction	0.5	0.5	0.6
Trigger SF	0.6	0.6	0.6
$E_{\mathrm{T}}^{\mathrm{miss}}$	1.0	1.0	1.0
PDF	1.8	1.8	1.8
AtlfastII	3.0	3.0	3.0
Luminosity	1.8	1.8	1.8
Total	+6.8/−7.0	+7.7/−8.2	+6.6/−7.4

Table 10.6: Assigned systematics to signal Monte Carlo for events with two same-sign muons, two or more jets, $E_{\mathrm{T}}^{\mathrm{miss}} < 35$ GeV and m(jj) in the W mass window as a percentage of the central value.

Source of Uncertainty	m_{N} =160 GeV	m_{N} =180 GeV	m_{N} =200 GeV
Statistical	1.0	0.9	0.9
JES↑	3.2	2.7	2.2
JES↓	−3.6	−3.6	−3.1
JER	3.7	3.6	3.7
MS↑	−0.1	−0.2	−0.2
MS↓	0.1	0.1	0.2
ID↑	0.0	0.0	0.0
ID↓	0.0	0.1	−0.1
Muon Reconstruction	0.6	0.6	0.6
Trigger SF	0.7	0.7	0.6
$E_{\mathrm{T}}^{\mathrm{miss}}$	1.0	1.0	1.0
PDF	1.8	1.8	1.8
AtlfastII	3.0	3.0	3.0
Luminosity	1.8	1.8	1.8
Total	+6.4/−6.6	+6.1/−6.6	+5.9/−5.6

Table 10.7: Assigned systematics to Monte Carlo derived backgrounds for events with two same-sign muons, two or more jets, $E_{\mathrm{T}}^{\mathrm{miss}} < 35$ GeV and m(jj) in the W mass window as a percentage of the central value.

Source of Uncertainty	m_{N} =240 GeV	m_{N} =280 GeV	m_{N} =300 GeV
Statistical	0.8	0.8	0.8
JES↑	2.1	1.4	1.3
JES↓	−2.3	−1.6	−1.4
JER	4.1	3.6	4.8
MS↑	−0.3	−0.4	−0.5
MS↓	−0.3	−0.4	−0.4
ID↑	0.0	0.0	0.0
ID↓	−0.1	−0.0	−0.1
Muon Reconstruction	0.6	0.6	0.6
$E_{\mathrm{T}}^{\mathrm{miss}}$	1.0	1.0	1.0
PDF	1.8	1.8	1.8
Trigger SF	0.7	0.7	0.7
AtlfastII	3.0	3.0	3.0
Luminosity	1.8	1.8	1.8
Total	+6.2/−6.3	+5.6/−5.7	+6.5/−6.5

Table 10.8: Assigned systematics to signal Monte Carlo for events with two same-sign muons, two or more jets, $E_{\mathrm{T}}^{\mathrm{miss}} < 35$ GeV and $m(\mathrm{jj})$ in the W mass window as a percentage of the central value.

and 100 members). For MSTW08NLO and CTEQ66 the error $\Delta\epsilon$ on the central value of the signal efficiencies were computed as

$$\Delta\epsilon = \frac{1}{2}\sqrt{\sum_{i=1}^{N} |\epsilon_i - \epsilon_0|^2} \tag{10.1}$$

where ϵ_0 is the signal efficiency from the central PDF value, ϵ_i the signal efficiency computed from the i^{th} error set and N the number of available error sets. The central value was also computed for the LO PDFs CTEQ6L and MSTW08LO. The results are shown in Figure 10.14. These central values were compared with the signal efficiency using the default CTEQ5L. Taking this into account the uncertainty on the signal acceptance was taken as 1.8 %. As shown in Figure 10.14 this uncertainty covers the outer envelope of the error bands from CTEQ66, MSTW08NLO and NNPDF2.0 and is larger than the difference between the LO PDFs CTEQ6L, CTEQ5L and MSTW08LO.

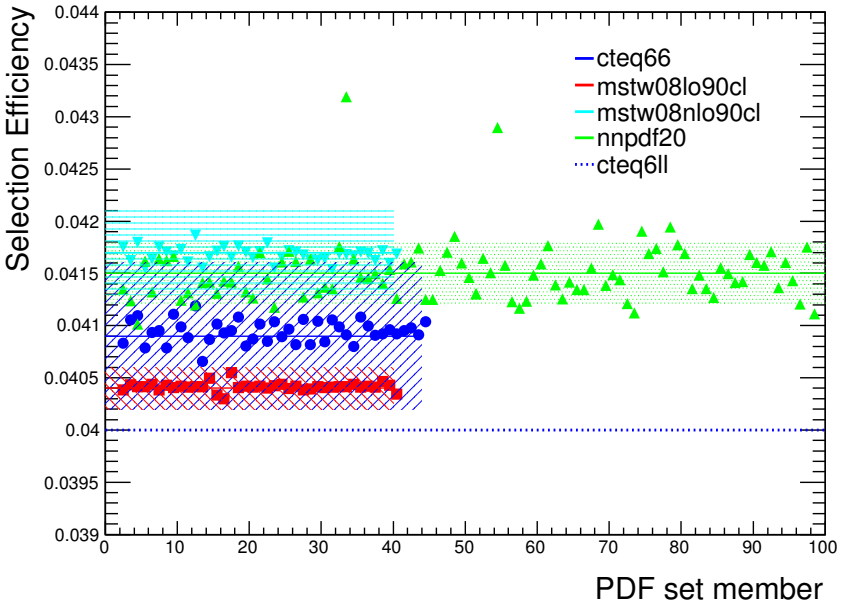

(a)

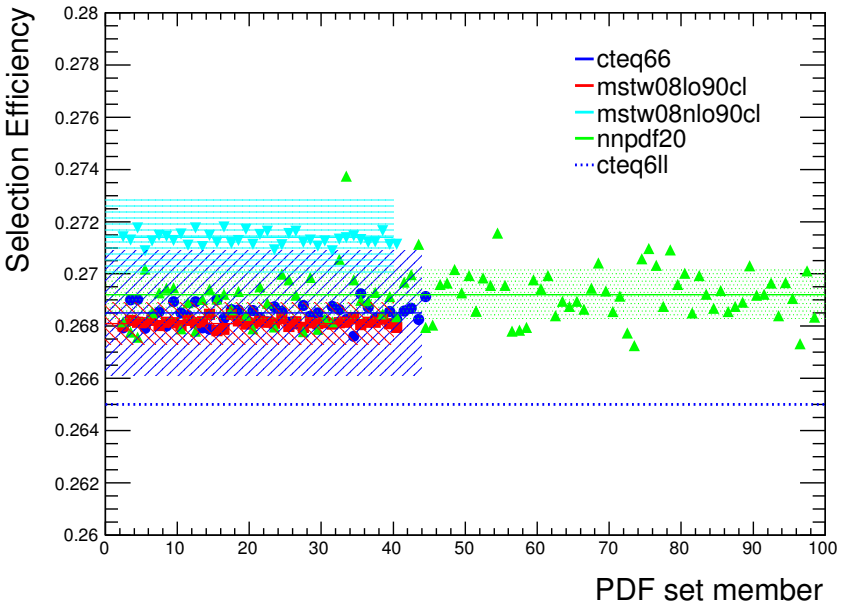

(b)

Figure 10.14: Selection efficiency for the process $pp \to W^*\mu$ followed by decay $W^* \to \mu N$ at 7 TeV for different PDF sets, for (a) $m_{\mathrm{N}} = 100$ GeV and (b) $m_{\mathrm{N}} = 200$ GeV. The bands correspond to the uncertainty on the efficiency, $\Delta\epsilon$.

10.2.2 Monte Carlo Uncertainties

There are several types of systematic uncertainties that can have an effect on both the acceptance and kinematic distributions for signal and background predictions, these include:

Muon Reconstruction

The uncertainties on the muon reconstruction and identification are obtained by taking the uncertainties on the scale factors provided by the Muon Combined Performance (MCP) Group. Generally this results in a $\pm 0.6\,\%$ uncertainty for both signal and background processes.

In addition to the recommended baseline muons cuts, from the MCP group requirements on the isolation and impact parameter cuts are made in this analysis (section 8.1.3). The efficiencies of these cuts are checked in $Z \to \mu\mu$ Monte Carlo and Z enriched data. A systematic uncertainty of $-1.4, +2.4\,\%$ is assigned for the efficiency of the muon isolation and impact parameter cuts.

Muon Momentum Resolution

As discussed in section 8.1.4 the momentum of the muon tracks are corrected in the MC simulation by applying a Gaussian smearing to the track momenta, using factors measured in Z data events by the MCP group. The smearing factors are measured in the data [116], and are assigned both a systematic and statistical uncertainty based on their measurement. The smearing factors are varied by their $\pm 1\sigma$ uncertainties for both the inner detector and muon spectrometer momentum measurements. These measurements propagate through to the combined muon track p_{T} measurement, which can result in a change in the number of events having two muons passing the muon p_{T} cut used in the analysis. The change in the event yields varies from $0{-}4.5\,\%$ depending on the process.

Trigger Efficiencies

Trigger scale factors are applied to the Monte Carlo simulation as discussed in section 8.2. The scale factors have an assigned systematic and statistical uncertainty, σ. The scale factors are shifted by $\pm 1\sigma$ and are re-applied to the Monte Carlo. The effect on the yield in the signal region is $\pm 0.6\,\%$ for all processes.

Jet Energy Scale

The systematic error on the jet energy scale were provided by the ATLAS Jet and $E_{\mathrm{T}}^{\mathrm{miss}}$ performance group [117]. The jet energy scale uncertainties are a function of jet p_{T} and η and take into account the effect of pile-up on a per event basis according to the number of vertices found in the event. The overall uncertainty due to the jet energy scale is obtained by scaling momenta of the jets up and down by the assigned uncertainty. The change in jet momenta

Process	Expected	Observed
3μ + 1 Jet	33.3 ± 9.9	34
3μ + 2 Jet	13.9 ± 4.7	13

Table 10.9: Expected and observed number of events from WZ and ZZ decays with three isolated muons and one or two additional jets using 4.7 fb^{-1} of data, after subtracting contributions from Z and top processes.

can change the number of jet objects in the event for jets with momenta near the threshold cut. In addition the shift in the jet momenta can change the reconstructed W mass. The effect of varying the jet momenta by the uncertainties on the jet energy scale on the final yields ranges from 1−6 % for signal MC samples and 8−57 % for background MC samples. The 1 % change in the $W^{\pm}W^{\pm}$ background for the scaling of the jet momenta by $+1\sigma$ in Table 10.5 is due to the fact that although several events failed the selection after this scaling the total number of events after all cuts remained the same.

Jet Energy Resolution

The systematic uncertainty on the jet energy resolution is investigated, following the jet and $E_{\mathrm{T}}^{\mathrm{miss}}$ performance group prescription, by correcting the transverse momentum of the jets [118] with a Gaussian smearing. The smearing is applied using a random Gaussian distribution to both signal and background MC samples with variations on signal yields ranging between 2−5 % and up to 50 % for certain background processes.

Uncertainty on Diboson Background Normalisation

The uncertainties associated with the normalisation of the WZ and ZZ diboson backgrounds are taken from the data control sample. Events are considered that contain three muons dominated by both WZ and ZZ (for more details see section 10.1.2). Table 10.9 shows the number of events observed in the data and predicted by the MC for events with three muons and one or two additional jets. The MC prediction agrees well with the data and the uncertainty on the normalisation of the diboson backgrounds in the signal region is taken from the statistical uncertainty in the data in the events with two additional jets, 28 %. In addition the processes W^+W^+jj, $Wt\bar{t}$ and $Zt\bar{t}$ contribute to our signal region, for which an uncertainty of 50 % [119] is assigned to the normalisation of all three samples.

Pile-up and $E_{\mathrm{T}}^{\mathrm{miss}}$

The objects used to reconstruct the $E_{\mathrm{T}}^{\mathrm{miss}}$ have an associated uncertainty in their momentum scale and resolution (including jet and muons), and any scaling factors applied as an uncertainty on these are propagated through to the $E_{\mathrm{T}}^{\mathrm{miss}}$, depending on the object type and the number of calorimeter cells associated with that object. The average number of interactions per bunch crossing is corrected to accurately model the data. The effect that the correction

has on the signal efficiency is found to be at the level of 0.1 % and is considered negligible.

The distribution of $E_{\mathrm{T}}^{\mathrm{miss}}$ in Z dominated data and MC with two jets is shown in Figure 10.15 and very good agreement is observed. The efficiency of the $E_{\mathrm{T}}^{\mathrm{miss}}$ selection cut in the inclusive Z dominated data sample is shown in Table 10.10, where we see the difference between data and MC in our signal like region of 2 or more jets is at the level of 1 %. This is assigned as a systematic uncertainty on the modelling of the missing transverse energy in the MC events.

Region	ϵ_{data}	ϵ_{MC}	$\epsilon_{\mathrm{MC}}/\ \epsilon_{\mathrm{data}}$
Inclusive	94.55	94.57	1.00
>2 Jets	88.73	90.00	1.01

Table 10.10: Efficiency (%) for events in a Z dominated sample with at least two jets for data and MC to pass the analysis cut on the missing transverse energy.

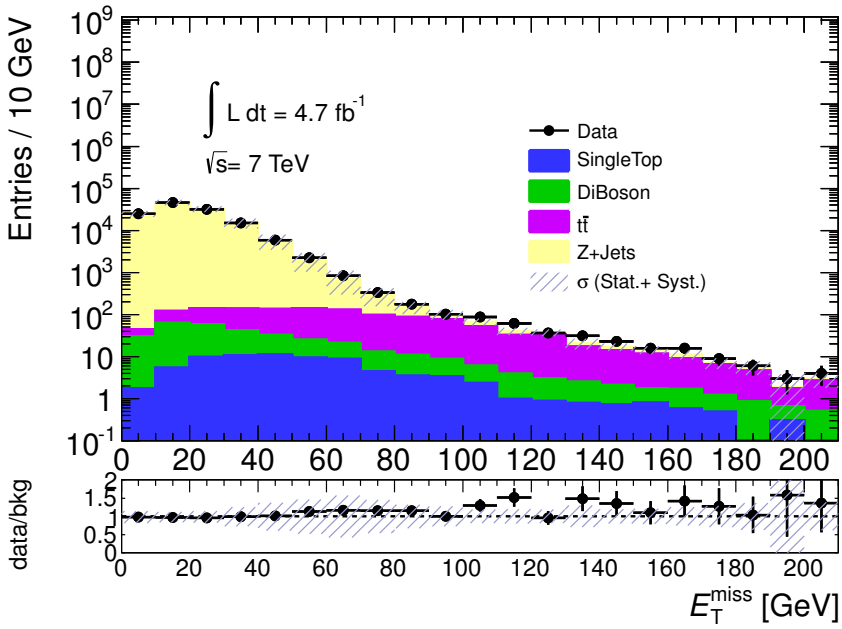

Figure 10.15: Missing Transverse Energy ($E_{\mathrm{T}}^{\mathrm{miss}}$) reconstructed in events containing two or more jets with two opposite-sign muons that have an invariant mass within a 10 GeV window of the Z mass.

Luminosity

The standard ATLAS 1.8 % [83] luminosity uncertainty is applied to all MC-based estimates.

Monte Carlo statistical uncertainties

In addition to the systematic uncertainties an uncertainty is applied for the limited statistics available in the Monte Carlo samples used in this analysis. This statistical error is added in quadrature to the systematic uncertainties mentioned above. This is generally small for

Jet Multiplicity	Nominal	R↑	R↓	F↑	F↑
0	10.2	10.6	9.5	10.9	8.3
1	5.3	5.4	4.9	6.4	3.7
2	2.7	2.8	2.5	3.2	1.7
3	2.6	2.7	2.4	3.2	1.9
4	1.7	1.7	1.6	2.1	1.1

Table 10.11: Systematic effect on the yield of expected background from non-prompt sources as a function of jet multiplicity for 4.7 fb^{-1} of data. R↑ and R↓ refer to the background estimation when the real lepton efficiencies are increased/decreased by the uncertainty on the measured efficiencies. F↑ and F↓ refer to the background estimate when non-prompt lepton efficiencies increases/decreased by the uncertainty on the measured efficiencies.

our signal, with an uncertainty of 1−2 %, but larger for all backgrounds; this is typically 10−70 % in our signal region.

10.2.3 Data Driven Uncertainties

Uncertainty on non-prompt background

The statistical uncertainty on the non-prompt background due to the limited number of events is 47 % in the signal region compared to 17 % in the inclusive same-sign sample. The uncertainties on the non-prompt and real efficiencies discussed in section 9.2.3 are propagated through the matrix method to give the systematic uncertainty on the non-prompt background estimate. In the signal region the systematic is of the level of 30 %, which is added in quadrature to the statistical error. Table 10.11 shows the predicted non-prompt background as a function of jet multiplicity with the real and non-prompt efficiencies shifted by $1 \pm \sigma$.

Each systematic source (e.g. the jet energy scale) is considered to be correlated between all the background and signal processes, while each systematic source is assumed to be uncorrelated from every other systematic source.

Chapter 11

Results

After validating the background estimates in data with four different control samples the observed number of events and kinematics of the inclusive sample of same-sign events with the full 4.7 fb^{-1} of data are checked. Comparisons of predicted backgrounds and observed data are performed for each selection cut applied to increase the signal significance and are presented in section 11.1. The results of the search are presented in section 11.2 using the data events in the signal region.

11.1 Comparison of Data and MC in Signal Region

Events in the inclusive same-sign sample are required to contain two same-sign muons as defined in section 7.2.1, with no veto on a third muon as described in section 7.2.3. Table 11.1 shows the data compared to the expected background predictions for the inclusive same-sign dataset. There is very good agreement seen between the number of predicted events and the observed number of events in data. It is necessary to also show that this agreement is seen in the modelling of the kinematic variables, especially those that are used to discriminate background events. The dominant source of backgrounds at this stage are events from semi-leptonic decays of WZ events, responsible for approximately 60% of the expected backgrounds.

Figures 11.1 and 11.2 show several kinematic distributions that are not sensitive to the signal shape. The expected signal contribution in this region ranges from $0.4-7.9\%$, depending on the mass of the heavy neutrino. The distributions for the muon transverse momentum of the leading and trailing muon are shown, with the data peaking at low momentum, with a broader distribution for the leading muon momentum. The distributions for the ϕ and the pseudo-rapidity of the muons are modelled well by the MC simulation. The angular separation for the two muons peak around $\Delta R = 3$, with a tail down to $\Delta R = 0$ as predicted, since muons pairs tend to be produced back to back in the detector. The quality of the

Source	Inclusive (SS)	3rd Muon Veto	DiJet	$E_{\mathrm{T}}^{\mathrm{miss}}$	W Window
WZ	65 ± 18	40 ± 11	8.0 ± 2	2.4 ± 0.8	1.0 ± 0.4
ZZ	17 ± 5	7.0 ± 2.0	0.7 ± 0.3	0.5 ± 0.2	0.22 ± 0.08
$W^{\pm}W^{\pm}$+2p	4.8 ± 2.4	4.6 ± 2.3	3.9 ± 2.0	0.7 ± 0.3	0.15 ± 0.09
$Zt\bar{t}, Wt\bar{t}$	4.1 ± 2.0	3.0 ± 1.5	3.0 ± 1.5	0.5 ± 0.3	0.23 ± 0.13
Non-prompt	29 ± 11	24 ± 10	9.0 ± 5	2.1 ± 1.2	1.1 ± 0.8
CMM	< 0.3	< 0.3	< 0.2	< 0.1	< 0.1
Total	120 ± 22	78 ± 15	24 ± 6	6 ± 2.0	2.7 ± 0.8
Data	124	85	31	11	3

Table 11.1: The expected and observed number of events containing two same-sign isolated muons after different event selection cuts are applied. The numbers correspond to 4.7 fb^{-1}of data. The uncertainties are both statistical and systematic.

muon tracks can be seen in Figure 11.2(c) with the majority of muon tracks having χ^2 per degree of freedom of less than 5. Figure 11.2(d) shows the fractional momentum difference between the muon track in the MS and the ID, relative to the MS measurement, which peaks at -0.1. This is predicted by our estimate and expected due to the loss of muon energy in the calorimeters. The split of events into positive and negative muon pairs (Figure 11.2(e)) agrees with the predicted background. More positive pairs are observed than negative pairs.

As explained in section 3.7 the data events are distributed between different streams by the trigger. For this analysis the muon stream is considered, as this is the collection of all events selected by the trigger to contain a muon. In addition the debug stream is analysed. The debug stream contains a small number of events, however with the low number of predicted background events after all cuts a single event found in the debug stream would impact the observed limits. No events in the debug stream were found to contain same-sign muon pairs.

After validation of some kinematics in the inclusive same-sign sample the data and background predictions are compared after each selection criteria. The number of loose muons, as described in section 7.2.3, seen in the inclusive sample is shown in Figure 11.3(a). The efficiency for the selection of only two loose muons is seen to be 68% in the data and $65 \pm 12\%$ in background. This requirement mainly removes events from WZ and ZZ background, although the WZ decays are still the dominant source of backgrounds after this requirement. The jet multiplicity per event after this selection is seen in Figure 11.3(b). After selecting events with two jets the WZ and ZZ backgrounds are significantly reduced. After this selection non-prompt backgrounds are more pronounced. A range of distributions relating to the jet kinematics for events with two or more jets with same-sign muon pairs are presented in Figure 11.4. The jets are well modelled. The ϕ of the jets is seen to be flat and the angular separation between jets in the events peak at π. This is understood as jet pairs produced in $b\bar{b}$ are produced back-to-back in the detector. Figure 11.6(a) shows the distribution for $E_{\mathrm{T}}^{\mathrm{miss}}$ before the selection cut on $E_{\mathrm{T}}^{\mathrm{miss}} < 35$ GeV. The signal peaks near zero, while the background processes peak around 50 GeV, due to the presence of high transverse momentum

neutrinos. The selection requirements remove most of the contribution from backgrounds associated with $t\bar{t}$ production, WZ and non-prompt backgrounds, removing between $70-80\%$ for all three. This leads us to believe that the composition of the non-prompt backgrounds are mainly W+jets and $t\bar{t}$, with only a small contribution from $b\bar{b}$. This observation is also consistent with the small number number of LL events compared to TL or LT events used to determine the non-prompt background in section 9.2. There is a small excess of data events compared to background predictions after requiring low $E_{\mathrm{T}}^{\mathrm{miss}}$ in the event. The probability of this happening given the number of predicted background events, the number of data events and the uncertainty of the backgrounds is 8% and is not considered significant.

The distribution of the invariant mass of the leading two jets in the events is shown in Figure 11.5(a), requiring events with low $E_{\mathrm{T}}^{\mathrm{miss}}$. The signal peaks around the W boson mass, while the backgrounds have a broader distribution. The distribution of the invariant mass of the leading two jets with the leading muon and the invariant mass of the leading two jets with the second leading muon are illustrated in Figures 11.5(c) and 11.5(d). Most of the predicted signal is expected in the bin around the mass of the neutrino, with a small leakages of the signal into neighbouring bins as a result of pairing the two jets with the incorrect muon. The background has again a broader distribution. Also shown is the p_{T} of the muons in these events. The muon p_{T} peaks in the lowest bin with $20-30$ GeV. This is consistent with non-prompt muon sources.

After requiring the invariant mass of the two leading jets to be found in the range $55-120$ GeV only three events are observed in the data. The distributions of the muon transverse momentum and summed charge of the two muons are given in Figure 11.7(a) and 11.7(b). The data events are consistent with the background expectations.

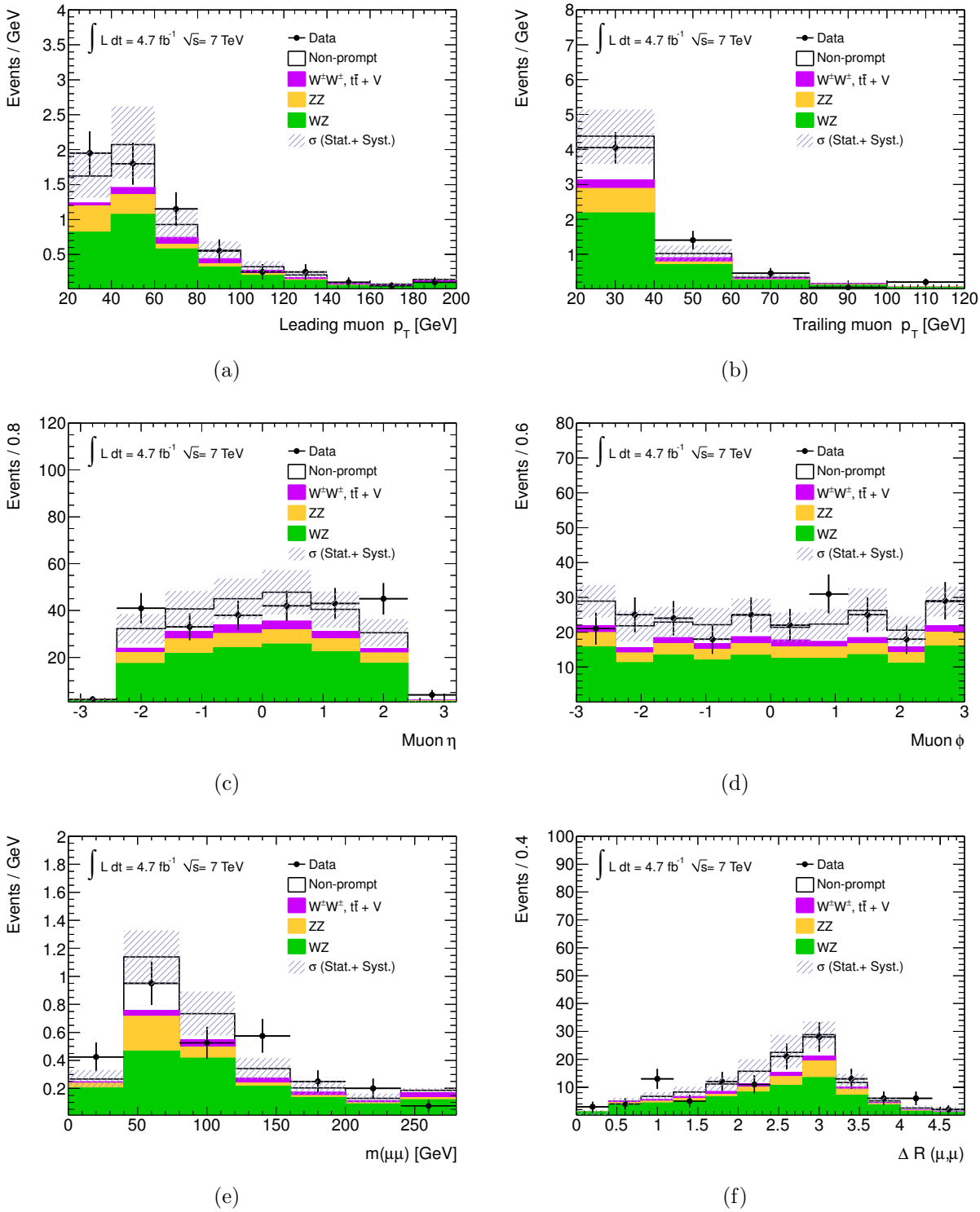

Figure 11.1: Distributions of (a) the leading muon p_{T}, (b) the trailing muon p_{T}, (c) the muon η, (d) the muon ϕ, (e) the invariant mass of the two muons and (f) the angular separation between the two muons in events with two same-sign muons.

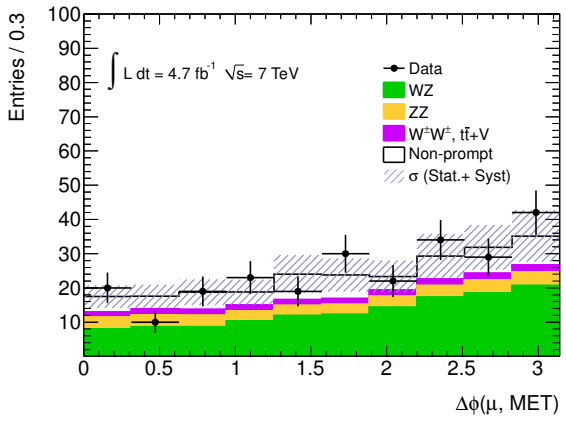

(a)

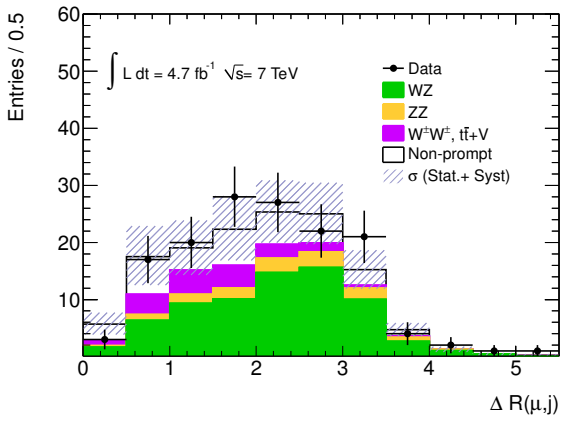

(b)

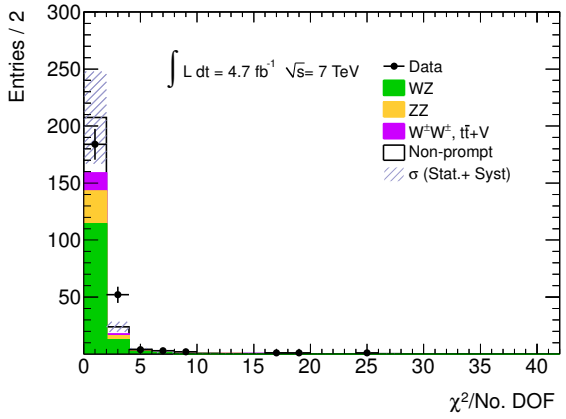

(c)

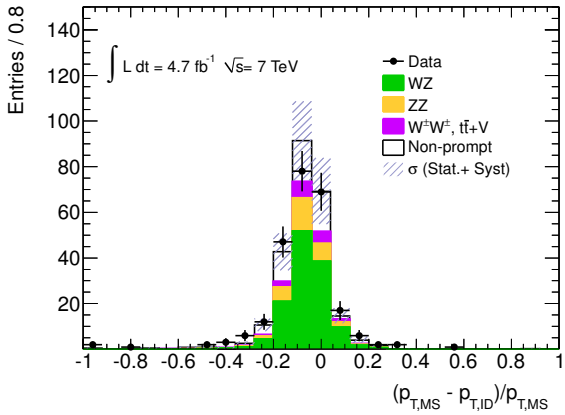

(d)

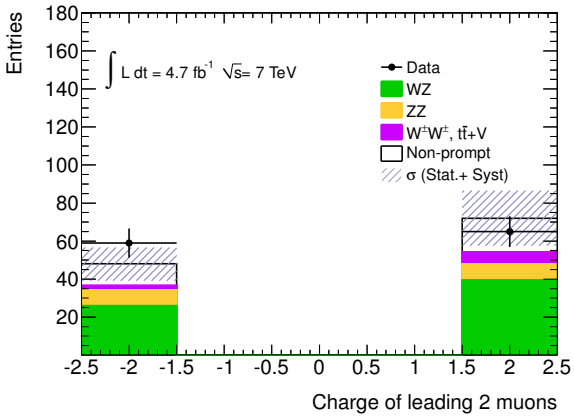

(e)

Figure 11.2: Distributions of (a) the difference in ϕ between the muon and $E_{\mathrm{T}}^{\mathrm{miss}}$, (b) the angular separation between the muon and jet, (c) the χ^2 of the track fit, per degree of freedom, (d) the relative difference in the track momentum as measured in the ID and MS detectors and (e) the summed charge of the two muons, in events with two same-sign muons.

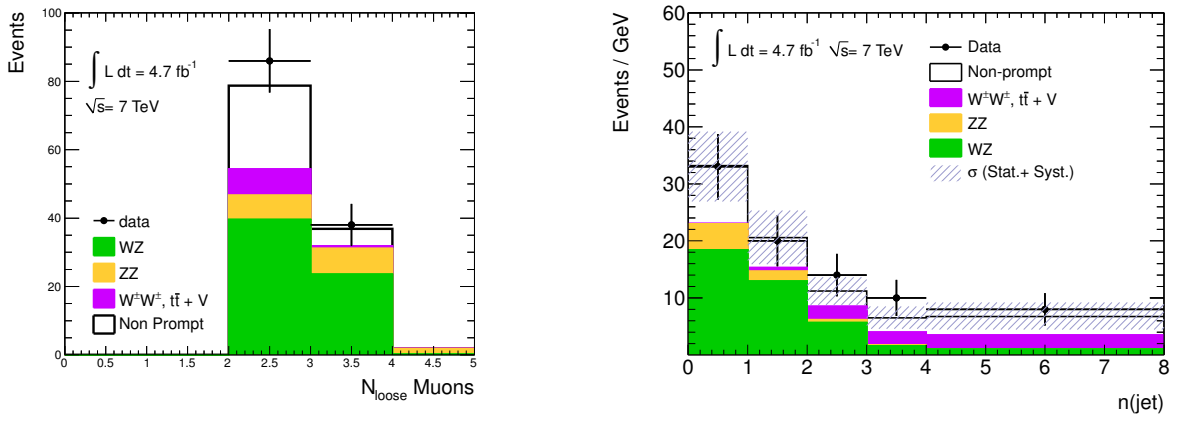

(a) (b)

Figure 11.3: Distributions of (a) the number of loose muons in events with two same-sign muons, (b) number of reconstructed jets per event in events with two same-sign loose muons.

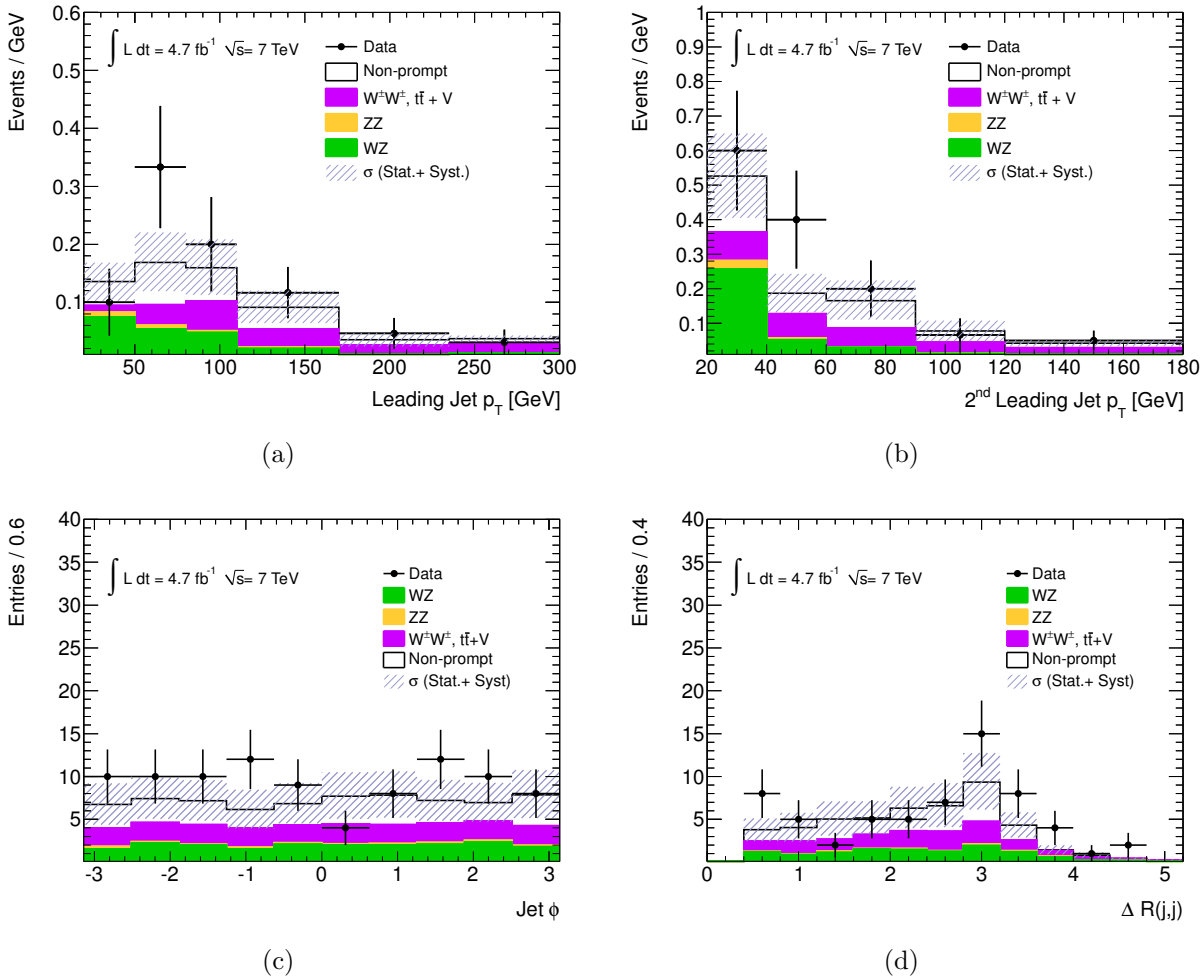

(a) (b)

(c) (d)

Figure 11.4: Distributions of (a) the p_{T} of the leading jet, (b) the p_{T} of the sub leading jet, (c) the ϕ position of all jets and (d) the angular separation between jets in events with two same-sign muons and two jets.

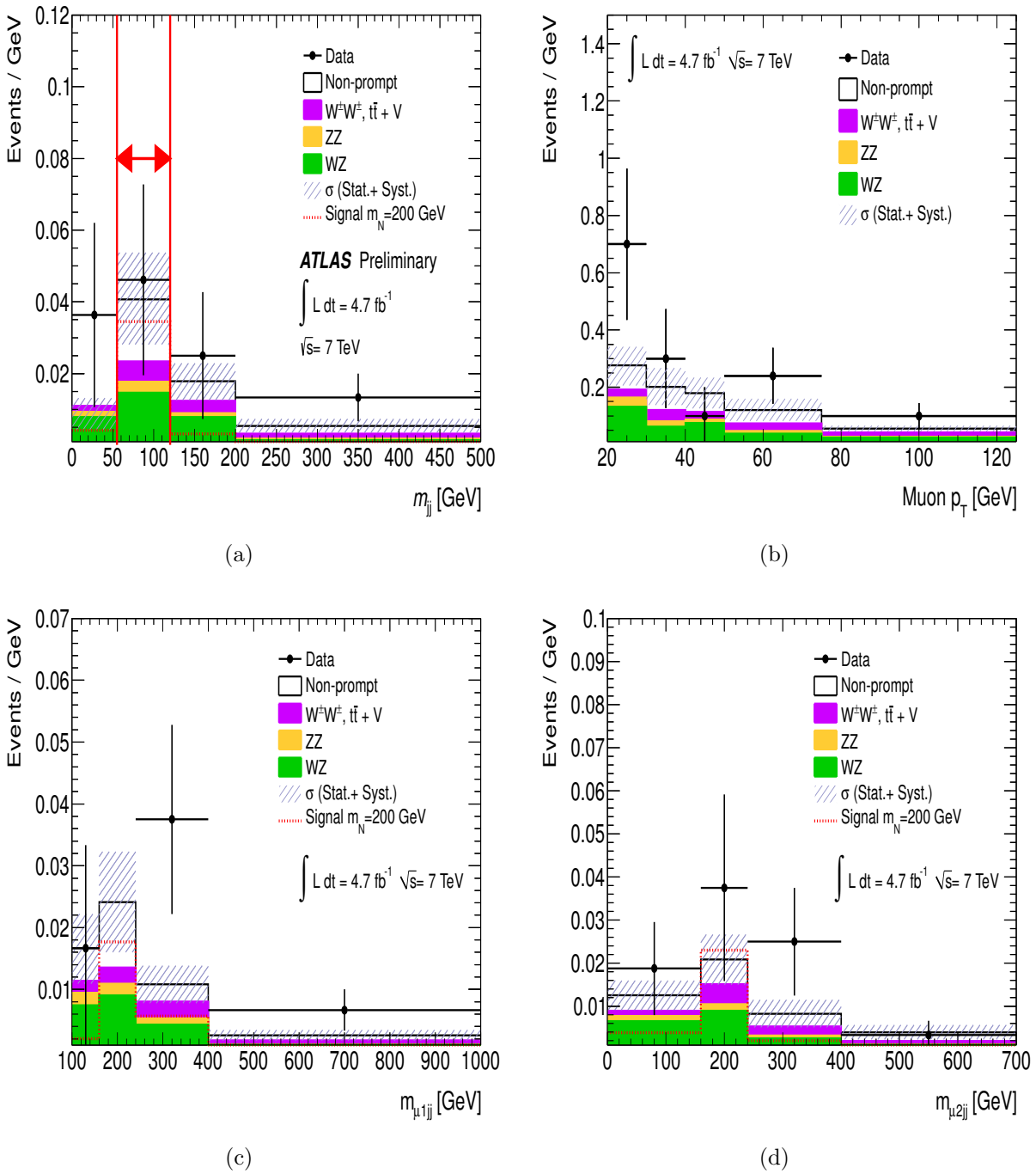

(a) (b)

(c) (d)

Figure 11.5: Distributions of (a) the invariant mass of the leading two jets, with the signal region labelled by the arrow, (b) the p_{T} of the muons, (c) the invariant mass of the two leading jets and leading muon and (d) the invariant mass of the two leading jets and sub-leading muon in events with two same-sign muons, two jets and low missing transverse momentum. The signal region is denoted by the red arrow.

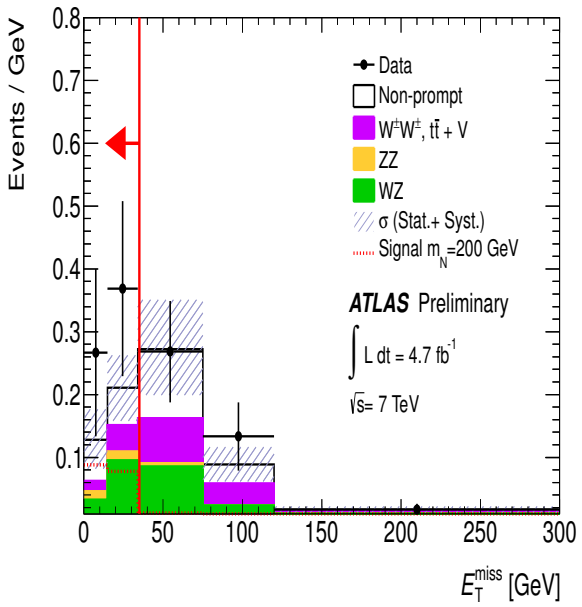

(a)

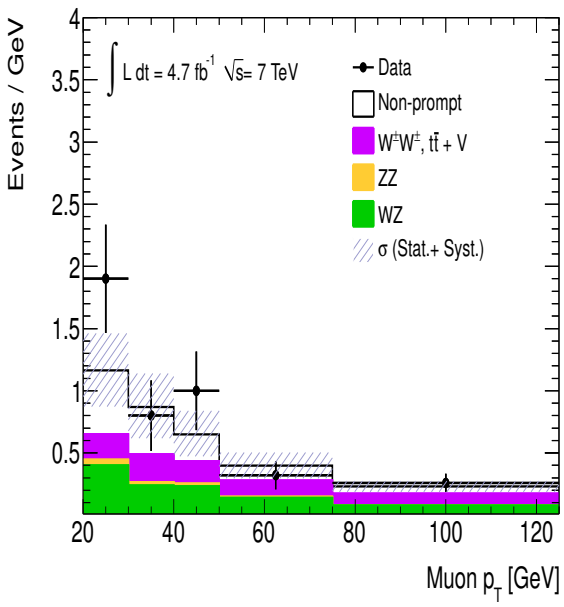

(b)

Figure 11.6: Distributions of (a) the missing transverse momentum and (b) the transverse momentum of the muons in events with two same-sign muons and two jets. The signal region is denoted by the red arrow.

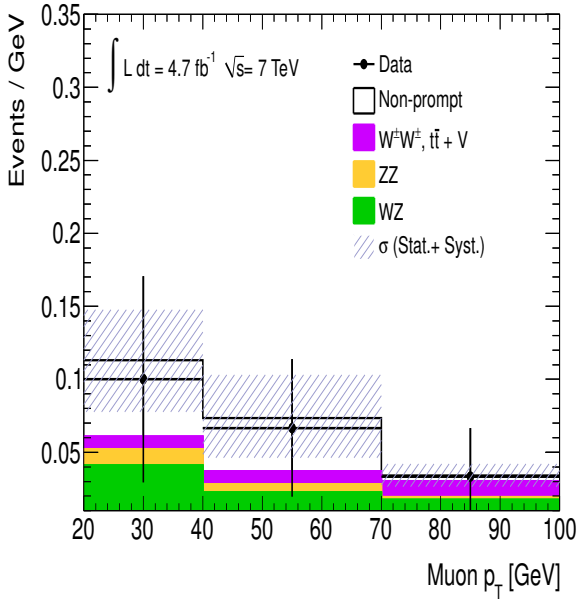

(a)

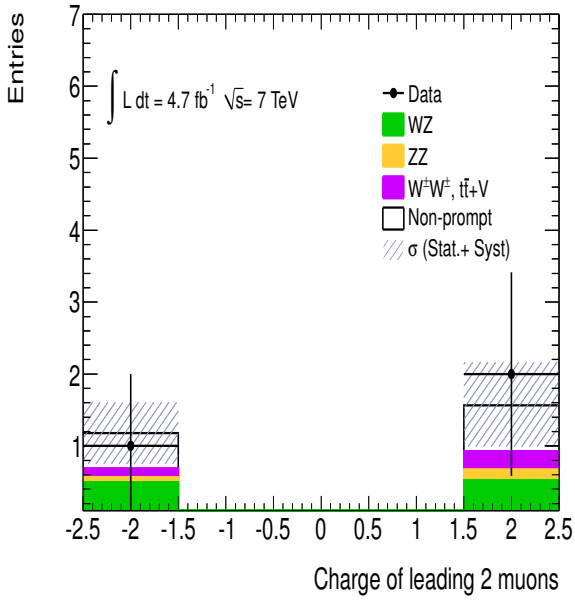

(b)

Figure 11.7: Distributions of (a) the muon p_{T} and (b) the summed charge of the two muons after all event selection cuts.

Signal Region Events

After all event selections are applied on the dataset there are $2.7 \pm 0.5^{+0.7}_{-0.6}$ events predicted and 3 data events observed. The properties of the three data events are presented in Table 11.2 and shown visually in Figures 11.8-11.10. The events all contain two muons and jets, with all the objects well separated in pseudo-rapidity and ϕ. The muons are well isolated in the detector with respect to both track and calorimeter isolation. All three events contain one high momentum muon, with the second muon high in the case of event 33533610 and soft in the other two events. The muons contain a large number of muon chamber hits and ID hits, typically 8 SCT hits, 3 pixels hits and greater than 26 TRT hits in the case of all six muons. The three events were recorded with similar pile-up conditions, originating from lumi-blocks with an average number of interactions per bunch crossing between 7 and 8. It is concluded that there are no obvious issues concerning the three events.

Event Number	Run Number	$m_{\mu_1 jj}$ [GeV]	$m_{\mu_2 jj}$ [GeV]	$p_{\mathrm{T}}^{\mu_1}$[GeV]	$p_{\mathrm{T}}^{\mu_2}$[GeV]	N_{jets}
33533610	186877	323	165	110	61	2
137182607	191139	492	188	73	22	2
133825830	190933	278	155	68	22	2

Table 11.2: Basic properties for events passing all selection criteria.

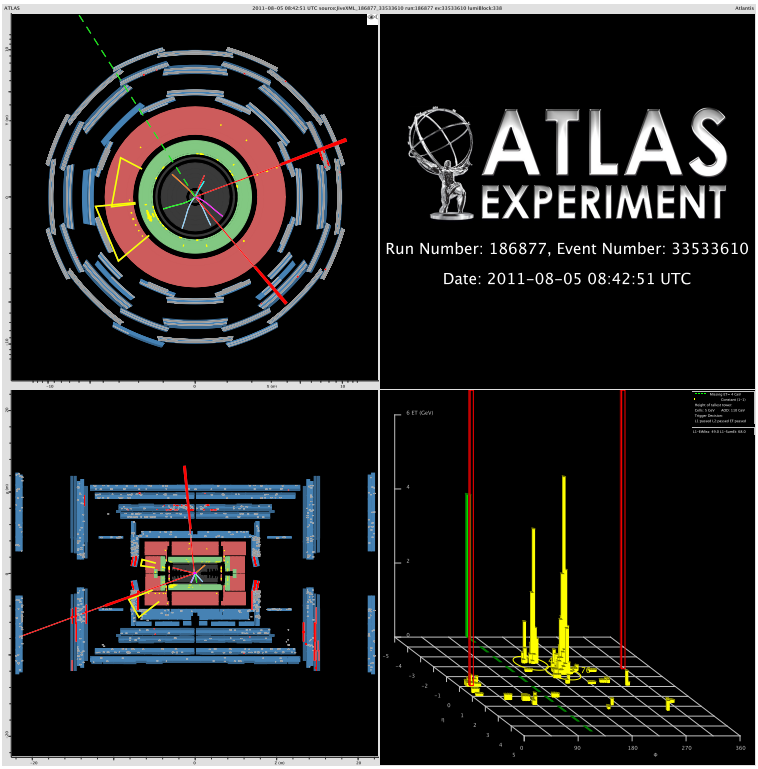

Figure 11.8: Event displays for 1$^{\mathrm{st}}$ data event passing all selection requirements.

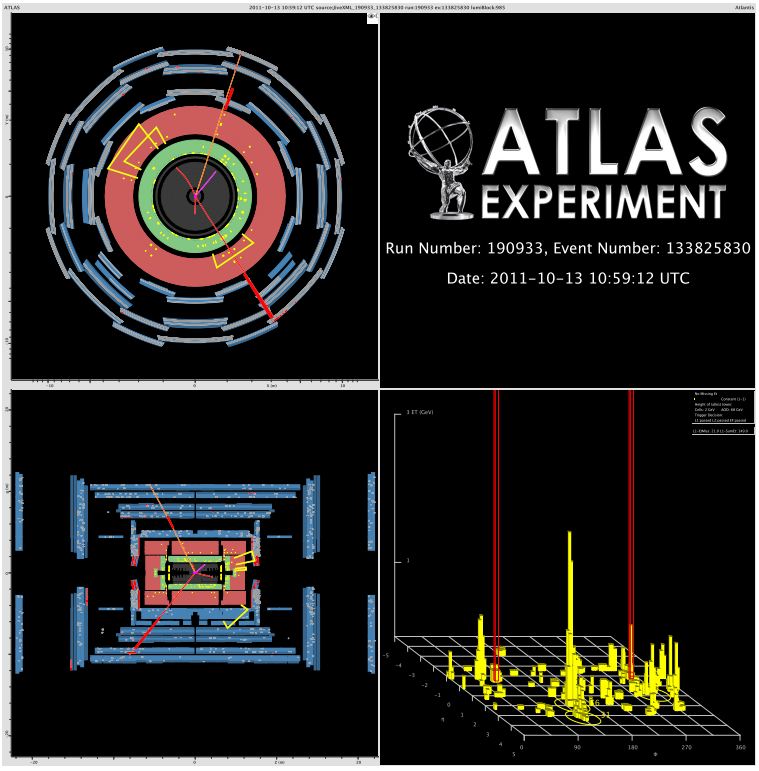

Figure 11.9: Event displays for 2nd data event passing all selection requirements.

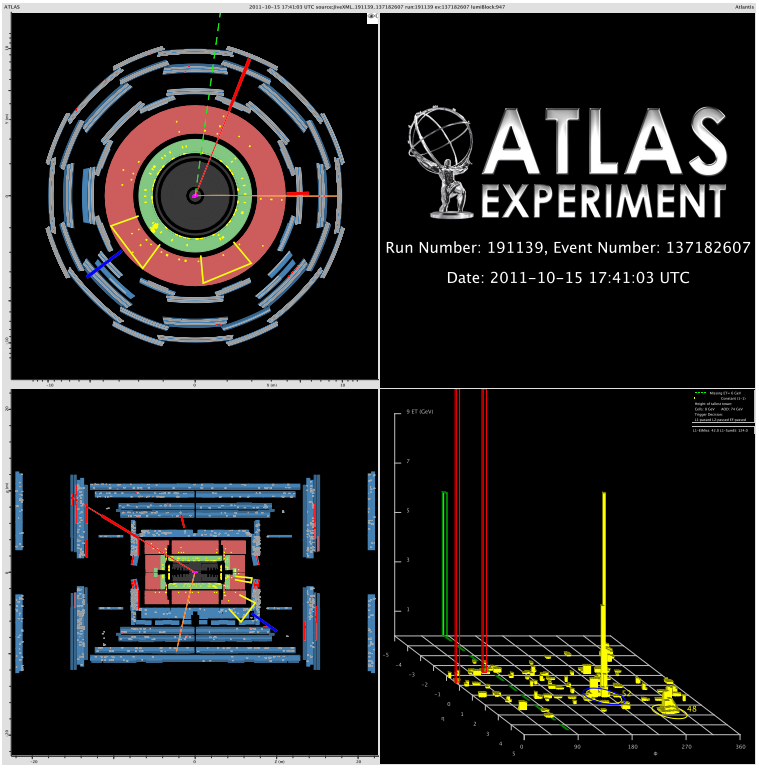

Figure 11.10: Event displays for 3rd data event passing all selection requirements.

Source	$\mu^{\pm}\mu^{\pm}$
WZ	$1.0 \pm 0.2 \pm 0.3$
ZZ	$0.22 \pm 0.05^{+0.07}_{-0.06}$
$W^{\pm}W^{\pm}$	$0.15 \pm 0.04 \pm 0.08$
$t\bar{t} + V$	$0.23 \pm 0.04 \pm 0.12$
Charge mis-measurement	< 0.03
Non−prompt	$1.1 \pm 0.5^{+0.6}_{-0.5}$
Total background	$2.7 \pm 0.5^{+0.7}_{-0.6}$
Data	3

Table 11.3: Expected and observed number of events containing two same-sign isolated muons after all selection cuts. The uncertainties are stated as statistical followed by systematic except for the case where zero events are expected, where a 68% upper limit is shown.

11.2 Limits on Heavy Neutrino Production

With no observed excess above the SM predictions we set direct limits on the cross section times branching ratio for the production of heavy neutrinos decaying into two same-sign muons and two jets. This cross section is then interpreted as a limit on the coupling squared between the heavy neutrino and muon, $|V_{\mu N}|^2$.

The number of events observed after the selection requirements is shown in table 11.3. The number of events is used to set 95% confidence level limits on the cross section times branching ratio, $\sigma(pp \to \mu^{\pm}N \to \mu^{\pm}\mu^{\pm}W^{\mp} \to \mu^{\pm}\mu^{\pm}q\bar{q}')$. The limits are obtained using the statistical CL_s modified frequentist formalism [120] with the profile likelihood test statistic [121] as discussed in Section 6.3, taking the statistical and systematic uncertainties discussed in section 10.2 as nuisance parameters.

The p_0-value for the observed number of events, defined as the probability that a background-only experiment is more signal-like in terms of the test statistic than the observed data is found to be 0.42. This indicates that the data is consistent with the expectation from the background model. The limits are presented in Figure 11.11 and table 11.4 as a function of the heavy neutrino mass. The shape of the limits on the cross section times branching ratio are controlled by the acceptance of the signal, which falls rapidity between masses of 100−120 GeV and then has little dependence on the neutrino mass. The limit on the coupling squared are obtained by dividing the limit on cross section times branching ratio with the signal cross sections calculated in Section 2.5.2. The limits are strongest for neutrino masses of 120 GeV, while the limit gets weaker for larger neutrino masses, due to the shape of the signal cross section.

This procedure assumes that only the lightest of the heavy neutrinos contributes to the cross section, and the other neutrinos are heavy enough that any interference is negligible at

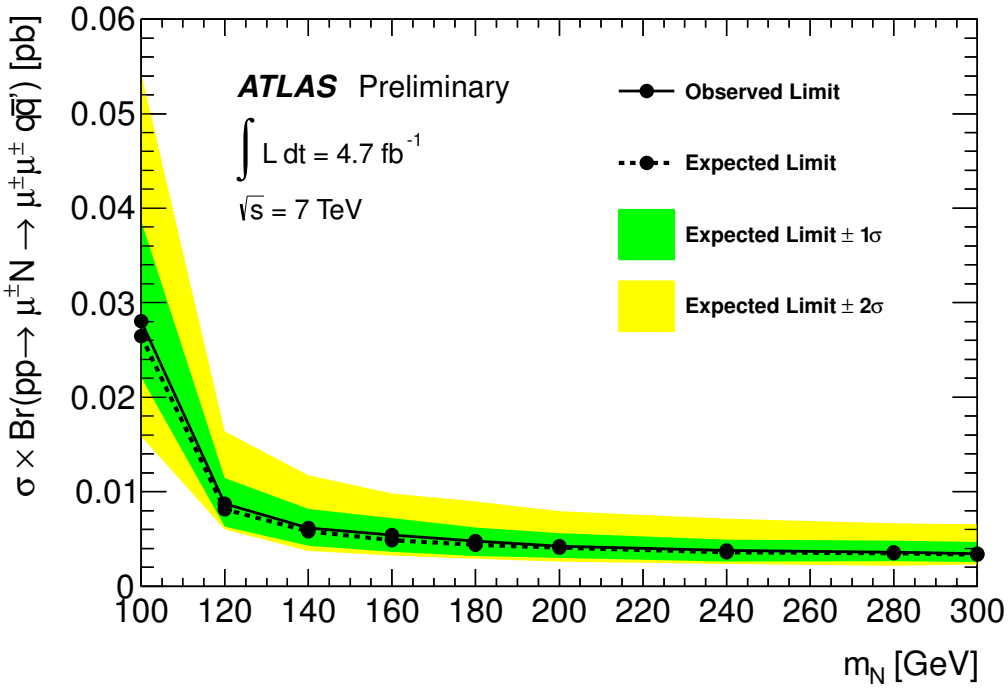

Figure 11.11: Observed and expected 95% confidence level limits on the cross section times branching ratio for the production of heavy Majorana neutrinos as a function of the heavy neutrino mass.

Neutrino mass [GeV]	Expected limit [fb]	Observed limit [fb]
100	26	28
120	8.2	8.8
140	5.8	6.2
160	4.9	5.4
180	4.1	4.2
200	4.1	4.2
240	3.6	3.8
280	3.5	3.6
300	3.3	3.4

Table 11.4: Observed and expected 95% confidence level limits on the cross section times branching ratio for the production of heavy Majorana neutrinos.

any given heavy neutrino mass. A search for heavy Majorana neutrinos have recently been performed by the CMS experiment [122] using the same dataset as used in this thesis. The resulting limits on the coupling squared for this analysis are compared to the limits from CMS in Figure 11.12. The limits on $|V_{\mu N}|^2$ presented in this thesis are more stringent than those set by CMS and are the strongest direct limits to date for neutrinos masses above 100 GeV. This is due to the optimisation of the event selection performed in this analysis to increase signal significance, particularly the isolation as presented in section 6.2.

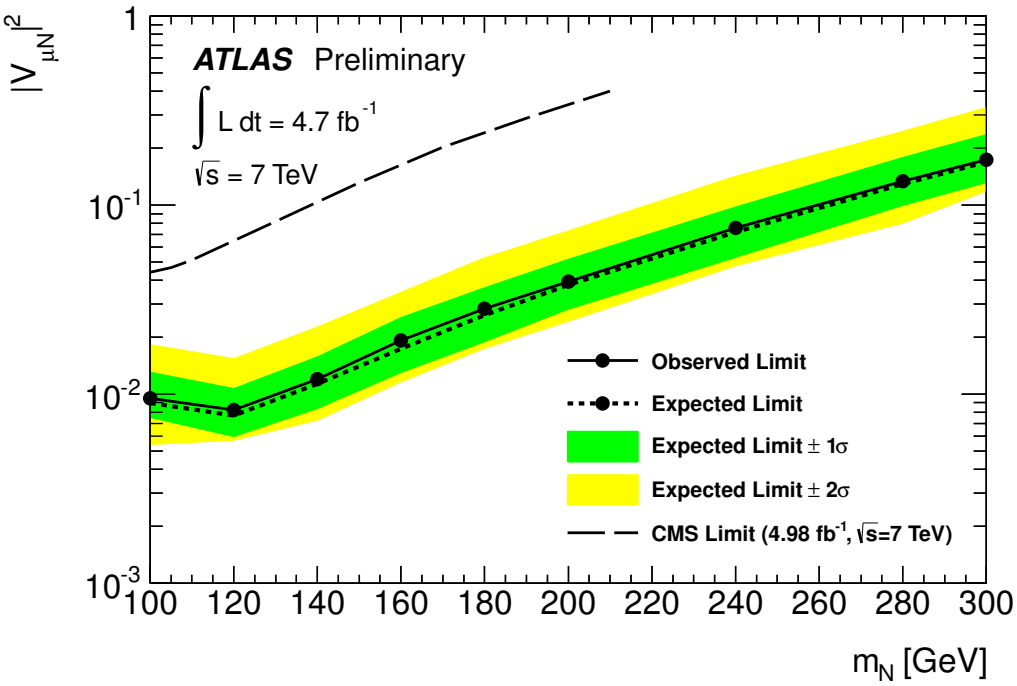

Figure 11.12: Observed and expected 95% confidence level limits on the cross section times branching ratio on the coupling parameter $V_{\mu N}$ as a function of the heavy neutrino mass.

The search for a heavy neutrino in the LRSM was also performed by the ATLAS and CMS collaborations with 2.1 fb^{-1} [52] and 4.7fb^{-1}respectively. In this search the shapes of the reconstructed mass of the right-handed W_R and the heavy neutrino N are used as templates in each dilepton channel. The limits on the mass of the heavy neutrino N versus the mass of W_R can be seen in Figure 11.13. This analysis was able to place limits on the mass of the W_R up to 2.5 TeV, and exclude masses of N up to 1.4 TeV for specific masses of W_R. These limits use a Bayesian [123] approach, where the systematic uncertainties are treated as nuisance parameters with a truncated Gaussian as a prior shape. The prior shape on the parameter of interest, $\sigma \times BR$ is assumed to be flat. The best sensitivity appears in the Majorana case, since this uses both opposite-sign (OS) and same-sign (SS) final states.

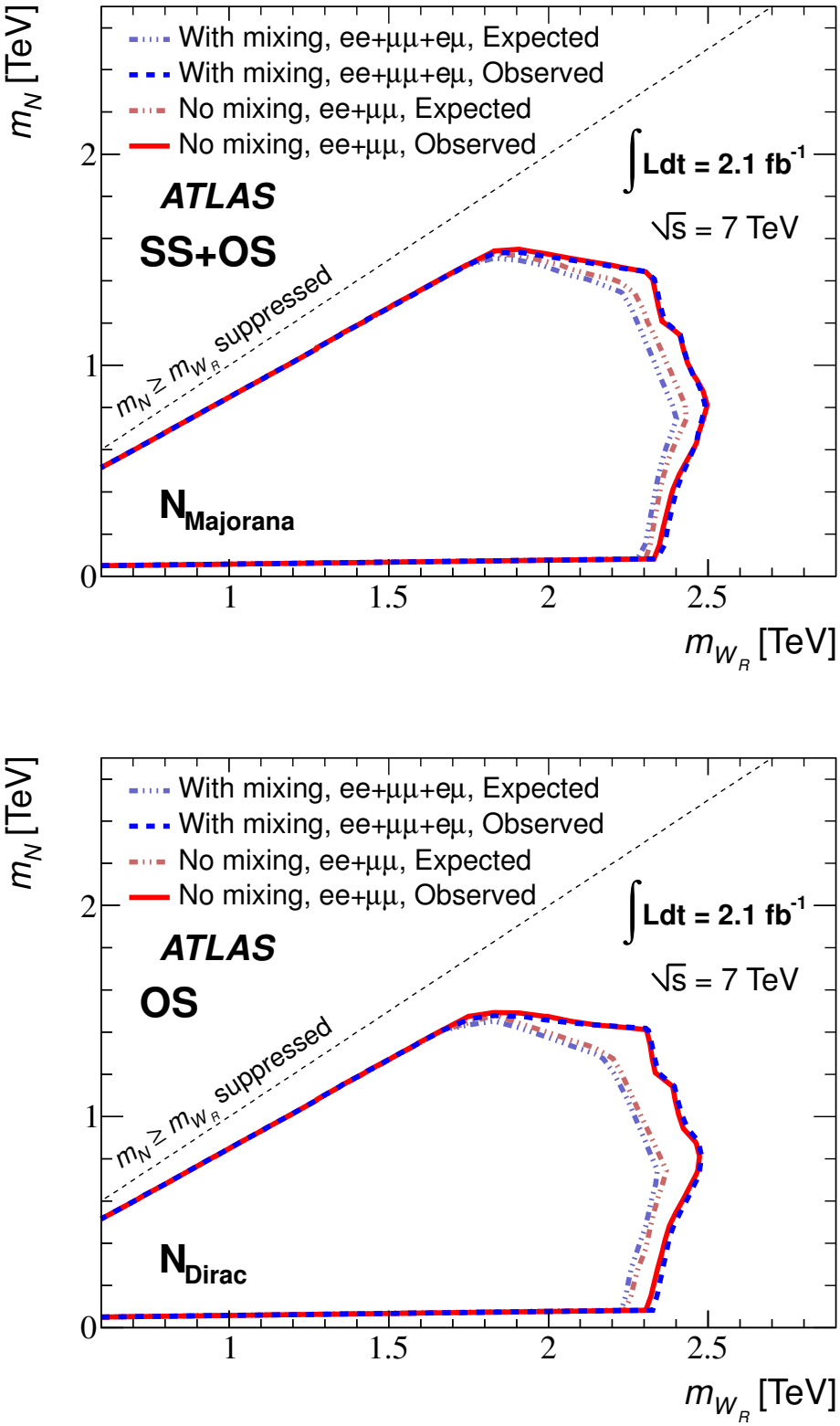

Figure 11.13: Expected and observed 95% C.L. upper limits on the heavy neutrino and W_R masses for the Majorana (top) and Dirac (bottom) cases.

Chapter 12

Conclusions

A search for a Majorana neutrino in the minimal extension to the Standard Model using events with same-sign muon pairs and jets is presented using 4.7 fb^{-1} of collision data recorded in 2011 with the ATLAS detector at CERN. No significant signal is found and the limits on the cross section times branching ratio for heavy Majorana neutrino production are set.

Only the muon channel is analysed, looking for distinct lepton number violating processes. The data events are required to pass the single muon trigger, with a threshold of 18 GeV, which was available due to the improvements in the processing times [84] discussed in this thesis. Events are selected containing two muons with transverse momentum $p_{\mathrm{T}} > 25$ and 20 GeV respectively, and two jets with transverse momentum $p_{\mathrm{T}} > 20$ GeV. The main backgrounds to the signal are events from diboson production, events where a W/Z boson is produced in association with a $t\bar{t}$ pair and events containing non-prompt muons. The non-prompt backgrounds are determined from the data using the matrix method. This method relies on applying weights to a loose data sample using efficiencies of prompt and non-prompt muons to pass the isolation requirements that are measured in the data. The rest of the background processes are estimated using Monte Carlo (MC) simulation and normalised by their known cross section. The uncertainties on the normalisation of the diboson backgrounds were taken from control samples of three or four muons in the data, while the $W/Z + t\bar{t}$ samples are taken from a conservative uncertainty on the next to leading order cross sections. The simulation is corrected for known differences between the MC and data. All the background samples are verified in a number of data control samples.

The backgrounds from Z+jets are to a good approximation entirely removed by requiring the charge of the muons to be the same, and the charge of the track measurements in the muon spectrometer and inner detector to be consistent. Backgrounds from semi-leptonic decays of b hadrons are significantly reduced by having strict requirements on the isolation and impact parameters of the muon tracks.

With no excess of data observed, 95% confidence level limits are set on the cross section

times branching ratio of heavy neutrino production for neutrino masses in the range $100 < m_{\mathrm{N}} < 300$ GeV. The observed limits range from 28 fb at $m_{\mathrm{N}} = 100$ GeV to 3.4 fb at $m_{\mathrm{N}} = 300$ GeV [108]. These are the world's best direct limits between the mass range of 100 to 210 GeV and the world's first limits for heavy neutrino masses between 210 and 300 GeV. The limits are a factor of 5 better than the latest CMS published results with 4.98 fb^{-1}.

The ATLAS experiment is currently running with a centre of mass energy of 8 TeV. This offers an increase of between 60 and 90% in the signal cross section relative to the 7 TeV collisions used in this analysis. The luminosity expected in the 2012 running is expected to be upward of 25 fb^{-1}. The search for heavy neutrinos will be extended into the di-electron channel, and flavor mixing e-μ channels. Since the LEP experiments has no sensitivity above 100 GeV this will be the first direct limits in both of these channels for this kinematic region (excluding the neutrino less double beta decay results). It is also worth noting that while the limits on the coupling V_{eN} from the neutrino less double beta decay results are vert tight there can in principle be cancellations which weaken this limit. This updated analysis will use a factor of 8–10 times the dataset used in this analysis and will use many of the studies and techniques performed by the author. This can allow ATLAS to make a discovery of a heavy Majorana neutrino which would have a profound impact on particle physics and open the path to understand the origin of the mass of the neutrinos and provide a direct observation of lepton number violation.

Bibliography

[1] P. W. Higgs, Phys. Lett. **12**, 132 (1964).

[2] ATLAS Collaboration, G. Aad *et al.*, Phys. Lett. **B 710**, 49 (2012).

[3] CMS Collaboration, C. Serguei *et al.*, Phys. Lett. **B 716**, 30 (2012).

[4] Y. Fukuda *et al.*, Phys. Rev. Lett. **81**, 1158 (1998).

[5] R. N. Mohapatra and G. Senjanovic, Phys. Rev. Lett. **44**, 912 (1980).

[6] R. N. Mohapatra and G. Senjanovic, Phys. Rev. Lett. **D 23**, 165 (1981).

[7] A. Davidson and K. C. Wali, Phys. Rev. Lett. **60**, 1813 (1988).

[8] A. Pilaftsis, Z. Phys. **C 55**, 275 (1992).

[9] F. Halzen and A. Martin, *Quarks and Leptons*, 1st edition ed. (John Riley & Sons, New York, 1984).

[10] J. Beringer *et al.*, Phys. Rev. **D 80** (2012).

[11] CDF and D0 Collaborations, R. Lopes De Sa and C. Rafael, FERMILAB-CONF-12-103-E (2012).

[12] M. Yao *et al.*, Journal of Physics G: Nuclear and Particle Physics **33**, 1 (2006).

[13] N. Cabibbo, Physics Review. Letters **10**, 531 (1963).

[14] M. Kobayashi and T. Maskawa, Prog. Theor. Phys. **49**, 652 (1973).

[15] C. L. Cowan, Jr., F. Reines, F. B. Harrison, H. W. Kruse, and A. D. McGuire, Science **124**, 103 (1956).

[16] K. Nakamura *et al.*, J. Phys. G **37** (2010), (Partice Data Group).

[17] R. Davis, Phys. Rev. Lett. **12**, 303 (1964).

[18] V. Gribov and B. Pontecorvo, Physics Letters B **28**, 493 (1969).

[19] B. Pontecorvo, Soviet Journal of Experimental and Theoretical Physics **26**, 984 (1968).

[20] Z. Maki, N. M., and S. Sakata, Progress of Theoretical Physics **28**, 870 (1962).

[21] A. Goobar, S. Hannestad, M. Edvard, and H. Tu, JCAP **0606**, 019 (2006).

[22] T. Schwetz, M. Tortola, and J. Valle, New J. Phys. **13**, 063004 (2011).

[23] E. Otten and C. Weinheimer, Rept. Prog. Phys. **71**, 086201 (2008).

[24] KATRIN Collaboration, A. Osipowicz *et al.*, (2001), hep-ex/0109033.

[25] R. Mohapatra and A. Smirnov, Ann. Rev. Nucl. Part. Sci. **56**, 569 (2006).

[26] S. Weinberg, Phys. Rev. Lett. **43**, 1566 (1979).

[27] P. Minkowski, Phys. Lett. **B 67**, 421 (1977).

[28] R. N. Mohapatra and G. Senjanovic, Phys. Lett. **44**, 912 (1980).

[29] J. Schechter and J. W. F. Valle, Phys. Rev. **D 22**, 2227 (1980).

[30] Kersten, Joern, Smirnov, and Y. Alexei, Phys. Rev. **D 76**, 073005 (2007).

[31] T. Han and B. Zhang, Phys. Rev. Lett. **97**, 171804 (2006).

[32] F. del Aguila, J. Aguilar-Saavedra, and R. Pittau, JHEP **0710**, 047 (2007).

[33] F. M. L. Almeida Jr, Y. A. Coutinho, J. A. Martins Simoes and M. A. B. do Vale, Phys. Rev. **D 62**, 075004 (2000).

[34] A. Atre, T. Han, P. Silvia, and B. Zhang, JHEP **0905**, 030 (2009).

[35] S. Bray, J. S. Lee, and A. Pilaftsis, Nucl. Phys. **B 786**, 95 (2007).

[36] M. Magg and C. Wetterich, Phys. Lett. **B 94**, 61 (1980).

[37] T. P. Cheng and L. F. Li, Phys. Rev. **D 22**, 2860 (1981).

[38] G. Lazarides, Q. Shafi, and C. Wetterich, Nucl. Phys. **B 181**, 287 (1981).

[39] R. N. Mohapatra and G. Senjanovic, Phys. Rev. **D 23**, 165 (1981).

[40] ATLAS Collaboration, G. Aad *et al.*, Eur. Phys. J. **C 72**, 2244 (2012).

[41] CMS Collaboration, S. Chatrchyan *et al.*, CERN Report No. CMS-PAS-HIG-12-005, 2012 (unpublished).

[42] Foot, Robert, H. Lew, X. He, and G. C. Joshi, Z. Phys. **C44**, 441 (1989).

[43] CMS Collaboration, S. Chatrchyan *et al.*, Phys. Lett. **B 718**, 348 (2012).

[44] R. N. Mohapatra, Phys. Rev. Lett. **56**, 561 (1986).

[45] R. N. Mohapatra and J. W. F. Valle, Phys. Rev. D **34**, 1642 (1986).

[46] P. B. Dev and A. Pilaftsis, Phys. Rev. **D 86**, 113001 (2012).

[47] Chen, Chien-Yi, and P. B. Dev, Phys. Rev. **D 85**, 093018 (2012).

[48] J. C. Pati and A. Salam, Phys. Rev. **D 10**, 566 (1974).

[49] R. N. Mohapatra and J. C. Pati, Phys. Rev. **D 11**, 2558 (1975).

[50] G. Senjanoic and R. N. Mohapatra, Phys. Rev. **D 12**, 1502 (1975).

[51] CMS Collaboration, Chatrchyan *et al.*, Phys. Rev. Lett. **109**, 261802 (2012).

[52] ATLAS Collaboration, G. Aad *et al.*, Eur. Phys. J. **C 72**, 2056 (2012).

[53] M. Daum *et al.*, Phys. Rev. Lett. **85**, 1815 (2000).

[54] M. Cirelli, G. Marandella, S. Alessandro, and F. Vissani, Nucl. Phys. **B 708**, 215 (2005).

[55] MiniBooNE Collaboration, A. Aguilar-Arevalo *et al.*, Phys. Rev. Lett. **98**, 231801 (2007).

[56] R. Shrock, Physics Letters B **96**, 159 (1980).

[57] ATLAS Collaboration, G. Aad *et al.*, JHEP **1110**, 107 (2011).

[58] D. I. Britton *et al.*, Phys. Rev. D **46**, R885 (1992).

[59] CHARM Collaboration, F. Bergsma *et al.*, Physics Letters B **128**, 361 (1983).

[60] L3 Collaboration, O. Adriani *et al.*, Phys. Lett. **B 295**, 371 (1992).

[61] DELPHI Collaboration, P. Abreu *et al.*, Z. Phys. **C 74**, 57 (1997).

[62] A. Kusenko, S. Pascoli, and D. Semikoz, JHEP **0511**, 028 (2005).

[63] R. A. N. Orloff, J. and C. Santoni, Phys. Lett. **B 550**, 8 (2002).

[64] NOMAD Collaboration, P. Astier *et al.*, Phys. Lett. **B 506**, 27 (2001).

[65] R. E. Nardi, Enrico and D. Tommasini, Phys. Lett. **B 327**, 319 (1994).

[66] S. Bergmann and A. Kagan, Nucl. Phys. **B 538**, 368 (1999).

[67] B. Bekman, J. Gluza, J. Holeczek, J. Syska, and M. Zralek, Phys. Rev. **D 66**, 093004 (2002).

[68] C. Aalseth *et al.*, (2004), hep-ph/0412300.

[69] D. Tommasini, G. Barenboim, J. Bernabeu, and C. Jarlskog, Nucl. Phys. **B 444**, 451 (1995).

[70] H1 Collaboration, C. Adloff *et al.*, Eur. Phys. J. **C 21**, 33 (2001).

[71] H1 and ZEUS Collaboration, N. Raicevic, (2006), hep-ex/0605050.

[72] R. Devenish and A. Cooper-Sakar, *Deep inelastic Scattering* (Oxford University Press, 2004).

[73] E. Eichten, I. Hinchliffe, K. D. Lane, and C. Quigg, Rev. Mod. Phys. **56**, 579 (1984).

[74] J. Pumplin *et al.*, JHEP **0207**, 012 (2002).

[75] S. E. Koorin, *Computational Physics, ISBN 0805354301*, 3rd ed. (Benjamin-Cummings, 1985).

[76] F. del Aguila, J. Aguilar-Saavedra, and R. Pittau, JHEP **0710**, 047 (2007).

[77] R. Scrivens *et al.*, CERN-ATS-2011-172 (2011).

[78] *ATLAS detector and physics performance: Technical Design Report 1* , Technical Design Report ATLAS No. CERN-LHCC-99-014 (CERN, Geneva, 1999).

[79] S. Haywood, CERN Report No. ATL-INDET-94-091. ATL-I-PN-91, 1994 (unpublished).

[80] ATLAS Collaboration, G. Aad *et al.*, JINST **3**, S08003 (2008).

[81] C. Cuenca Almenar, CERN Report No. ATL-DAQ-PROC-2010-018, 2010 (unpublished).

[82] P. Waller, CERN Report No. ATL-DAPR-PROC-2010-001, 2010 (unpublished).

[83] ATLAS Collaboration, G. Aad *et al.*, Eur. Phys. J. **C 71**, 1630 (2011).

[84] J. Almond *et al.*, CERN Report No. ATL-COM-DAQ-2012-021, 2012 (unpublished).

[85] T. Sjöstrand *et al.*, JHEP **05**, 026 (2006).

[86] G. Corcella *et al.*, JHEP **0101**, 010 (2001).

[87] R. D. Field and S. Wolfram, Nucl. Phys. **B 213**, 65 (1983).

[88] B. Andersson, G. Gustafson, G. Ingelman, and T. Sjostrand, Phys. Rept. **97**, 31 (1983).

[89] M.L. Mangano *et al.*, JHEP **07**, 001 (2003).

[90] J. Alwall *et al.*, JHEP **0709**, 028 (2007).

[91] T. Gleisberg *et al.*, JHEP **0902**, 007 (2009).

[92] S. Catani *et al.*, JHEP **0111**, 063 (2001).

[93] P. Nason, JHEP **0411**, 040 (2004).

[94] S. Frixione and B. R. Webber, JHEP **0206**, 029 (2002).

[95] GEANT4, S. Agostinelli *et al.*, Nucl. Instrum. Meth. **A 506**, 250 (2003).

[96] D. Adams *et al.*, CERN Report No. ATL-PHYS-INT-2009-110, 2009 (unpublished).

[97] C. ATLAS *et al.*, CERN Report No. ATL-PHYS-PUB-2010-013, 2010 (unpublished).

[98] B. P. Kersevan and E. Richter-Was, Computer Physics Communications **184**, 919 (2013).

[99] ATLAS Collaboration, G. Aad *et al.*, Phys. Rev. **D 85**, 032004 (2012).

[100] A. Lazopoulos, T. McElmurry, K. Melnikov, and F. Petriello, Phys. Lett. **B 666**, 62 (2008).

[101] J. M. Campbell and R. K. Ellis, JHEP **1207**, 052 (2012).

[102] ATLAS Collaboration, G. Aad *et al.*, ATLAS-CONF-2012-043 (2012).

[103] M. Cacciari, G. P. Salam, and G. Soyez, JHEP **04**, 063 (2008).

[104] ATLAS Collaboration, G. Aad *et al.*, (2011), 1112.6426.

[105] ATLAS Collaboration, G. Aad *et al.*, CERN Report No. ATLAS-CONF-2011-080, 2011 (unpublished).

[106] J. Butterworth, A. Davidson, M. Rubin, and G. Salam, Phys. Rev. **Lett 100**, 242001 (2008).

[107] G. Cowan, K. Cranmer, E. Gross, and O. Vitells, Eur. Phys. J. **C 71**, 1554 (2011).

[108] J. Almond, J. Klinger, M. Owen, and U. Yang, CERN Report No. ATLAS-CONF-2012-139, 2012 (unpublished).

[109] S. F.Campanario, C.Oleari and D.Zeppenfeld, (2009), hep-ph/0809.0790.

[110] K. M. A, Lazopoulos and F.Petriello, (2007), hep-ph/0703273.

[111] ATLAS Collaboration, G. Aad *et al.*, Phys. Lett. **B 709**, 137 (2012).

[112] S. Alekhin *et al.*, (2011), 1101.0536.

[113] A. Martin, W. Stirling, R. Thorne, and G. Watt, Eur. Phys. J. **C 63**, 189 (2009).

[114] P. M. Nadolsky *et al.*, Phys. Rev. **D 78**, 013004 (2008).

[115] R. D. Ball *et al.*, Nucl. Phys. **B 838**, 136 (2010).

[116] ATLAS Collaboration, G. Aad *et al.*, CERN Report No. ATLAS-CONF-2011-046, 2011 (unpublished).

[117] ATLAS Collaboration, G. Aad *et al.*, ATLAS-CONF-2011-032 (2011).

[118] ATLAS Collaboration, G. Aad *et al.*, ATLAS-CONF-2010-054 (2010).

[119] ATLAS Collaboration, G. Aad *et al.*, ATL-COM-PHYS-2011-979 (2011).

[120] A. L. Read, J. Phys. G **28**, 2693 (2002).

[121] G. Cowan, K. Cranmer, E. Gross, and O. Vitells, Eur. Phys. J. **C 71**, 1554 (2011).

[122] CMS Collaboration, S. Chatrchyan *et al.*, Phys. Lett. **B 717** (2012).

[123] T. Junk, Nucl. Instrum. Meth. **A 434**, 435 (1999).